



**HAL**  
open science

# Formulation d'un matériau cimentaire fibré ultrafluide : application au stockage des déchets radioactifs

Fariza Sultangaliyeva

## ► To cite this version:

Fariza Sultangaliyeva. Formulation d'un matériau cimentaire fibré ultrafluide : application au stockage des déchets radioactifs. Génie mécanique [physics.class-ph]. Université de Pau et des Pays de l'Adour, 2020. Français. NNT : 2020PAUU3041 . tel-03466298

**HAL Id: tel-03466298**

**<https://theses.hal.science/tel-03466298v1>**

Submitted on 5 Dec 2021

**HAL** is a multi-disciplinary open access archive for the deposit and dissemination of scientific research documents, whether they are published or not. The documents may come from teaching and research institutions in France or abroad, or from public or private research centers.

L'archive ouverte pluridisciplinaire **HAL**, est destinée au dépôt et à la diffusion de documents scientifiques de niveau recherche, publiés ou non, émanant des établissements d'enseignement et de recherche français ou étrangers, des laboratoires publics ou privés.



Université de Pau et des Pays de l'Adour  
École Doctorale des Sciences Exactes et leurs Applications

Thèse présentée pour obtenir le grade de  
Docteur en Génie Civil

Fariza Sultangaliyeva

**Formulation of fluid fire-resistant  
fiber-reinforced cementitious composite:  
Application to radioactive waste  
disposal**

Soutenance le 04/12/2020 devant le jury composé de:

Roberto Felicetti	Politecnico di Milano	Rapporteur
Arnaud Perrot	Université Bretagne Sud	Rapporteur
Sylvie Yotte	Université de Limoges	Président du jury
Christophe Lanos	Université de Rennes I	Examineur
Fabienne Robert	CERIB	Examineur
Guillaume Camps	ANDRA	Examineur
Christian La Borderie	UPPA	Directeur de thèse
Hélène Carré	UPPA	Encadrant
Nicolas Roussel	IFSTTAR	Encadrant
Pierre Pimienta	CSTB	Invité



## Acknowledgements

This poem written by Richard Feynman is dedicated to all the people who made a part of my doctoral journey. And special greetings to Olivier Nouailletas.

*There are the rushing waves  
mountains of molecules  
each stupidly minding its own business  
trillions apart  
yet forming white surf in unison.*

*Ages on ages  
before any eyes could see  
year after year  
thunderously pounding the shore as now.  
For whom, for what?  
On a dead planet  
with no life to entertain.*

*Never at rest  
tortured by energy  
wasted prodigiously by the Sun  
poured into space.  
A mite makes the sea roar.*

*Deep in the sea  
all molecules repeat  
the patterns of one another  
till complex new ones are formed.  
They make others like themselves  
and a new dance starts.*

*Growing in size and complexity  
living things  
masses of atoms  
DNA, protein  
dancing a pattern ever more intricate.*

*Out of the cradle  
onto dry land  
here it is  
standing:  
atoms with consciousness;  
matter with curiosity.*

*Stands at the sea,  
wonders at wondering: I  
a universe of atoms  
an atom in the Universe.*

## **Abstract**

The aim of this thesis is to design a self-compacting concrete with polypropylene fibers resistant to fire for a use in disposal containers for medium activity long-lived radioactive waste. The challenge of the work is presented by the use of polypropylene fibers that enhance fire resistance but drastically diminish workability of fresh concrete even when added at small volume fractions. Tests on laboratory scale are conducted with a purpose of evaluating rheological and high temperature behavior of cementitious materials containing polypropylene fibers.

In the first part, a study of rheological behavior of cement-based materials containing polypropylene fibers is accomplished. The aim of this study is to investigate the influence of polypropylene fibers on the yield stress of cement pastes and mortars. As a result, a model able to evaluate the volume of supplementary paste necessary to compensate the addition of polypropylene fibers on the fluidity of fresh concrete is proposed.

In the second part, an experimental and numerical investigation of high temperature behavior of cementitious materials with polypropylene fibers is completed in order to optimize the choice of polypropylene fibers for cementitious material for its improved thermal stability. Three different cementitious materials with three different granular skeletons containing various fiber geometries and dosages are tested (residual radial permeability and fire tests) in order to select an optimal fiber geometry and dosage. Following this, thermo-mechanical computations are developed at macro and meso scale using Cast3M. Consequently, a choice of polypropylene fiber diameter, length and dosage is proposed according to the maximum size of aggregate.

Finally, a method of concrete formulation with polypropylene fibers optimized from rheology and resistance to fire perspectives is presented. Fresh and hardened state properties of mixes are verified to ensure accordance with performance criteria specified by the project. At the end, designed mixes are subjected to fire tests conducted on uniaxially compressed prisms and, based on outcomes; final mixes are selected for further fire tests on higher scale concrete samples.

## Résumé en Français

Le but de ce travail est développer le béton fluide résistant au feu renforcé en fibres de polypropylène pour les colis de stockage des déchets radioactifs de moyenne activité à vie longue. Le défi de ce travail consiste de l'utilisation des fibres de polypropylène qui, même en ajoutant en petite quantité, améliorent la résistance au feu mais diminuent de manière significative la maniabilité des bétons frais. Des essais à l'échelle du laboratoire sont effectués afin d'évaluer les comportements rhéologique et à haute température des matériaux cimentaires contenant des fibres de polypropylène.

Dans la première partie, une étude du comportement rhéologique des matériaux cimentaires avec des fibres de polypropylène a été réalisée. Le but de cette étude est d'étudier l'influence de ces fibres sur le seuil d'écoulement des pâtes de ciment et des mortiers. Un modèle qui permet d'évaluer la quantité de pâte supplémentaire nécessaire pour compenser l'effet des fibres de polypropylène en fonction de la fluidité du béton frais a été développé.

Dans la deuxième partie, une étude expérimentale et numérique sur le comportement des matériaux cimentaires avec des fibres de polypropylène à haute température a été réalisée afin d'optimiser le choix des fibres pour améliorer la stabilité thermique d'un matériau cimentaire. Des essais de perméabilité résiduelle radiale et des essais feu sur les trois matériaux avec squelettes granulaires différents contenant des fibres de polypropylène de différentes géométries et dosages ont été réalisés dans un but de sélectionner une géométrie et un dosage optimal des fibres. Puis, des simulations thermomécaniques ont été développées sur Cast3M à l'échelle macroscopique et mésoscopique. Le choix du diamètre, de la longueur et du dosage des fibres de polypropylène a été fait en fonction de la taille maximale des granulats.

Finalement, une méthode de formulation du béton autoplaçant avec des fibres de polypropylène optimisé à la fois du point de vue de la rhéologie et de la résistance au feu a été présentée. Avec cette méthode, la conformité aux critères imposés sur les propriétés à l'état frais et à l'état durci du béton est vérifiée. Des éprouvettes de bétons sont testées sous chargement mécanique uniaxial et, en fonction des résultats, les formulations finales sont sélectionnées pour les futurs essais feu à l'échelle plus importante.

# Table of Contents

<b>Acknowledgements</b>	<b>iii</b>
<b>Abstract</b>	<b>iv</b>
<b>Résumé en Français</b>	<b>v</b>
<b>1 Introduction</b>	<b>1</b>
1.1 Context: Radioactive waste disposal in France	1
1.1.1 Sources of radioactive waste and existing disposal solutions	1
1.1.2 Novel solution: Underground waste disposal	3
1.2 Motivations of the thesis	5
1.3 Structure of the thesis	5
1.4 Reference list	7
<b>2 Fresh state behavior of fiber reinforced cementitious composites</b>	<b>8</b>
2.1 Introduction	8
2.2 Theoretical background	9
2.2.1 Rheology of cementitious materials	9
2.2.2 Packing regimes of inclusions	13
2.2.3 Fibers as special inclusions	14
2.3 Presentation of the study	19
2.3.1 Materials	19
2.3.2 Mixing protocols	21
2.3.3 Measurement protocols	21
2.4 Results	24
2.4.1 Polypropylene fibers in cement paste	24
2.4.2 Polypropylene fibers in mortar	31
2.5 Discussion	32
2.5.1 Random and self-avoiding walks	32
2.5.2 Yield stress prediction	34
2.5.3 Influence of paste consistency	38
2.5.4 Influence of presence of other inclusions	39
2.5.5 Application to self-compacting concrete design	41
2.6 Conclusions	41
2.7 Reference list	42
2.8 Basis notations	45
<b>3 High temperature behavior of fiber reinforced cementitious composites</b>	<b>46</b>
3.1 Introduction	46
3.2 Literature review	47
3.2.1 General information on concrete	47
3.2.2 Evolution of concrete constituents with temperature	49
3.2.3 Concrete permeability at high temperature	54
3.2.4 Thermal instability of concrete at high temperature	59
3.2.5 General information on polypropylene	68
3.2.6 How do polypropylene fibers prevent spalling of concrete?	73
3.2.7 Influence of fibers on intrinsic permeability	78
3.2.8 Optimization of fiber choice for spalling prevention	79

3.2.9	Mesoscale thermo-mechanical modelisation of concrete	81
3.3	Presentation of the experimental study	83
3.3.1	Materials, mixes and sample preparation	83
3.3.2	Apparatus and test procedures	91
3.4	Results and discussions of the experimental study	101
3.4.1	Thermal analysis of polypropylene	101
3.4.2	Residual radial permeability test	104
3.4.3	Fire test	114
3.4.4	Linking fire tests and permeability	125
3.5	Presentation of the numerical study	127
3.5.1	Numerical model	127
3.5.2	Influence of fiber expansion on mortar damage at HT	128
3.5.3	Mesoscale HT modelisation of cementitious materials	132
3.5.4	Conclusions of the numerical study	142
3.6	Conclusions	143
3.7	Reference list	144
<b>4</b>	<b>Formulation of fire resistant self-compacting concrete with polypropylene fibers</b>	<b>151</b>
4.1	Introduction	151
4.2	Basis of mix design	152
4.2.1	Requirements on concrete	152
4.2.2	Conclusions from rheology and fire tests	153
4.2.3	Mix design protocol	153
4.3	Formulation of self-compacting concrete	154
4.3.1	Materials choice	154
4.3.2	Experimental protocols	160
4.3.3	Design of reference mix	164
4.3.4	Design of fiber-reinforced mix	166
4.4	Presentation of final mixes	167
4.4.1	Overview of mixes	167
4.4.2	Validation of fresh and hardened state properties	167
4.5	Fire tests on final mixes	170
4.5.1	Samples and curing conditions	170
4.5.2	Numerical simulations of moisture distribution	171
4.5.3	Experimental apparatus and procedure	177
4.5.4	Fire test results	178
4.6	Conclusions	186
4.7	Reference list	187
<b>5</b>	<b>Conclusions and perspectives</b>	<b>189</b>
5.1	Overview of the thesis	189
5.2	Main conclusions	191
5.3	Perspectives	195
<b>Annex</b>		<b>197</b>

# CHAPTER 1

## INTRODUCTION

### 1.1 Context: Radioactive waste disposal in France

#### 1.1.1 Sources of radioactive waste and existing disposal solutions

Human activity produces a significant amount of radioactive waste. From the official site of ANDRA, French National Radioactive Waste Management Agency, following statistics are available on amount of radioactive waste produced in France in 2016 [1]:

- 2 kg of radioactive waste per year and per person
- 360 kg of household waste per year and per person
- 2500 kg of industrial waste per year and per person.

Radioactive waste in France comes from five sectors: research, electronuclear, defense, non-electronuclear and medical industries. Distribution of radioactive waste volume generated in each sector is provided in Figure 1.1. Nuclear power generation section contributes the most to radioactive waste production.

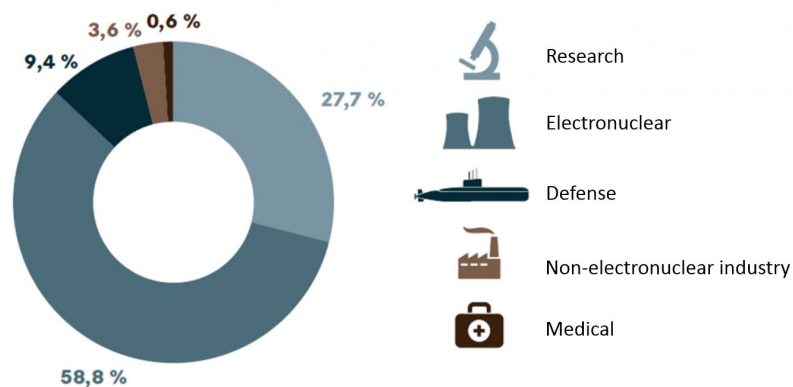


**Figure 1.1** Distribution of the volume of radioactive waste by economic sector at the end of 2016 adapted from [1].

France relies mainly on nuclear power energy as a source of electricity. Figure 1.2 presents location, number and power of each nuclear power reactor located across France. Majority of these reactors have power capacity of 900 and 1300 MWe.

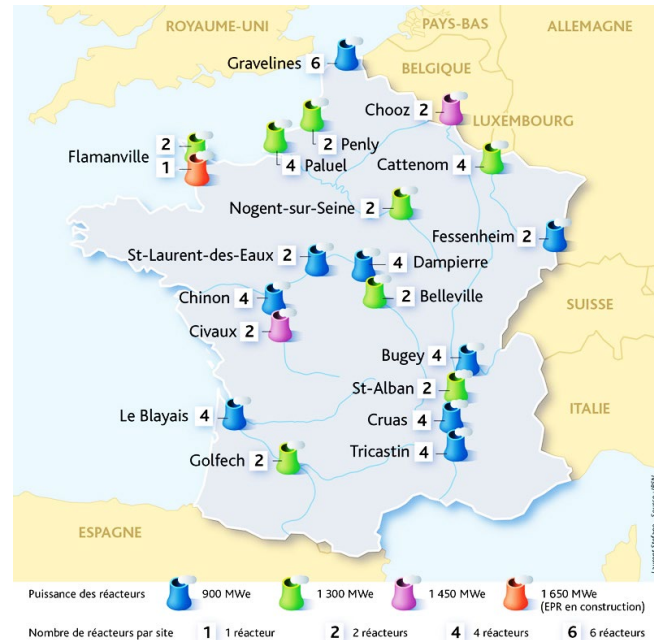


**Figure 1.2** Nuclear reactors across France [2].

Based on the radioactivity and life length, radioactive waste is classified into [1]:

- Very short-lived waste ( $\leq 31$  years)
- Very low level activity waste
- Low and intermediate level short-lived waste
- Low level long-lived waste ( $> 31$  years)
- Intermediate level activity long-lived waste
- High level waste.

For each waste category, an appropriate disposal type is adapted and summary of the disposal types is shown in Table 1.1. According to this table, ANDRA proposes a underground repository for long-lived waste of medium and high activity.

**Table 1.1** Category of waste and adapted disposal adapted from [1].

Category	Very short-lived waste	Short-lived waste	Long-lived waste
Very low level waste	Management by radioactive decay	Surface repository	
Low level waste		Surface repository	Low depth repository
Intermediate level waste			Underground disposal
High level waste	-		

### 1.1.2 Novel solution: Underground waste disposal

#### Project description

Project Cigéo of ANDRA involves a deep geological disposal (500 meters underground) of intermediate level and long-lived (ILW-LL) and high level radioactive waste (HLW). With a future localization in the east of France, between Meuse and Haute-Marne, the project involves surface and underground facilities presented in Figure 1.3.

Main concepts for this disposal project are [1]:

- Human and environment protection

Underground disposal of radioactive waste allows avoiding risks associated with human activity and provides sufficient time for radioactivity decay of waste.

- Stability of geological zone

Selected geological zone is suitable for this application due to a very low seismicity.

- Prevention of radioactive elements' dispersion

Expansive clay rock present on site is used as a protective barrier against the most mobile elements; it has a very low permeability for confining waste during decay of its radioactivity.

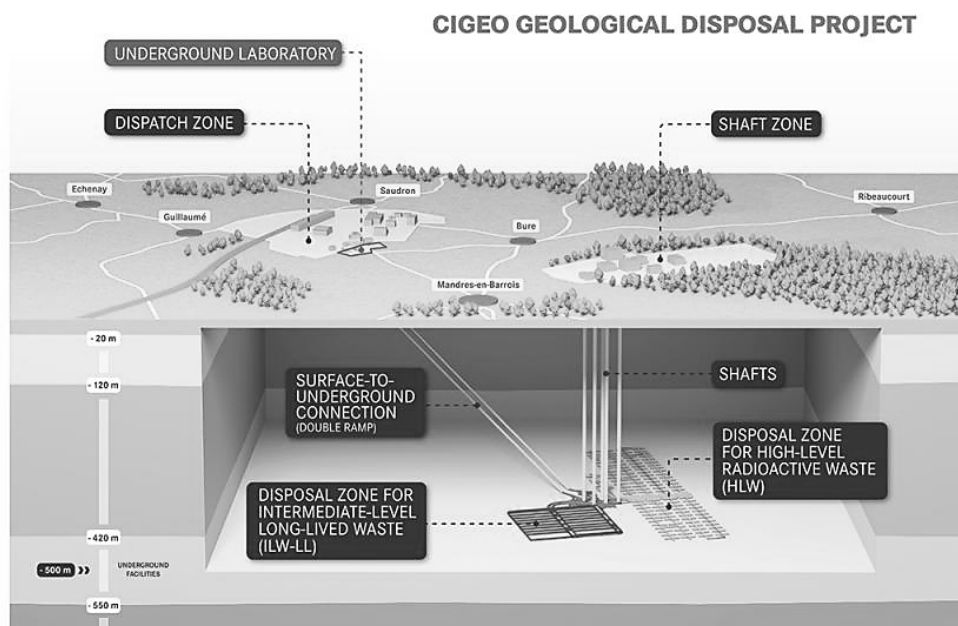
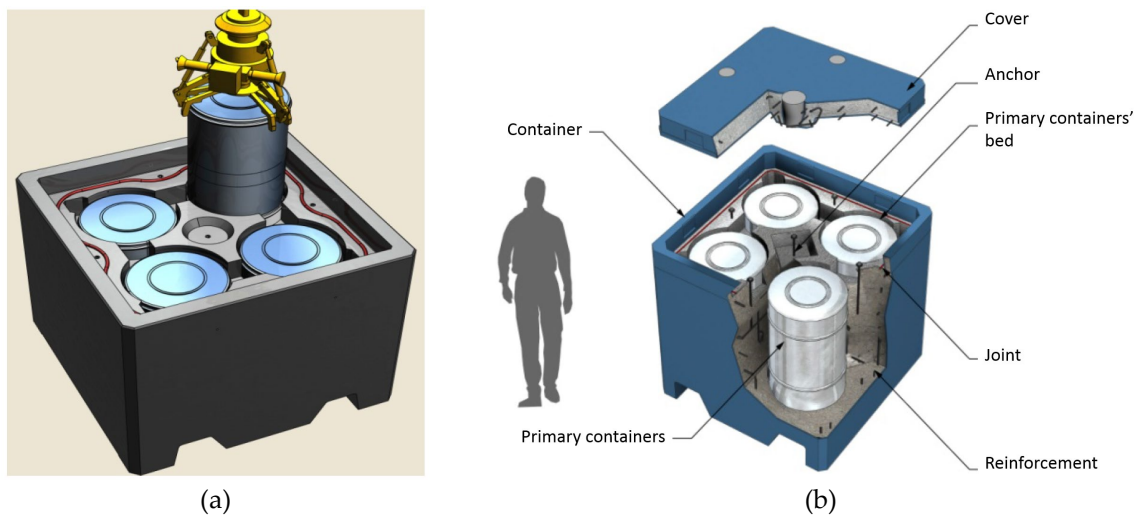


Figure 1.3 Industrial center for geological disposal (Cigéo) [1].

## Intermediate level and long-lived radioactive waste containers

In 2006, a law on radioactive materials and waste management imposed a 100-year period of reversibility on waste disposal. The term ‘reversibility’ is defined by a period during which disposal container could be removed from repository and rerouted to surface [3].

For intermediate level and long-lived radioactive waste, project proposes a disposal in prefabricated reinforced concrete containers. Packaging principle and container components for ILW-LL for a container with 4 reservations are presented in Figure 1.4a and 1.4b.



**Figure 1.4** Packing principle (a) and container structure (b) adapted from [3].

Project provides several estimations on disposal conditions of containers [3]:

- No freeze-thaw cycles; however, a slight heat originating from waste can be evacuated by natural ventilation
- Maximum temperature of container is approximately 65 °C
- Estimated relative humidity between 40 and 70% depending on underground conditions.

Project describes possible risks associated with containers:

- Risk of falling: Recovery of containers to surface and multilevel disposal (two to three levels, on top of each other) increases the risk of falling. It is necessary to ensure that at container fall, concrete container maintains its protecting function for primary reservations containing radioactive waste.
- Risk of fire accident: Concrete container should be able to withstand fire and protect primary waste reservations.

- Production of gas by radiolysis: Process of radiolysis of organic products produces gases. The evacuation of this gas should be ensured.

ANDRA imposes requirements on concrete formulation for radioactive waste containers [3]:

- High performance concrete durable for a period of 100 years
- Reinforced concrete with polypropylene fibers for fire resistance
- Self-compacting concrete mix
- Permeability for gas escape.

## **1.2 Motivations of the thesis**

The aim of the thesis is to design a self-compacting concrete with polypropylene fibers resistant to fire for a use in disposal containers of intermediate activity long-lived waste. The challenge of the work is represented by the use of polypropylene fibers that enhance fire resistance but drastically diminish workability of concrete even when added at small volume fractions. Tests on laboratory scale are conducted with a purpose of evaluating rheological behavior and high temperature behavior of cementitious materials containing polypropylene fibers.

A few studies examine the influence of polypropylene fibers on fresh state behavior of concrete without a possibility to predict their influence on the yield stress. For fire tests, literature shows a large set of experimental data with various controlling parameters, which creates a difficulty in identification of an optimal dosage and geometry of fibers required to avoid spalling. This thesis combines and optimizes these two research directions with a purpose of designing a self-compacting fire resistant concrete.

The particularity of this thesis lies in its contribution to scientific and technological knowledge on development of new cementitious composites. It is important to note that conclusions from this work are transferable and not limited to radioactive waste disposal.

## **1.3 Structure of the thesis**

This thesis is organized in six chapters including present introduction with a brief summary of each chapter provided below.

### **Chapter 2 – Fresh state behavior of fiber reinforced cementitious composites**

In Chapter 2, a study of rheological behavior of cement-based materials containing polypropylene fibers is presented. The aim of this chapter is to investigate the influence of polypropylene fibers on the yield stress of cement pastes and mortars.

First, a theoretical background on rheology of cementitious composites required for an understanding of experimental work is presented. The background covers interactions and flow regimes, used rheological model and packing regimes of inclusions. In the second part of the chapter, the experimental measurements of the yield stress of fiber reinforced cement pastes and mortars are performed. From these measurements, a physical model able to predict the yield stress of cement pastes with polypropylene fibers is developed. X-ray tomography scans of cement pastes with polypropylene fibers confirm the validity of this model. Finally, discussions on the influence of presence of other inclusions than fibers on the yield stress of cementitious composites are followed. At the end of this chapter, application to self-compacting concrete design is presented.

### **Chapter 3 –High temperature behavior of fiber reinforced cementitious composites**

In Chapter 3, an experimental and numerical investigation of behavior of cementitious materials with polypropylene fibers at high temperature is presented. This chapter is aimed at optimizing the choice of polypropylene fibers for cementitious material to improve its thermal stability.

First, a literature review required for an understanding of a current state-of-the-art in the subject is provided. The literature review covers topics such as evolution of concrete constituents and properties with temperature, concrete spalling due to fire exposure and use of polypropylene fibers as a preventative measure against spalling and, finally, mesoscopic thermo-mechanical simulations of cementitious materials at high temperature.

The second part of the chapter is dedicated to an experimental study of cementitious composites at high temperature. In this study, three different cementitious materials with three different granular skeletons containing various polypropylene fiber geometries and dosages are tested (residual radial permeability test and fire test) in order to select an optimal fiber geometry and dosage.

The third part of the chapter covers thermo-mechanical simulations of (i) fiber expansion in heated mortar and (ii) mesoscale simulations of three cementitious materials tested in the experimental part. The objective of these simulations is to study the damage responses of cementitious materials at high temperature due to: (i) expansion of fibers, (ii) change of granular skeleton.

## **Chapter 4 – Formulation of fire resistant self-compacting concrete with polypropylene fibers**

In Chapter 4, a method of concrete formulation with polypropylene fibers optimized from perspectives of rheology and resistance to fire is presented. The main goals of this work are following: (i) mix design for self-compacting fiber-reinforced concrete, (ii) verification of finalized mixes in fire tests and (iii) selection of concrete mixes for fire tests at intermediate scale (small slabs) and full scale (waste disposal containers).

First, the basis for formulation of fire resistant concrete is presented. It is composed of design specifications and conclusions from rheology and fire tests (Chapter 2 and 3) on choice of polypropylene fibers. Then, the mix design based on packing method is presented with each stage of the method applied to produced concrete mixes. In this method, fresh and hardened state properties are verified to ensure an accordance with performance criteria specified by the project. Finally, designed mixes are tested in fire tests conducted on uniaxially compressed prisms and, based on outcomes, final mixes are selected for further fire tests on higher scale concrete.

## **Chapter 5 – Conclusions and perspectives**

This chapter provides an executive summary of the entire work conducted during the thesis. Main findings of this research are highlighted and followed by a discussion of perspectives for future work.

### **1.4 Reference list**

[1]ANDRA. Official website. [andra.fr/index.php](http://andra.fr/index.php)

[2]IRSN. Institut de Radioprotection et de Sûreté Nucléaire. Official Website. [https://www.irsn.fr/FR/connaissances/Installations\\_nucleaires/Les-centrales-nucleaires/reacteurs-nucleaires-France/Pages/0-sommaire-parc-reacteurs-nucleaires-France.aspx#.XsSHQkQzapp](https://www.irsn.fr/FR/connaissances/Installations_nucleaires/Les-centrales-nucleaires/reacteurs-nucleaires-France/Pages/0-sommaire-parc-reacteurs-nucleaires-France.aspx#.XsSHQkQzapp)

[3]ANDRA. (2012). Cahier des charges- Développement d'une formulation béton pour conteneur de stockage MAVL et réalisation de prototypes.

## CHAPTER 2

# FRESH STATE BEHAVIOR OF FIBER REINFORCED CEMENTITIOUS COMPOSITES

### 2.1 Introduction

Self-compacting concretes possess a densely packed matrix, which leads to a decrease of flowability when fibers are added into the system. This conclusion is widely accepted for steel fibers [1]-[4], carbon fibers [5] and polypropylene fibers [6]-[12]. Studies show that increase of fiber volume fraction  $\phi_f$  induces an increase of the yield stress  $\tau_0$  (a minimum value of stress necessary for material flow) [4], [5], [9], [12] or reduction of slump/slump flow of cementitious material [6], [8], [11]. Increase of fiber length is found to provoke an increase in the yield stress for carbon fibers [5], polypropylene [9] and steel fibers [1]. An influence of fiber diameter is far less studied: for steel fibers, an increase of the diameter has shown no influence on the yield stress [13]. In terms of the influence of aspect ratio  $R$  (a ratio between fiber length and diameter), literature agrees that the yield stress increases with fiber aspect ratio in case of steel fibers [2], [3], [13]. It is generally agreed that in case of rigid fibers, the yield stress of cementitious materials scales with a fiber factor  $\phi_f R$  [2], [3], [14]-[16].

The aim of this chapter is to study the influence of flexible polypropylene fibers on the behavior of fresh cementitious composites. First, we present a brief introduction into the rheology of fiber reinforced concrete. We then show our experimental study on the influence of polypropylene fibers on fresh state behavior of cementitious materials. Using our results, we show that it is possible to predict the yield stress of cement pastes with polypropylene fibers. Finally, we suggest that the rheology of fiber-reinforced cementitious composites can

be estimated through simple addition of its inclusions' contributions to the yield stress development.

## 2.2 Theoretical background

The aim of this section is to provide essential basics of the rheology of cementitious composites. We first start by explaining the rheological behavior of cementitious materials and presenting interactions governing its flow regimes. Then, we focus on Bingham model, a simple rheological model for the yield stress fluids, selected for our study. As inclusions play a significant role in the evolution of rheological properties, we explain possible packing regimes on example of spheres and fibers in order to predict the yield stress of cementitious composites containing fibers.

### 2.2.1 Rheology of cementitious materials

#### Interactions and flow regimes

Rheological behavior of fresh cementitious materials is governed by the interactions to which its constituents are subjected. Size of concrete constituents varies from few nanometers (for superplasticizer molecules) to several centimeters (for coarse aggregates). Such polydispersity suggests a presence of various interactions. Depending on the size and the volume fraction of particles, one or several of listed interactions are dominant ones. It is possible to group these interactions into four types:

- (i) Brownian forces
- (ii) Colloidal forces
- (iii) Hydrodynamic forces
- (iv) Direct frictional forces between particles [17].

Macroscopic flow of cementitious materials is a result of competition between these interactions. We present in Figure 2.1 an evolution of apparent viscosity  $\eta$  (a ratio between shear stress and shear rate) as a function of shear rate  $\dot{\gamma}$ . Depending on mix-proportion and shear rate, cementitious materials exhibit shear-thinning (decreasing apparent viscosity with shear rate), Newtonian (constant apparent viscosity) and shear-thickening behavior (increasing apparent viscosity with shear rate) [17].

For the lowest  $s^{-1}$ , the shear thinning behavior of cementitious materials is observed. It is characterized by the competition between hydrodynamic dissipation of energy, colloidal

interactions and direct contacts between cement grains and friction between inclusions. Then, pseudo-Newtonian behavior, during which no evolution of the apparent viscosity appears, is reached. This flow regime is governed by direct contacts between particles and hydrodynamic dissipation of energy. Lastly, at high shear rate, shear thickening behavior of cementitious materials is expected. Inertia effect due to presence of inclusions and direct frictional contacts between inclusions present in the suspending medium contribute greatly to the dissipation of energy. In industrial application, this regime is unattainable. Therefore, at high shear rate the apparent viscosity converges to a constant value (see a plateau presented in Figure 2.1) [17].

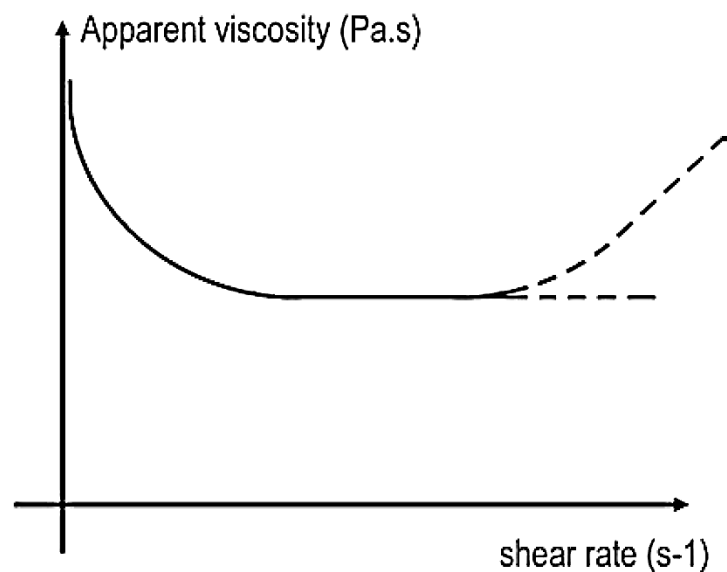


**Figure 2.1** Typical behavior of cementitious materials presented in terms of apparent viscosity  $\eta$  as a function of shear rate  $\dot{\gamma}$ . The dashed lines present a possible evolution of the property depending on mix proportion and shear rate [17].

### Time dependent behavior: hydration and thixotropy

It is important to note that rheological behavior of cementitious materials depends not only on physico-chemical properties of material and flow history but on time as well.

When water is mixed with cement, a creation of hydrates from dissolved phases of cement begins. This process is called as hydration. Main products created from hydration of  $C_2S$  and  $C_3S$  in cement are C-S-H (where C stands for CaO, S for  $SiO_2$  and H for  $H_2O$ ) or calcium hydrosilicate and  $Ca(OH)_2$  or calcium hydroxide (portlandite). The most reactive component of cement,  $C_3A$ , produces ettringite (AFt or calcium trisulfoaluminate) and AFm or hydrated

calcium monosulfoaluminate as hydration products. Hydration is a slow and irreversible process, which involves transition of the fresh cement paste into solid hard material.

Cement pastes present an evolution of the yield stress within time of several minutes after mixing phase. In the absence of the shear, structuration of the cement paste also known as thixotropy begins. The phenomenon of thixotropy is reversible: if the shear is high enough to destroy the structure formed during rest time, it leads to breaking of newly created connections [18]. A recent study on the origin of thixotropic presented in [19] reveals that the origin of thixotropy lies in the creation of the C-S-H bridges between cement particles. Even though thixotropy is reversible phenomenon, its implications in such civil engineering applications like multi-layer casting are very important due to their deteriorating effect [20].

It is necessary to note that in this study time dependent behavior of cementitious materials is not considered due to a limited time of paste rest and testing (less than a few minutes) after mixing phase.

### **Rheological model for cementitious materials**

It is agreed that cementitious materials are yield stress fluids. The yield stress  $\tau_0$  is defined as energy necessary to introduce into the system in order to break the interactions between the particles [17]. In other words, it is a threshold value of stress necessary to exert on the body to initiate its flow. Below this value, no deformation occurs and material does not flow. Many civil engineering materials behave in this manner such as ceramics, paints, concretes and mortars. Food products such food pastes, soups and foams exhibit similar type of rheological behavior [21].

Bingham model is often used to describe the rheology of fresh cementitious materials:

$$\tau = \tau_0 + \dot{\gamma}\mu_p \quad (2.1)$$

where  $\tau$  is the total stress,  $\tau_0$  is the yield stress,  $\dot{\gamma}$  is the shear rate and  $\mu_p$  is the plastic viscosity. Schematic presentation of the model is given in Figure 2.2.

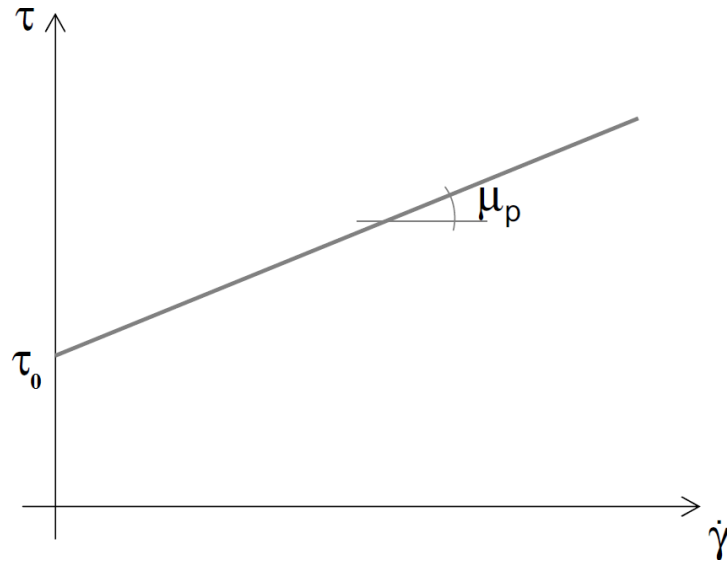


**Figure 2.2** Bingham model used to represent yield stress fluids [3].

We can consider cementitious materials as a dispersion of non-Brownian non-colloidal inclusions (sand, gravel and fibers) into the yield stress fluid (presumably homogeneous cement paste). In this case, size of cement grains in suspending fluid is negligible compared to size of inclusions and there are no physico-chemical interactions between inclusions and cement paste. In this approach, the finest inclusions (with a size comparable to cement grains) are neglected from consideration. Based on this approach, the evolution of rheological behavior of cementitious material is related to the yield stress of cement paste without inclusions  $\tau_{00}$  and size, shape and volume fraction of inclusions  $\phi$  [22]. In this case, based on the relation developed in [23], the evolution of the yield stress of suspension is written as [2],[24]:

$$\tau_0 \approx \tau_{00} f\left(\frac{\phi}{\phi_m}\right) \quad (2.2)$$

where  $\tau_0$  is the yield stress of cementitious material,  $\tau_{00}$  is the yield stress of cement paste,  $\phi$  is the volume fraction of inclusions and  $\phi_m$  is the dense packing fraction of inclusions.

In this work, we are interested in characterization of the influence of fibers on the rheology of cementitious composites. We, therefore, will present our results in the form of the relative yield stress (a ratio between the yield stress of suspending fluid with inclusions and the yield stress of suspending fluid).

## 2.2.2 Packing regimes of inclusions

Addition of inclusions into suspending fluid provokes interactions of type fluid-particle or particle-particle depending on the packing regime of inclusions. At low volume fractions, hydrodynamic interactions take place. There exists a diluted regime for which particles are located so far from each other that they stay undisturbed by their relative motion. In a semi-diluted packing regime, the movement of inclusions in the cement paste causes a deformation of the cement paste and generates an additional energy dissipation. In this case, apparent viscosity of suspension is greater than apparent viscosity of cement paste alone [25].

At higher volume fractions, direct frictional contacts between particles occur. A creation of sufficient contacts between the particles would allow achieving random loose packing or percolation fraction  $\phi_c$  which corresponds to a creation of the connected network of contacts between particles able to transmit an effort. Dense packing regime  $\phi_m$  is defined as a volume fraction of inclusions for which contacts between particles remain undisturbed even under energy being introduced into the system. Lastly, maximum packing regime  $\phi_M$  is achieved through an introduction of the infinite amount of energy [25]. For an asymptotic case of spherical monodisperse inclusions, the values for packing regimes are  $\phi_c \approx 0.5$ ,  $\phi_m \approx 0.64$  and  $\phi_M \approx 0.74$  [26]. A schematic presentation of packing regimes in case of spherical inclusions is shown in Figure 2.3.

Different models have been proposed in the literature to evaluate the packing of polydisperse aggregate mix. One of the works [27] presents a semi-empirical relation that estimates the packing  $\phi_m$  of the granular mix as:

$$\phi_m = 1 - 0.45 \left( \frac{d_{min}}{d_{max}} \right) \quad (2.3)$$

where  $d_{min}$  and  $d_{max}$  are the smallest and largest sizes of the particles in granular skeleton. The improved packing model is the compressible packing model of de Larrard [28], which allows determining the dense packing fraction of aggregate mix based upon the dense packing fraction of each aggregate and their volume fraction.

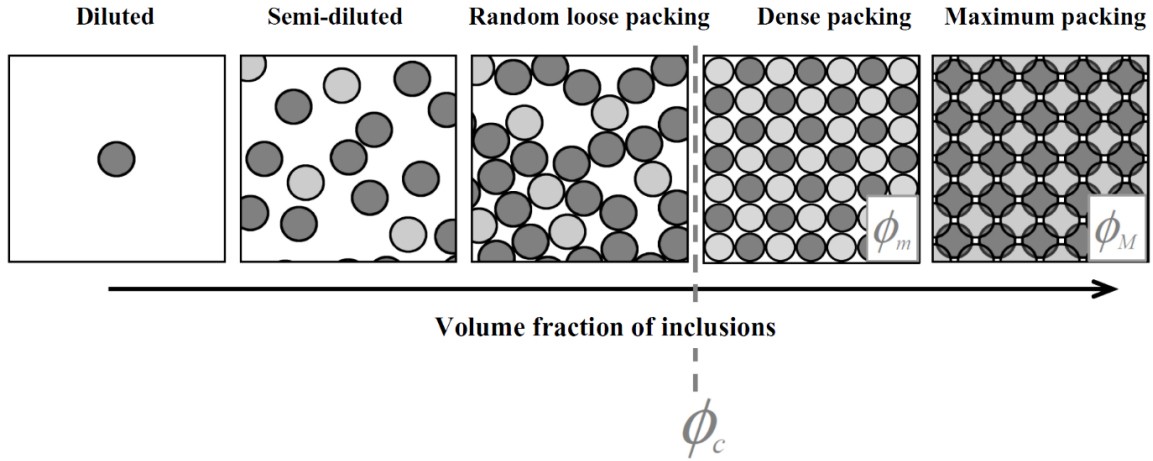


**Figure 2.3** Packing regimes for monodisperse spheres adapted from [3].

### 2.2.3 Fibers as special inclusions

Development of concrete applications has required an addition of other inclusions than aggregates into cement paste, for example, fibers. Fibers are inclusions of an elongated shape characterized by aspect ratio (a ratio of fiber length and diameter). There exists a variety of type of fibers: synthetic fibers (polypropylene, polyethylene), natural fibers (wool, jute, lax) and mineral fibers (glass, steel).

The elongated shape of fibers permits for these inclusions to influence a packing of aggregates. Rigid fibers, such as steel fibers, influence significantly the packing of the aggregates by pushing the aggregates apart (see Figure 2.4b). Opposed to rigid fibers, flexible fibers (see Figure 2.4c) tend to fill out the spaces between aggregates, they do not modify the packing as much as rigid ones [29].

It is worth mentioning that the flow of cementitious materials containing fibers induces a preferential orientation of fibers that alters its fresh state behavior, and when hardened, its mechanical properties [30]-[32].

Commercially available polypropylene fibers can be monofilament and fibrillated. Fibrillated fibers (see Figure 2.5a) consist of micro fibrils attached to a fibrillated network, whereas, monofilament fibers are singular filaments of polypropylene (see Figure 2.5b). In addition to this, based on their geometry, polypropylene fibers can be either microfibers (generally,  $L = 6 - 20$  mm,  $D = 18 - 50$   $\mu\text{m}$ ) or macrofibers (around  $L > 20$  mm and  $D = 100 - 600$   $\mu\text{m}$ ). In this work, we work with monofilament polypropylene microfibers.

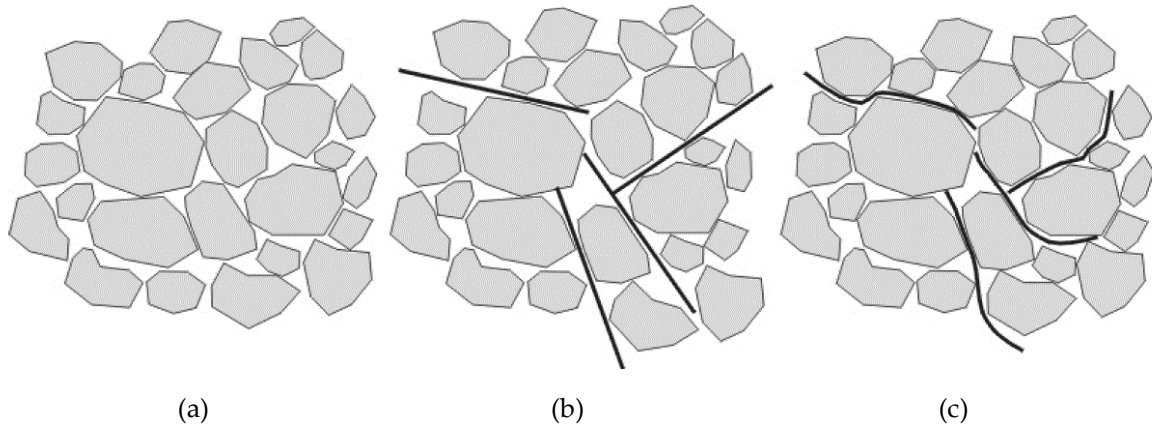


**Figure 2.4** Influence of fibers on the granular skeleton: a) without fibers, b) with rigid fibers, c) with flexible fibers [12].

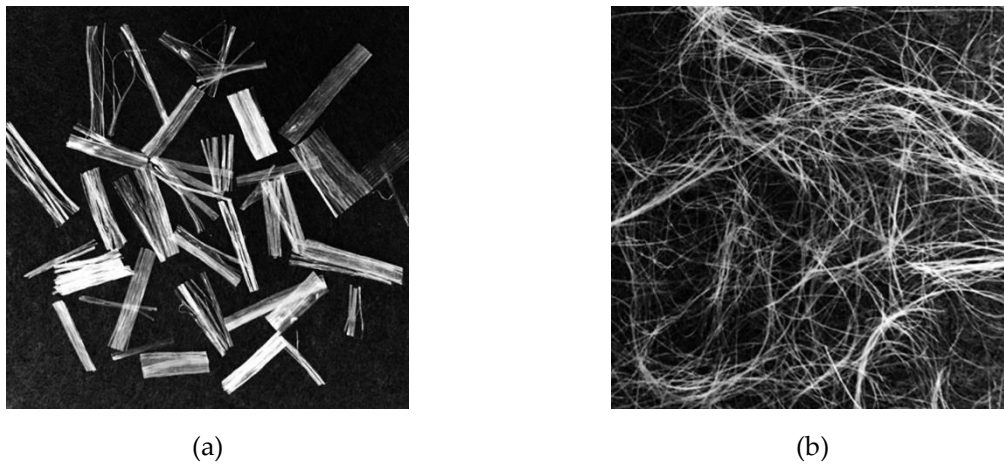


**Figure 2.5** Fiber types: a) Fibrillated, b) Monofilament [33].

In the following sections, a review of the influence of rigid fiber on the yield stress of cement pastes and mortar is presented with a purpose of application to study of the influence of flexible fibers.

### Rigidity criterion

Fibers can behave as rigid or flexible fibers. Criterion that distinguishes flexible fibers from rigid has been developed in [2], [3]. Fiber is represented as uniformly loaded beam submitted to the load of  $\tau_{00}D$  (in N/m) where  $\tau_{00}$  is the yield stress of the paste without fibers,  $D$  and  $L$  are the fiber diameter and length accordingly.

Then, fiber deflection  $f$  is:

$$f \cong \frac{\tau_{00}DL^4}{EI} \quad (2.4)$$

where  $E$  is elastic modulus of fiber (GPa) and  $I$  is quadratic moment of area of fiber (of order  $D^4$ ). The relative deflection  $f/L$  is then:

$$\frac{f}{L} \cong \frac{\tau_{00}R^3}{E} \quad (2.5)$$

We consider fiber rigid when [3]:

$$\frac{f}{L} \ll 1 \quad (2.6)$$

Using the rigidity criterion, a steel fiber with an aspect ratio of 50 and elastic modulus of 210 GPa in self-compacting concrete with the yield stress of 50 Pa has a relative deflection of 0.003%, while for polypropylene fibers with an aspect ratio of 300, elastic modulus of 1 GPa in the similar mix this value is of the order of a several hundred %.

### Rigid fiber packing regimes

Due to their elongated shape, fibers can rotate presenting different packing compared to spherical inclusions. Figure 2.6 presents random loose  $\phi_{cf}$ , dense  $\phi_{mf}$  and maximum packing fraction  $\phi_{Mf}$  on example of steel fibers. Philipse [34] states that random loose and dense packing fraction of slender bodies with an aspect ratio higher than 1 can be found as:

$$\phi_{cf} = \frac{\alpha_c}{R} \quad (2.7)$$

$$\phi_{mf} = \frac{\alpha_m}{R} \quad (2.8)$$

where  $\alpha_c$  and  $\alpha_m$  are coefficients determined experimentally.

It is found in [2] that these coefficients  $\alpha_c$  and  $\alpha_m$  are equal to 3.2 and 4 for steel fibers with aspect ratios between 50 and 100. For these fibers, for the volume fraction lower than  $3.2/R$ , interaction type is hydrodynamic and low influence of fibers is observed. For fractions between  $3.2/R$  and  $4/R$ , direct frictional contacts between fibers dominate the system and

contribute significantly to the dissipation of energy. Volume fractions higher than  $4/R$  almost stop the flow of suspension due to a formation of balls or clumps.

Opposite to rigid fibers, flexible polypropylene fibers can bend and create entangled structures or jams [35], therefore, their packing is different from packing of rigid fibers.

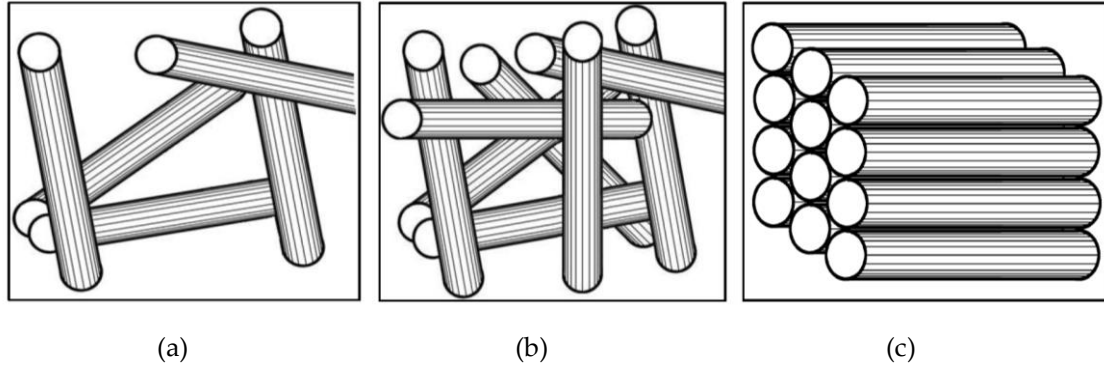


**Figure 2.6** Rigid fibers packing regimes: a) Random loose packing, b) Dense packing and c) Maximum packing [3].

### Yield stress prediction for cement paste with rigid fibers

We know that the relative yield stress evolves as a function of the relative packing fraction of fibers  $\phi_f/\phi_{mf}$ . Since dense packing fraction  $\phi_{mf}$  of steel fibers equals to  $4/R$ , the relative yield stress for cement pastes containing rigid fibers scales with relative fiber packing fraction  $\phi_f R/4$ . We present in Figure 2.7 (see circles for data) an experimental data from [2] that shows a good depiction of an evolution of the relative yield stress of cement paste with rigid fibers.

In order to establish an exact relationship, we apply a simple parabolic form between the yield stress  $\tau_0$  and relative fiber packing fraction  $\phi_f/\phi_{mf}$  presented in Equation 2.9. Tracing this model in Figure 2.7 (see a line), we note a good correlation between a fitted model and experimental data.

$$\tau_0 = \tau_{00} \left(1 - \frac{\phi_f}{\phi_{mf}}\right)^{-2} \quad (2.9)$$

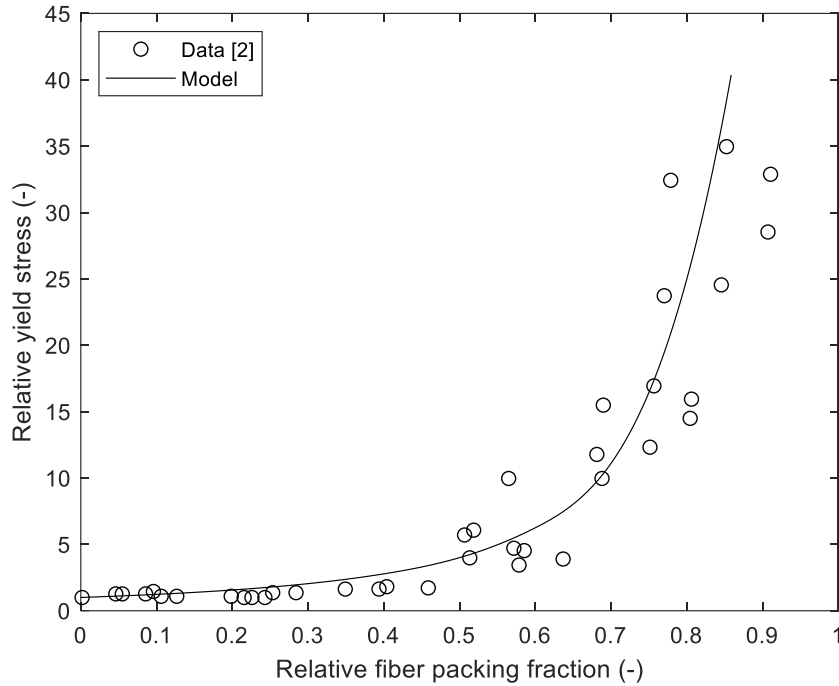


**Figure 2.7** Evolution of the relative yield stress (a ratio between the yield stress of cement paste with fibers and the yield stress of cement paste without fibers) as a function of the relative fiber volume fraction of steel fibers. Data is extracted from [2]. A parabolic equation is fitted as a model.

Majority of civil engineering applications require a presence of aggregates in cement paste, therefore, rising a need for packing model of aggregate-fiber mix. For this reason, a simple approach for a packing of sand particles and rigid fibers is proposed in [2]. Assuming that contributions of each type of inclusions are summed linearly and without taking into account the interactions between fibers and aggregates, total relative packing fraction of sand and rigid fibers equals to:

$$\frac{\phi_f}{\phi_{mf}} + \frac{\phi_s}{\phi_{ms}} = \frac{\phi_f R}{4} + \frac{\phi_s}{\phi_{ms}} \quad (2.10)$$

where  $\phi_s$  is the volume fraction of sand,  $\phi_{ms}$  is the dense packing fraction of sand.

Using this scaling, the relative yield stress of mortar with steel fibers evolves as a function of total relative packing fraction (Equation 2.10) as seen in Figure 2.8. This shows that for applications as ultra-high performance concrete, or UHPC, a simple linear model for inclusion mix of fiber-sand can be applied to predict an evolution of the yield stress.

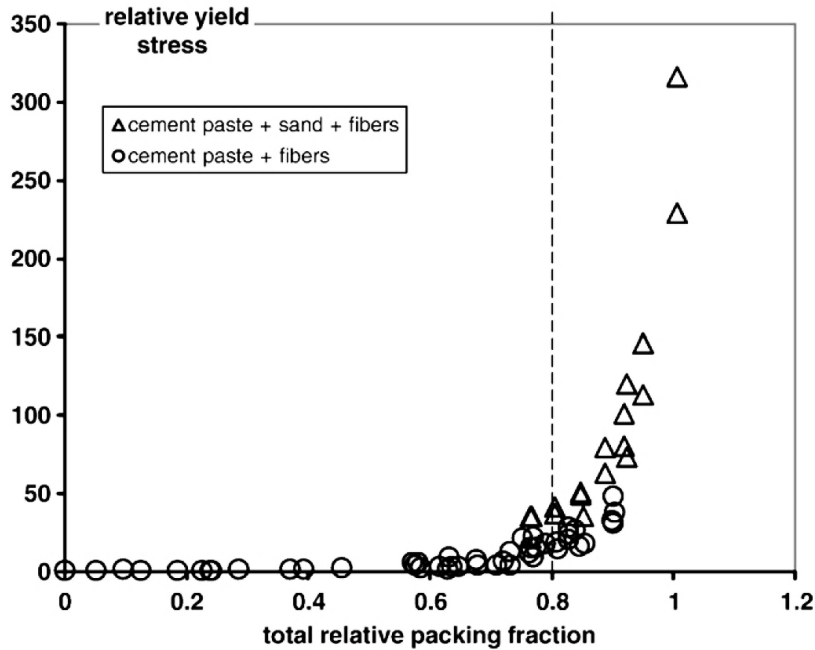


**Figure 2.8** Evolution of the relative yield stress as a function of the total relative packing fraction for steel fibers [2].

Presented literature review on rheological basics and influence of rigid fibers on the yield stress of cement pastes and mortars serves as a basis for an experimental program aimed at studying the influence of flexible fibers on fresh cementitious materials. Main concepts and experimental methods developed for rigid fibers in [2] are transferable to the case of flexible fibers. The principal difference between rigid and flexible fibers remains in the deformability of flexible fibers when subjected to stresses. This deformability of flexible fibers is a very important factor to take into account; therefore, new development on this matter is essential. Our objective is thus to develop a model for the yield stress of cement paste with flexible fibers, which could account for deformation of flexible fibers.

## 2.3 Presentation of the study

### 2.3.1 Materials

Cement pastes and mortars are prepared using CEM I 52.5N from Brest. The density of the cement is  $3150 \text{ kg/m}^3$  and its Blaine surface is  $4330 \text{ cm}^2/\text{g}$ . The composition of cement is given in Table 2.1. Sand Palvadeau 1/4 is used for preparation of mortars. Its particle size distribution is given in Figure 2.9. In order to have a distinct phase separation of cement paste from the finest particles of the sand, the fines smaller than 1 mm of the sand are avoided.

Density and water absorption coefficient of the sand are 2640 kg/m<sup>3</sup> and 0.9 % respectively. Prior to mortar preparation, the sand is dried in oven at 105 °C for 24 hours and then cooled down to an ambient temperature. Fibers studied are commercially available monofilament polypropylene fibers of different geometries from various providers listed in Table 2.2.

**Table 2.1** Chemical composition in % of cement.

CaO/SiO <sub>2</sub>	MgO	C <sub>3</sub> S	C <sub>2</sub> S	C <sub>3</sub> A	C <sub>4</sub> AF
3	0.8	60	13	2	13

**Table 2.2** Geometry of polypropylene fibers studied.

No	Aspect ratio (-), R	Length (mm), L	Diameter (μm), D	Provider
1	61	3	49	Baumhüter
2	176	6	34	Belgian Fibers
3	188	6	32	Baumhüter
4	300	6	20	Baumhüter
5	333	6	18	SIKA
6	353	12	34	SIKA
7	400	6	15	Baumhüter
8	414	12	29	SIKA
9	429	12	28	MGSI
10	529	18	34	BASF
11	588	20	34	SIKA
12	600	12	20	Würth
13	667	12	18	SIKA
14	706	24	34	Belgian Fibers

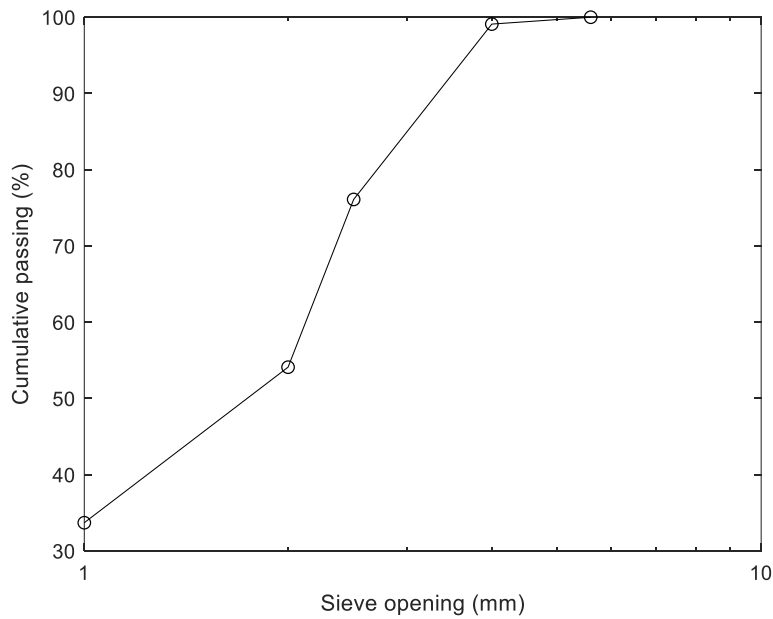


**Figure 2.9** Particle size distribution of sand Palvadeau 0/4.

### 2.3.2 Mixing protocols

Cement pastes with W/C = 0.35, 0.45 and 0.5 are prepared. Water and cement are added together and mixed for 2 minutes. Mixer is stopped, polypropylene fibers are added and the mix is remixed for 1 minute.

Mortars are prepared using 40 % volume of sand 1/4. First, sand and cement are mixed for 2 minutes. Then mixer is stopped and water is added and another 2 minutes of mixing is done. Finally, after mixing stop polypropylene fibers are added into the mortar and mass is mixed for one minute more.

The mixing protocol is the same for all the mixes. The test on each formulation is conducted once and for each test, new mix is prepared. Samples exposing any signs of instability are discarded from consideration.

### 2.3.3 Measurement protocols

#### Dense packing fraction measurements

Dense packing fraction  $\phi_{ms}$  of the sand is measured using the vibro-compaction method [36]. The experimental setup is demonstrated in Figure 2.10. A container with diameter  $\emptyset$  of 16 cm and height of 32 cm containing a mass of sand  $M_{dry}$  is fixed to a vibration table and submitted to 150 Hz vibration. A mass equivalent to 1 kPa is applied on the container as an external pressure. Container is vibrated for 1 minute and the final height of the sample  $h$  is measured. Then, dense packing fraction is found as:

$$\phi_{sm} = \frac{4 M_{dry}}{\pi \emptyset h \rho_{dry}} \quad (2.11)$$

where  $\rho_{dry}$  is the apparent density of sand = 2640 kg/m<sup>3</sup>.

The dense packing fraction of the sand measured using this method is found as 0.64. The random loose packing or percolation packing  $\phi_{cs}$  for sand particles to create a connected network is then [24] 80 % x 0.64 = 51 %.



**Figure 2.10** Packing fraction using microvibration: mass, container and vibrating table [37].

### Yield stress measurements

In this study, we measure the yield stress of cement pastes using a simple spread test and the yield stress of mortars using standard slump test.

Cement paste is poured on a flat horizontal surface. When flow stops, the smallest and largest diameters of deposit are measured. Then, the yield stress of the cement paste is determined from spread radius and tested volume of the sample as [38]:

$$\tau_0 = \frac{225\rho g\Omega^2}{128\pi^2 r^5} \quad (2.12)$$

where  $\rho$  is the density of cement paste,  $g$  is the specific gravity,  $\Omega$  is the volume tested and  $r$  is the radius of spread. It is necessary to note that this relation only applies to the cases when the ratio between the radius of the deposit and its thickness at the center is at least 5.

The yield stress of mortars is assessed using Abram's cone from the standard slump test. The yield stress is calculated using slump  $S$  from the following relationship [39]:

$$S = 25.5 - 17.6 \frac{\tau_0}{\rho g} \quad (2.13)$$

The domain of the validity for this relationship is for slumps between 5 and 20 cm. Outside of this domain, the yield stress is found as [40]:

$$\tau_0 = \frac{\rho g H}{\sqrt{3}} \quad (2.14)$$

where  $H$  is the final height after test.

It is necessary to remind that thixotropic and hydration effects are excluded from consideration due to a short time of testing and paste rest. As a flow time is kept short, its influence on the creation of the preferential orientation of fibers is neglected, i.e. an isotropic orientation is considered.

### Total organic carbon measurements

Surface coating/glue on polypropylene fibers presents an organic molecule that can influence the yield stress of cement paste. As any organic matter contains carbon, we use total organic carbon analyzer or TOC to measure the quantity of total organic carbon in solution. The analyzer measures simultaneously quantity of total carbon (TC) and of inorganic carbon (IC), subtraction of two allows determination of TOC of the sample.

In our study, measurements of TOC in distilled water and cement pore solution containing fiber concentrate are performed. Cement pore solution, which represents interstitial fluid (pH around 13), is prepared by magnetic stirring of salts in distilled water. Composition of cement pore solution is given in Table 2.3. Fiber concentrate is obtained through sieving out of polypropylene fibers left for one hour in distilled water or cement pore solution. Virgin solutions without fiber concentrate and solutions with fiber concentrate are then analyzed using TOC analyzer for an amount of detected total organic carbon.

**Table 2.3** Cement pore solution composition.

Salts	Quantity (g/L)
CaSO <sub>4</sub> ·2H <sub>2</sub> O	1.720
Na <sub>2</sub> SO <sub>4</sub>	6.959
K <sub>2</sub> SO <sub>4</sub>	4.757
KOH	7.120

### Microtomography measurements

The aim of microtomography measurements is to validate the fiber conformations proposed with a model. Microtomography measurements are completed for cement paste W/C = 0.35 with two fibers of 6 mm and 24 mm and diameter of 34 μm (R = 176 and R = 706 respectively) at 0.1 % vol of fibers. Selection of this fiber dosage allows a better distinguishing of separate fibers and a low W/C is chosen for more bending of fibers. For each

fiber, separate sample is prepared using the same protocol as for other pastes. Cement pastes are cast into plastic containers with 24 mm diameter and 40 mm height and then sealed.

The  $\mu$ -CT images are produced at Navier Laboratory, ENPC using Ultrasom - RX-solution scanner presented in Figure 2.11. The settings of scans are following: 160 kV and 24  $\mu$ A. Frame rate is 2 images per second. Scanning time for each specimen is 7 hours. 16-bit 2D radiographs are obtained by making an average of radiographs at each angle and recording through continuous sample rotation. Final voxel size is  $8.46 \times 8.46 \times 8.46 \mu\text{m}^3$ . The 3D images of the specimen have resulted from reconstructed volume of  $3000 \times 3000 \times 2500$  voxels. Due to the fact that attenuation coefficients of cement paste and fibers are different, fibers are easily distinguished from paste using simple segmentation in Image J/ Fiji software.

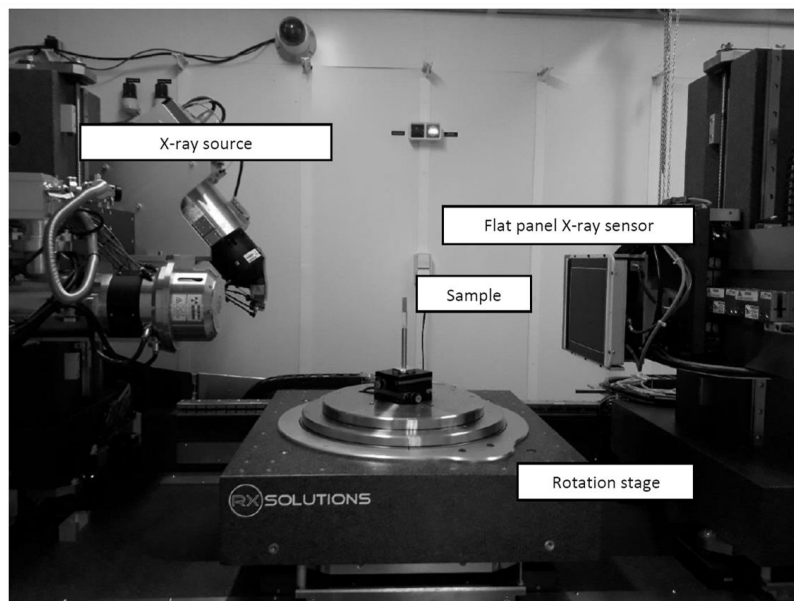


**Figure 2.11** Ultrasom - RX solution microtomography scanner in Navier Laboratory: source of X-Rays, sample in the middle on the rotation table and flat panel sensor for X-rays.

## 2.4 Results

### 2.4.1 Polypropylene fibers in cement paste

#### **Influence of organic compound in fibers on the yield stress**

At fiber volume fraction less than 0.5 % volume, instead of expected increase in the yield stress with fiber dosage we observe a slight decrease (or increase in the spread). To explain this behavior, we have conducted two tests: spread test and TOC measurements. For spread

tests, cement paste using distilled water and paste with cement pore solution both containing fiber concentrate of 3 % vol. of fibers are prepared and compared to pastes without fiber concentrate. The results reveal that presence of fiber concentrate decreases the yield stress by 7 % and 3.5 % for pastes with distilled water and cement pore solution respectively.

We then have used TOC analyzer for these solutions containing fiber concentrate at various dosages. We present the results in the form of relative TOC (a ratio of total organic carbon of solutions containing fiber concentrate and total organic carbon of virgin solutions) in Figure 2.12. The results indicate a presence of organic matter in distilled water and cement pore solution. Based on these results, we suggest that the organic compound on fiber surface serves as a deflocculant decreasing the yield stress of cement paste. However, it is important to note that for industrial applications this decrease of the yield stress due to this phenomenon is very slight should be considered negligible.

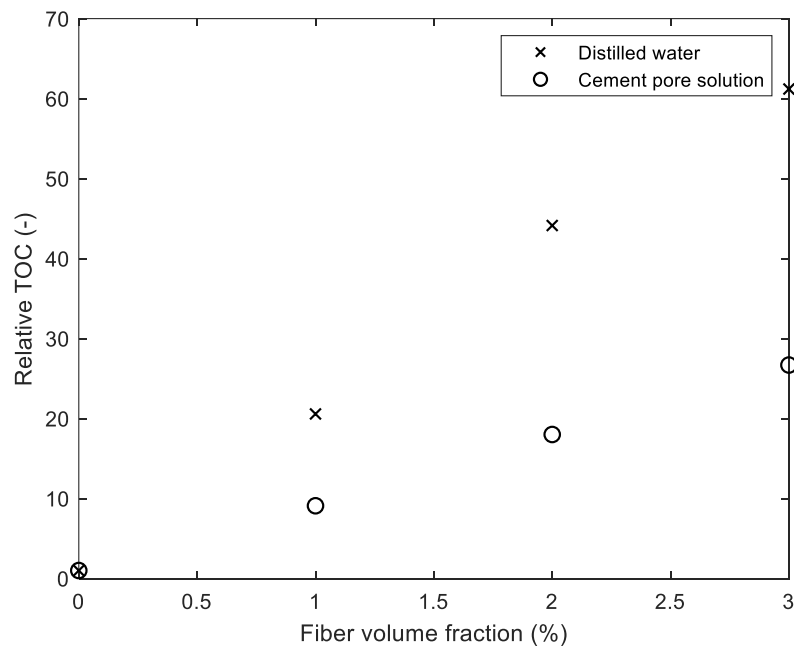


**Figure 2.12** Relative total organic carbon (a ratio of total organic carbon of solutions containing fiber concentrate and total organic carbon of virgin solutions) plotted as a function of fiber volume fraction used for the fiber concentrate preparation.

### Influence of fibers on the yield stress of cement pastes

In general, addition of polypropylene fibers is found to decrease spread and increase the yield stress of cement pastes. Images of cement paste spreads containing various dosages of 12 mm fibers with 34  $\mu\text{m}$  diameter are shown in Figure 2.13. First, we see that as fiber volume

fraction is increased, the shape of the spread changes due to perturbation of flow with addition of fibers noted in [15]. Secondly, for 0.3 % of fiber volume a slight increase of the spread due to a deflocculating effect of fiber coating is noticed. As fiber dosage reaches 1 % vol., a decrease of paste spread is observed.

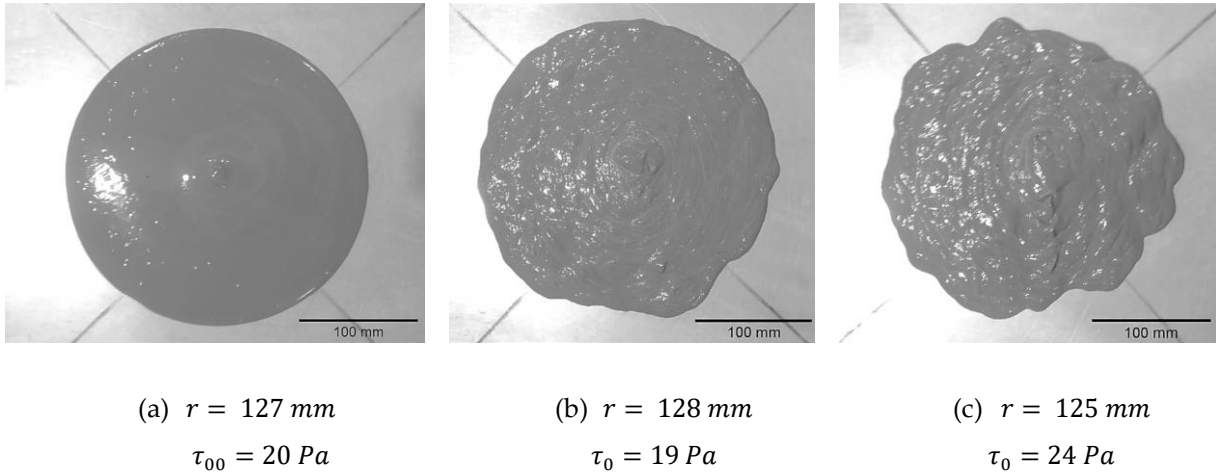


**Figure 2.13** Spread of cement paste  $W/C = 0.5$  (with measurements of spread radius and the yield stress): a) Reference without fibers, b) With 0.3 % vol. of fibers  $R = 353$ , c) With 1% vol. of fibers  $R = 353$ .

We plot the relative yield stress (a ratio of the yield stress of cement pastes with fibers and the yield stress of cement paste without fibers) as a function of fiber volume fraction in Figure 2.14. The yield stress of the cement paste without fibers is 20 Pa. The variability of 13% is found through the repetition of the test on 1% vol. of fibers  $R = 353$  and is considered for all the tests conducted in this study. We notice that the relative yield stress of cement paste with fibers increases with fiber volume fraction for all fiber geometries. In addition, the relative yield stress does not increase directly with an aspect ratio of fibers as it would for steel fibers [2], [3], [13]. For example, for 2% vol. of fibers the yield stress increases 1.6 times for  $R = 176$ , 3.6 times for fibers  $R = 414$  and 2.9 times for  $R = 706$  the initial yield stress of the cement paste.

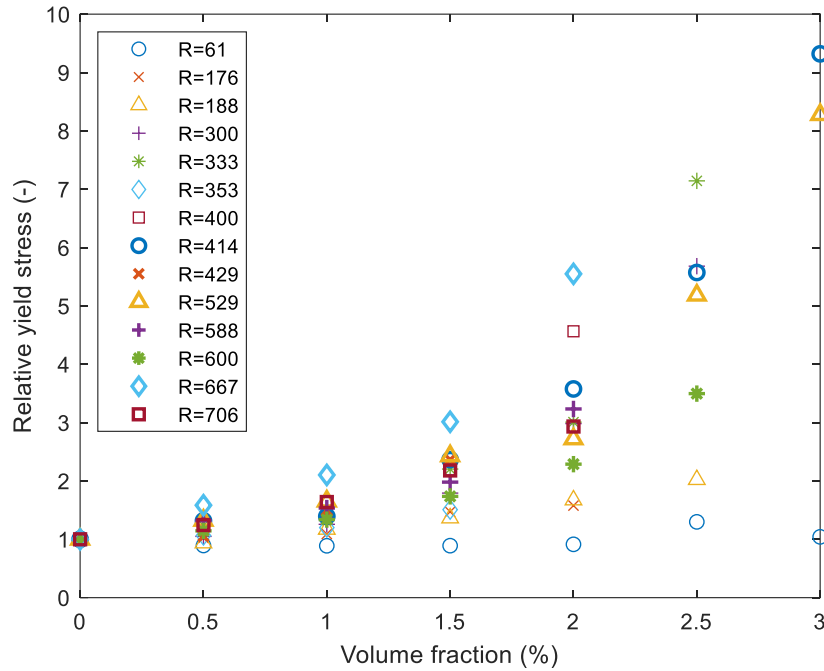
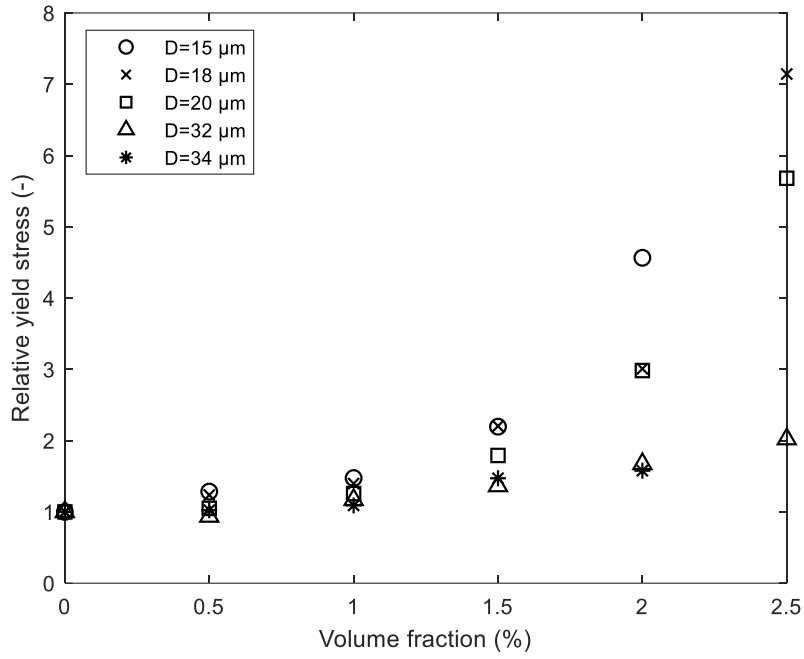
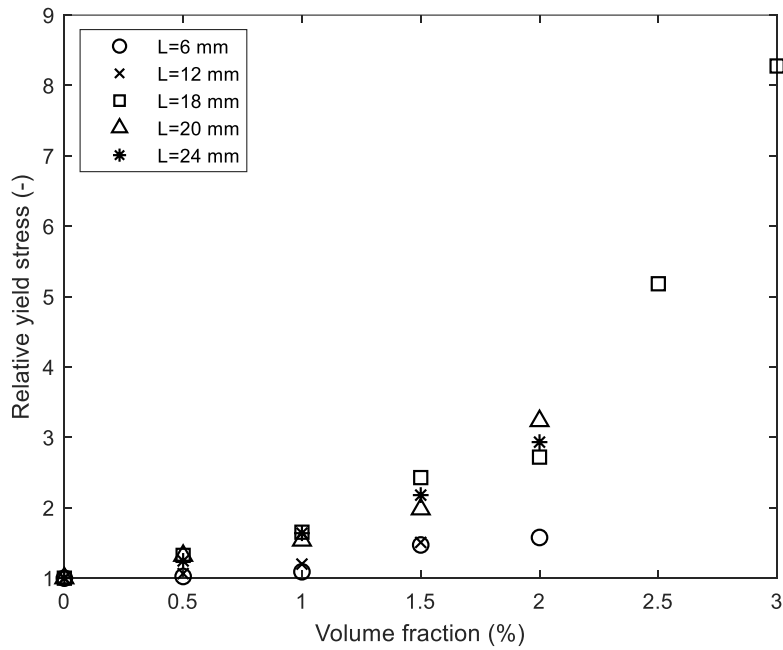


**Figure 2.14** Relative yield stress plotted as a function of the fiber volume fraction.

In order to study the influence of fiber diameter and length on the relative yield stress of cement pastes, we plot Figure 2.15a and Figure 2.15b. In Figure 2.15a, the evolution of the yield stress of cement paste containing polypropylene fibers with  $L = 6$  mm and various diameters ranging from 15 to 34  $\mu\text{m}$  with increasing fiber volume fraction is presented. It can be observed that decrease of the diameter provokes increase of the relative yield stress. Thinner fibers are more flexible and total number of filaments is higher for the same volume fraction. Both of these effects promote jamming and hence increase of the yield stress. For the fibers of same diameter ( $D = 34$   $\mu\text{m}$ ) but different length ( $L=6-24$  mm) in Figure 2.15b, it is harder to establish the relationship between fiber length and the yield stress due to absence of discarded data points. It however seems that increase of the fiber length decreases the relative yield stress. Shorter fibers, for example, fibers of 6 mm, despite their high number compared to longer fibers at same volume fraction, are more rigid than longer ones and promote less jamming.



(a)



(b)

**Figure 2.15** Relative yield stress plotted as a function of volume fraction: a) for fibers  $L = 6$  mm with different diameters, b) for fibers  $D = 34 \mu\text{m}$  with different lengths.

From the literature, we know that the yield stress of the cement paste with rigid fibers scales with a fiber factor  $\phi_f R$  [2], [39]-[41]. We plot in Figure 2.16 the results of the relative yield stress presented in Figure 2.14 as a function of fiber factor  $\phi_f R$ . As expected, flexible fibers do not behave as rigid fibers and this scaling cannot predict the yield stress of cement paste with flexible polypropylene fibers due to their flexure.

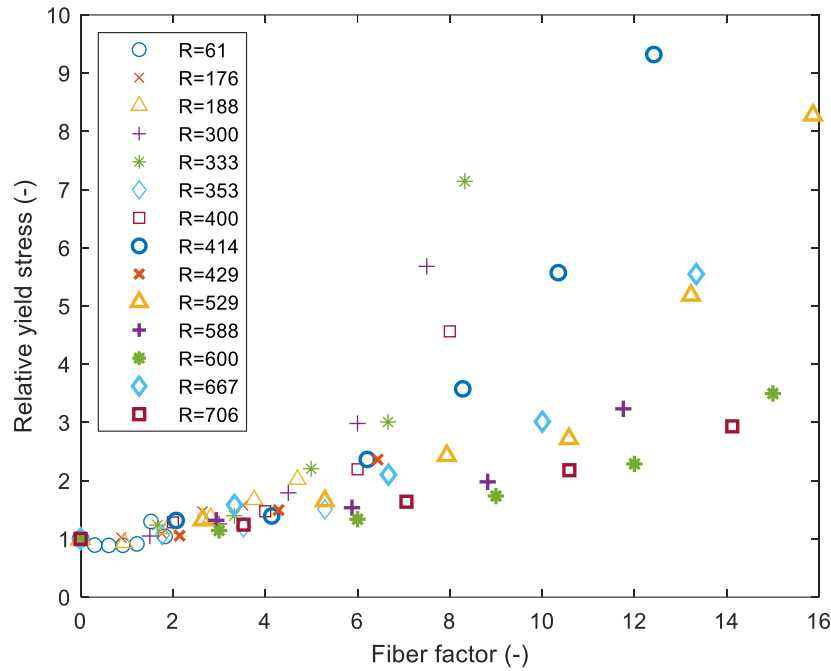


**Figure 2.16** Relative yield stress plotted as a function of fiber factor used for rigid fibers.

### Influence of paste rigidity on fiber flexure

Flexure of polypropylene fibers depends significantly on the pressures exerted on them. We plot in Figure 2.17 the relative yield stress of cement pastes with  $W/C = 0.45$  and  $0.5$  as a function of the volume fraction of fibers. Single fiber geometry of  $L = 12$  mm and  $D = 34$   $\mu\text{m}$  is used in this study. The values of the yield stress of cement paste without fibers for  $W/C = 0.5$  and  $0.45$  are 20 and 45 Pa respectively.

The results show that the relative yield stress of the cement paste containing fibers depends significantly on the yield stress of cement paste itself. The fibers contribute less to the development of the yield stress for stiffer paste  $W/C = 0.45$  opposed to less rigid paste with  $W/C = 0.5$ . This effect is very pronounced at high fiber dosages ( $\geq 2\%$  vol. of fibers). Similar result was obtained in [7] for ordinary concretes of different  $W/C$  containing polypropylene

fibers. The results show clear dependence of behavior polypropylene fibers on the yield stress of cement paste.

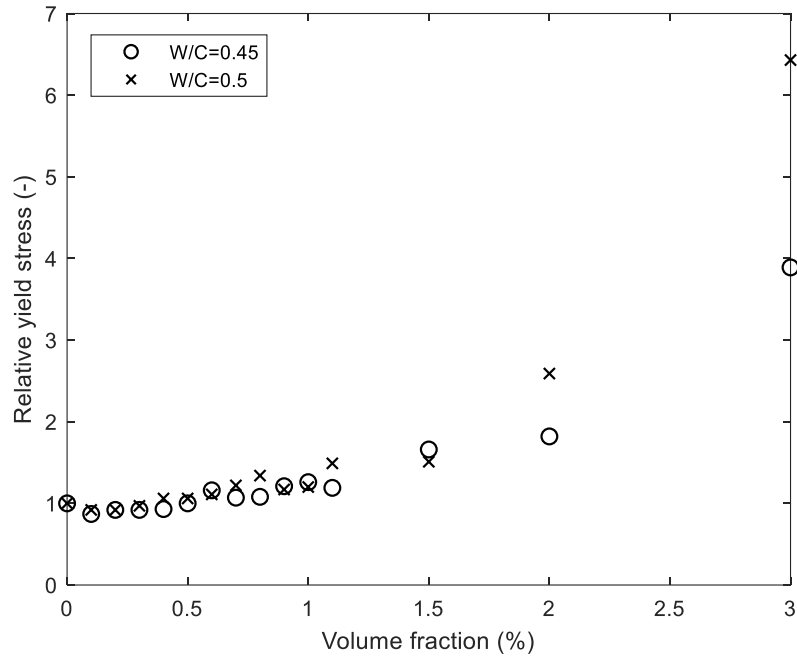


**Figure 2.17** Relative yield stress plotted as a function of volume fraction for two different cement pastes with fibers  $R = 353$ .

### Microtomography observations of fibers

We have produced microtomography scans in order to visualize fibers in cement paste. We present in Figure 2.18 polypropylene fibers with lengths of 6 and 24 mm and diameter of  $34 \mu\text{m}$  ( $R=176$  and  $706$ ) in cement paste  $W/C=0.35$  (the yield stress is approximately 100 Pa). It should be noted that two separate scans are plotted together for the sake of comparison. Image shows that polypropylene fibers do bend in cement paste and their deformation increases with fiber length. Using 3D images analysis and starting from the tip of one fiber, we compared the shape of the fiber to the line tangent to the fiber at its tip. We then looked for the point on the fiber where the perpendicular distance between the tangent and the trajectory of the fiber was 10% of the studied fiber length since its tip. Starting from this point and considering it as the tip of a new segment, we repeated the above procedure. For 6 mm fibers, we have a simple bending with 2 segments, while for 24 mm fibers, multiple curvatures with 6 segments are detected.

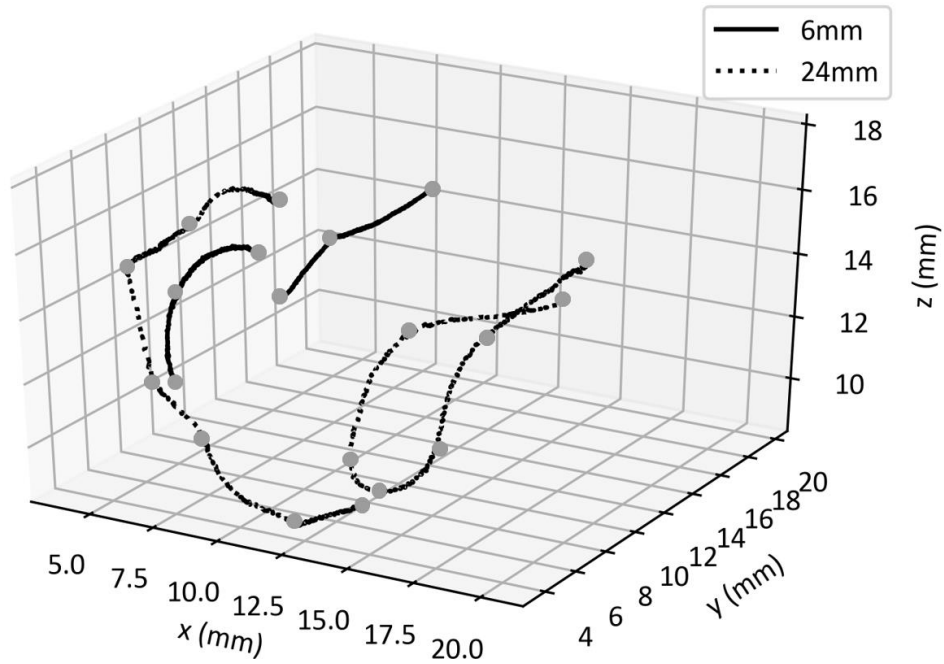


**Figure 2.18** Flexure of fibers 6 mm (full line) and 24 mm (dotted line) fibers in the cement paste  $W/C=0.35$  obtained using microtomography scans. For the sake of comparison, results of two separate scans are plotted together. The grey dots mark the end of a fiber segment, on which the deflection of the segment is less to 10% of its length.

## 2.4.2 Polypropylene fibers in mortar

We present the results on the influence of polypropylene fibers on the relative yield stress of mortar in Figure 2.19. Four fiber geometries are tested:  $R = 176, 333, 414$  and  $667$ . The yield stress of the reference mortar without fibers is 75 Pa.

The results suggest that higher is aspect ratio of fibers, more is its' influence on the yield stress of the mortar. For example, for 1.26 % vol. of fibers, the yield stress is increased 17 times for fibers with  $R=176$  ( $L = 6$  mm and  $D = 34$   $\mu\text{m}$ ) whereas this factor equals to 46 in case of fibers  $R = 667$  ( $L = 12$  mm and  $D = 18$   $\mu\text{m}$ ).

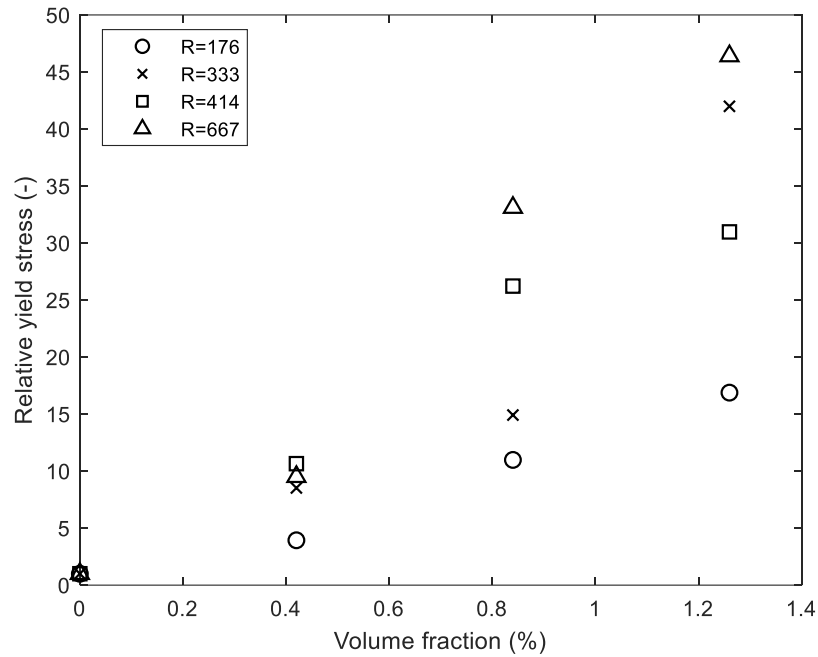


**Figure 2.19** Relative yield stress (a ratio of the yield stress of mortar with fibers and the yield stress of mortar without fibers) plotted as a function of the volume fraction of fibers.

## 2.5 Discussion

In the previous sections, we have presented the results of the relative yield stress evolution with volume fraction of flexible polypropylene fibers. We are now interested in developing a new model that will predict the yield stress of the cement paste containing flexible fibers.

### 2.5.1 Random and self-avoiding walks

We can consider a flexible fiber as a chain composed of number  $N$  of rigid segments of length  $L_0$  as seen in Figure 2.20. We are interested in determination of the effective length of the polymer chain  $L_{eff}$ , which is the distance between two ends of the chain.

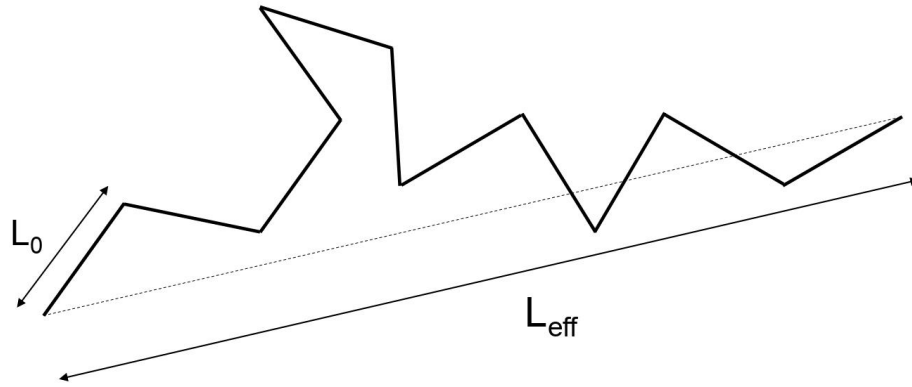


**Figure 2.20** Schematic presentation of polymer chain composed of number of segments  $N$  of a length  $L_0$  and effective length of  $L_{eff}$ .

We can then define a flexible fiber as a sequence of rigid segments with a persistence length  $L_0$ . When  $L_0 \ll L$ , where  $L$  is the real length of the chain, rigid segments that constitute the chain are too small compared to the whole chain; therefore, at macroscopic level the chain is regarded as flexible. When  $L_0 > L$ , we consider that at all scales the chain is rigid [41].

The simplest way to represent a polymer chain is to imagine a random walk (see Figure 2.21a). The walk consists of successive steps  $N$  taken by a body from one end to another with a jump of the same statistical possibility towards any neighbouring site [41]. Considering a segment of length  $L_0$  as a mechanical persistence length in case of ‘random walk’, the effective length writes as [41]:

$$L_{eff} \cong L_0 N^{\frac{1}{2}} \quad (2.15)$$

We now consider the case of ‘self-avoiding walk’ for polymers schematically presented in Figure 2.21b. The main difference between ‘random walk’ and ‘self-avoiding walk’ is the fact that the latter cannot intersect itself. We know that for self-avoiding walk, the effective length can be written as [41]:

$$L_{eff} \cong L_0 N^{\frac{3}{5}} \quad (2.16)$$

We are now interested in using effective length determined for ‘random’ and ‘self-avoiding walks’ to develop the model for the yield stress.

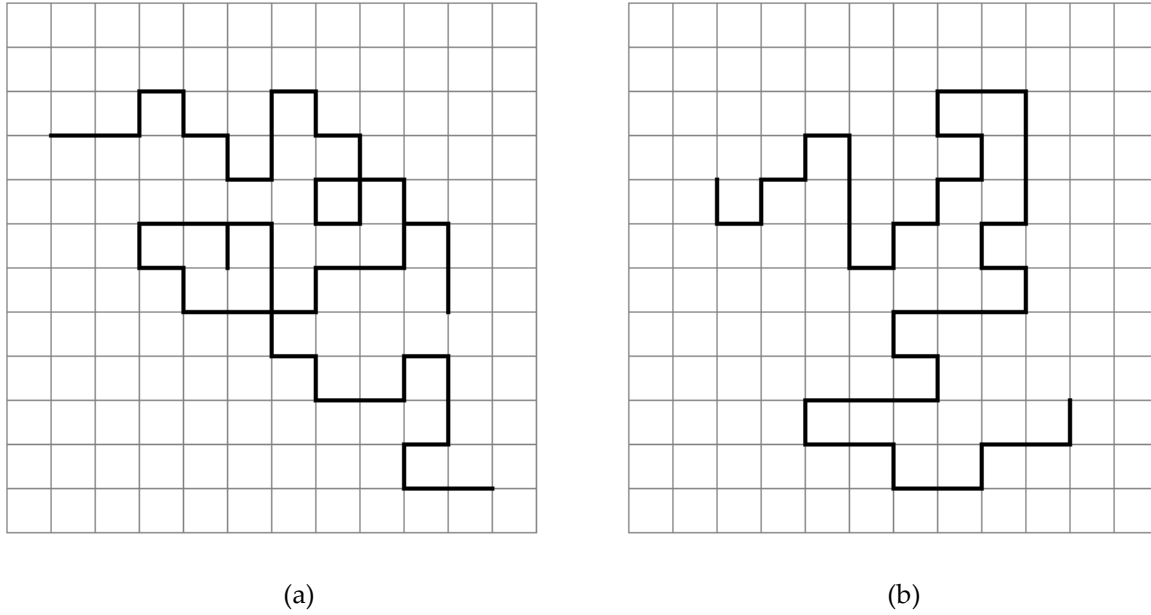


**Figure 2.21** Scheme of walks plotted on lattice: a) Random walk, b) Self-avoiding walk.

### 2.5.2 Yield stress prediction

We can consider a flexible polypropylene fiber to behave as an infinitely long and flexible chain represented by ‘random walk’. Using the rigidity criterion presented in Equation 2.4 for a deflection of 1 mm and considering persistence length  $L_0$  as a length of rigid segment, we find:

$$L_0 \cong \left( \frac{ED^3}{\tau_{00}} \right)^{\frac{1}{4}} \quad (2.17)$$

When we use this equation in order to determine number of segments  $N$  of flexible fiber, we find 2 segments for polypropylene fibers with  $L = 6$  mm and  $D = 34$   $\mu\text{m}$  in cement paste with  $W/C = 0.35$  (the yield stress of 100 Pa). As for fibers of 24 mm length, the number of segments reaches 5. These results are in accordance with microtomography observations presented in Figure 2.18.

We are now interested in calculating the effective length of the fiber. Taking into account that number of segments  $N = L/L_0$  and substituting Equation 2.17 into Equation 2.15, we find the effective fiber length for ‘random walk’ such as:

$$L_{eff} \cong \left( \frac{E}{\tau_{00}} \right)^{\frac{1}{8}} D^{\frac{3}{8}} L^{\frac{1}{2}} \quad (2.18)$$

We know that the relative fiber packing fraction describes the volume occupied by fibers in the total volume. Despite its flexure, we can imagine that each fiber in transition between semi-diluted and semi-concentrated regimes fiber has two degrees of rotational freedom [3]: it can rotate along its axis and in one plane. Apparent volume of the fiber in Figure 2.22 is then:

$$V_{app} = \frac{\pi D L_{eff}^2}{4} \quad (2.19)$$

The relative packing fraction  $\phi_f/\phi_{mf}$  can then be described using the apparent volume of a fiber by the following equation [3]:

$$\frac{\phi_f}{\phi_{mf}} = N_f \times V_{app} \quad (2.20)$$

where  $N_f = 4 \phi_f / (\pi D^2 L)$  is the number of fibers in volume  $\phi_f$ .

Substituting Equation 2.18 and 2.19 into Equation 2.20, one finds the dense packing fraction of fibers in the case of ‘random walk’ to scale as:

$$\phi_{mf} \cong \left( \frac{D \tau_{00}}{E} \right)^{\frac{1}{4}} \quad (2.21)$$

where  $E = 1$  GPa for polypropylene fibers and  $\tau_{00} = 20$  Pa for cement paste.

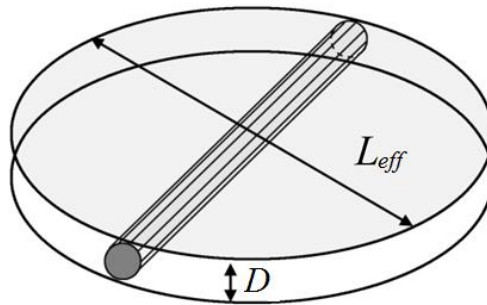


**Figure 2.22** Apparent volume occupied by the fiber [3].

Having determined a relation for dense packing fraction  $\phi_{mf}$ , we plot in Figure 2.23 the relative yield stress as a function of relative fiber packing fraction  $\phi_f/\phi_{mf}$  for infinitely long

and flexible chains. It is clear that with a model developed for dense packing fraction of flexible chains  $\phi_{mf}$ , we cannot represent adequately the evolution of the relative yield stress of cement paste with fibers.

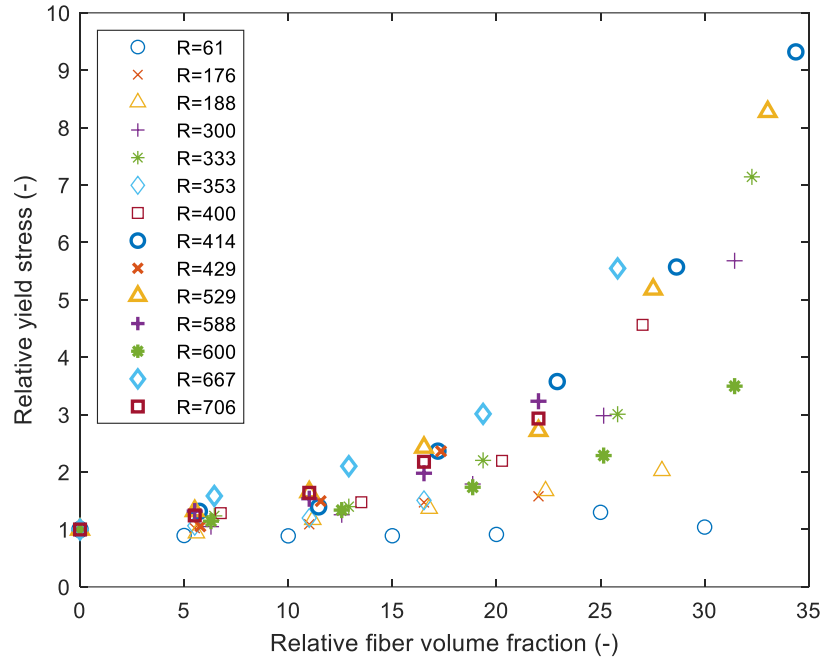


**Figure 2.23** Relative yield stress plotted as a function of scaling for continuously long and flexible fibers.

### A novel model for the yield stress prediction

We consider a flexible polypropylene fiber to bend as a polymer in ‘self-avoiding walk’. Then substituting Equation 2.17 into Equation 2.16, we find the effective length to be:

$$L_{eff} \cong \left( \frac{E}{\tau_{00}} \right)^{\frac{1}{10}} D^{\frac{3}{10}} L^{\frac{3}{5}} \quad (2.22)$$

Finally, the dense packing fraction for ‘self-avoiding walk’ writes as:

$$\phi_{mf} \cong \left( \frac{\tau_{00} D^2}{EL} \right)^{\frac{1}{5}} \quad (2.23)$$

We plot in Figure 2.24 the relative yield stress as a function of relative fiber packing fraction  $\phi_f / \phi_{mf}$  using dense packing fraction  $\phi_{mf}$  determined in Equation 2.23. Using this

predictive scheme, we obtain a master curve for most of the geometries except for two fibers  $R = 61$  ( $L = 3$  mm and  $D = 49$   $\mu\text{m}$ ) and  $R = 600$  ( $L = 12$  mm and  $D = 20$   $\mu\text{m}$ ). When calculating the relative deflection using Equation 2.5 we obtain the value of 0.45 % for fibers of  $R = 61$  which shows that they should be considered as rigid. For fibers of  $R = 600$ , there is no clear reason of this deviation: one possible explanation is a difference in fiber section.

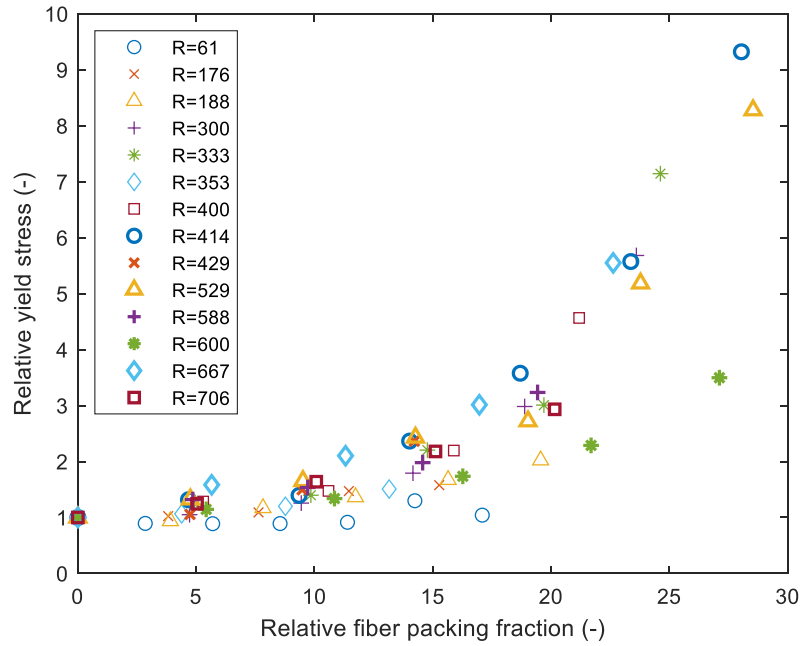


**Figure 2.24** Relative yield stress plotted as a function of relative fiber packing fraction.

In reality, we expect a relative packing fraction to diverge around 1 as seen in Figure 2.7. We empirically adjust a coefficient that would predict this divergence around 1 in Equation 2.9. The adjusted fiber dense packing fraction is then:

$$\phi_{mf} \cong 45 \left( \frac{\tau_{00}}{E} D^2 L^{-1} \right)^{\frac{1}{5}} \quad (2.24)$$

We exclude fibers  $R = 61$  and  $R = 600$  from our consideration and plot in Figure 2.25 the relative yield stress as a function of “corrected” relative fiber packing fraction  $\phi_f / \phi_{mf}$ . As a result, we obtain a full master curve that describes the evolution of the relative yield stress using elastic modulus of fibers, their geometry and dosage and the yield stress of the suspending fluid. Developed physical model covers a wide range of polypropylene fiber

geometries from aspect ratio of 100 to 800 and can be used to predict the yield stress evolution containing any synthetic flexible fibers.

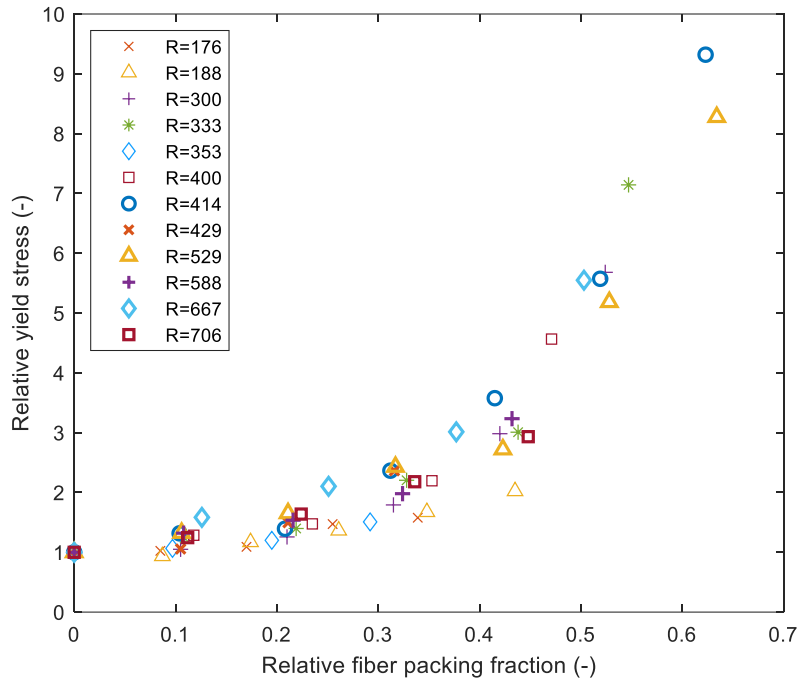


**Figure 2.25** Relative yield stress plotted as a function of “corrected” relative fiber packing fraction.

### 2.5.3 Influence of paste consistency

It is now clear that polypropylene fibers bend in cement paste and this bending depends on the yield stress of cement paste. Tests conducted on two cement pastes with  $W/C = 0.45$  and  $W/C = 0.5$  with fibers of  $R=353$  ( $L = 12$  mm and  $D = 34$   $\mu\text{m}$ ) show a variation of the relative yield stress in Figure 2.17. We know from Equation 2.24 that the relative yield stress is proportional to the yield stress of cement paste in power of  $(-1/5)$ . We plot in Figure 2.26 the relative yield stress as a function of  $\phi_f \tau_{00}^{-1/5}$  of each paste. We shall remind that the yield stress of pastes with  $W/C=0.45$  and  $0.5$  is 20 and 45 Pa accordingly. The results prove that paste rigidity is an important factor that influences the flexure of fiber reinforced cement pastes.

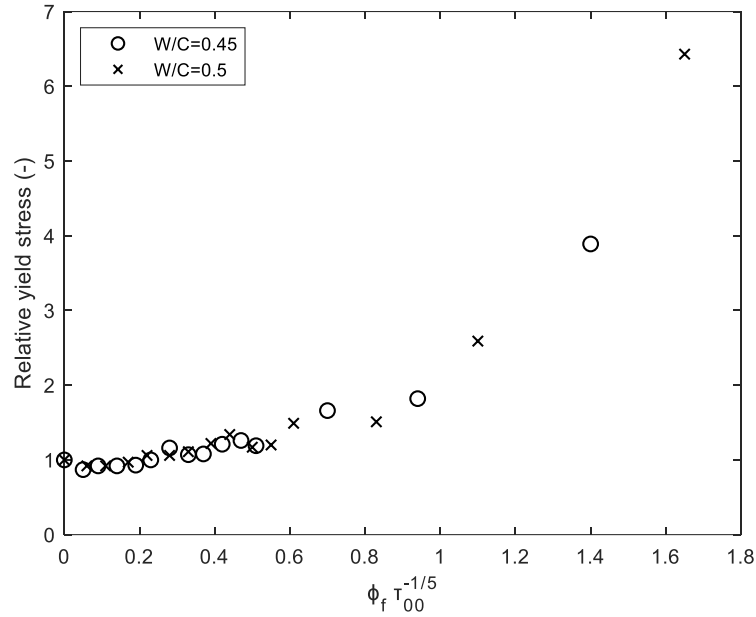


**Figure 2.26** Relative yield stress plotted as a function of  $\phi_f \tau_{00}^{-1/5}$  for cement pastes with W/C = 0.45 and W/C = 0.5.

#### 2.5.4 Influence of presence of other inclusions

Aggregates contribute to the development of the yield stress of cementitious materials as well as fibers. Having determined the dense packing fraction for flexible fibers  $\phi_{mf}$ , we are now interested in evaluating the total relative packing fraction in the presence of fibers and sand. As a first estimation, we propose a simple estimation of the total packing of sand and fiber mix that sums up the contributions of each inclusion as in [2]:

$$\frac{\phi_f}{\phi_{mf}} + \frac{\phi_s}{\phi_{ms}} = \frac{\phi_f}{45 \left( \frac{\tau_{00}}{E} D^2 L^{-1} \right)^{1/5}} + \frac{\phi_s}{\phi_{ms}} \quad (2.25)$$

The dense packing fraction of the sand  $\phi_{ms}$  used in mortar is 51% and the volume fraction of sand is fixed to 40 % meaning that sand contribution  $\phi_s/\phi_{ms}$  is constant and equals to 0.78. In cement paste, increase of the yield stress due to addition of fibers was around 10 and the influence of the yield stress was in the power of (-1/5). In mortar, there is however a question on stresses that would act on polypropylene fibers. There are three possibilities for exerted stress  $\tau_{00}$  :

- fibers are deformed under the influence of reference cement paste  $\tau_{00} = 20$  Pa
- fibers are deformed under the influence of reference mortar  $\tau_{00} = 75$  Pa
- fibers are deformed under the influence of suspension (paste, fibers and sand)  $\tau_{00} = 350$  Pa.

We plot Figure 2.27a, 2.27b and 2.27c for each scenario and theoretic curve from Equation 2.9 presented above. For the cases when the stress exerted on fibers comes from paste or mortar, total relative packing fraction exceeds 1, which is not physically possible. This suggests that stresses acting on fibers take their origin from full suspension. Consequently, flexure of fibers would depend on fiber concentration.

To address this issue, the mathematical model is required with complex non-linear computations. This model should consider the interactions between fibers, and aggregates as well as flexure of fibers due to suspending fluid and fibers themselves.

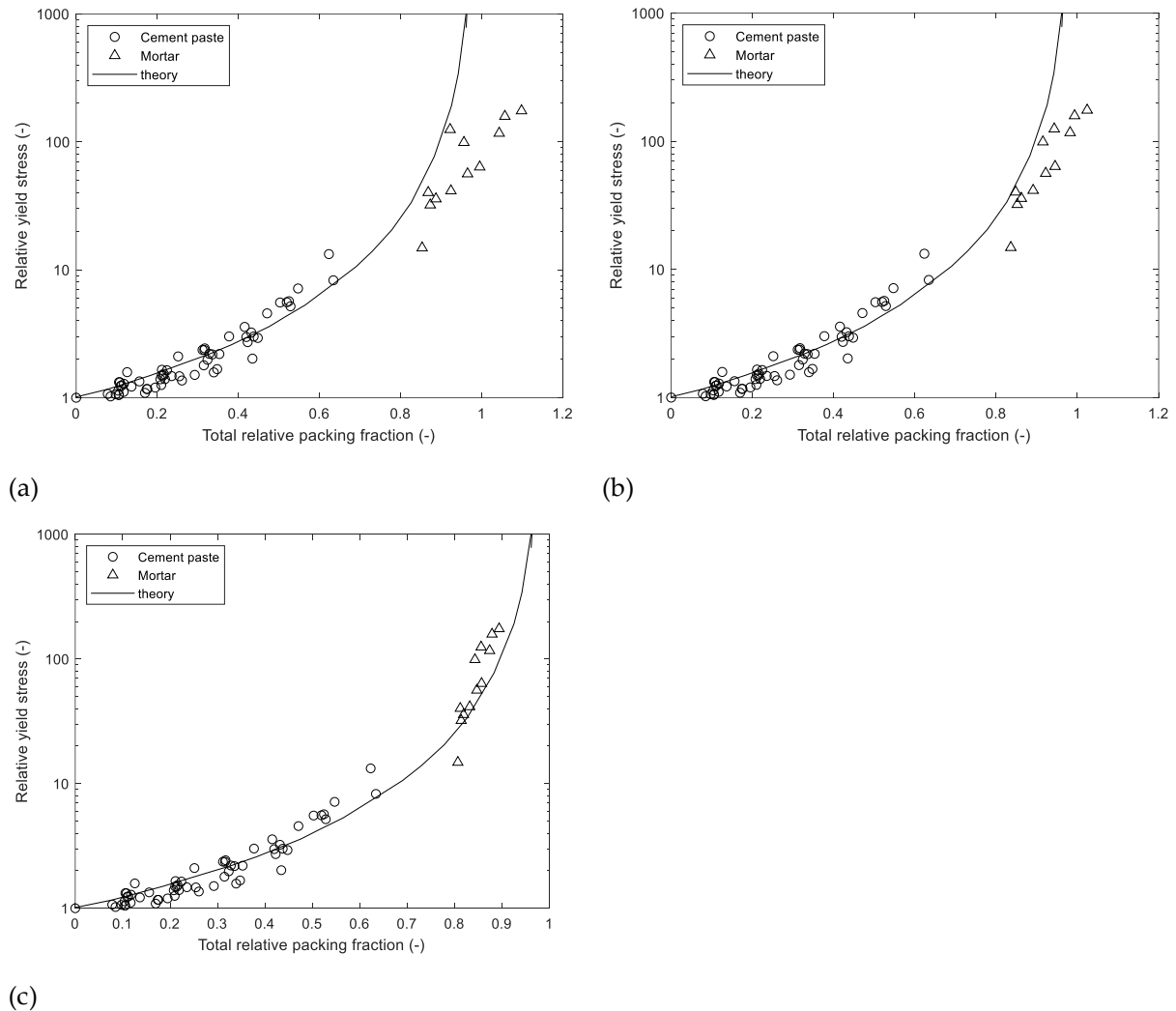


**Figure 2.27** Relative yield stress plotted as a function of total relative packing fraction for: a) deformation of fibers by paste, b) deformation of fibers by mortar, c) deformation of fibers by suspension.

### 2.5.5 Application to self-compacting concrete design

Based on these results, it is possible to add a design criterion for self-compacting concrete. In order to limit the influence of addition of polypropylene fibers on fresh state behavior of self-compacting concrete, we can remove of a volume fraction of aggregate or add supplementary paste volume. We can compute a volume of additional paste (or volume of aggregates removed) that would allow compensating the negative influence of polypropylene fibers on fluidity of fresh concrete. For inclusions consisting of flexible fibers and aggregate mix, a simplified approximation for total relative packing fraction of inclusions developed in Equation 2.25 then writes as:

$$\frac{\phi_f}{\phi_{mf}} + \frac{\phi_a}{\phi_{ma}} \quad (2.26)$$

where  $\phi_a$  is aggregate volume fraction and  $\phi_{ma}$  is dense packing fraction of aggregate mix.

We can then consider limiting the contribution of polypropylene fibers by removing a volume  $\phi_a$  of aggregates which equals to  $\frac{\phi_f}{\phi_{mf}} \times \phi_{ma}$ . It is important to remind that this estimation

is the first estimation and that further developments are necessary.

## 2.6 Conclusions

In this chapter, we have studied the influence of flexible polypropylene fibers on the rheology of cementitious composites. Before presentation of our study, we have provided to reader essentials on the subject of the rheology of cementitious materials presenting basic notions, selected model and possible scenarios of packing of inclusions. As we focus on fibers, we have demonstrated current state of knowledge, specifically: 1) the rigidity criterion that distinguishes flexible fibers from rigid on example of steel fibers 2) packing regimes and 3) predictive scheme for the evolution of the yield stress of cementitious composites with rigid fibers.

We have then proceeded with experimental study. In the first part of our study, we have measured the yield stress of cement pastes and mortars containing flexible synthetic fibers using spread and slump tests. A general trend of increase of the relative yield stress with fiber volume fraction is observed for both cement paste and mortar. At low fiber dosages (<0.5 %), a slight decrease of the yield stress of cement paste is noted. From the results of total organic carbon analyzer, traces of organic matter suggest that surface compound of fibers could serve

as a deflocculant that slightly decreases the yield stress. The results of the study show that the relative yield stress of cement pastes increases with fiber length and decreases with fiber diameter. On mortar scale, the yield stress appears to increase with the aspect ratio of tested fibers. Most importantly, we have made it clear that polypropylene fibers bend in cement paste and this bending is strongly influenced by consistency of the paste.

In the second part, we consider fiber as a polymer chain composed of rigid segments and we describe the persistence length using ‘random’ and ‘self-avoiding’ walks for polymers. We show that we are able to develop a physical model for predicting the yield stress of cement paste with flexible fibers. This model depends on the yield stress of cement paste, elastic modulus of fiber, and its length and diameter and volume fraction. We then suggest a first attempt in prediction scheme for fiber-reinforced mortars, where we linearly sum up the contributions of each inclusion. We have found that in fresh mortars, deformation of fibers occurs under the influence of overall suspension. One of conclusions of the work is design criterion for self-compacting concrete that can limit the contribution of polypropylene fibers to the yield stress by addition of supplementary volume of cement paste. It should, however, be noted that presented scheme is a first approach and further development of mathematical model is necessary.

## 2.7 Reference list

- [1] Tattersall G.H. and Banfill P.F.G. (1983). *The Rheology of Fresh Concrete*. London, Pitman.
- [2] Martinie L., Rossi P. and Roussel N. (2010). Rheology of fiber reinforced cementitious materials: classification and prediction. *Cement and Concrete Research* 40 : 226-234.
- [3] Martinie L. (2010). *Comportement rhéologique et mise en œuvre des matériaux cimentaires fibrés*. PhD Thesis. Université Paris Est.
- [4] Kuder K.G., Ozyurt N., Mu E. B. and Shah S.P. (2007). Rheology of fiber-reinforced cementitious materials. *Cement and Concrete Research* 37: 191-199.
- [5] Banfill P.F.G, Starrs G., Derruau G., McCarter W.J. and Chrisp T.M. (2006). Rheology of low carbon fibre content reinforced cement mortar. *Cement and Concrete Composites* 28:773-780.
- [6] Widodo S. (2012). Fresh and hardened properties of Polypropylene fiber added Self-Consolidating Concrete. *International Journal of Civil and Structural Engineering* 3: 85-93.
- [7] Al-Tayyib A.J., Al-Zahrani M.M., Rasheeduzzafar and Al-Sulaimani G.J. (1987). Effect of polypropylene fiber reinforcement on the properties of fresh and hardened concrete in the Arabian Gulf environment. *Cement and Concrete Research* 18: 561-570.
- [8] Mazaheripour H., Ghanbarpour S., Mirmoradi S.H. and Hosseinpour I. (2001). The effect of polypropylene fibers on the properties of fresh and hardened lightweight self-compacting concrete. *Construction and Building Materials* 25: 351-358.

- [9] Szwabowski J. and Ponikiewski T. (2002). Rheological properties of fresh concrete with polypropylene fibres. Proceedings of the 3<sup>rd</sup> International conference on Concrete and Concrete Structures. Zilina, Slovakia.
- [10] Leung H. and Balendran R.V. (2003). Properties of fresh polypropylene fibre reinforced concrete under the influence of pozzolans. *Journal of Civil Engineering and Management* 9:271-279.
- [11] Ponikiewski T. and Katzer J. (2017). Fresh Mix Characteristics of Self-Compacting Concrete Reinforced by Fibre. *Periodica Polytechnica Civil Engineering* 61: 226-231.
- [12] Krage G. and Wallevik O.H. (2007). Rheology of synthetic fiber reinforced SCC. Proceedings of the 5<sup>th</sup> International RILEM Symposium on Self-Compacting Concrete.
- [13] Laskar A.I. and Talukdar S. (2008). Rheology of steel fiber reinforced concrete. *Asian Journal of Civil Engineering* 9: 167 – 177.
- [14] Ding Y., Liu S., Zhang Y. and Thomas A. (2008). The investigation on the workability of fibre cocktail reinforced self-compacting high performance concrete. *Construction and Building Materials* 22: 1462-1470.
- [15] Grünewald S. and Walraven J.C. (2001). Parameter-study on the influence of steel fibers and coarse aggregate content on fresh properties of self-compacting concrete. *Cement and Concrete Research* 31:1793-1798.
- [16] Ferrara L., Park Y.D. and Shah S.P. (2007). A method for mix-design of fiber-reinforced self-compacting concrete. *Cement and Concrete Research* 37:957-971.
- [17] Roussel N., Lemaître A., Flatt R.J. and Coussot P. (2010). Steady state flow of cement suspensions: A micromechanical state of the art. *Cement and Concrete Research* 40:77-84.
- [18] Roussel N. (2005). Steady and transient flow behaviour of fresh cement pastes. *Cement and Concrete Research* 35: 1656-1664.
- [19] Roussel N., Ovarlez G., Garrault S. and Brumaud C. (2012). The origins of thixotropy of fresh cement pastes. *Cement and Concrete Research* 42:148-157.
- [20] Roussel N. and Cussigh F. (2008). Distinct-layer casting of scc: The mechanical consequences of thixotropy. *Cement and Concrete Research* 38 : 624-632.
- [21] Coussot P. (2012). *Rhéophysique - La matière dans tous ses états*. EDP Sciences/ CNRS Editions.
- [22] Mahaut F., Chateau X., Coussot P. and Ovarlez G. (2008). Yield stress and elastic modulus of suspensions of non-colloidal particles in yield stress fluids. *Journal of Rheology* 52: 287–313.
- [23] Krieger I.M. and Dougherty T.J. (1959). A mechanism for non-newtonian ow in suspensions of rigid spheres. *Transactions of the Society of Rheology* 3:137-152.
- [24] Mahaut F., Mokéddem S., Chateau X., Roussel N. and Ovarlez G. (2008). Effect of coarse particle volume fraction on the yield stress and thixotropy of cementitious materials. *Cement and Concrete Research* 38:1276-1285.
- [25] Yammine J., Chaouche M., Guerinet M., Moranville M. and Roussel N. (2008). From ordinary rheology concrete to self compacting concrete: A transition between frictional and hydrodynamic interactions. *Cement and Concrete Research* 38 : 890-896.
- [26] Onoda G.Y. and Liniger E. (1990). Random loose packings of uniform spheres and the dilatancy onset. *Physical Review Letters* 64 : 2727–2730.
- [27] Hu C. and de Larrard F. (1996). The rheology of fresh high performance concrete. *Cement and Concrete Research* 26: 283–294.
- [28] de Larrard F. (1999). *Concrete Mixture Proportioning*. E & FN Spon, London.

- [29] Grünewald S. (2012). Fibre reinforcement and the rheology of concrete. Understanding the rheology of concrete. Roussel N. (ed.). Woodhead Publishing Limited.
- [30] Morton J., Groves G.W. (1974). The cracking of composites consisting of discontinuous ductile fibers in a brittle matrix: effect of orientation. *Journal of Materials Science* 9:1436–1445.
- [31] Markovic I. (2006). High-performance hybrid-fiber concrete —development and utilization. PhD Thesis, Delft University of Technology.
- [32] Stähli P. and van Mier J.G.M. (2007). Manufacturing, fiber anisotropy and fracture of hybrid fiber concrete. *Engineering Fracture Mechanics* 74:223–242.
- [33] Microsynthetic fibers. Fibermesh. <https://fibermesh.com/our-fibers/microsynthetic-fibers/>
- [34] Philipse A.P. (1996). The random contact equation and its implications for (Colloidal) rods in packings, suspensions and anisotropic powders. *Langmuir* 12:1127-1133.
- [35] Yamanoi M., Maia J.M. and Tae-Soo K. (2010). Analysis of the rheological properties of fibre suspensions in a Newtonian fluid by direct fibre simulation. Part 2: Flexible fibre suspensions. *Journal of Non-Newtonian Fluid Mechanics* 165: 1064 – 1071.
- [36] Sedran T. and De Larrard F. (1994). RENE LCPC : Un logiciel pour optimiser la granularité des matériaux du génie civil, *Bulletin de Liaison du LCPC* 194.
- [37] Hafid H. (2012). Influence des paramètres morphologiques des granulats sur le comportement rhéologique des bétons frais : étude sur systèmes modèles. PhD Thesis. Université Paris Est.
- [38] Roussel N., Stefani C. and Leroy R. (2005). From mini-cone test to Abrams cone test: measurement of cement-based materials yield stress using slump tests. *Cement and Concrete Research* 35:817-822.
- [39] Roussel N. (2006). Correlation between yield stress and slump: Comparison between numerical simulations and concrete rheometers results. *Materials and Structures* 39: 501-509.
- [40] Roussel N. and Coussot P. (2005). “Fifty-cent rheometer” for yield stress measurements: From slump to spreading flow, *Journal of Rheology* 49: 705-718.
- [41] de Gennes P. - G. (1979). *Scaling concepts in polymer physics*. Cornell University Press.

## 2.8 Basic notations

$\tau$	shear stress (Pa)
$\tau_0$	yield stress (Pa)
$\tau_{00}$	yield stress of cement paste without fibers(Pa)
$\eta$	apparent viscosity (Pa.s)
$\mu_p$	plastic viscosity (Pa.s)
$\dot{\gamma}$	shear rate ( $s^{-1}$ )
$\phi$	volume fraction of inclusions (-)
$\phi_f$	volume fraction of fibers(-)
$\phi_s$	volume fraction of sand(-)
$\phi_a$	volume fraction of aggregates(-)
$\phi_c$	random loose or percolation packing fraction (-)
$\phi_{cf}$	random loose or percolation packing fraction of fibers (-)
$\phi_{cs}$	random loose or percolation packing fraction of sand (-)
$\phi_f$	dense packing fraction (-)
$\phi_{mf}$	dense packing fraction of fibers (-)
$\phi_{ms}$	dense packing fraction of sand (-)
$\phi_{ma}$	dense packing fraction of aggregate mix (-)
$\phi_M$	maximum packing fraction (-)
$\phi_{Mf}$	maximum packing fraction of fibers (-)
$d_{min}$	size of the smallest aggregate (m)
$d_{max}$	size of the largest aggregate (m)
$L$	fiber length (m)
$D$	fiber diameter (m)
$R$	aspect ratio (-)
$N_f$	number of fibers (-)
$f$	deflection of fiber (m)
$E$	elastic modulus of fiber (Pa)
$I$	moment of area ( $m^4$ )

## **CHAPTER 3**

# **HIGH TEMPERATURE BEHAVIOR OF FIBER REINFORCED CEMENTITIOUS COMPOSITES**

### **3.1 Introduction**

Advances on the question of fire protection of cementitious composites conventionally propose an addition of polypropylene fibers into mixes for reduction of risk of spalling. Unfortunately, abundance of experimental data with various controlling parameters make it hard to identify the optimal dosage and geometry of fibers required to avoid spalling. In this chapter, we aim at contributing to existing knowledge on optimization of choice of polypropylene fibers for high performance concrete to ensure its thermal stability.

First, we present literature review describing evolution of concrete constituents and properties with high temperature. We introduce the phenomenon of spalling of concrete due to fire including its governing mechanisms and influencing parameters. We discuss the use of polypropylene fibers as a preventative measure against spalling and we provide a brief information about polypropylene. We finish this literature review by giving an overview on thermo - mechanical simulations of cementitious materials at high temperature present in literature. In the second part of this chapter, we present our experimental study aimed at identifying an optimal fiber geometry and dosage for a cementitious material to prevent spalling. The final part of this chapter is a numerical study that includes studies of influence of polypropylene fibers diameter and mesoscale simulations of cementitious materials at high temperature. Finally, some recommendations on choice of polypropylene fibers dosage and geometry for fire spalling of high performance concrete are provided.

## 3.2 Literature review

### 3.2.1 General information on concrete

#### Concrete microstructure

Concrete is a material made at least of three main components: aggregates, cement and water. Cement paste, mix of cement and water, serves as a binding component for aggregates in concrete. Mixing cement with water activates hydration process, which results in formation of two principal hydrates: calcium hydrosilicate CSH (where C stands for CaO, S for SiO<sub>2</sub> and H for H<sub>2</sub>O) and portlandite Ca(OH)<sub>2</sub> or briefly CH. For ordinary cement paste with W/C = 0.5, CSH represents 50 to 70 % of paste while portlandite - from 25 to 30 % [1]. As CSH occupies most of the cement paste and is responsible for mechanical strength, we particularly focus on microstructure of this hydrate.

Model describing CSH structure proposed by Feldman and Serada [2] is presented in Figure 3.1. In this model, CSH is presented as lamella of size of 100 to 200 Å composed of 2 to 4 simple poorly crystallized layers or sheets spaced by 150 to 300 nm approximately [3]. These CSH particles are held together by Van der Waals, electrostatic and steric forces [4].

- adsorbed water
- × interlayer water
- A interparticle links
- B C-S-H layers

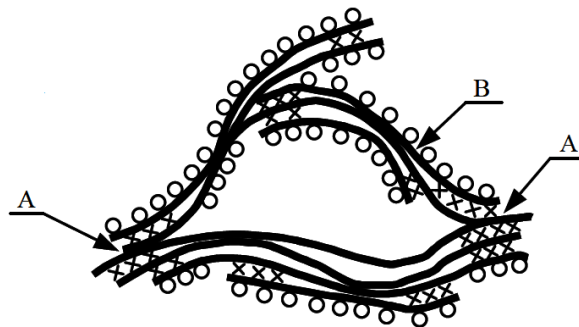


**Figure 3.1** Model of CSH microstructure [2].

In addition to hydrates, microstructure of hardened cement paste is presented by a variety of pores. We distinguish the following types of porous network:

- Capillary pores related to spaces in cement initially filled with water; their size varies from 10 nm to 10 μm. Capillary pores are refined with hydration time, their final volume and size depends significantly on W/C ratio [5]

- Gel pores linked to intrinsic porosity in hydrates. Their size is much smaller than of capillary pores ( $< 10$  nm). In CSH gel, gel pores can be found as interlayer and interparticle pores
- Air bubbles with a diameter varying from  $10\ \mu\text{m}$  to  $1\ \text{mm}$  due to mixing protocol or addition of air-entraining admixtures
- Air voids related to vibration and compaction processes
- Microcracks (order of several  $\mu\text{m}$ ) and macrocracks (order of several mm) resulting from shrinkage, mechanical and thermal loading, chemical reaction.

### Water in concrete

Water is present in concrete in form of free, adsorbed and chemically bound water. A schematic representation of these water forms in concrete is provided in Figure 3.2. We distinguish these water forms:

- Free water is water that is located far from surface adsorption forces.
- Adsorbed water is water linked to the surface of hydrates physically by Van der Waals forces and chemically by electrostatic forces. These forces act inversely proportional to distance between hydrate and water molecule. In CSH microstructure, adsorbed water is confined in gel pores and forms from 1 to 5 layers of water molecules.
- Chemically bounded water is water which reacts with cement to create products of hydration.

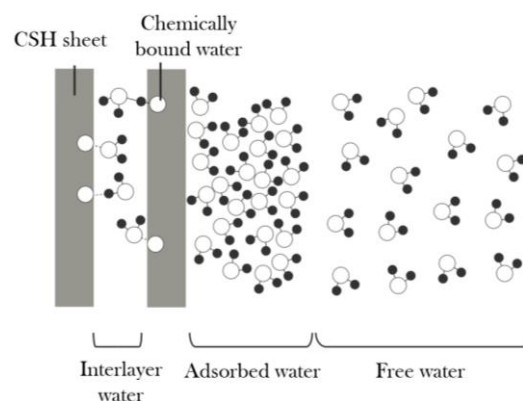


**Figure 3.2** Water forms in concrete [6].

Another classification divides water present in concrete into two groups based upon their evaporation: evaporable and non-evaporable water.

- Evaporable water comprises free and adsorbed water that can evaporate freely between 30 and 120 °C. The speed of evaporation depends on heating rate and degree of saturation.
- Non-evaporable water includes interlayer and chemically bound water. This type of water requires higher and longer heating and alters properties of cement paste.

### 3.2.2 Evolution of concrete constituents with temperature

#### Physico-chemical transformations of constituents

Hardened concrete exposed to high temperature is a subject to physico-chemical transformations that influence its' physical, thermal and mechanical properties. Figure 3.3 presents an evolution of phases of cement paste with temperature obtained by neutron diffraction. First, a range between 20 and 100 °C is characterized by departure of free water and decomposition of ettringite. Dehydration of CSH gel due to departure of chemically bound water occurs gradually and has its first peak around 150 °C [7]. When crystalline phase of CSH disappears, the increase of anhydrous phases as larnite and calcite is observed [8]. Portlandite remains stable until 500 °C. Between 500 and 600 °C, its decomposition produces CaO by following this reaction:

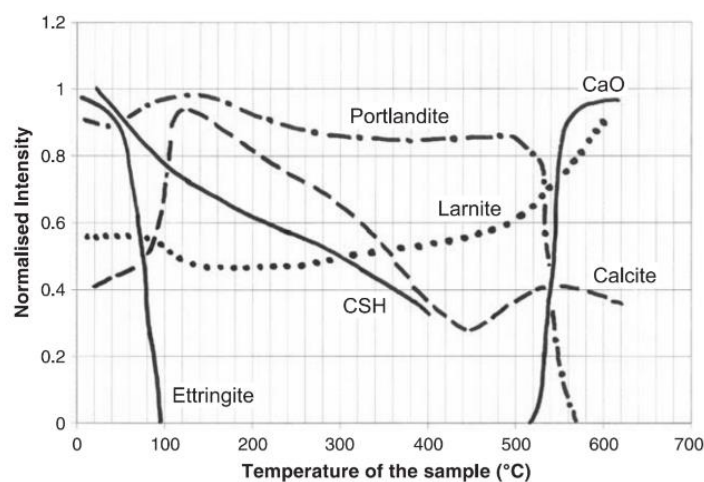
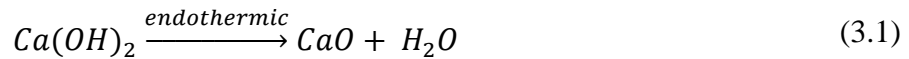


**Figure 3.3** Evolution of normalized intensity for phases of hardened cement paste with temperature obtained by neutron diffraction [8].

Between 600 and 700 °C, second stage of CSH gel decomposition is observed [9]. Starting from 700 °C, decomposition of  $\text{CaCO}_3$  leads to a release of carbon dioxide following Equation 3.2. Further increase of the temperature leads to melting of cement paste around 1200 °C [9].



Mineralogical nature of aggregates is the governing factor that determines their high-temperature behavior. Figure 3.4 presents thermo-differential analysis (TDA) accomplished on aggregates of different petrographic nature. Siliceous aggregates produce an endothermic reaction around 600 °C presented by a peak. This peak is related to a transformation of crystallinity of quartz from  $\alpha$  - quartz to  $\beta$  - quartz at 573 °C. Calcareous aggregates containing limestone have a peak between 700 and 1000 °C related to decarbonation of  $\text{CaCO}_3$  (see Equation 3.2).

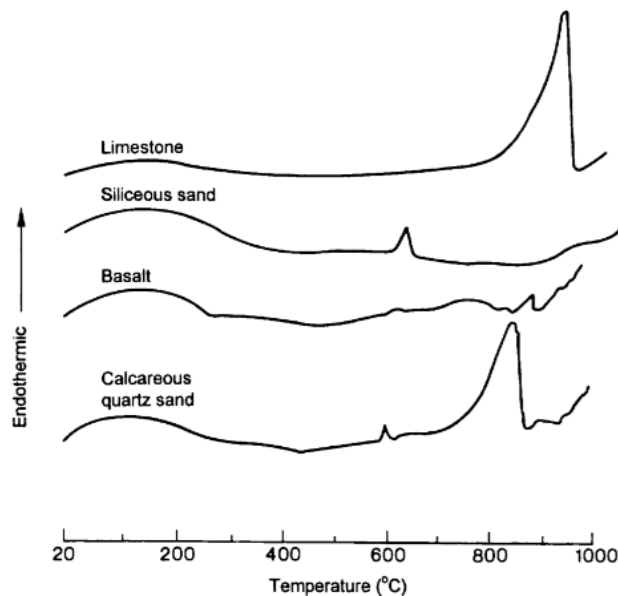


**Figure 3.4** Thermo-differential analysis (TDA) for different aggregates [10].

### Thermal deformations of cement paste and aggregate

Thermal expansion of concrete is controlled by thermal expansion of its constituents: cement paste and aggregates. A schematic representation of thermal expansion of cement paste and aggregates is presented in Figure 3.5. Cement paste experiences a thermal expansion between 20 and 150 °C due to a movement of water molecules and a decrease of capillary forces [9]. Starting from 150 °C, cement paste shrinks under the influence of dehydration of CSH gel [9], [11]. On contrary to cement paste, aggregates only expand under the influence of temperature.

Depending on their nature of aggregates and type of paste, thermal strain may vary as shown in Figure 3.6a. Silica-containing aggregates expand the most among the aggregates [9], [11], [12], [13]. It is found that coefficient of expansion of siliceous aggregates depends on both content and crystallinity of quartz [13].

As 50-80 % volume of concrete is composed of aggregates, thermal strain of concrete mainly depends on thermal strain of its aggregates. Figure 3.6b shows thermal strains of concrete containing aggregates of different nature. We note again that concretes with siliceous aggregates expand more than concretes with calcareous aggregates.

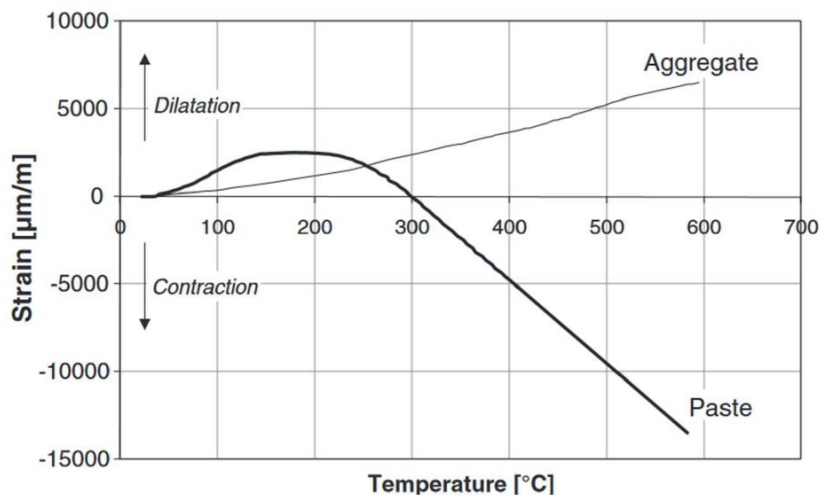


Figure 3.5 Difference in thermal strains of aggregates and pastes [14].

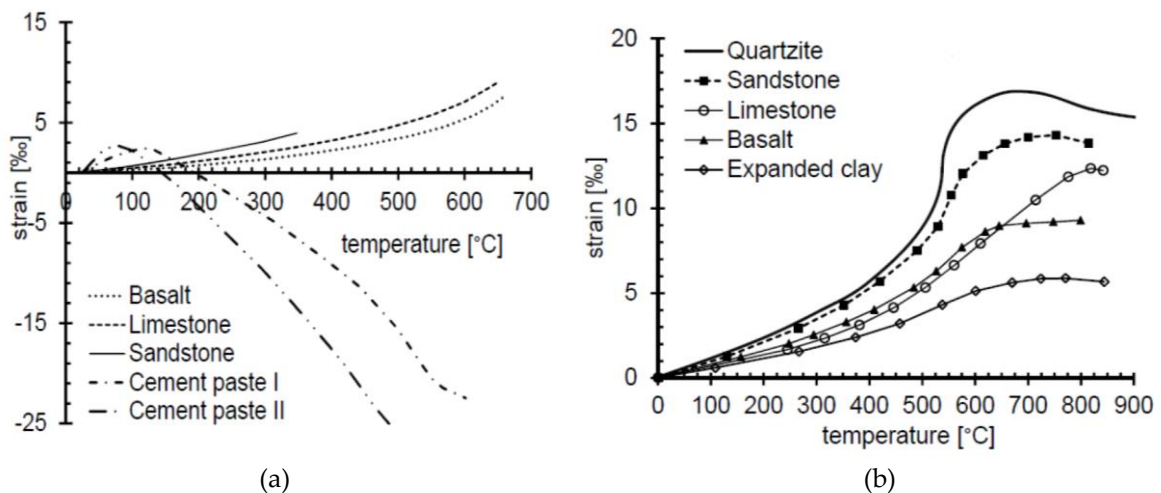
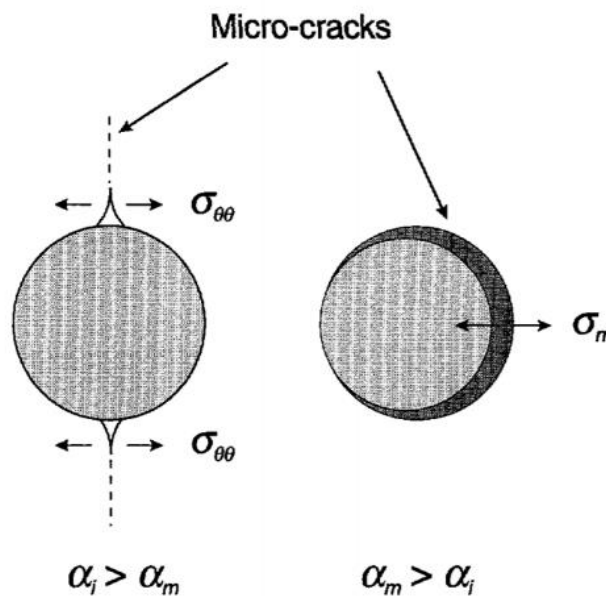


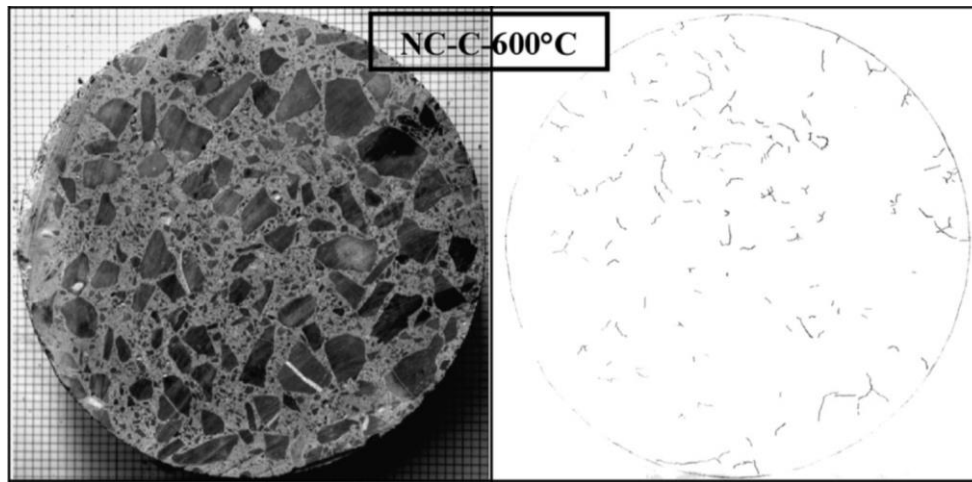
Figure 3.6 Thermal strain of: a) three types of aggregates and two types of paste, b) concrete containing different aggregates adapted from [12].

Difference in thermal deformation of cement paste and aggregates provokes a so-called ‘thermal mismatch’ or ‘thermal incompatibility’, which generates stresses that result in crack propagation (see Figure 3.7). Between 20 and 150 °C, expansion of cement paste exceeds the expansion of aggregates leading to radial stresses at the interface of cement paste and aggregate that result in circumferential cracks. Starting from 150 °C, expansion of aggregates dominates the contraction of cement paste. Aggregate expansion induces circumferential stresses producing radial types of cracks of cement paste.

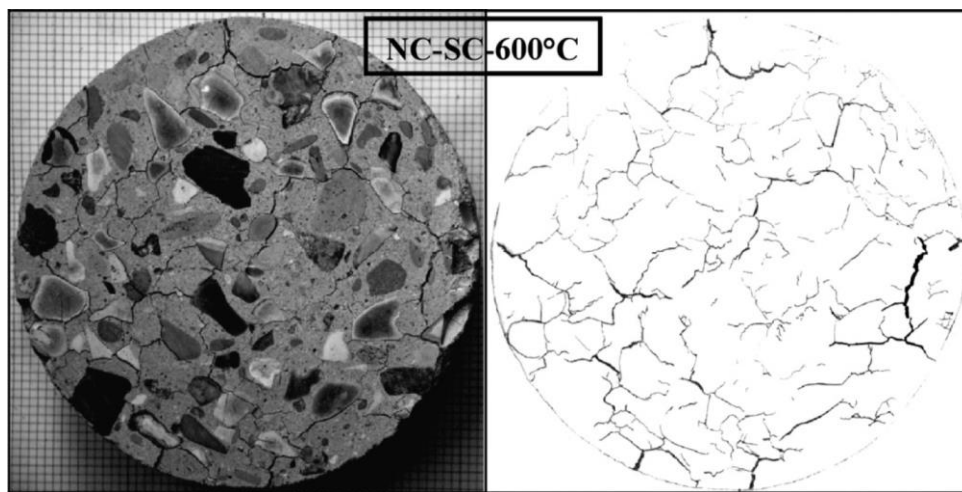


**Figure 3.7** On the left, for coefficient of thermal expansion of inclusion  $\alpha_i > \alpha_m$  of matrix, circumferential stresses provoke radial cracks. On the right, for  $\alpha_m > \alpha_i$ , radial stress provoke tangential cracks [15].

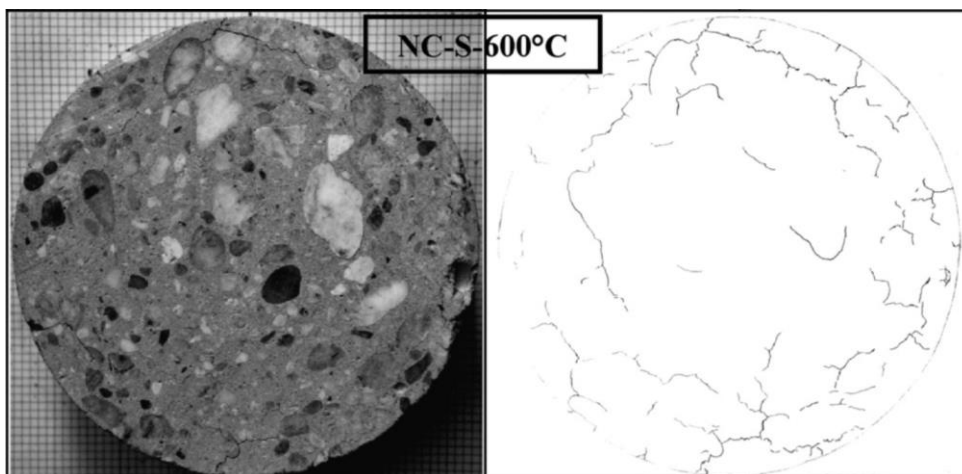
Depending on the nature of aggregates and cement paste, different cracking patterns occur. Figure 3.8 presents images and crack maps of ordinary concrete with calcareous (Figure 3.8a), silico-calcareous (Figure 3.8b) and siliceous aggregates (Figure 3.8c) subjected to 600 °C. We notice that concrete with silico-calcerous aggregates is more cracked and cracks form a network. This finding is reported as well in [11], [16]. As for concrete with siliceous aggregates, there are less cracks and they are mainly present at the edges. For concrete with calcareous aggregates, cracks are short and disconnected from one another.



(a)



(b)



(c)

**Figure 3.8** Image of sample and crack maps for ordinary concrete heated to 600 °C containing different aggregates: a) calcareous aggregates, b) silico-calcareous aggregates and c) siliceous aggregates [17].

### 3.2.3 Concrete permeability at high temperature

Evolution of concrete constituents with temperature imposes as well an evolution of its properties. We focus in this part on evolution of concrete permeability at high temperature. Other properties such as mechanical, thermal and physical are not covered in here. We first start by presenting basic notions on permeability. We then present literature available on the influence of temperature on permeability of cementitious materials.

#### Basic notions

Darcy's law is used to describe a laminar flow of percolating fluid in a porous medium [18]:

$$v = -\frac{K_i}{\mu} \text{grad } P \quad (3.3)$$

where  $v$  is flow velocity,  $K_i$  is intrinsic permeability,  $\mu$  is dynamic viscosity of fluid and  $P$  is pressure. Using Darcy's law, volumetric flow of incompressible viscous liquid flowing in laminar regime through section  $S$  of porous material with length  $L$  is then:

$$Q_v = \frac{K_i}{\mu} \frac{\Delta P}{L} S \quad (3.4)$$

Velocity profile for a viscous fluid flowing in capillary tube is presented in Figure 3.9. It is important to note that the velocities at the walls of the capillary tube are equal to zero.

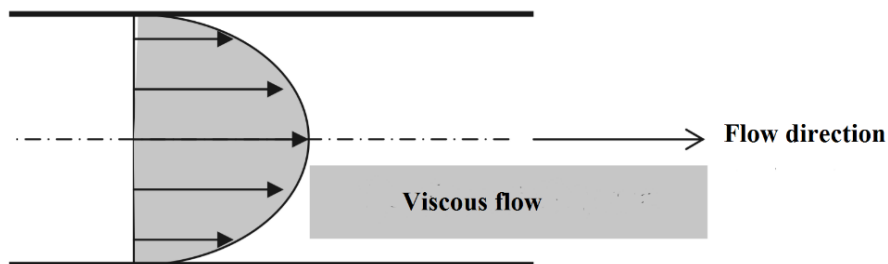


**Figure 3.9** Velocity profile for viscous fluid in capillary tube adapted from [19].

For compressible fluids such as gas, we consider mass conservation and ideal gas behavior. Then, volumetric gas flow through porous medium under pressure gradient  $\Delta P = P_1 - P_2$  is:

$$Q_v = \frac{1}{2} \frac{K_a}{\mu} \frac{(P_1^2 - P_2^2)}{LP_2} S \quad (3.5)$$

where  $P_1$  and  $P_2$  are injection and atmospheric pressures,  $K_a$  is an apparent permeability. For hollow cylinder geometry presented in Figure 3.10, apparent permeability is found as [20]:

$$K_a = \frac{Q_v \mu \ln\left(\frac{R_2}{R_1}\right)}{\pi h (P_1^2 - P_2^2)} \quad (3.6)$$

where  $R_1$  and  $R_2$  are internal and external radii of hollow cylinder and  $h$  is cylinder height.

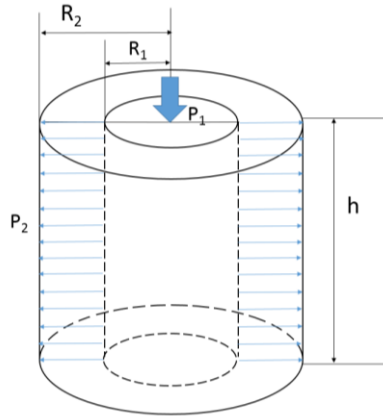


**Figure 3.10** Geometry of hollow cylinder.

Nitrogen dynamic viscosity variation with temperature is computed with Sutherland's formula [21]:

$$\mu = \mu_0 \left(\frac{a}{b}\right) \left(\frac{T}{T_0}\right)^{\frac{3}{2}} \quad (3.7)$$

$$\begin{aligned} a &= T_0 + 111 \\ b &= T + 111 \end{aligned} \quad (3.8)$$

where  $T_0$  is nitrogen reference temperature = 293.15 K,  $T$  is gas temperature,  $\mu_0$  is viscosity at  $T_0 = 1.781 \times 10^{-6}$  Pa.s.

For compressible fluids, in addition to viscous flow there exists a slip flow. The slip flow constitutes a part of flow of gas related to non-adherence of gas molecules to the surface of capillaries. Velocity at walls of capillary tube is not zero as can be seen in Figure 3.11.

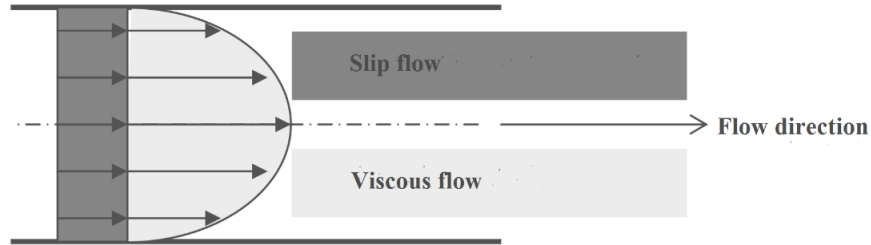


**Figure 3.11** Velocity profile for gas in capillary tube adapted from [19].

Klinkenberg's method [22] allows determining intrinsic permeability through linear regression of apparent permeability values at different pressures with inverse mean pressure  $1/P_m = 1/(P_1 + P_2)$  as:

$$K_a = K_i \left( \frac{\beta}{P_m} \right) \quad (3.9)$$

where  $\beta$  is Klinkenberg's constant. An example of the use of Klinkenberg's method on the data set is presented in Figure 3.12. We notice that intrinsic permeability is located at the minimum value of apparent permeability, i.e., it is a threshold permeability of viscous flow.

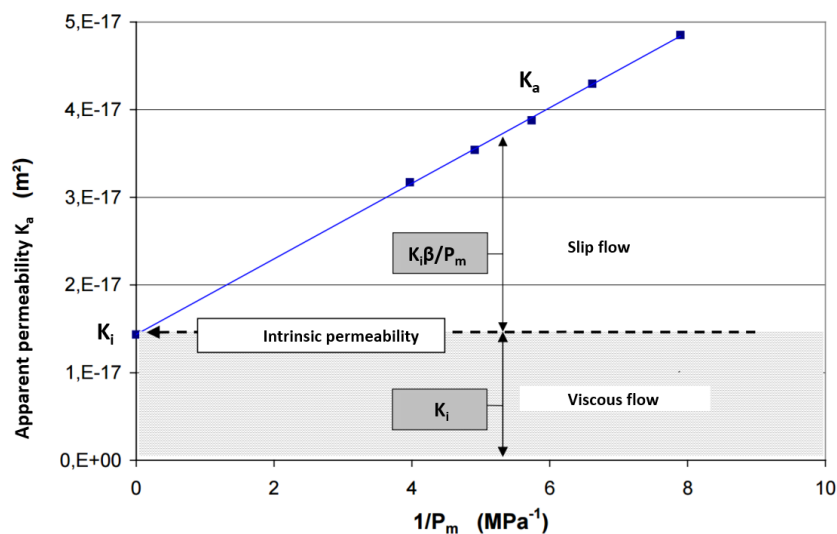


**Figure 3.12** Example of application of Klinkenberg's method on set of experimental data adapted from [23].

### Evolution of concrete permeability at high temperature

Several studies have investigated the influence of temperature on the permeability of cementitious materials to gas after cooling (residual permeability) [24], [25], [26], [27] while others during heating [28], [29]. Figure 3.13 presents an evolution of intrinsic permeability to nitrogen of ordinary and high-performance mortars and concretes with temperature. Reference temperature of the samples is 105 °C and samples are heated with a rate of 0.2 °C/min to a target temperature. Residual axial permeability tests are accomplished on concrete samples (D = 150 mm, H = 50 mm) and mortars (D = 54 mm, H = 30 mm). We note that residual intrinsic permeability of mortars and concretes increases with temperature. Between 105 and 400 °C, the increase of the intrinsic permeability is greater for high performance materials than for ordinary: two orders of magnitude for high performance materials and one order of magnitude for ordinary ones. Author links the increase of permeability to changes in microstructure, in particular, increase of pore size and volume.

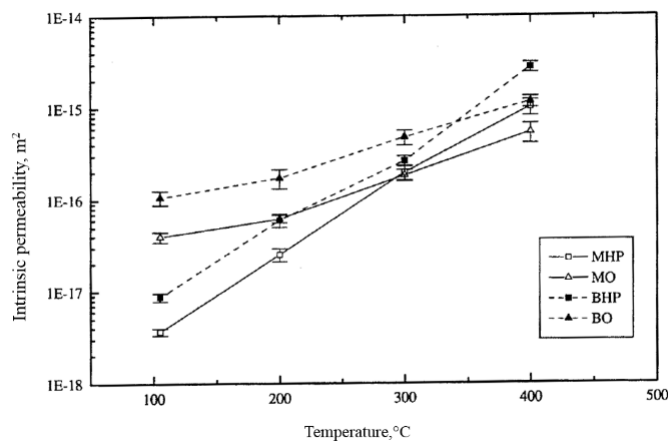


**Figure 3.13** Evolution of intrinsic permeability of high performance mortars and concretes (MHP and BHP) and ordinary mortars and concretes (MO and BO) with temperature adapted from [24].

Mechanical loading initiates an additional damage of concrete and alters its permeability. Residual axial permeability measurements accomplished on samples preheated to 400 °C under uniaxial loading show an increase of intrinsic permeability with compressive loading. It is important to note that even a small loading of 0.5 MPa has provoked a significant increase in permeability. Uniaxial loading induces a propagation of cracks parallel to the direction of load application, which modifies permeability. Since gas flow is aligned with loading direction, a significant increase of intrinsic permeability is measured.

Residual radial permeability and relative residual radial permeability (a ratio of permeability and initial permeability) results for concrete heated at different temperatures under variable uniaxial compressive loading are presented in Figure 3.15a and 3.15b respectively. Following trend is observed: first, there is a slight decrease of permeability (related to partial closure of heat-induced cracks oriented perpendicular to loading direction), then stabilization (due to counterbalance between crack closure, initiation of new cracks and growth of heat-induced cracks) and consequent increase of permeability (due to prevalence of mechanically induced cracks) [25]. Results obtained for 400 °C show a slight decrease of permeability is observed at lower loading level (< 2 MPa), followed by stabilization (2-5 MPa) and increase of permeability (5-10 MPa).

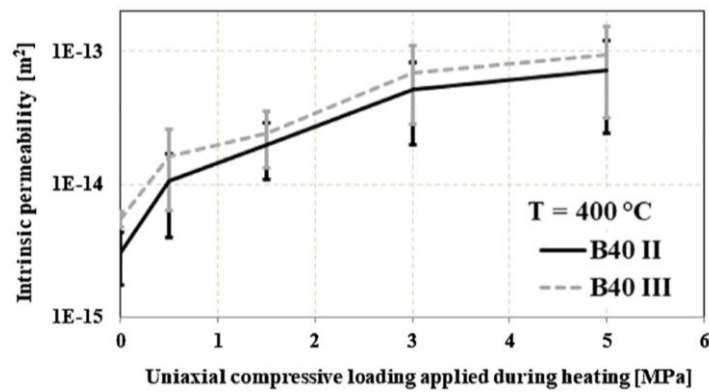


Figure 3.14 Evolution of residual axial intrinsic permeability of concrete as a function of uniaxial compressive stress for sample preheated to 400 °C [25].

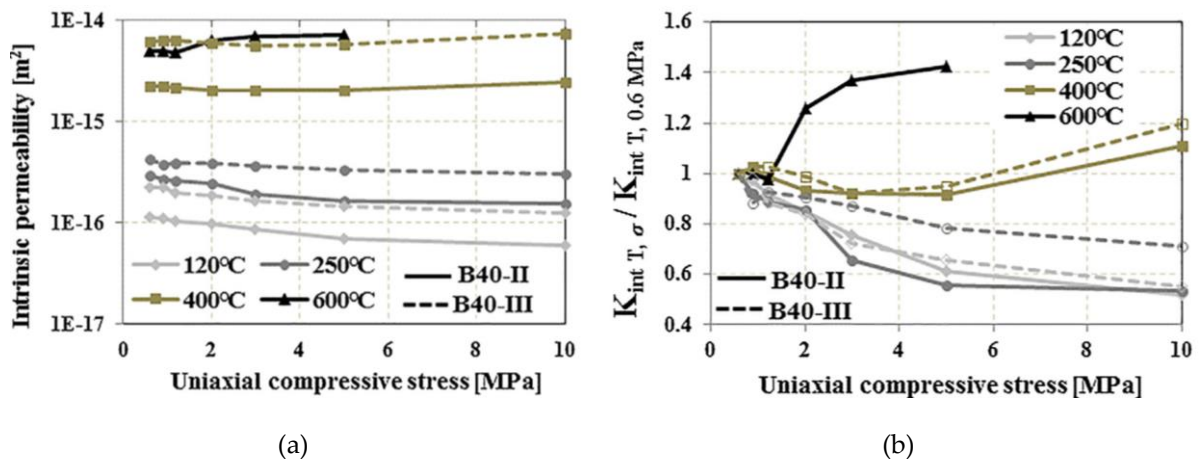
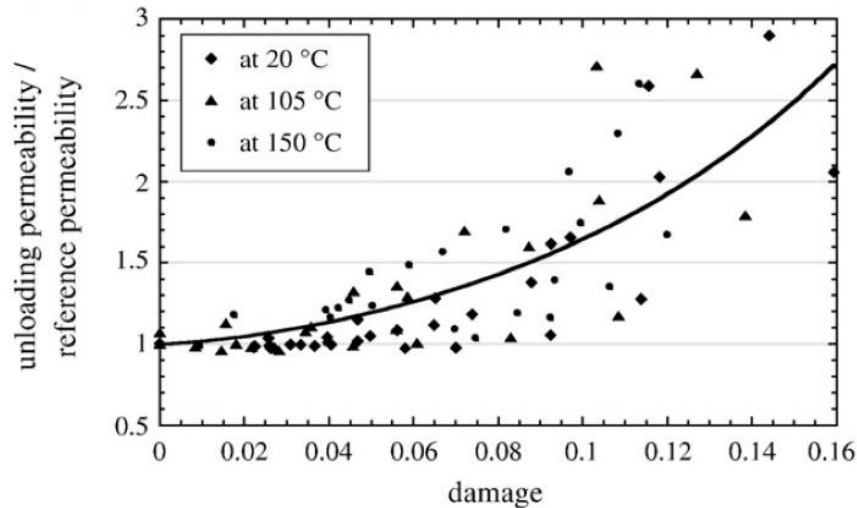


Figure 3.15 Evolution of residual radial intrinsic permeability of concrete (a) and relative residual radial intrinsic permeability (b) as a function of uniaxial compressive stress for different temperatures after heating-cooling cycles [25].

The evolution of the relative intrinsic permeability (a ratio of permeability and permeability measured at 20 °C) measured after unloading from uniaxial compressive loading during heating is presented as a function of damage (see Equation 3.10) in Figure 3.16. The results show a good fitting of master curve for relative intrinsic permeability measured for three temperatures, despite some dispersion of data. Based on these findings, author [30] states that evolution of permeability should be viewed as coupled effects of damage and temperature.

$$d = \frac{E_0 - E_{unloading}}{E_0} \quad (3.10)$$

where  $d$  – damage,  $E_0$  – initial elastic modulus of material,  $E_{unloading}$  – elastic modulus of material after unloading.



**Figure 3.16** Evolution of permeability/reference permeability as a function damage for different temperatures [30].

### 3.2.4 Thermal instability of concrete at high temperature

In previous sections, we have presented a general information on concrete, evolution of concrete constituents and permeability with temperature. In the following sections of literature review, we present the phenomenon of thermal instability of concrete at high temperature and provide an explanation of its origins.

## Major fires accidents

A number of major fires has increased rapidly over the last two decades leading to human and financial losses. Some of the fires are:

- La Manche tunnel, 11 km tunnel between United Kingdom and France in 1996 (2 injured) and in 2008 (14 injured);
- Mont Blanc tunnel, 11.6 km-long tunnel between France and Italy, in 1999 (39 dead);
- Tunnel of Tauern of 6.5 km in Austria in 1999 (12 dead and 42 injured);
- Tunnel St. Gothard in Switzerland, 16.9 km-long tunnel, in 2001 (11 dead);
- Swiss tunnel Viamala, 750 m – long tunnel, in 2006 (9 dead, 6 injured);
- French 12.9 km-long tunnel Fréjus in 2005 (2 dead).

History shows disastrous accidents in the buildings such as a fire in 2005 in 32- story Windsor Tower in Spain and an accident in 2009 in 44-story Mandarin Oriental Hotel in China (1 dead and 7 injured).

In buildings, fires are more frequent, accidental and less violent leading to damage of concrete surface without a loss of structural stability. In tunnels, an increased density of traffic and heavy transportation of flammable products amplify the risks of major fire accidents. The particularity of fires in tunnels lies in severity of thermal loading due to confined space of structure and heavy ventilation that encourages fire propagation. Severity of fires is characterized by the time necessary to reach a maximum temperature and the duration of fire, in case of tunnels highest thermal loads are obtained in few minutes after fire start with a total fire duration of several hours (linked to difficulties of site access, loss of visibility). The post-fire images in La Manche tunnel and Mont Blanc tunnel presented in Figure 3.17 show a complete or partial detachment of concrete and exposure of steel reinforcement from structure. This phenomenon is linked to thermal instability of concrete named ‘spalling’.

Gary [31] has classified thermal instability forms into four categories:

- Aggregate spalling – instability that occurs at surface due to instability of aggregates
- Angle spalling – non-violent type of instability that occurs at the angles
- Surface spalling or spalling – a phenomenon of decohesion or departure of concrete during the fire caused by thermal instability followed by the sound resembling the "popcorn" effect
- Explosive spalling – violent form of spalling followed by a detachment of large pieces of concrete and excessive energy release.



**Figure 3.17** After fire: a) tunnel under La Manche in 1996 [32], b) tunnel Mont Blanc [33].

### Origins of thermal instability

Question on the origins of thermal instability of cementitious materials has provoked a number of theories; some are more accepted by scientific community, some less. The latest agreement on the origin of thermal instability in concrete exposed to high temperature states that the phenomenon originates from a coupled mechanism: thermo–hydro–mechanical (THM). A schematic representation of coupled mechanism is provided in Figure 3.18. We first present thermo - mechanical and thermo - hydral mechanisms individually. We then proceed with explanation of the coupling mechanism as an origin of phenomenon.

#### *Thermo-mechanical mechanism*

When concrete is heated, thermal gradients develop along the thickness of material due to a hot heated surface and a cold center and non-heated surface. The area near heated surface thrives to expand but is restrained from expansion by cold inner zone and unheated face [34]. Indeed, fire resistance tests on slabs show bending in longitudinal and transverse directions caused by expansion of heated surface [35]. The restraint of expansion creates auto constraints that provoke development of compressive stresses in the heated part and tensile and compressive stresses in cold zones such as center and non-heated surfaces. With time, compressive stresses, generated near heated surface, increase and exceed compressive strength of material, thus, contributing to thermal instability of the material. Bažant [36] gives an accurate definition of spalling due to thermo-mechanical mechanism as “brittle fracture and delamination buckling caused by compressive biaxial thermal stresses parallel to the heated surface”.

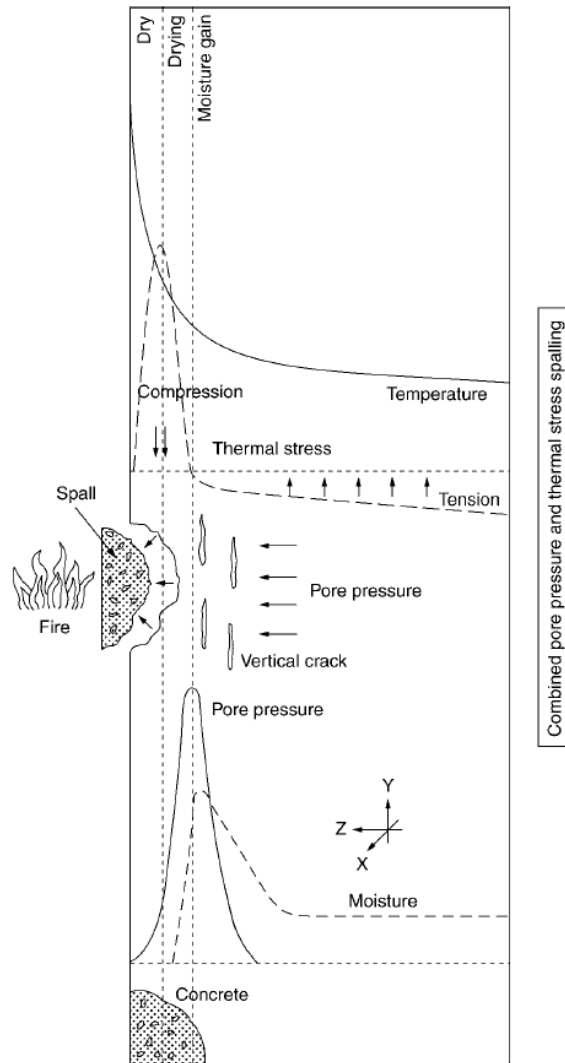


**Figure 3.18** Schematic explication of origin of concrete spalling due to fire: combined pore pressures and thermal stresses [37].

*Thermo-hydral mechanism*

During heating of concrete, evaporation of water leads to formation of dry zone and increase of pore pressure. Due to pressure gradients, migration occurs in two directions: towards the heated face and towards the inside of the material which constitutes a colder zone. When thermodynamic conditions are satisfied, an accumulation of condensed water vapor in the colder part occurs and the process continues until fully saturated layer is formed. This impermeable layer known as ‘moisture clog’ restricts the movement of vapor towards colder regions and provokes a built up of pore pressures that induce tensile stresses. When these stresses exceed tensile strength of concrete, concrete spalling occurs [38],[39],[40].

Experimental pore pressure measurements accomplished by [41] show that pore pressure increase follows saturated vapor pressure curve as explained in ‘moisture clog’ theory. It is necessary to note that in thermo-hydral mechanism, permeability plays a major role. High strength concretes having lower permeability compared to ordinary ones are prone to development of higher pore pressures due to a decelerated process of vapor evacuation. An experimental evidence is provided in Figure 3.19 that present measurements of pore pressures on high performance and ordinary concretes.

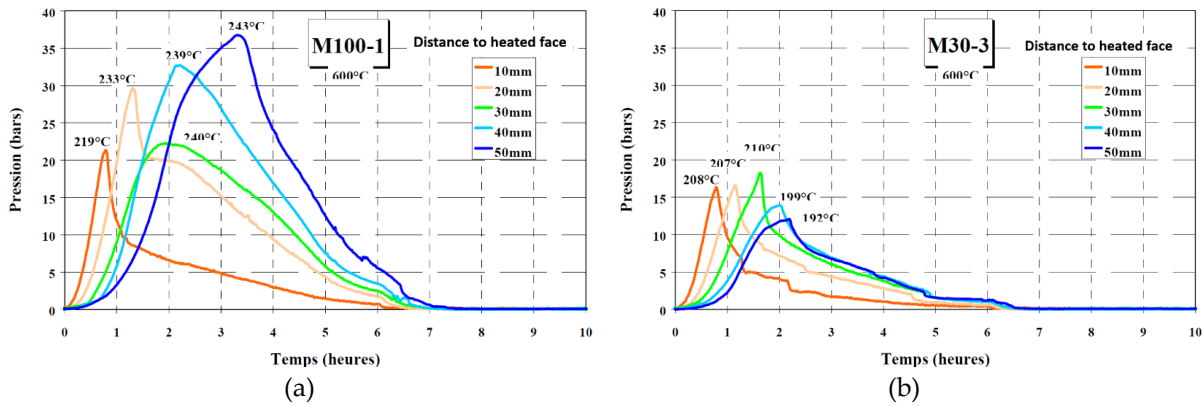


**Figure 3.19** Evolution of pore pressures as function of time: a) high-performance concrete, b) ordinary concrete [41].

*Why spalling is a coupled THM phenomenon?*

We shall note that several important factors are not considered in each mechanism. Thermo-mechanical mechanism does not take into account presence of moisture. Bazant [36] states that water vapor cannot trigger spalling, however, it can play a secondary role in spalling. In reality, when crack is opened, pore pressure drops to zero due to crack propagation that increases available space for steam. According to [34], this explanation should apply only to steams, as for liquid water a high thermal dilation of water provokes hydraulic fracturing.

We should note as well that compressive strength in the heated zone decreases as well both with temperature [11],[42] and moisture [34],[42]. Presence of moisture weakens compressive strength near heated face and provokes a significant expansion that induces additional stresses. Recent studies have questioned whether pore pressures that play a major role in thermo-hydral mechanism do serve as a trigger for concrete spalling. Numerous tests accomplished by [43] on the concrete slabs of different size heated with various temperature curves show low pore pressures, especially for spalled samples. Authors conclude that even though pore pressures are

not at origin of concrete spalling, they are involved in moisture redistribution in concrete. According to [43], there exists a critical zone susceptible to spalling located a few centimeters away from heated face whose mechanical resistance is weakened by temperature.

It is concluded in [44] that concrete spalling is less likely to occur without combined efforts of pore pressure, external loading and thermal strains. Both thermo-mechanical and thermo-hydral mechanisms occur simultaneously during concrete heating and contribute to concrete spalling. Therefore, a coupled thermo-hydro-mechanical mechanism should be taken into account when analyzing the reasons of concrete spalling.

### **Parameters influencing thermal instability**

Concrete spalling due to fire exposure depends on various parameters that may reduce or amplify the risk of thermal instability. We group the factors into three types: ‘material’ type, ‘sample’ type and ‘test’ type.

#### *‘Material’ type factors*

- (i) Related to composition: cement, aggregates, additions, admixtures, fibers

Influence of concrete composition on the sensitivity to spalling is presented in multiple studies. Miah [45] has studied the influence of cement types CEM II and CEM III on spalling sensitivity. He finds that under uniaxial loading concrete with CEM II spalls more than concrete with CEM III; however, when tested under biaxial loading no difference between two cements is observed. A study on the influence of filler shows an increase of maximum spalling depth with an increase of limestone filler up to 150 kg/m<sup>3</sup> in [46]. Presence of silica fume [47] has no influence on concrete spalling. Ordinary concrete containing silico-calcareous aggregates has presented less spalling than one with calcareous aggregates in [16]. In terms of fibers, literature reveals a beneficial influence of addition of fibers such as steel fibers [48], [49] and polypropylene fibers [40], [50], [51], [52] on spalling resistance.

- (ii) Related to water content and curing conditions

Water content plays a major role in risk of thermal instability of concrete. Literature notes increase of spalling with water content in concrete [53], [54], [55]. An importance of free water on spalling propensity is shown by several authors who observe no spalling for dried concretes even in presence of high thermal gradients [38], [56], [57]. Eurocode 2 suggests a threshold

value for water content of 3 % necessary to avoid spalling disapproved by multiple studies showing cases when spalling is observed for concretes with moisture content  $\leq 3$  % [16], [54],[58].

- (iii) Related to material properties: compactness, concrete strength, porosity, permeability

Influence of concrete compactness studied by [16] shows that compact concretes are more prone to spalling due to lower porosity and permeability, which reduces transport properties. It is found that increase of compressive strength increases spalling depth of concrete [16].

*'Sample' type factors*

- (i) Related to sample geometry and size

Studies show that spalling depends on the sample size [16], [55], [58], [59], [60]. In [58], larger samples spall more than smaller samples with a same sample thickness and same mechanical loading. Increase of sample thickness appears to provoke an increase in spalling as seen by [16], [55], [58], which shows a presence of size effect.

*'Test' type factors*

- (i) Related to structural: mechanical loading or restraint

Mechanical loading or mechanical restraint is an important factor that increases concrete spalling due to fire [45], [61], [62], [63]. In the work of Carré [64], no spalling is observed for samples loaded up in compression to 10 MPa, however, a significant spalling is noted for loading of 15 MPa. Another factor that increases spalling of concrete is restriction of thermal strains. Figure 3.20 shows an influence of presence of cold rim (or unheated zone) on the spalling propensity. We observe that spalled volume increases with increase of the thermally restrained area. Since in reality structural members are loaded or restrained, it is suggested that experiments should be accomplished either in loaded or restrained conditions [45].

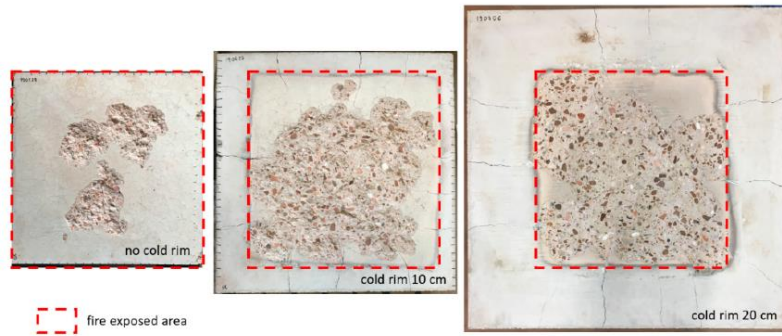


**Figure 3.20** Influence of cold rim sizes on the spalling response for samples with the same fire exposed area [65].

(ii) Related to heating: heating rate and exposed surface

Literature states that increase of heating rate increases spalling of concrete [39], [66], [67]. However, several studies note explosive spalling with a slow heating rate of several °C/min [47], [68] whereas some cases show less spalling under much severe heating curve [16], [69]. Mindeguia [16] states that under severe heating load (for example, HCM presented in Figure 3.21) concrete spalls more than under slower heating rate of several °C/min due to a quick formation of high thermal gradients on thinner layer of concrete that provokes higher damage and improve permeability.

Surface exposed to heating plays an important role as well. Heating of one side of sample is different than heating all sides. One side of concrete may as well be more sensitive to spalling than another due to heterogeneity of material.

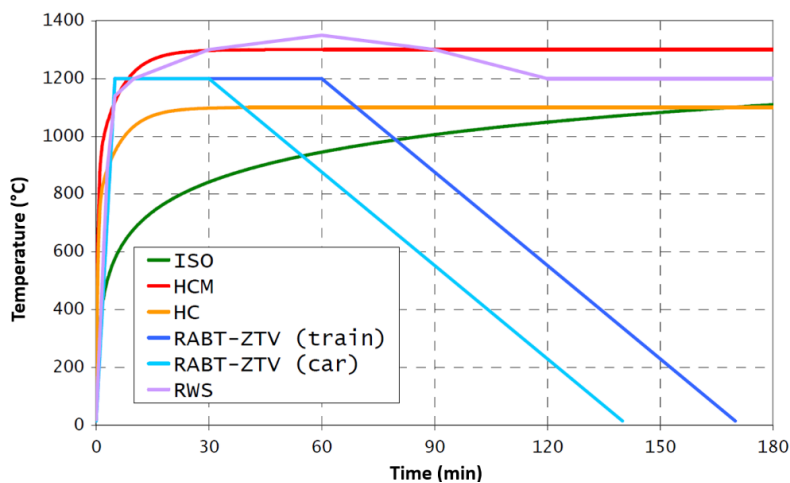


**Figure 3.21** Heating curves [16]: ISO - standard curve, HCM – modified hydrocarbon curve, HC- hydrocarbon curve, RABT-ZTV – German curve, RWS – Dutch curve.

### Fibers as an effective tool for spalling risk reduction

Numerous studies conducted by researchers indicate a positive effect produced by polypropylene fibers in terms of concrete spalling risk reduction [40], [50], [51], [52], [56], [65], [70], [71], [72]. Figure 3.22 demonstrates the results of the work conducted by [52] on concrete samples with and without polypropylene fibers after exposure to fire. We can see from the picture that addition of polypropylene fibers has prevented concrete spalling. Eurocode 2 EN 1992-1-2:2004 on “Design of concrete structures - Part 1-2: General rules - Structural fire design” suggests that for high performance concretes of class strength of 80/95 to 90/105 the addition of more than  $2 \text{ kg/m}^3$  of monofilament polypropylene fibers is necessary in order to reduce risk of spalling. French annex of the code provides geometry specifications: fiber diameter should be less  $\leq 50 \mu\text{m}$  and fiber length should be between  $D_{\text{max}}$  and  $4D_{\text{max}}$  where  $D_{\text{max}}$  is the size of the largest aggregate. Multiple studies that aim to understand the influence of polypropylene and optimize fiber geometry and dosage with respect to concrete do not yet allow a full understanding of the mechanism of polypropylene fibers in prevention of concrete spalling.

Apart from polypropylene fibers, other fiber possibilities for reducing concrete spalling not covered in this thesis include steel fibers [73], [74], [75], polyvinyl alcohol fibers [76], [77], [78], nylon fibers [79] and hybrid fiber mix [75], [76], [79].



**Figure 3.22** Efficiency of polypropylene fibers against spalling due to fire. On the left: a sample without fibers, on the right: a sample with polypropylene fibers [52].

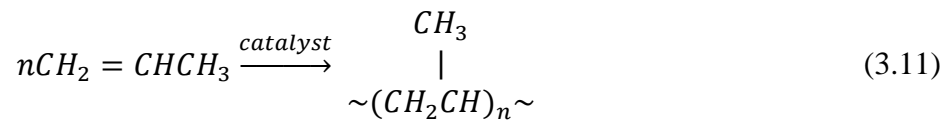
### 3.2.5 General information on polypropylene

This section presents a general information on polypropylene, its properties and high-temperature behavior.

#### Introduction

Polypropylene is a polyolefin thermoplastic and semi-crystalline resin. It has a broad range of applications due to its physical, mechanical and thermal properties. Main disadvantage of polypropylene oxidation, which requires addition of antioxidants into its composition. Other additions in polypropylene might include antistatic agents and colorants.

Polypropylene is a product of catalysis [80] presented in Equation 3.11:



Polypropylene is present on the market in the pure form called homopolymer and with additions (co-polymer) depending on application. Properties of polypropylene are presented in Table 3.1.

**Table 3.1** Several properties of polypropylene at room temperature

Property	Value
Density at solid state	910 kg/m <sup>3</sup> [81]
Density at amorphous state	850 kg/m <sup>3</sup> [81]
Elastic modulus	1.2-2 GPa [82]
Poisson's ratio	0.42-0.45
Tensile strength	33 MPa [82]
Elongation at break	10-25 %
Specific heat	1.68 kJ/g °C [83]
Thermal conductivity	0.17-0.24 W/m °C[83]

#### Structure of polypropylene

As a semi-crystalline material, polypropylene consists of crystalline and amorphous phases presented in Figure 3.23. In general, at room temperature polypropylene consists of 55 % crystalline phase and 45 % amorphous [81]. In order to possess crystalline phase, stereoregularity or a specific orientation of methyl groups, is required: isotactic or syndiotactic [80]. Figure 3.24 presents various orientations of methyl groups possible for polypropylene.

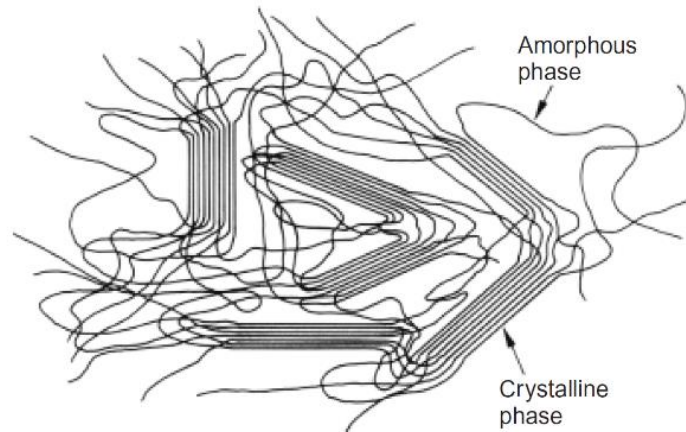


**Figure 3.23** Crystalline and amorphous phases of polypropylene [82], previously redrawn from [84].

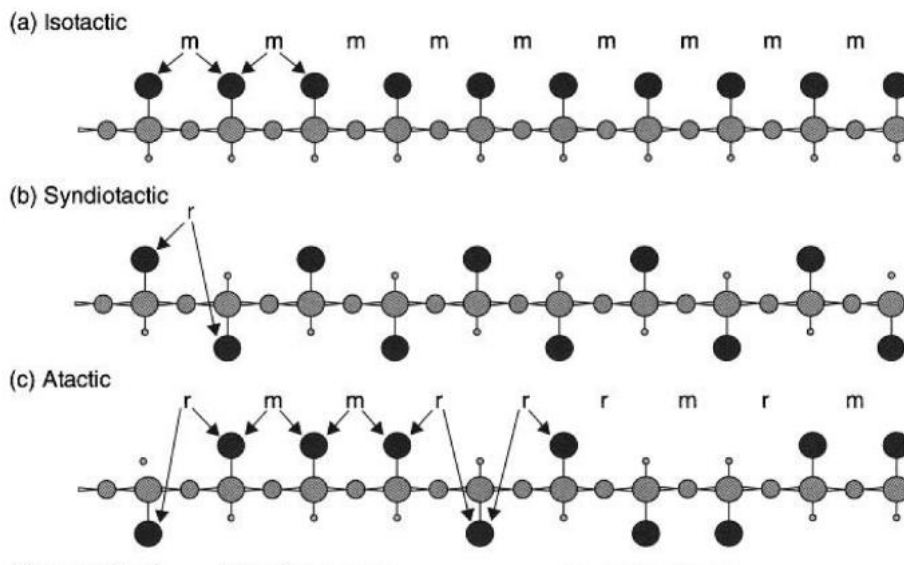


**Figure 3.24** Orientation of methyl groups (m) within polypropylene [80].

### Transition temperatures

Polypropylene as any thermoplastic material has two important transition temperatures that induce a change in the material state: glass transition temperature and melting temperature.

Below the glass transition temperature, the amorphous phase becomes fragile, above this temperature - soft and rubbery. For polypropylene, glass transition temperature is between -35 and 26 °C [82].

Melting of polypropylene is followed by a destruction of crystalline phase (and of mechanical properties that are related to crystallinity). Depending on the crystallinity phases, melting temperatures may deviate. The  $\alpha$ -phase crystallinity melts at 160 °C while  $\beta$ -phase melts around 145 °C. The state of the completely melted polypropylene can be either liquid and viscous or rubbery depending on the molar mass of the polypropylene. According to [81], melting of polypropylene starts at 150 °C with maximum rate of melting at 165 °C and finishes around 176 °C. For practical purposes, a peak value of DSC curve is considered as melting temperature as seen in Figure 3.25.

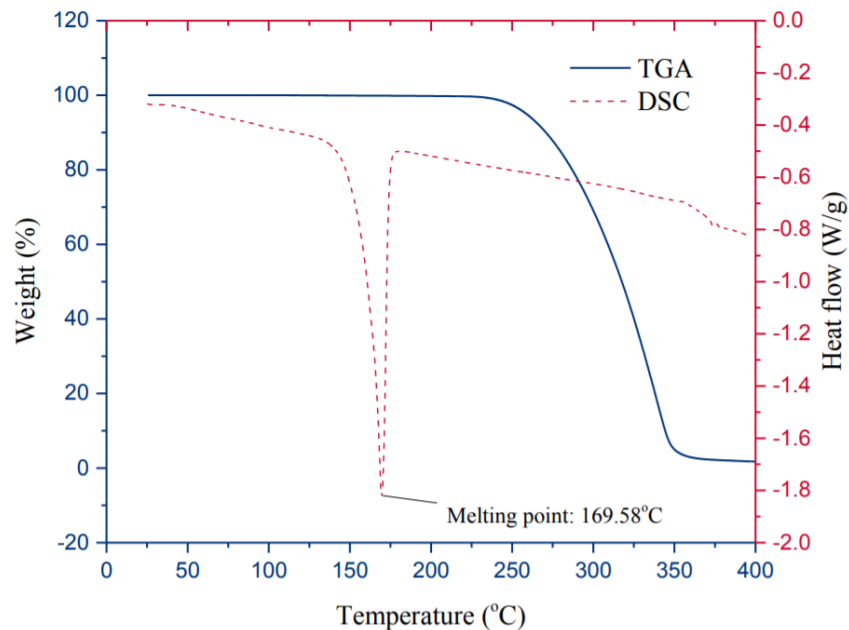


**Figure 3.25** TGA-DSC analysis of polypropylene by [85].

### Evolution of polypropylene properties with temperature

Polypropylene as a material is isotropic and polypropylene fibers are anisotropic. The orientation imposed during manufacturing at glass transition temperature creates anisotropy of polypropylene fibers properties. During heating, stresses imposed during the manufacture are released and preferential orientation is retrieved. This causes an anisotropic volume expansion of 7 % [81] of polypropylene fibers: contraction in length and expansion in width.

Elastic modulus of polypropylene decreases with temperature as seen in Figure 3.26. Mechanical properties are related to crystallinity, latter evolves with temperature and is destroyed during melting.

As any material expands with temperature, so does polypropylene. The evolution of coefficient of thermal expansion (CTE) of polypropylene is presented in Figure 3.27. We note that CTE increases with temperature and skyrockets around 160 °C due to destruction of crystalline phase. CTE reported in [83] is  $1 \times 10^{-5} / ^\circ\text{C}$  for  $T = 20 - 60 \text{ }^\circ\text{C}$ ,  $15 \times 10^{-5} / ^\circ\text{C}$  for  $T = 60 - 100 \text{ }^\circ\text{C}$  and  $21 \times 10^{-5} / ^\circ\text{C}$  for  $T = 100 - 140 \text{ }^\circ\text{C}$  which is similar to values in Figure 3.27. After melting, polypropylene shrinks due to compressibility of the melt flow.

Melted polypropylene is a non-Newtonian fluid, whose viscosity decreases with shear rate and temperature (see Figure 3.28). Viscosity of polymer is controlled by the molecular weight which depends on the lengths of polymer chains. In applications, where lower viscosity is desirable, intentional fragmentation of polymer chain, which reduces its length, is accomplished. In industry, viscosity of melted polypropylene is defined using the term melt flow rate (MFR), a flow rate of the molten material under the weight of 2.16 kg. MFR can vary from 0.3 g/10min to 1000 g/10 min depending on the molar mass of the material.

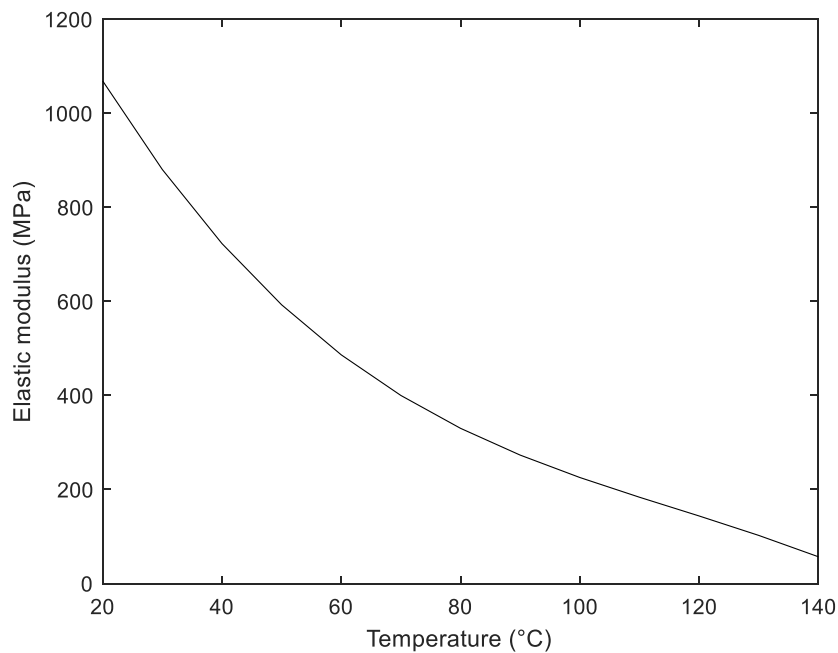


**Figure 3.26** Elastic modulus as a function of temperature for polypropylene [82].

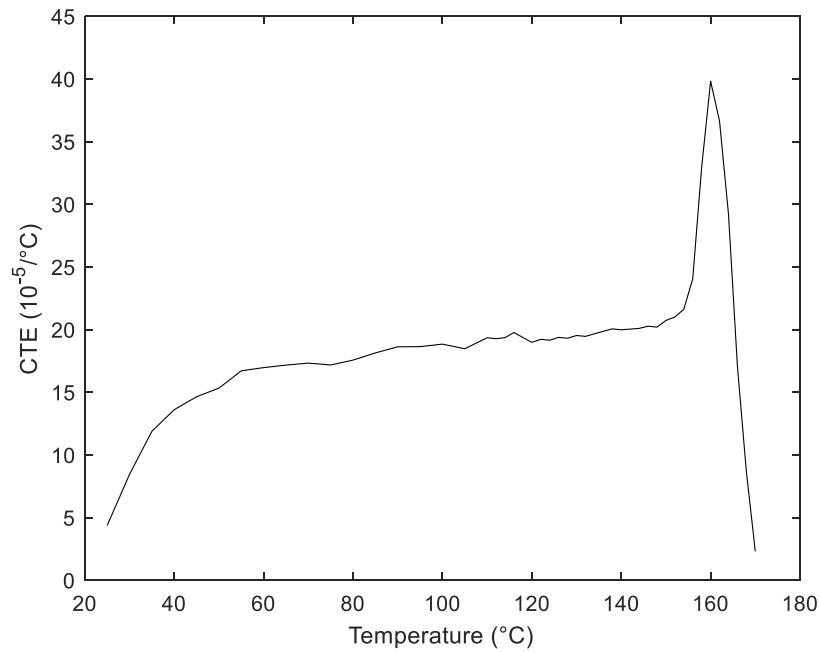


**Figure 3.27** Coefficient of thermal expansion as a function of temperature for polypropylene [86].

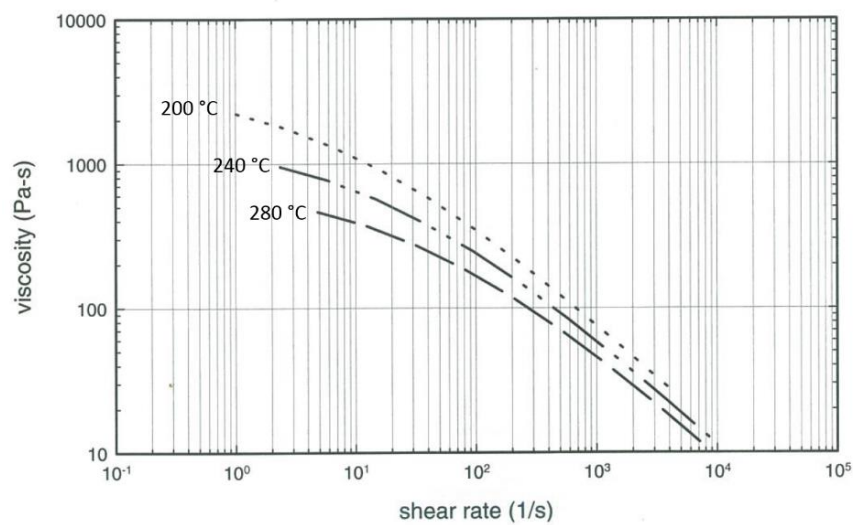


**Figure 3.28** Viscosity of polypropylene with shear rate for different temperatures [82].

### 3.2.6 How do polypropylene fibers prevent spalling of concrete?

We present current knowledge on mechanisms of polypropylene fibers in concrete subjected to fire that allow reducing/preventing risk of spalling. We explain here phenomena related to polypropylene fibers that lead to improvement of concrete resistance to fire.

#### *Additional air bubbles*

Presence of polypropylene fibers introduces air bubbles during mixing that weaken mechanical strength of material [87], [88], [89] and serve as additional paths for vapor evaporation.

#### *ITZ (interface transitional zone) around fibers*

Fibers as well as aggregates are surrounded by ITZ (see Figure 3.29a), a thin zone of a higher porosity compared to porosity of matrix [89], [90]. According to [38], ITZ represents “the weakest link of the matrix regarding permeability”; thus, presence of ITZ increases the vapor transport possibilities.

#### *Non-adhesion of polypropylene fibers to matrix*

Lack of affinity and polarity mismatch between polypropylene fibers and matrix may form adhesion issues at the interface. These cavities between fiber and matrix present a sufficient space for steam transport according to [88] as seen in Figure 3.29b.

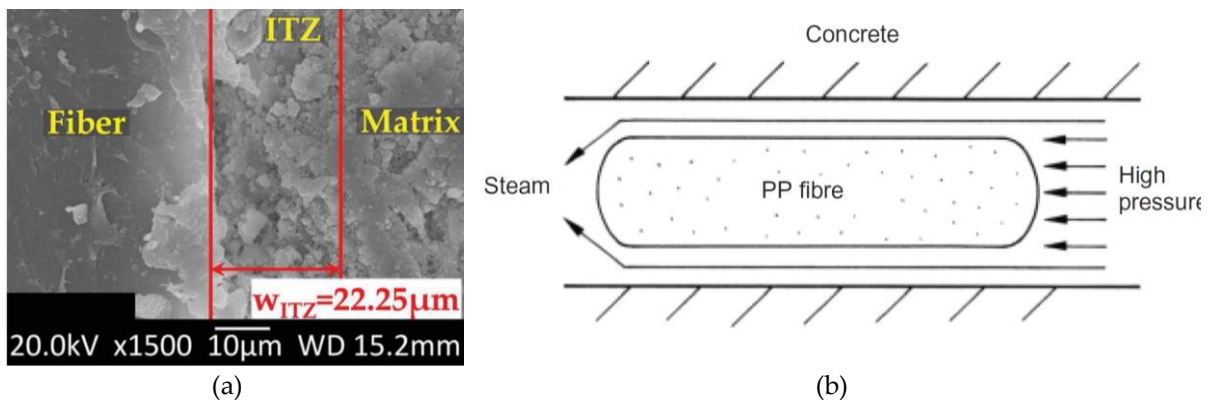


**Figure 3.29** Zone around polypropylene fibers: a) ITZ of fiber [90], b) Non-adhesion of polypropylene fiber acting for improved steam transport [88].

*Creation of vacated channels*

It is believed that melted polypropylene fibers flow into pores and cracks of cementitious matrix leaving empty channels for evacuation of vapor steam. Figure 3.30 presents images of polypropylene fibers in the matrix before and after polypropylene fiber melting obtained using field scanning electron microscope (SEM), which show empty channels for polypropylene fibers after melting. Some works indicate a presence of traces of polypropylene fibers after melting [29], [91], [92] as presented in Figure 3.31. When polypropylene fibers are melted, the polypropylene is partially or fully absorbed by cementitious matrix. A simple experiment of absorption of polypropylene by concrete matrix during heating is shown in Figure 3.32. Porous network created by these vacated channels is complementary to existing porosity of cement paste and it induces an increase of intrinsic permeability of concrete at high temperature [16], [40], [65] and reduction of pore pressure [40].

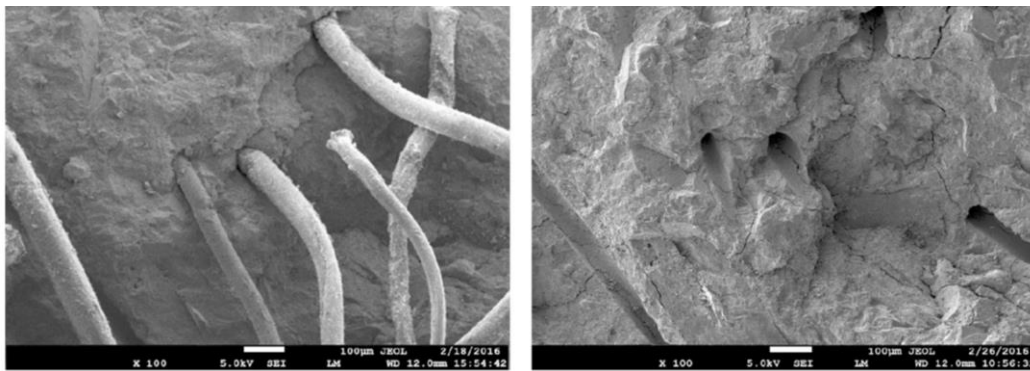


**Figure 3.30** Microstructure of UHPC with polypropylene fibers: on left, before heating; on right, after heating to 180 °C for 4 hours [29].

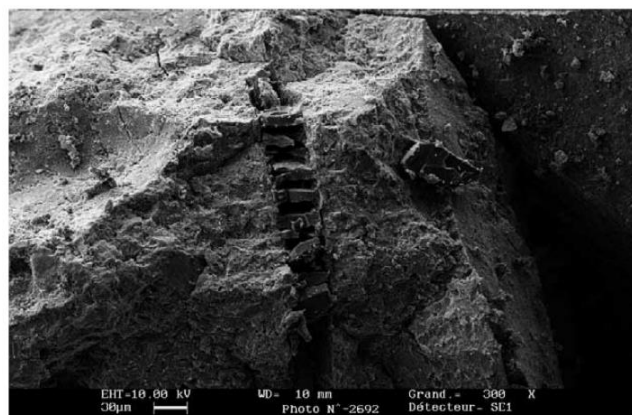


**Figure 3.31** Traces of polypropylene after melting [91].

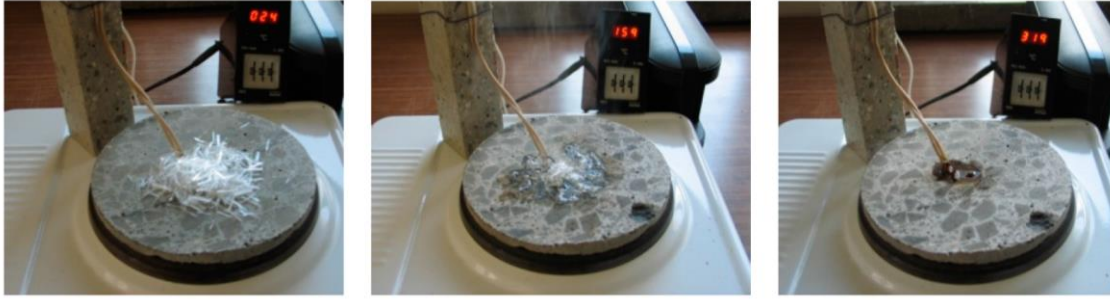


**Figure 3.32** Absorption of polypropylene fibers by matrix. Images from left to right are taken at 24, 159 and 319 °C measured using a thermocouple placed near fibers [65].

Bentz [93] has estimated a time required for polypropylene fiber melt to empty the channel by flowing through cylindrical path using Hagen-Poiseuille equation:

$$t = \frac{V}{Q} = \frac{8\mu L^2}{\Delta P R^2} \quad (3.12)$$

where  $V$  is fiber volume,  $Q$  is volumetric flow rate,  $\mu$  is polypropylene melt viscosity,  $L$  is fiber length,  $R$  is fiber radius,  $\Delta P$  is a pressure drop across length of the fiber. He finds that for pressures of 1 to 4 MPa measured on high performance concretes, with melt viscosity of 1000 Pa.s for 20 mm long 250  $\mu\text{m}$  thick fibers, time to empty channel would constitute between 50 to 200 seconds. This time to liberate the channel would only apply to fiber located at surface of concrete, as fibers inside of concrete would need to flow through path comprised of capillary pores. For pore size of 10  $\mu\text{m}$ , he finds that it would take from 2.25 to 9 hours to flow through a distance of 10 mm for a melted polypropylene. By the rough estimations that do not consider heat-induced cracking, he concludes that empty channels from fibers located at surface of concrete at depth susceptible to spalling and produced by flow from channels or burning out reduce risk of spalling. Interior fibers would remain intact until melting and after melting would flow into cementitious matrix [93].

#### *Microcracking around fibers*

Literature reveals a development of microcracks around polypropylene fibers due to differential thermal expansion of fiber and cementitious matrix. Figure 3.33a presents thermal strains for aggregates, polypropylene fibers and cement paste. We note that coefficient of thermal expansion of polypropylene fiber is several times that of cement paste which results in microcracking due to fiber – paste thermal mismatch. As discussed in previous section, heating

of polypropylene fibers is followed by volumetric change: expansion in width and contraction in length. Restrained expansion causes development of strong circumferential stresses at interface that result in propagation of radial cracks.

The images of evolution of microcracking around fibers with temperature are presented in Figure 3.33b. The microcracks are observed at 105 °C, before melting of polypropylene fibers due to fiber-matrix thermal mismatch. Some detachment of polypropylene fiber due to softening of fiber-paste interface appears at 150 °C. It is noted that microcracking due to thermal mismatch evolves with a temperature until fiber melting at 170 °C.

Conventionally, polypropylene fibers are used for their ability to increase permeability of concrete due to melting and evacuation of channels. Development of microcracking around fibers before their melting provokes a significant increase of intrinsic permeability of concrete confirmed by [85], [94], [95]. In comparison, the contribution of melting of polypropylene fibers and creation of empty channels is found to be less significant as seen in Figure 3.34.

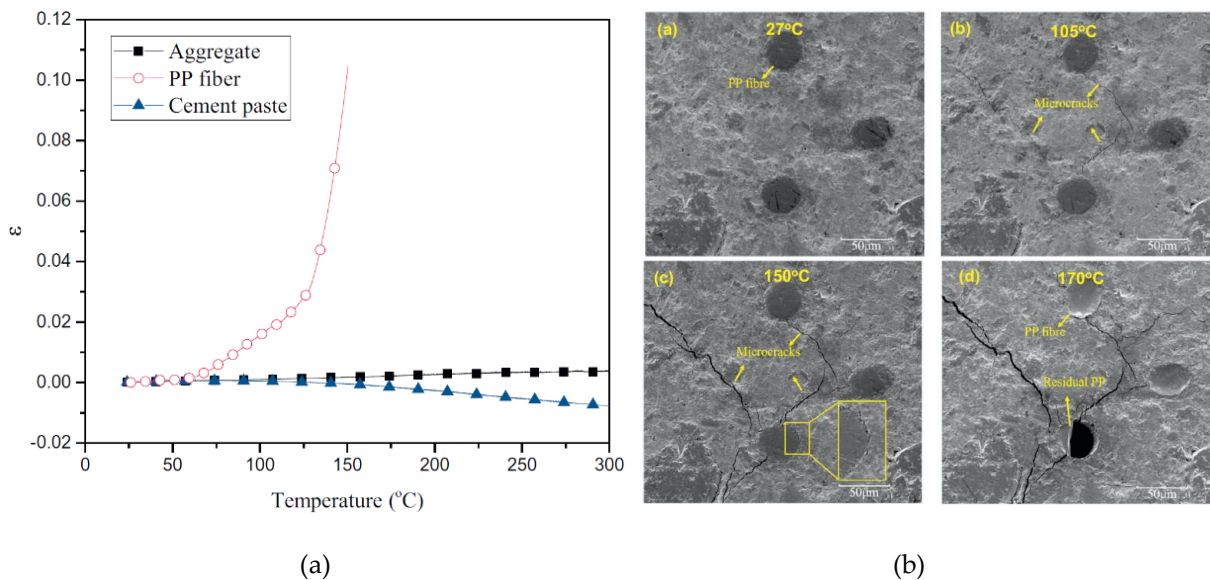


**Figure 3.33** Fiber-paste thermal mismatch: a) thermal strains of aggregate, polypropylene fiber and cement paste [85], b) microcracking state around fibers at different temperatures [85].

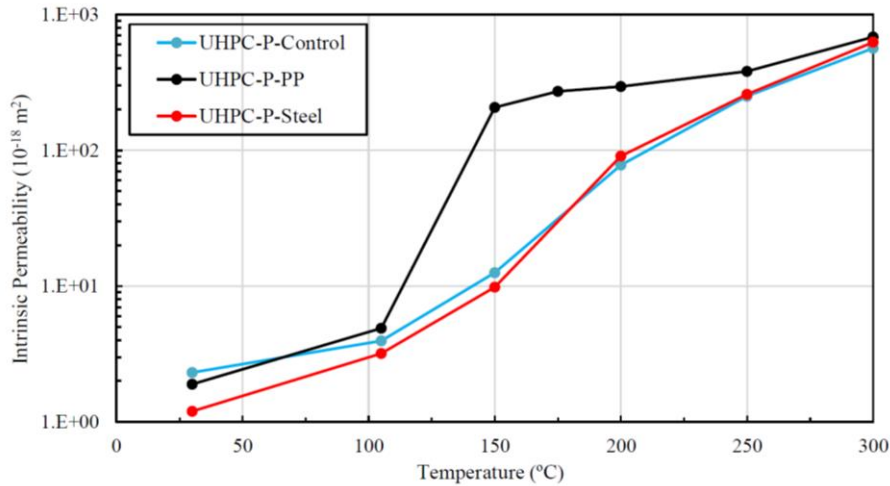


**Figure 3.34** Evolution of intrinsic permeability of UHPC with temperature (control: no fibers; PP: polypropylene fibers, steel: steel fibers) [95].

### *Contribution to percolation*

Percolation of transport channels is a key element for a successful moisture transport in heated concrete. This is where a question of percolation of individual fibers becomes relevant. Thresholds for percolation of freely overlapping randomly placed ellipsoids, a simple geometrical presentation of fibers, are estimated by [96]. Percolation is achieved for fibers of aspect ratio of 100 and 200 at volume fraction of 0.69 % and 0.32 % accordingly (in mass dosage - 6.28 and 2.91 kg/m<sup>3</sup>). These numbers show that percolation of individual fibers for conventional fire protection of concrete is hardly achievable (2 kg/m<sup>3</sup> is equivalent of 0.22 % vol. of fibers) and that other ways for percolation should be found. Bentz [93] has proposed improvement of percolation through bridging of ITZ of aggregate by fibers of 0.2 to 0.5 % vol. In terms of fiber length, he finds the use of longer fibers to be more efficient. A permeability model based on percolation of ITZ is presented in Figure 3.35a. Concrete is presented with circular aggregates with a thin ITZ aureole around and synthetic flexible fibers with ITZ. The percolation of the gas is controlled by bridging of ITZ of aggregates and fibers. Some works suggest use of polypropylene fibers for connecting the microcracks established by paste-aggregate thermal mismatch [97]. In this way, after melting of polypropylene, an interconnected path from empty channels and thermal microcracks from restrained aggregate expansion is ensured. An advanced version of this model presented in Figure 3.35b considers microcracking provoked by thermal expansion of polypropylene fiber.

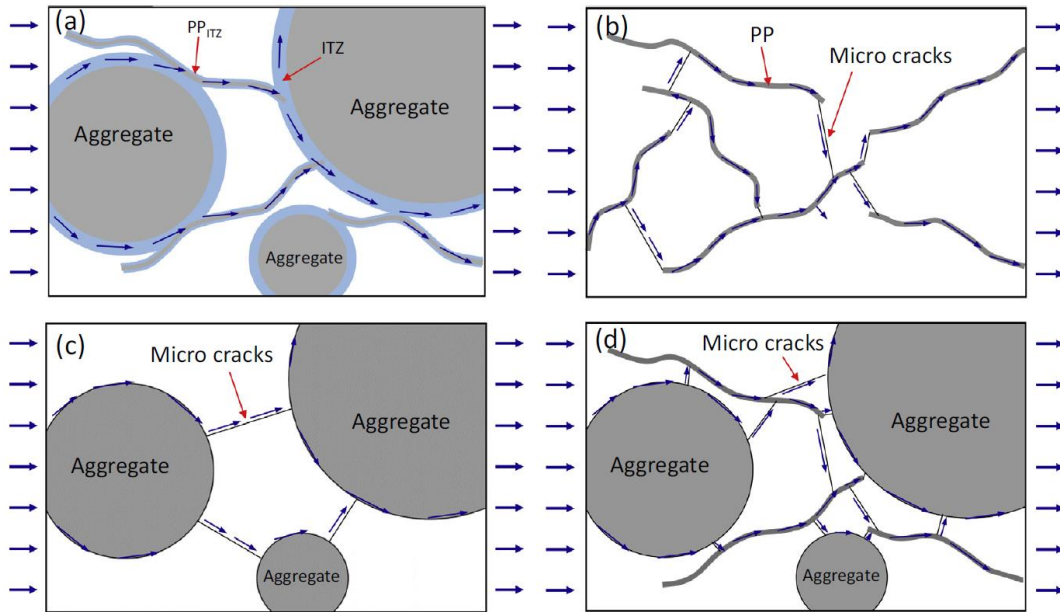


**Figure 3.35** Schematic presentation of permeability model : a) concrete with fibers, aggregates, and their ITZ [98], b) microcracks due to restrained fiber expansion, c) microcracks due to restrained aggregate expansion, d) connectivity of microcracks. The arrow presents flow of the gas [29].

### 3.2.7 Influence of fibers on intrinsic permeability

Addition of polypropylene fibers increases permeability of heated concrete through creation of empty channels, microcracking and improvement of percolation probability for release of steam vapour. Beneficial influence of polypropylene fibers on permeability depends on fiber dosage and geometry. Figure 3.36 presents an evolution of relative intrinsic permeability, a ratio between intrinsic permeability and intrinsic permeability at 105 °C, as a function of temperature. On the Figure 3.36a we note that increase of dosage of polypropylene fibers provokes an increase of intrinsic permeability. This conclusion is widely spread in the literature [11], [29], [40], [99], [100], [101]. Figure 3.36b shows an influence of polypropylene fiber length on relative intrinsic permeability. Increase of the fiber length induces a higher increase of intrinsic permeability due to improved percolation possibility compared to shorter fibers. Similar findings are concluded in [11], [97], [99]. Literature finds that for the same dosage of fibers, slender fibers are more efficient than thicker ones in terms of increase of permeability due to a higher total number of fibers. For a fixed number of fibers, a slight influence of increase of fiber diameter is noted as presented in Figure 3.37.

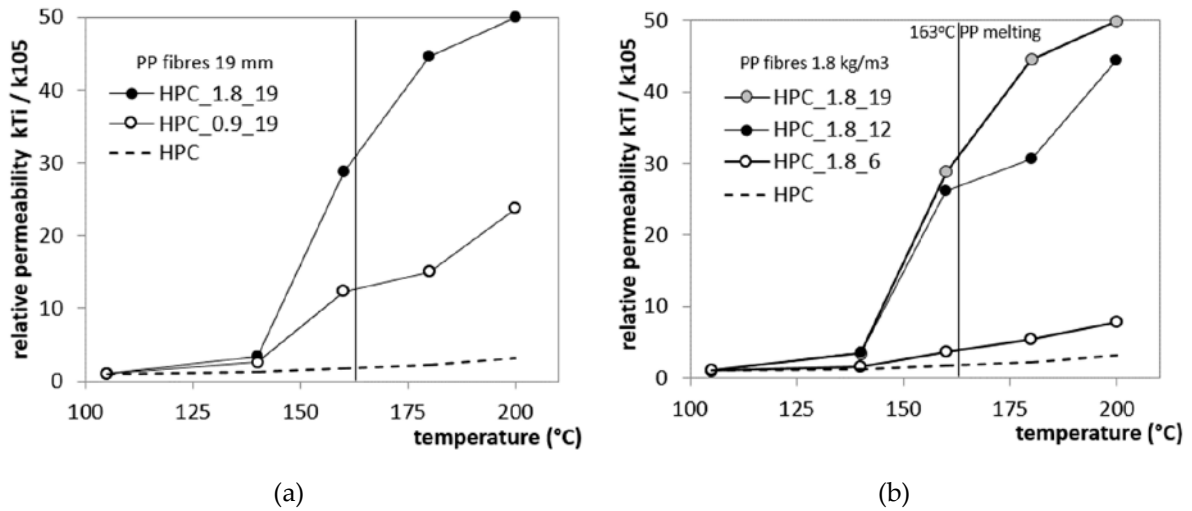


**Figure 3.36** Relative intrinsic permeability (a ratio between intrinsic permeability and intrinsic permeability at 105 °C) as a function of temperature for: a) concrete with 0, 0.9 and 1.8 kg/m<sup>3</sup> of 19 mm PP fibers, b) concrete without and with 1.8 kg/m<sup>3</sup> of 6, 12 and 19 mm PP fibers [65].

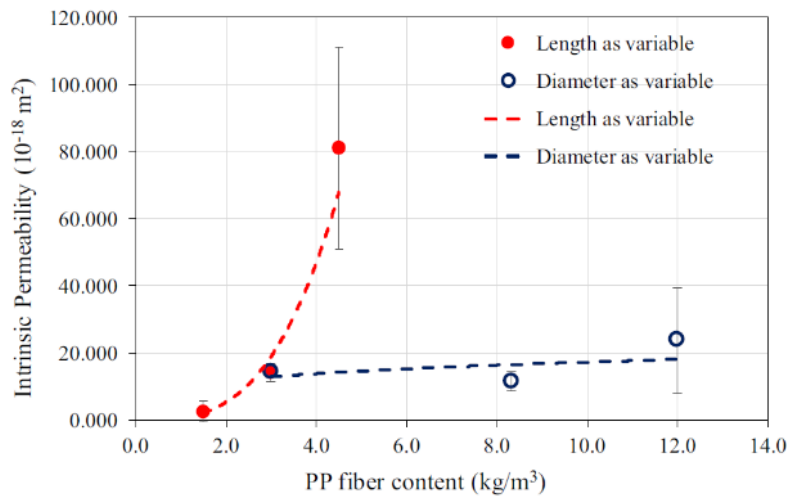


**Figure 3.37** Intrinsic permeability of UHPC as a function of polypropylene fiber content. Fiber dosage is increased in order to maintain the same total number of fibers [97].

### 3.2.8 Optimization of fiber choice for spalling prevention

Choice of polypropylene fiber dosage and geometry influences sensitivity of concrete to spalling. Generally, increase of polypropylene fiber dosage improves fire resistance of concrete. We present in Figure 3.38 images of the heated face of concrete blocks containing different dosages of polypropylene fibers after exposure to modified hydrocarbon fire. We note that increase of polypropylene fibers' dosage decreases spalling depth and volume. The decrease of

spalling with increase of polypropylene fiber dosage is noted as well in [70], [78], [79], [102]. Pore pressure decrease is observed with increase of fiber dosage in [40], [103].

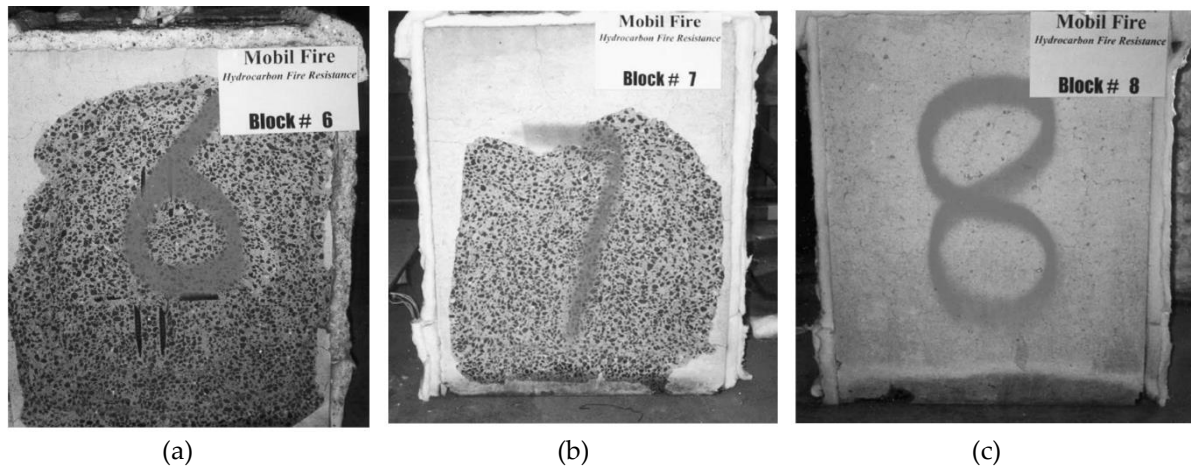


**Figure 3.38** View of blocks after modified HC fire tests using 20 mm fibers with different dosages: a) 1.5 kg/m<sup>3</sup>, b) 2.5 kg/m<sup>3</sup>, c) 3.5 kg/m<sup>3</sup> [50].

In terms of fiber length, longer fibers are found to be more efficient than shorter ones in terms of spalling prevention [50], [71], [104]. Longer fibers create longer evacuated channels and facilitate vapor transport. Pore pressure measurements comparing different fiber lengths confirm the efficiency of longer fibers over the shorter ones for a drop of pore pressure [76], [105]. Heo [71] presents a concept of ‘optimal fiber length’, which increases with the aggregate size as presented in Figure 3.39.

Data on the influence of polypropylene fiber diameter on spalling is not abundant. Studies show efficiency of thinner fibers [104] related to a higher number of fibers; however, when tested at same number of fibers, no influence of fiber diameter is noted [70].

Due to a variety of concrete mixes, sample size, curing and testing conditions available in literature, it is hard to select directly an optimized geometry and dosage for fibers. A question of optimization is challenging because of presence of two controlling parameters: fiber length and fiber number. Heo [71] stated an existence of critical fiber number  $N_c$  which allows determination of dominant parameter. When number of fibers  $N$  is less than  $N_c$ , fiber length is dominant and when number  $N$  exceeds critical number  $N_c$ , dosage is more important.

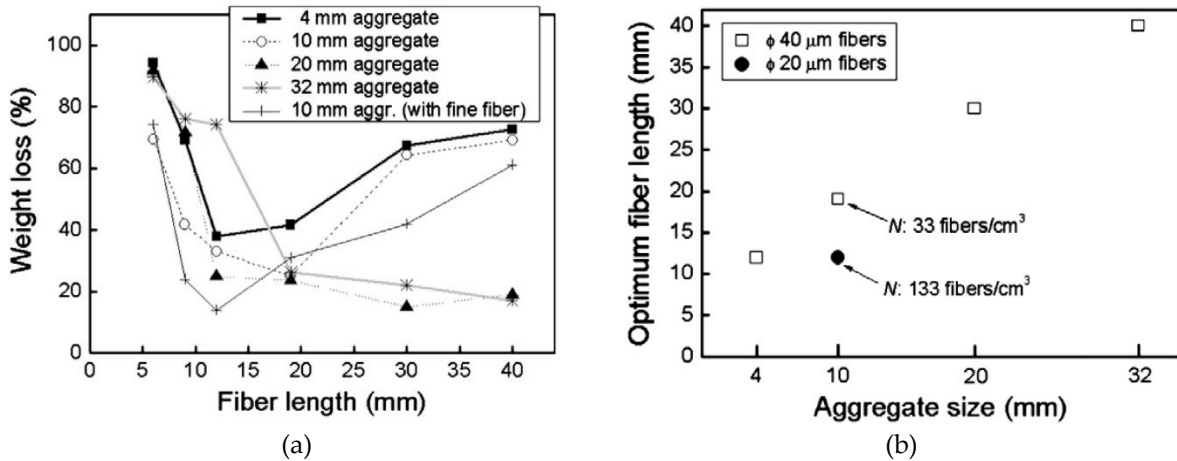


**Figure 3.39** Determination of optimum fiber length a) weight loss vs fiber length for different aggregate size, b) optimum fiber length vs aggregate size [71].

### 3.2.9 Mesoscale thermo-mechanical modelisation of concrete

Concrete is a heterogeneous multiscale material composed of various phases and constituents. Mesoscale modelling is a good compromise in terms of explicit modelling of its heterogeneity while still saving computational time. Modelling on mesoscopic scale captures well different components of concrete and their evolution with temperature opposed to homogenized continuum models. These computations are accomplished on a smaller scale, in general, on representative elementary volume.

For such calculations to be successful, a proper representation of granular skeleton is required. Figure 3.40 presents different representations of granular skeleton showing original, reference and idealized mesostructures. Reference mesostructure is obtained by exact meshing of aggregates using the images, SEM or tomography. Idealized presentation is accomplished by random filling of the volume with circles in 2D (or spheres in 3D) that represent aggregates using particle size distribution curve and volume occupied by aggregates.

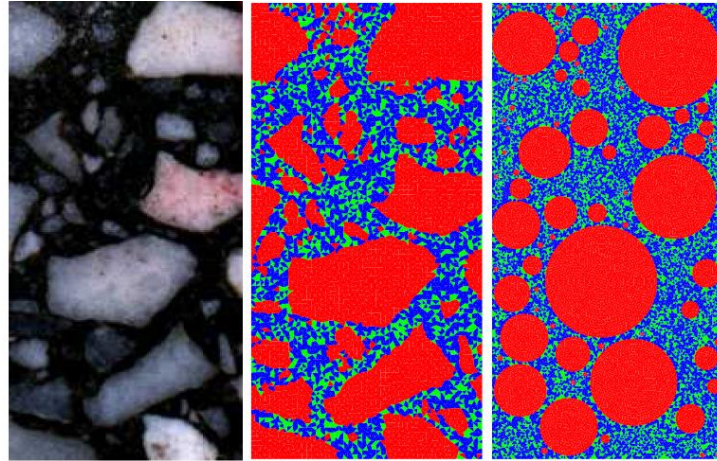


**Figure 3.40** Original, reference and idealized representation of granular skeleton [106].

Majority of existing models consider thermo-mechanical (TM) behavior of concrete only. An example of damage field for concrete meshed with exact and idealized aggregates at 600 °C obtained using TM model is presented in Figure 3.41. Presented results show a feasibility of this approach and validate the use of idealized meshing of structure for these models.

A few studies present a coupled thermo-hydro-mechanical (THM) models on mesoscale [98], [107], [108]. A major issue for these simulations lies in the need to reduced intrinsic permeability of concrete in order to reproduce experimentally measured pore pressures. Permeability, as a parameter difficult to assess, requires a more adapted experimental method in order to be properly determined.

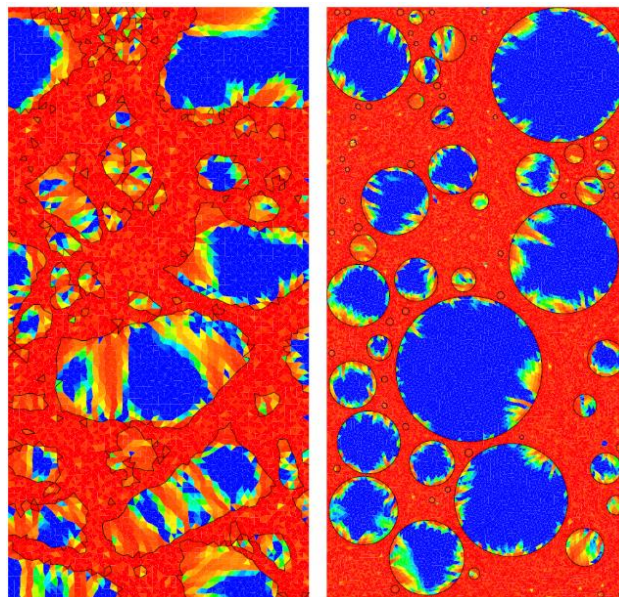


**Figure 3.41** Damage of concrete heated to 600 °C obtained using thermo-mechanical simulations of concrete at high temperature (red – damaged and blue- virgin material) [106].

### 3.3 Presentation of the experimental study

Having presented a literature review on high temperature behavior of fiber reinforced composites, we present an experimental study composed of residual permeability and fire tests conducted on three different cementitious materials. The aim of this study is to optimize the choice of polypropylene fiber size and dosage according to granular skeleton of cementitious material. As a conclusion of presented study, we present guidelines for optimal fiber choice for prevention of concrete spalling due to fire.

#### 3.3.1 Materials, mixes and sample preparation

##### Materials

###### *Cement*

For this study, we have used CEM III/A 52.5 L CE PM-ES – CP 1 NF from Heming provided by Eqiom. Its density and Blaine surface are 2990 kg/m<sup>3</sup> and 5350 cm<sup>2</sup>/g respectively. This cement is composed of clinker (35%), ground granulated blast furnaces slag (61%) and secondary constituents (4%). The chemical composition of the cement used is provided in the Table 3.2. Potential clinker composition is C<sub>3</sub>A (7 %), C<sub>3</sub>S (63 %) and C<sub>4</sub>AF (10 %).

**Table 3.2** Chemical composition in % of cement.

Ignition loss	SiO <sub>2</sub>	Al <sub>2</sub> O <sub>3</sub>	Fe <sub>2</sub> O <sub>3</sub>	CaO	MgO	SO <sub>3</sub>	K <sub>2</sub> O	Na <sub>2</sub> O	S <sup>-</sup>	Cl <sup>-</sup>	CO <sub>2</sub>	CaO free	Na <sub>2</sub> O eq active
1.5	30.1	8.8	1.5	48.7	6.2	2.6	0.85	0.38	0.56	0.27	1.1	1	0.75

###### *Filler*

Siliceous filler from Sibelco is used as a filler, it is composed 99.1 % of SiO<sub>2</sub>. It contains small quantities of Fe<sub>2</sub>O<sub>3</sub> (339 ppm), Al<sub>2</sub>O<sub>3</sub> (4933 ppm), TiO<sub>2</sub> (177 ppm), CaO (239 ppm) and K<sub>2</sub>O (3636 ppm). The density and Blaine surface of filler are 2650 kg/m<sup>3</sup> and 2879 cm<sup>2</sup>/g. The average diameter d<sub>50</sub> of particles is 35 μm.

###### *Aggregates*

Siliceous sand 0/1 from Messanges and two sizes of calcareous gravel 4/10 and 10/20 from Sare are selected for the study. All the aggregates are commercially available from Durruty.

Particle size distribution of the aggregates is provided in Figure 3.42. The density of sand is  $2650 \text{ kg/m}^3$  while the density of the gravel 4/10 and 10/20 is  $2680$  and  $2700 \text{ kg/m}^3$  respectively. Water absorption coefficients for sand 0/1, gravels 4/10 and 10/20 are 0.3, 0.2 and 0.3 % accordingly.

In order to obtain cementitious materials with different cracking patterns, discontinuous aggregate skeletons are selected (see Figure 3.43). Mortar is prepared using 100 % of sand 0/1, while concrete 1 (C1) and concrete 2 (C2) are prepared using 40 % of sand 0/1 + 60% of the gravel 6.3/10 and 40 % of sand 0/1 + 60% of the gravel 14/20 respectively. The coarse aggregates for C1 and C2 with sizes 6.3/10 and 14/20 are achieved by sieving and screening of coarse aggregates 4/10 and 10/20. It should be noted that prior to casting, all of aggregates are dried in oven at  $80 \text{ }^\circ\text{C}$  for 24 hours and cooled down to ambient temperature.

### *Polypropylene fibers*

Polypropylene fibers are commercially available from Baumhüter under commercial name Eurofibers. The information on polypropylene fibers studied is provided in Table 3.3.

**Table 3.3** Polypropylene fibers studied: Name, length (L), diameter (D), aspect ratio (R), and dosage in mass ( $\phi^{\text{mass}}$ ), dosage in volume ( $\phi^{\text{vol}}$ ), total number ( $N_{\text{tot}}$ ) and total length ( $L_{\text{tot}}$ ).

Name	L (mm)	D ( $\mu\text{m}$ )	R (-)	$\phi^{\text{mass}}$ ( $\text{kg/m}^3$ )	$\phi^{\text{vol}}$ (%)	$N_{\text{tot}}$ ( $\times 10^6/\text{m}^3$ )	$L_{\text{tot}}$ ( $\text{km/m}^3$ )
6/32	6	31.7	189	0.25	0.028	58	348
				0.50	0.055	116	696
				1	0.110	232	1392
				2	0.220	464	2785
12/32	12	31.7	379	0.25	0.027	29	348
				0.50	0.055	58	696
				1	0.110	116	1392
				2	0.220	232	2785
18/32	18	31.7	568	0.50	0.055	39	696
12/20	12	19.8	606	0.20	0.021	58	696
				0.39	0.043	116	1392

### *Superplasticizer*

In order to obtain fluidity of the material, superplasticizer SIKA Viscocrete Krono 26 is used. Its molecule is acrylic copolymer and its dry extract content is  $40.0 \pm 2.0 \%$ .

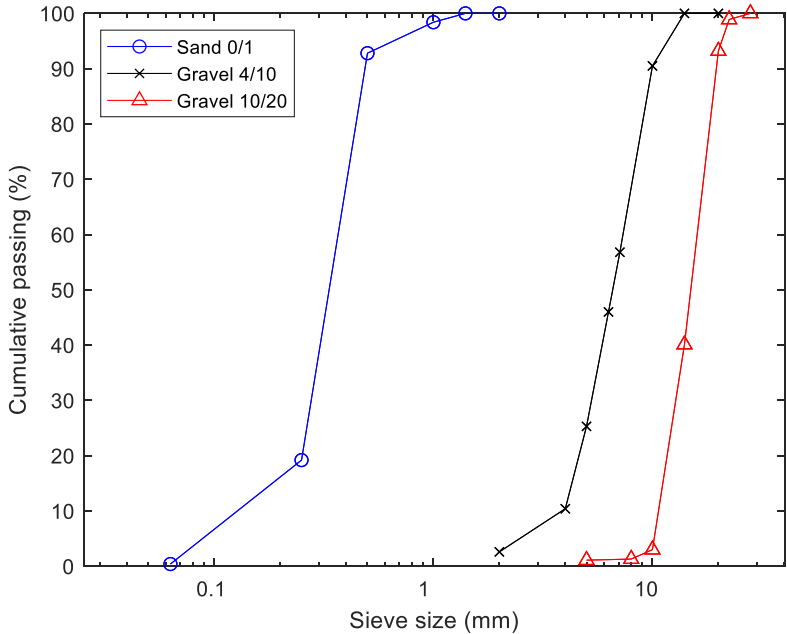


Figure 3.42 Particle size distribution of sand 0/1, gravel 4/10 and gravel 10/20.

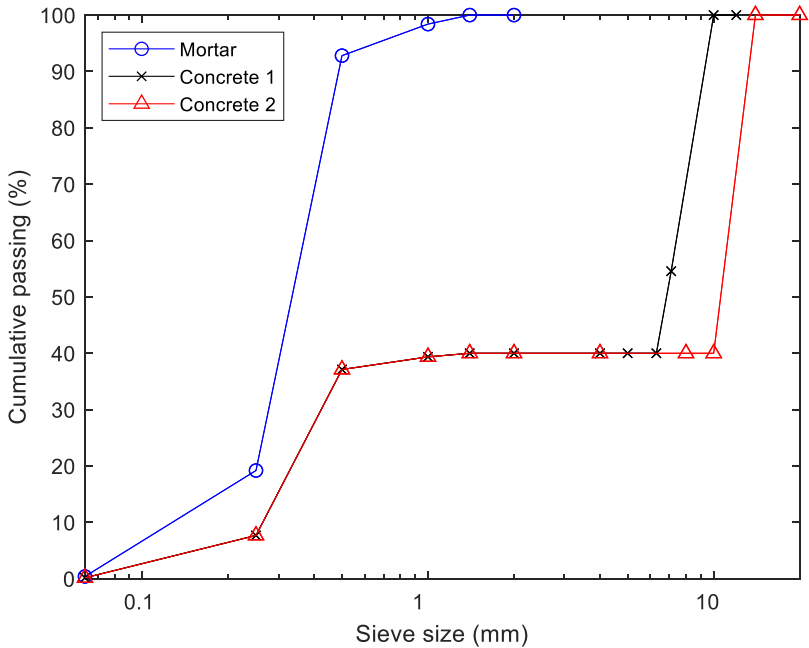


Figure 3.43 Particle size distribution of aggregate mixes used.

## Cementitious mixes

Three different cementitious materials are prepared based on aggregate size: mortar, concrete 1 and concrete 2. Table 3.4 presents all the mixes with their mix proportions resulting in 22 different mixes. The mix names contain information on type of cementitious material, polypropylene fiber geometry and dosage. For example, C1-12/32-1 means concrete 1 (40 % sand 0/1 + 60 % gravel 6.3/ 10) with polypropylene fibers of 12 mm length and 32  $\mu\text{m}$  diameter with a dosage of 1  $\text{kg}/\text{m}^3$ .

**Table 3.4** Mix proportions of cementitious mixes in  $\text{kg}/\text{m}^3$  \*.

N	Mix	Cement	Water	Filler	Sand	Gravel 6.3/10	Gravel 14/20	PP fibers 6/32	PP fibers 12/32	PP fibers 18/32	PP fibers 12/20	SP
1	M-0							-	-	-	-	
2	M-6/32-0.5							0.5	-	-	-	
3	M-6/32-1	500	200	120	1557	-	-	1	-	-	-	10
4	M-12/32-0.5							-	0.5	-	-	
5	M-12/32-1							-	1	-	-	
6	C1-0							-	-	-	-	
7	C1-6/32-0.25							0.25	-	-	-	
8	C1-6/32-0.5							0.5	-	-	-	
9	C1-6/32-1							1	-	-	-	
10	C1-6/32-2							2	-	-	-	
11	C1-12/32-0.25							-	0.25	-	-	
12	C1-12/32-0.5	500	200	120	623	945	-	-	0.5	-	-	3.75
13	C1-12/32-1							-	1	-	-	
14	C1-12/32-2							-	2	-	-	
15	C1-18/32-0.5							-	-	0.5	-	
16	C1-12/20-0.2							-	-	-	0.2	
17	C1-12/20-0.4							-	-	-	0.4	
18	C2-0							-	-	-	-	2.5
19	C2-6/32-0.5							0.5	-	-	-	
20	C2-6/32-1	500	200	120	623	-	952	1	-	-	-	2
21	C2-12/32-0.5							-	0.5	-	-	
22	C2-12/32-1							-	1	-	-	

\*the expressed values are theoretical, the real density of fresh concrete is not taken into account

## Preparation of samples

### *Mixing protocol*

Coarse aggregates, filler, cement and fine aggregates are placed in the mixer and mixed for 1 minute. When machine is stopped, water with superplasticizer is added. The mixing continues for 2 minutes and machine is stopped. Finally, polypropylene fibers are dispersed manually into the fresh mix and mixing for additional 2 minutes is done as presented in Figure 3.44a.

*Curing conditions*

All the samples are cast (see Figure 3.44b) and demolded 24 hours later. Two curing conditions are studied in this experimental program: cure in water for 59 days and cure in tight bag for 7 days and 52 days in air. The summary of the curing conditions and during for each sample is presented in Table 3.5.



**Figure 3.44** Images of a) mixing and b) casting of concrete.

**Table 3.5** Summary on curing conditions.

Test	Mixes	Type and duration of cure
Compressive test	M-0	Water 27 days
	C1-0	
	C2-0	
Water content	All mixes	Water 59 days
	C1-0-A	Tight bag 7 days then Air 52 days
Fire test	C1-12/32-0.5-A	
	C1-12/20-0.2-A	
Porosity accessible to water Permeability test	All mixes	Water 59 days

### Fresh and hardened state properties of mixes

Table 3.6 summarizes fresh state and hardened state properties of mixes. At fresh state, concrete 1 and concrete 2 are more fluid compared to mortar despite its high dosage in superplasticizer. Due to a high volume of fines in sand 0/1, presence of filler increases the packing of particles for mortar to a point that cementitious mix loses its fluidity. Slump varies between 33 and 38 mm for mortar mixes. Slump flow ranges between 584 and 843 mm for concrete 1 and for concrete 2 this range constitutes 578 and 690 mm.

In terms of hardened state properties, it should be noted that the compressive strength of mixes is measured at 28 days for the reference mixes without polypropylene fibers only. We observe that three materials have different values of average compressive strength at 28 days: 43, 90.1 and 79.7 MPa respectively for mortar, concrete 1 and concrete 2. This implies that direct comparison between materials should be proceeded with caution.

**Table 3.6** Fresh and hardened state properties of mixes

N	Mix	Fresh properties		Hardened properties		
		Slump (mm)	Slump flow (mm)	$f_{c28, cyl}$ (MPa)	w* (%)	$p_w$ (%)
1	M-0	36		$41.3 \pm 2.5$	6.2	13.9
2	M-6/32-0.5	33			6.9	15.2
3	M-6/32-1	34	-		5.9	13.6
4	M-12/32-0.5	36			6.6	14.8
5	M-12/32-1	38			7.0	15.4
6	C1-0		809	$90.1 \pm 5.3$	4.8	12.4
7	C1-6/32-0.25		795		6.0	14.1
8	C1-6/32-0.5		790		5.3	13.4
9	C1-6/32-1		776		5.4	13.6
10	C1-6/32-2		599		5.1	13.9
11	C1-12/32-0.25		790		5.7	13.7
12	C1-12/32-0.5	-	830		5.8	13.0
13	C1-12/32-1		792		5.4	13.8
14	C1-12/32-2		584		6.2	14.6
15	C1-18/32-0.5		648		5.9	14.1
16	C1-12/20-0.2		843		5.5	13.9
17	C1-12/20-0.4		764		5.6	14.1
18	C2-0		690	$79.7 \pm 0.3$	5.0	12.7
19	C2-6/32-0.5		578		6.1	14.8
20	C2-6/32-1	-	630		5.1	12.7
21	C2-12/32-0.5		609		5.8	14.3
22	C2-12/32-1		624		5.4	13.5

\* presented water content is for samples stored in water only

Water content is determined for both water-cured (Table 3.6) and air-cured conditions (Table 3.7). Geometry of samples for water-cured condition is a cylinder with 5 cm diameter and 14 cm height. These cylinders are obtained from coring cubes for permeability test presented in Figure 3.48c, thus, are representative of real material. For air-cured samples, geometry of samples is a cylinder with 11 cm diameter and 10 cm height at various depths presented in Figure 3.45. These slices are accomplished using a mechanical saw without use of water in order to avoid re-saturation of slices. The drying effects of this cutting technique due to heating of the saw blade are considered negligible.



**Figure 3.45** Schematic presentation of concrete slices cut for determination of water content at various depths for air-cured samples and water content values determined.

**Table 3.7** Water content in % for A-condition of slices of different depth.

	d=0-1 cm	d=1-3 cm	d=3-5 cm	d=5-10 cm
C1-0-A	3.3	4.3	4.5	4.8
C1-12/32-0.5-A	3.1	4.6	4.9	5.4
C1-12/20-0.2-A	3.9	4.8	5.1	5.3

The samples are dried in oven at 80 °C with consecutive mass loss measurements until stabilization of mass. The stabilization is reached when the measurements of the mass loss of dried sample within 24 hours is less than or equal to 0.02% of the mass of the dry sample. Mass loss and water content are calculated using Equations 3.13 and 3.14.

$$\text{Water content (\%)} = \frac{(m_i - m_f)}{m_f} \times 100 \% \quad (3.13)$$

$$\text{Mass loss (\%)} = \frac{(m_i - m_f)}{m_i} \times 100 \% \quad (3.14)$$

where  $m_i$  and  $m_f$  are initial and final masses of the samples.

Porosity accessible to water  $p_w$  is determined using the following equation:

$$p_w (\%) = \frac{(m_i - m_{f105})}{(m_i - m_w)} \times 100 \% \quad (3.15)$$

where  $m_{f105}$  and  $m_w$  are final mass of sample dried at 105 °C and mass of the sample immersed into water . Obtained porosity values vary between 12.4 and 15.4 %.

### Summary of experimental program

The experimental program for the optimization of the choice of polypropylene fibers includes the following tests on the following geometry and number of samples (see Table 3.8):

- 28 day compressive strength: cylinders of D 11 cm x H 22 cm
- water content: cylinders of D 5 cm H 14 cm for water cure and cylinders of D 11 cm H 10 cm for air cure
- fire test: prisms 20 cm x 20 cm x 10 cm
- permeability test: hollow cylinders  $D_{int}$  5.5 cm,  $D_{ext}$  11 cm and H 14 cm.

**Table 3.8** Summary of experimental campaign

N	Mix	28 d compression	Water content	Fire test	Porosity to water	Permeability test
1	M-0	3	1	2	1	2
2	M-6/32-0.5		1	3	1	2
3	M-6/32-1		1	3	1	2
4	M-12/32-0.5	-	1	3	1	2
5	M-12/32-1		1	3	1	2
6	C1-0	3	1	3	1	2
7	C1-0-A		1	3	-	-
8	C1-6/32-0.25		1	3	1	-
9	C1-6/32-0.5		1	2	1	2
10	C1-6/32-1		1	2	1	2
11	C1-6/32-2		1	3	1	1
12	C1-12/32-0.25		1	3	1	-
13	C1-12/32-0.5		1	3	1	2
14	C1-12/32-0.5-A	-	1	3	-	-
15	C1-12/32-1		1	3	1	2
16	C1-12/32-2		1	3	1	-
17	C1-18/32-0.5		1	3	1	1
18	C1-12/20-0.2		1	3	1	2
19	C1-12/20-0.2-A		1	3	-	-
20	C1-12/20-0.4		1	3	1	2
21	C2-0	3	1	3	1	2
22	C2-6/32-0.5		1	3	1	1
23	C2-6/32-1		1	3	1	1
24	C2-12/32-0.5	-	1	3	1	1
25	C2-12/32-1		1	3	1	2

### 3.3.2 Apparatus and test procedures

#### Thermal analysis of polypropylene

Thermal analysis of polypropylene is accomplished in IPREM Laboratory of Université de Pau et Pays de l'Adour includes: TGA, DSC and high temperature rheometer tests. Thermogravimetric test (TGA) is accomplished using thermogravimetric analyzer, which measures the mass with a temporal change of temperature. TGA allows determination of degradation temperature, criterion for degradation temperature is fixed to 0.1 % weight loss. Heating rate is fixed to 20 °C/min with a maximum heating temperature of 550 °C.

Differential scanning calorimetry test (DSC) is performed using differential scanning calorimeter that measures absorbed or released energy with a change in temperature. Heating rate for DSC test is fixed to 20 °C/min. Sample undergoes following thermal treatment:

- heating to 200 °C in order to return to amorphous state
- cooling to -90 °C in order to determine glass transition temperature
- heating to 200 °C in order to determine melting temperature.

High temperature rheometer tests are used in order to assess evolution of polypropylene viscosity with shear rate at temperature of 180 °C. Plane-plane geometry with disk diameter of 25 mm is used for this purpose as seen in Figure 3.46a. Following relations allow determining viscosity  $\dot{\gamma}$  and shear stress  $\tau$  such as:

$$\dot{\gamma} = \frac{3 \Omega R}{4 H} \quad (3.16)$$

$$\tau = \frac{3 C}{2 \pi R^3} \quad (3.17)$$

where  $\Omega$  is rotational speed, H is a distance between two planes, R is a radius of disk.

The shear rate is increased from 0.1 s<sup>-1</sup> to 100 s<sup>-1</sup>. The temperature is fixed to 180 °C and test starts when polypropylene is melted. In order to conduct the test, 25 mm diameter polypropylene disks (see Figure 3.46b) are prepared from polypropylene fibers using heating press. The image after test is presented in Figure 3.46c.

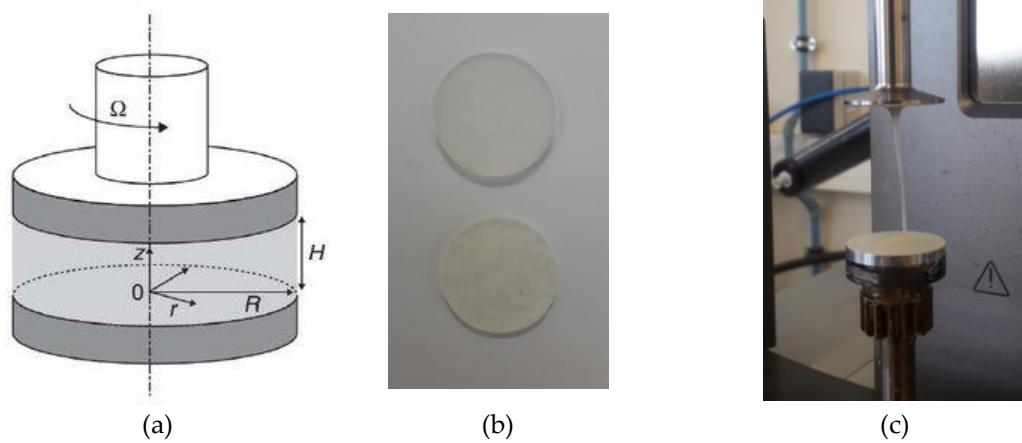


**Figure 3.46** Rheometer test: a) Plane-plane geometry for rheometer, b) 25 mm polypropylene disks, c) image after test.

### Residual radial permeability test

#### *Experimental setup*

Residual radial permeability test to nitrogen is performed on the hollow cylindrical samples using test method described in [20]. The experimental setup for this test presented in Figure 3.47 consists of:

- nitrogen gas bottle with regulator
- pressure sensor
- digital pressure gauge
- purge
- two mass flow meters of capacity 300 ml/min and 30 l/min connected in parallel.

Nitrogen, an inert dry gas that does not perturb the constituents of the concrete and does not saturate pores, is selected as test gas. The permeability test involves an injection of relative pressure  $\Delta P$  (a difference between absolute injection  $P_i$  and atmospheric pressure  $P_{atm}$ ) until reaching a stabilized flow across the thickness of the tested sample. Regulator attached to the bottle allows controlling injection pressure, which is displayed by digital pressure gauge. The flow of gas is measured by mass flow meters that are converted into volume flow rate. Depending on the flow rate, an appropriate flow meter is selected: either 300 ml/min or 30 l/min. The measurement of the volume flow rate accomplished using software, which allows graphical visualization of stabilization of the gas flow.

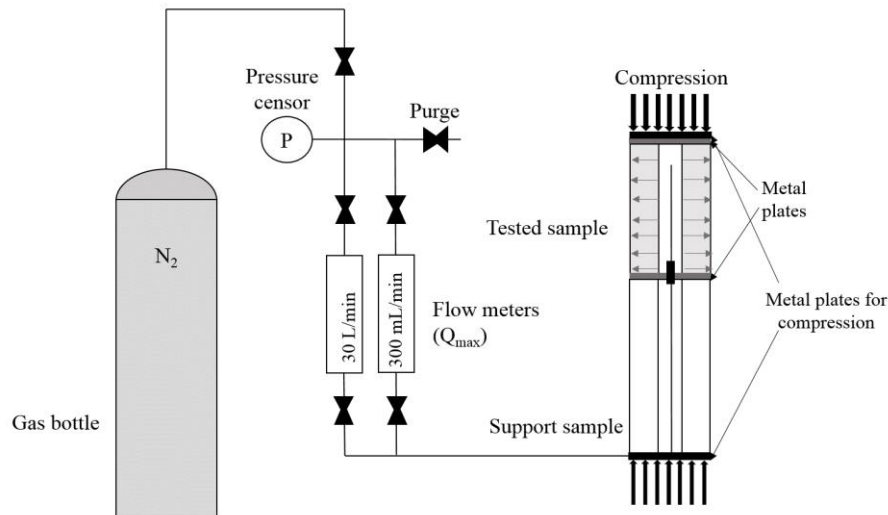


**Figure 3.47** Scheme of experimental setup for radial permeability test.

### *Sample preparation*

Gas permeability tests are performed on the hollow cylindrical samples. The test samples are obtained by coring cubic samples of  $15 \times 15 \times 15 \text{ cm}^3$  using a diamond double drilling unit (see Figure 3.48a and 3.48b). Use of double driller allows minimizing the effects of eccentricity and accelerates sample preparation time. The image of drilled sample is presented in Figure 3.48c. To ensure flatness and parallelism, top and bottom faces are grinded (see Figure 3.48d). The final sample geometry has the following dimensions: outer and inner radius  $R_1$  and  $R_2$  of 5.50 and 2.85 cm accordingly with a height of 14 cm. In order to obtain dry samples with a minimal perturbation of microstructure, all of the samples are dried at  $80 \text{ }^\circ\text{C}$  until mass stabilization.



**Figure 3.48** Stages of sample preparation : a) concrete cube, b) double coring of sample, c) after coring, d) grinding of the sample.

Steel inox plates are glued on tested sample to seal the sample and to prevent a gas leakage during permeability test as shown in Figure 3.49. Before gluing, the dimensions of the tested sample such as internal and external radii and heights are measured using digital caliper. The surfaces of the plates are cleaned with acetone. When plates are glued, samples are compacted by placing a weight of 1 kg on the top for 1 hour and cured at 80 °C to harden the glue.

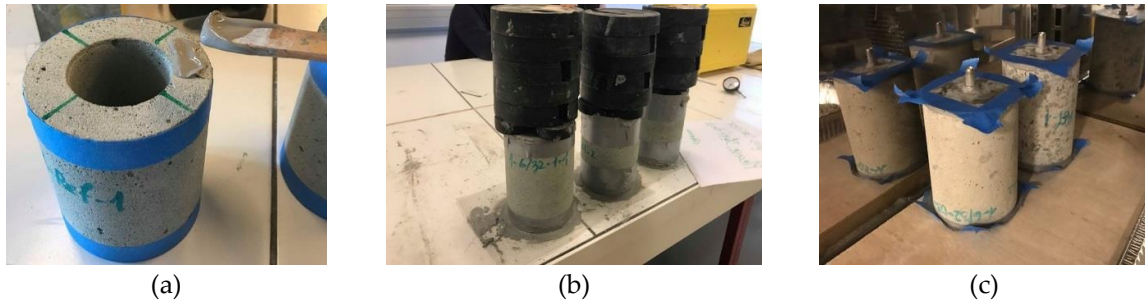


**Figure 3.49** Preparation of sample for test: a) gluing of plate on sample, b) compression of samples, c) heating of samples at 80 °C.

#### *Heating protocol*

Residual permeability measurements are performed, i.e. after heating, to 80 °C (reference temperature), 150 °C and 200 °C at room temperature. Schematic presentation of the heating protocol is provided in the Figure 3.50. Heating and cooling rate of furnace is fixed to 1 °C/min in order to avoid creation of high thermo-mechanical stresses. When desired temperature is reached, the stabilization during 3 hours is done ensuring uniformity of the temperature across the sample. This stabilization duration is considered sufficient as samples are dried prior to heating. For two mixes C2-0 and C2-12/32-1 permeability measurements were completed to additional temperatures: 130 °C (before melting), 165 °C (around melting temperature) and 180 °C (after melting).

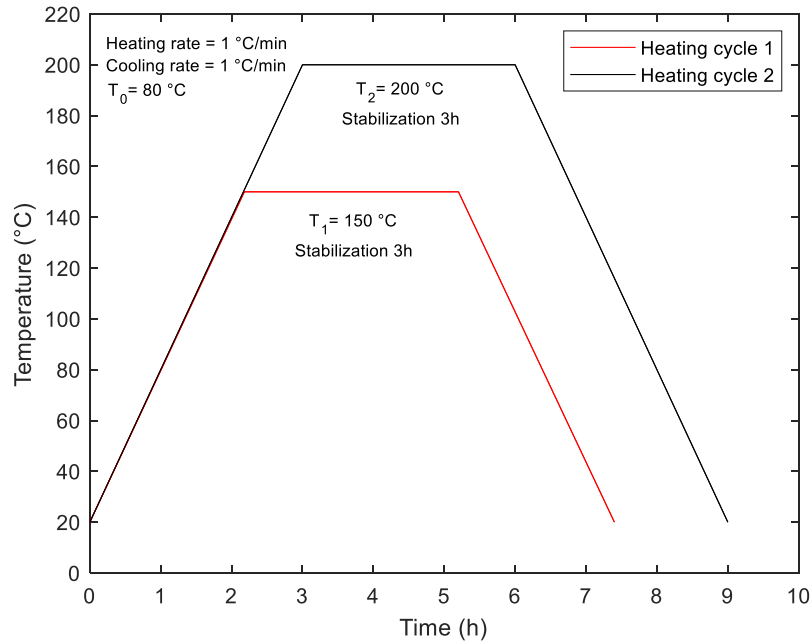


**Figure 3.50** Experimental program of the heating: tested temperatures are 80 °C (reference), 150 °C and 200 °C.

### *Testing protocol*

The bottom plate has a borehole to which a connector for the gas flow with a tube are fixed. The test sample is placed on the top of the hollow cylinder concrete sample with height of 22 cm and external and internal diameters of 11 and 5.6 cm respectively that serve for passing gas tube. The test sample and support sample are compressed uniaxially with a loading required to counteract the injection pressure. The loading necessary for each injection pressure is presented in Table 3.9. Synthetic rubber joints used to ensure the tightness of the setup are not considered in this test in order to avoid excessive loads that may alter microcracking in tested samples thus modify permeability. In [25], a compressive loading of 0.6 MPa was enough to alter intrinsic permeability. The steady-state flow of the gas is achieved within 20-30 minutes depending following gas injection due to a quick percolation of gas in dry material.

**Table 3.9** Injection pressure  $P_i$  and required compressive loading.

Injection pressure (Pa)	Loading applied (kN)
1	0.26
1.5	0.39
2	0.52
2.5	0.65
3	0.78

The error for this test that affects the measurement of permeability is calculated from the work of [109]. There are two types of errors that contribute to total error such as error due to measurement devices and error due to decentered sample.

- *Error due to measurement devices* ( $\varepsilon_m$ ): related to use of experimental equipment

$$\varepsilon_m = \frac{\Delta Q}{Q} + \frac{\Delta \mu}{\mu} + \frac{\Delta H}{H} + \Delta P_2 \left| \frac{1}{P_2} + \frac{2P_2}{P_1^2 - P_2^2} \right| + \Delta P_1 \left| \frac{2P_2}{P_1^2 - P_2^2} \right| + \frac{\frac{\Delta R_2}{R_2} + \frac{\Delta R_1}{R_1}}{\ln\left(\frac{R_2}{R_1}\right)} \quad (3.18)$$

where  $\Delta Q$ ,  $\Delta \mu$ ,  $\Delta H$ ,  $\Delta P_1$ ,  $\Delta P_2$ ,  $\Delta R_1$  and  $\Delta R_2$  are uncertainties related to measurements of flow, dynamic viscosity of nitrogen, height, absolute and atmospheric pressure, internal and external radii. The errors calculated according to injection pressure P1 are presented in Table 3.10.

**Table 3.10** Error due to measurement devices  $\varepsilon_m$  as a function of injection pressure

P1 (bars)	1	1.5	2	2.5	3
$\varepsilon_m$ (%)	4.08	3.41	3.08	2.90	2.70

- *Error due to decentered sample* ( $\varepsilon_c$ ): related to eccentricity of the center of inner and outer circle of the sample due to coring technique.

The decentered sample influences the permeability measurement since the flow in the thinner part is higher than in the thicker one. Figure 3.51 presents the examples of the centered and decentered samples with  $C_1$  and  $C_2$  being the centers of the inner and outer circles of the sample respectively and  $R_1$  and  $R_2$  – inner and outer radii of the sample.

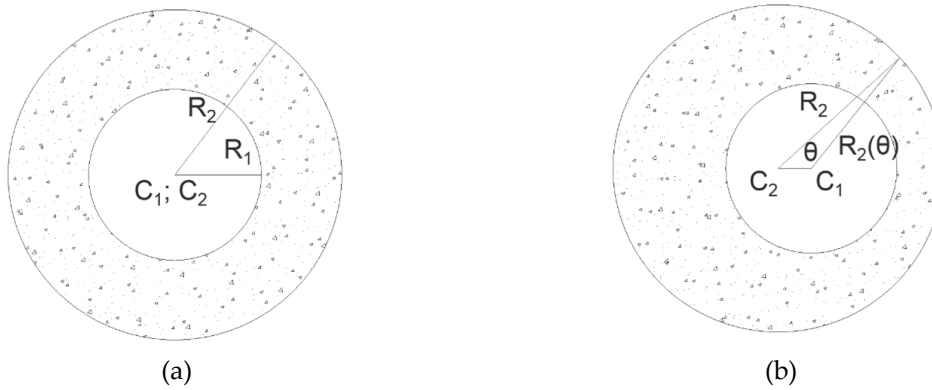


**Figure 3.51** Influence of eccentricity: (a) centered sample, (b) decentered sample.

The error due to decentered sample is found as:

$$\varepsilon_c = \frac{k_a^* - k_a}{k_a^*} \quad (3.19)$$

where  $k_a^*$  and  $k_a$  are corrected and measured permeability values. The maximum error of decentered sample  $\varepsilon_c$  is estimated as 0.002 %.

## Fire test

### *Experimental setup*

Fire tests are conducted using a furnace with a gas burner presented in Figure 3.52. The oven skeleton is made of metal and is covered with ceramic wool resistant to temperatures up to 1200 °C. The shape of the furnace allows an even distribution of the heat over the surface of the concrete sample. The opening of the furnace is 20 x 20 cm<sup>2</sup>. There is a gas vent located on the top of the furnace. Three shielded thermocouples placed at 4, 10 and 16 cm from the bottom of the furnace opening and 1 cm from the heated face of the concrete sample provide a constant measurement of temperature. The validation of this furnace heating conducted on cubes of 20 x 20 x 20 cm<sup>3</sup> can be found in [45]. An example of thermocouple readings plotted with a standard fire curve is presented in Figure 3.53. K-type thermocouples used (mix of nickel-chrome and mix of nickel-aluminum) can measure continuous temperature around 1100 °C maximum. Typical accuracy of the thermocouples is +/- 2.2 °C.

The gas used in the burner is butane. In order to maintain a pressure of gas and follow standard ISO 834-1 curve, the gas bottle is placed into thermostatic bath. It is composed of the container filled with water with heating resistance that maintains the desired temperature, thermocouple that measures a temperature of water and water pump that ensures circulation of water for homogenous heating. The heating resistance is set to heat and maintain the temperature of the water to 28 °C, which allows achieving required values of gas pressure.

Hydraulic press from ENERPAC used to apply uniaxial mechanical loading is presented in Figure 3.54. The precision of the force sensor is 0.01 kN and its maximum force is 1MN.

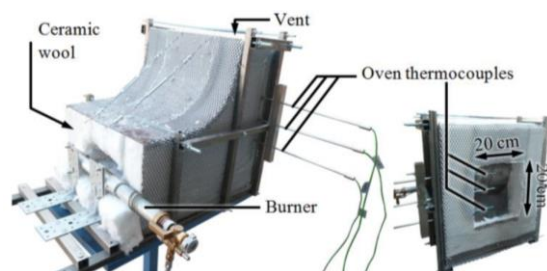


**Figure 3.52** Gas furnace with installed thermocouples.

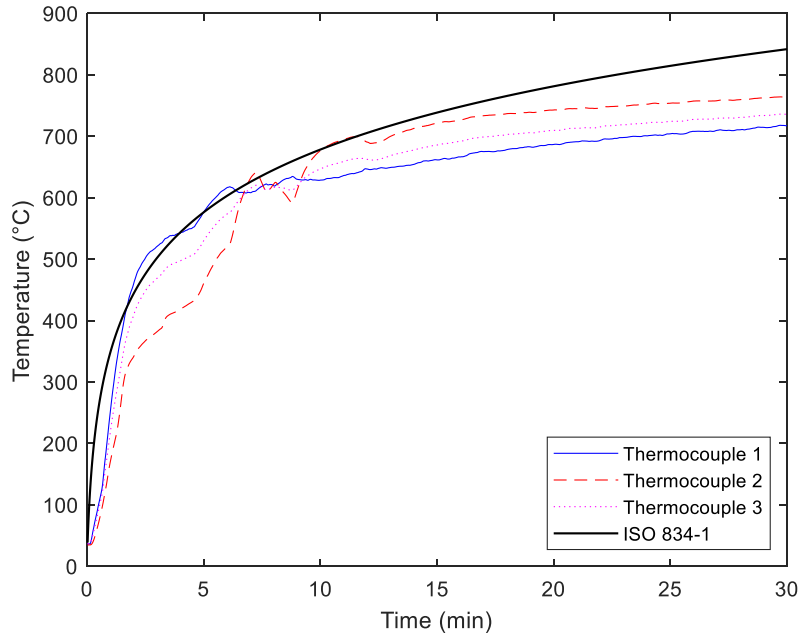


**Figure 3.53** An example of thermocouples readings vs. standard fire curve ISO 834-1.



**Figure 3.54** Hydraulic press ENERPAC used in the fire test as presented in [45].

### *Fire test protocol*

Fire test procedure is composed of various stages presented by images in Figure 3.55. First, in order to avoid moisture escape from the lateral sides of the sample, a resistant aluminum foil is glued using a refractory glue from Athermafix as seen in Figure 3.55a. The aluminum foil and glue resist to temperatures of 600 °C and 800 °C respectively. The tested sample is

placed between two fiber reinforced concrete samples in order to ensure distribution of the mechanical load. The face of the sample, which was located at the bottom of the mold while concrete casting, i.e. smooth one, is heated. All the fire tests are performed on samples loaded in uniaxial compressive loading for 30 minutes with a loading of 5 MPa maintained during the fire test as seen in Figure 3.55b. It is necessary to note that samples are insulated from both sides using 12 cm of rock wool for reinforcement of thermal insulation. The furnace is placed right in front of the heated surface of the sample making sure to avoid any opening between sample and furnace. The gas is opened and ignited in the gas burner as seen in Figure 3.55c. The duration of the fire test is 30 minutes and the fire curve is standard ISO 834-1 fire curve. During the test, time of the spalling events, sounds are recorded. At the end of the test, the gas is shut down, burner is closed and sample discharged. The cold side of the sample is examined for cracking and water escape. The results of the heated and cold sides of the tested specimen are presented in Figures 3.55d and 3.55e.

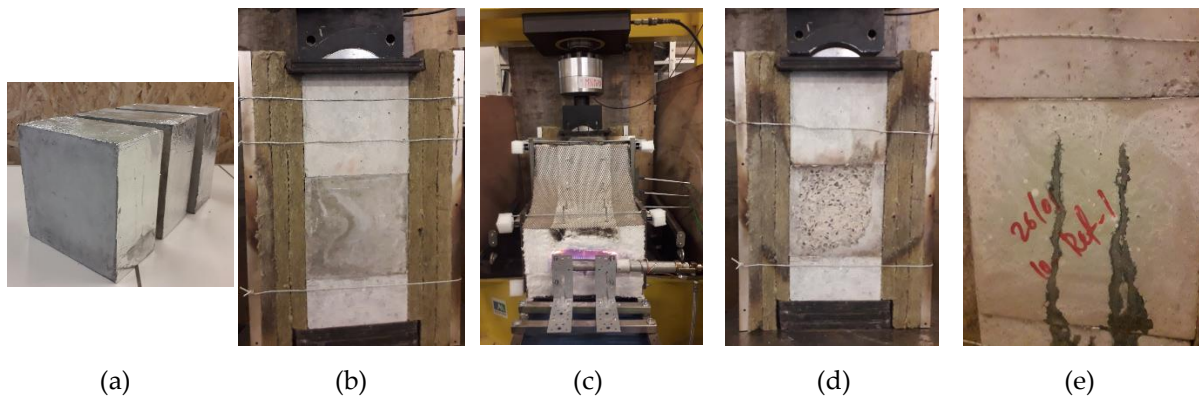


**Figure 3.55** Images of the fire test procedure: (a)  $20 \times 20 \times 10 \text{ cm}^3$  sample with glued aluminum foil, (b) test sample between two concrete supports, insulated by rock wool and uniaxially charged by 5 MPa, (c) sample during test, (d) heated side of the sample after test: spalling of the surface, (e) cold side of the sample after test: moisture escape.

### *Post treatment*

After the fire test, spalling depth and volume are evaluated using photogrammetry technique. The workflow of this technique is presented in Figure 3.56. The first step includes taking pictures of the spalled sample every  $10^\circ$  resulting in 36 pictures (see Figure 3.57a). Then, 3D modelling of the sample is accomplished using Meshroom software as seen in Figure 3.57b. In this step, cleaning, scaling and orientation of the 3D model (Figure 3.57c) is completed using Cloud Compare. The final product of this step, a cloud of points representing the spalled surface

and lateral sides, is then post processed in Cast3M in order to compute maximum and mean spalling depth and spalled volume. In addition to this, a color map of the spalled surface is obtained as seen in Figure 3.58. The maximum error of this technique found as 4.2 % is calculated by using photogrammetry on the objects of the etalon dimensions.

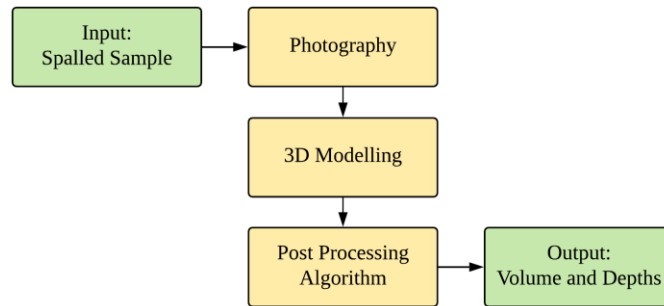


**Figure 3.56** Workflow of the photogrammetry for evaluation of the concrete spalling depth and volume.

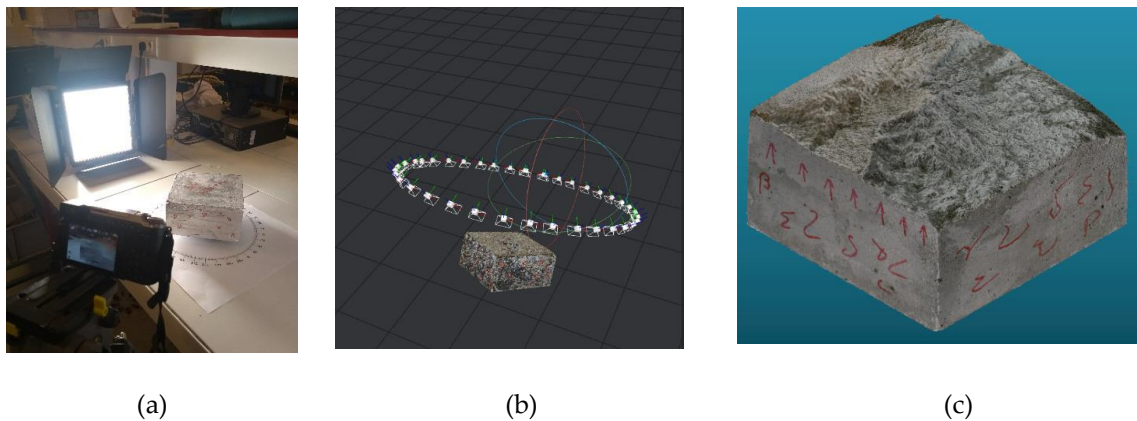


**Figure 3.57** Stages of the technique: a) Photo session, b) 3D reconstruction, c) reconstructed 3D model.

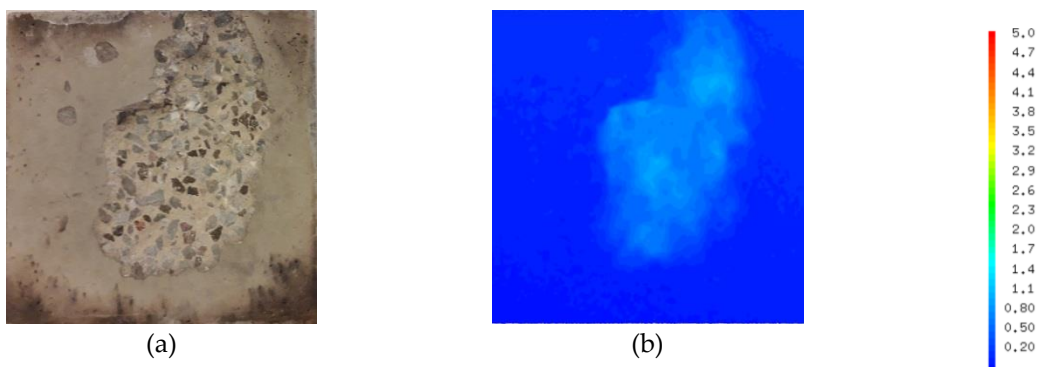


**Figure 3.58** Image of the spalled surface: a) sample, b) obtained color map of spalling depth. Color bar represents spalling depth with a scale in cm.

## 3.4 Results and discussions of the experimental study

### 3.4.1 Thermal analysis of polypropylene

We have completed thermal analysis of two types of polypropylene fibers: Eurofibers and Eurofibers HPR. The latter are fibers, which possess lower viscosity than ordinary fibers at melting due to a lower molar mass obtained by reduction of polymer chain length. Despite the fact that we only use ordinary Eurofiber fibers in our study, it is worth studying and comparing these two fiber types. As for thermal analysis, we have completed thermogravimetric analysis (TGA), differential scanning calorimetry (DSC) and high temperature rheometer test at 180 °C in order to determine degradation and melting temperatures as well as melt viscosity.

We plot in Figure 3.59 the results of TGA test obtained for both fibers. The graph shows that a variation of weight starting from 352 and 342 °C for Eurofiber and Eurofiber HPR which corresponds to the start of degradation of the material. This process, named thermal pyrolysis, is linked to a reduction of molecular weight of polypropylene due to breaking of the weakest carbon-carbon bonds in the carbon backbone. It is interesting to note degradation for Eurofiber HPR starts at lower temperature than for Eurofiber as well as the fact that its speed of degradation is faster. With continuous reduction of the mass, molecules of polypropylene become volatile. Around 500 °C, we observe that almost no material left for both fibers, which means that pyrolysis is complete and most of the polypropylene is vaporized.

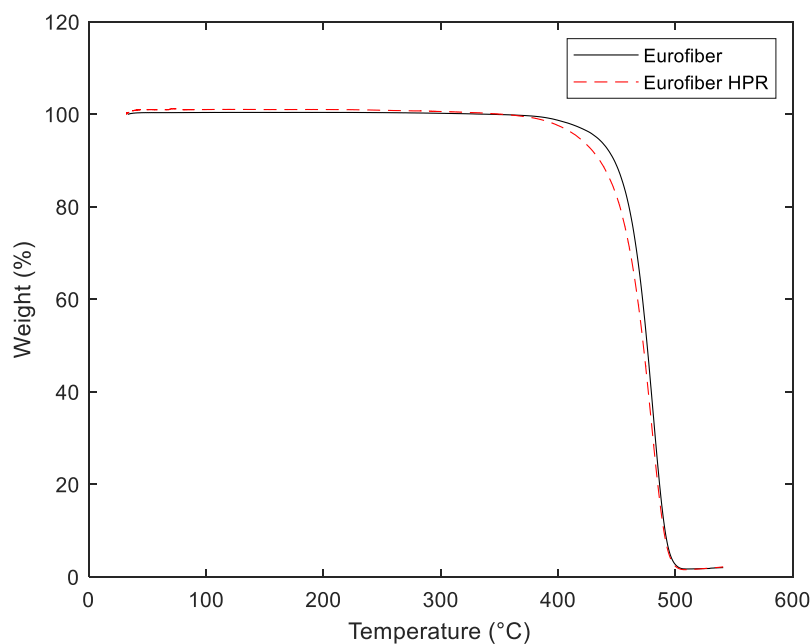


**Figure 3.59** Thermogravimetric analysis of polypropylene used in ordinary fibers (Eurofiber) and low melt viscosity fibers (Eurofiber HPR).

We plot the results of DSC analysis on two polypropylene fibers in Figure 3.60. We observe that melting of polypropylene used in Eurofiber starts as early as 139 °C and continues until 185 °C. The peak of DSC curve, considered as melting temperature of polypropylene, is found to be 165 °C. For Eurofiber HPR, melting starts at 135 °C, peaks at 160 °C and continues until 180 °C. We observe that Eurofiber HPR melts at lower temperatures than ordinary Eurofiber due to decreased size of polymer chains. In addition to this, we note a presence of small melting picks that show existence of different phases of crystallinity that melt at different temperatures.

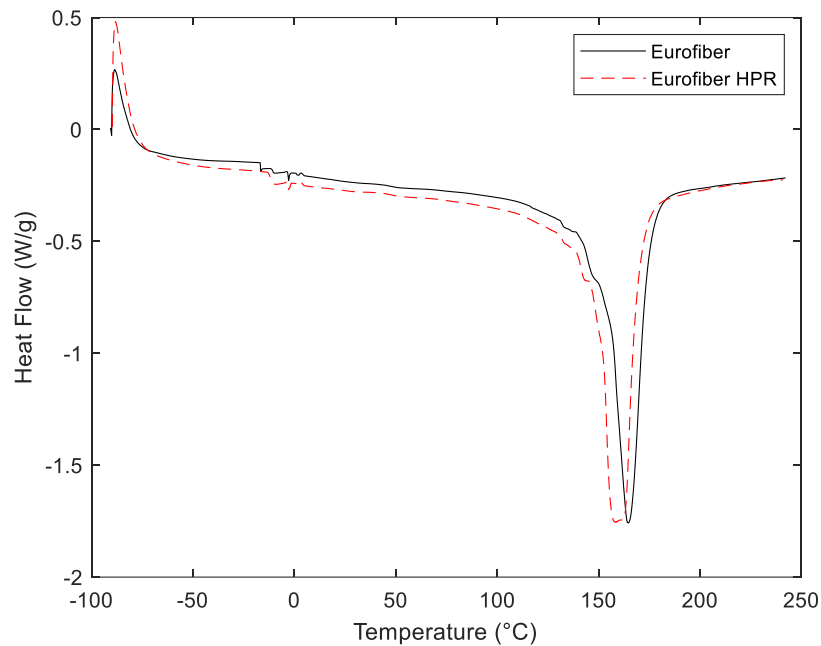


**Figure 3.60** Differential scanning calorimetry of polypropylene used in ordinary fibers (Eurofiber) and low melt viscosity fibers (Eurofiber HPR).

We plot in Figure 3.61 the evolution of viscosity of polypropylene with shear rate measured at constant temperature of 180 °C for both fibers Eurofiber and Eurofiber HPR. We note that viscosity of polypropylene at 0.1 s<sup>-1</sup> is 817 Pa.s for ordinary fibers (Eurofiber) and 17 Pa.s for Eurofiber HPR. This shows that ordinary fibers have viscosity at 180 °C that exceeds low-viscosity fiber by 48 times. Due to their low viscosity at melting, Eurofiber HPR are faster in terms of liberation of fiber channels, which would be more beneficial for increase of permeability and reduction of spalling as found in [104]. In terms of evolution of viscosity with shear rate, we note that viscosity of Eurofiber decreases with an increase of shear rate: an order of magnitude from 1 s<sup>-1</sup> to 10 s<sup>-1</sup> and one more from 10 s<sup>-1</sup> to 100 s<sup>-1</sup> and almost no evolution is

observed for Eurofiber HPR. We shall remind here as well that the viscosity of the material decreases not only with increasing shear rate but with increasing temperature as well.

Let us make a rough estimation of time melted polypropylene would require to flow along its length using Equation 3.12. Taking a range of pore pressures from 0.5 to 4 MPa and using melt viscosity measured at 180 °C of 817 Pa.s and of 17 Pa.s at  $0.1 \text{ s}^{-1}$  for Eurofiber and Eurofiber HPR, we find a time required to empty channel for studied geometries in Table 3.11. First, we notice that time to empty channel is significantly less for HPR fibers than for regular ones due to a lower melt viscosity. Secondly, using these estimations we can note an important influence of fiber geometry on time to empty the channel. It is important to remind that these estimations exclude the possibility of radial flow of polypropylene, which constitutes the shortest path, they do not account for decrease of viscosity of polypropylene with increase of temperature and thermo-mechanically induced cracks.

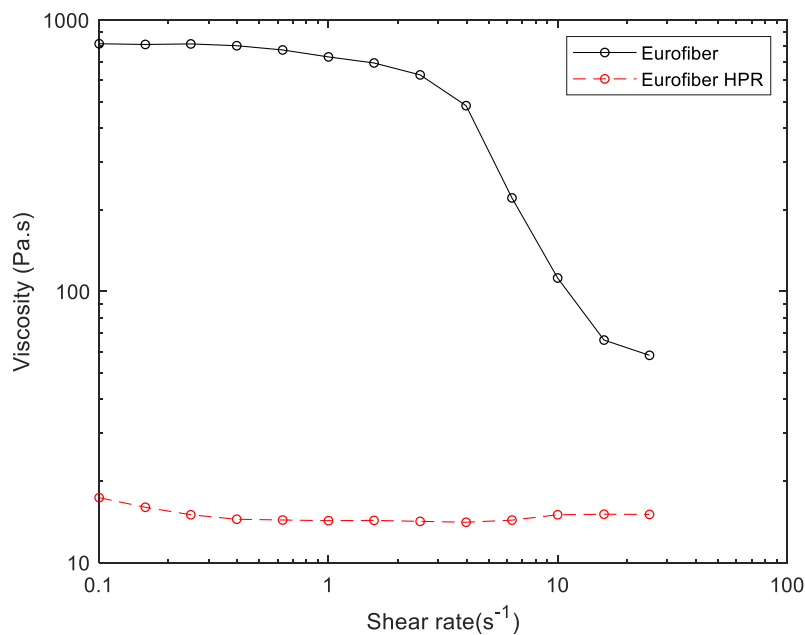


**Figure 3.61** Evolution of viscosity with shear rate measured at 180 °C for polypropylene used in ordinary fibers (Eurofiber) and low melt viscosity fibers (Eurofiber HPR).

Despite the fact that HPR fibers are not studied further, presented analysis shows that these fibers could be potentially more beneficial for spalling due to their slightly lower melting temperature and significantly lower melt viscosity.

**Table 3.11** Rough estimation of time required to empty channel for two types of fibers.*For ordinary fibers (Eurofiber)*

D ( $\mu\text{m}$ )	L (mm)	Time to empty channel (s) for pressures		
		$\Delta P=1$ MPa	$\Delta P=2$ MPa	$\Delta P=4$ MPa
32	6	900	480	240
32	12	3660	1860	900
20	12	9420	4680	2340
32	18	8220	4080	2040

*For low-viscosity fibers (Eurofiber HPR)*

D ( $\mu\text{m}$ )	L (mm)	Time to empty channel (s) for pressures		
		$\Delta P=1$ MPa	$\Delta P=2$ MPa	$\Delta P=4$ MPa
32	6	19	10	5
32	12	76	38	19
20	12	195	97	49
32	18	172	86	43

### 3.4.2 Residual radial permeability test

In this part, residual radial permeability test results for three different cementitious materials after heating-cooling cycles are presented with a discussion on influence of temperature, fiber dosage and geometry and percolation.

#### Drying of samples

Samples used for permeability test are dried at 80 °C prior to testing in order to evacuate free water without inducing major changes into microstructure. The measurements of the mass are accomplished in order to obtain mass loss curves for mortar, concrete 1 and concrete 2 samples presented in Figures 3.62a, 3.62b and 3.62c accordingly. We observe that stabilization of the mass for all the cementitious mixes is reached after 70 days of drying.

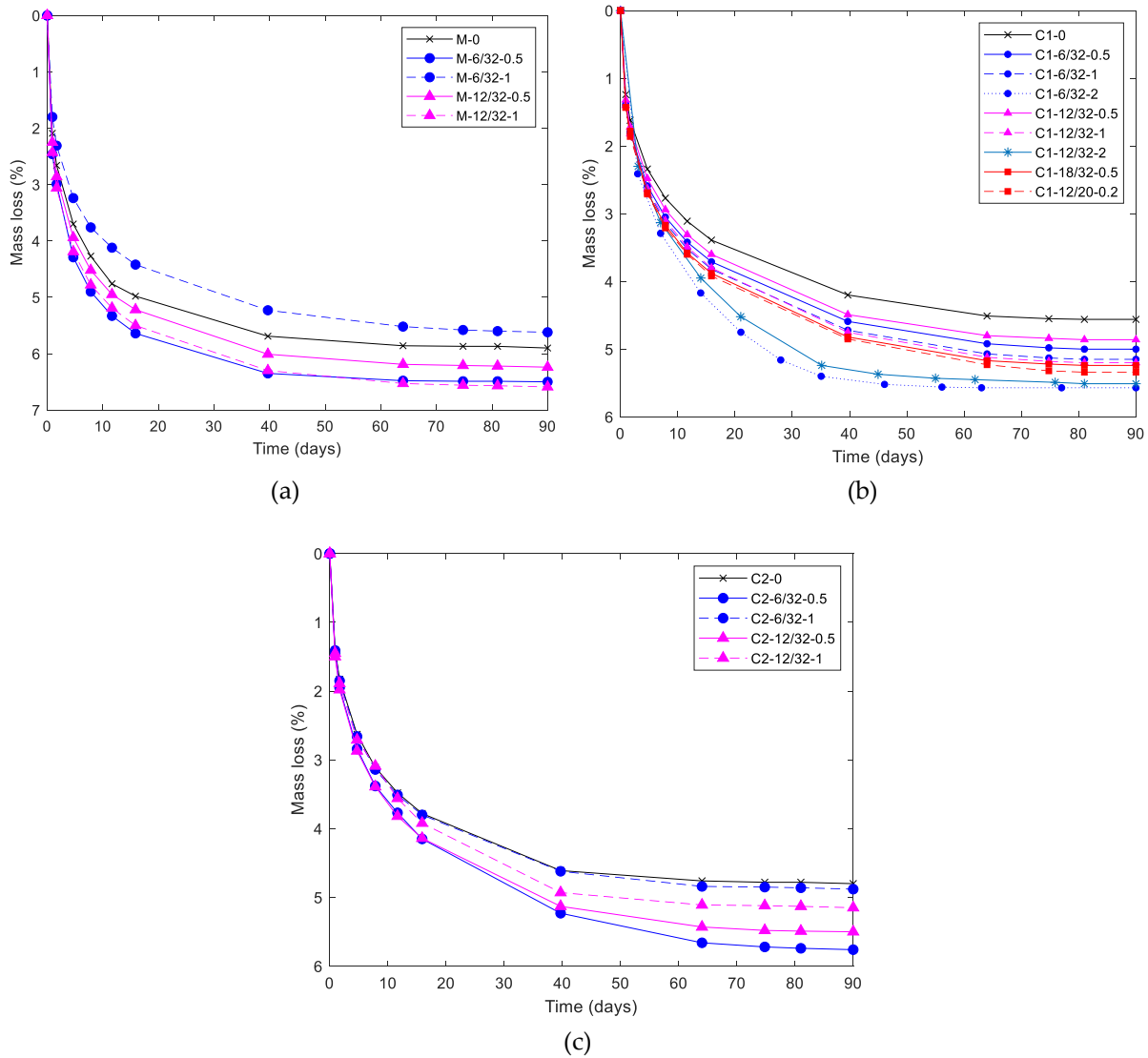


**Figure 3.62** Mass loss plotted as function of time: a) mortar (M), b) concrete 1 (C1), c) concrete 2 (C2) samples.

### Evolution of intrinsic permeability of reference mixes with temperature

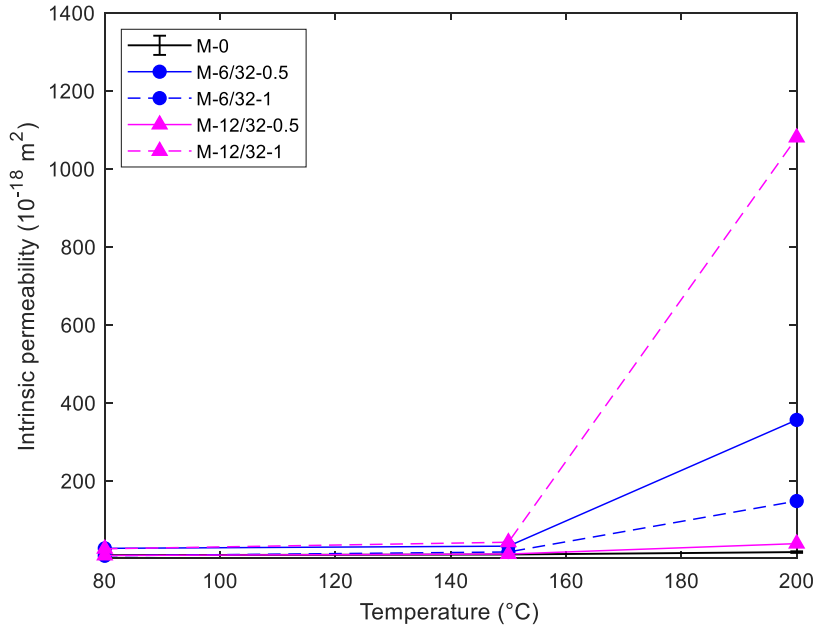
We plot an evolution of the intrinsic permeability with temperature for mortar, concrete 1 and concrete 2 in Figure 3.63a, 3.64a and 3.65a respectively. The values plotted on the graphs are average values with error bars corresponding to maximum and minimum values. Values without error bars represent mixes tested with one sample.

Average intrinsic permeability for reference cementitious materials measured at 80 °C, reference temperature, are equal to  $9.32 \times 10^{-18}$ ,  $1.54 \times 10^{-17}$  and  $3.56 \times 10^{-17} \text{ m}^2$  respectively for mortar, concrete 1 and concrete 2. We note that mortar is the least permeable of three materials and concrete 2 is the most permeable of all. This could be explained by porous

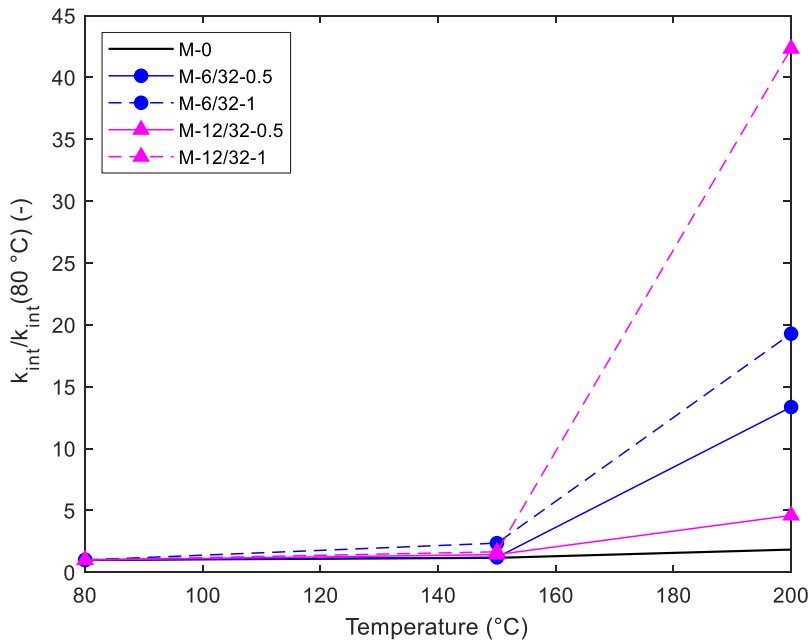
network of mortar: despite its high porosity, size of pores in mortar is smaller than pores of concrete due to shrinkage. As permeability is more dependent on size of pores than on their volume, this explains why mortar is least permeable material. However, no direct link between porosity of concrete 1 and concrete 2 and intrinsic permeability is established as both concretes have relatively same values of porosity.

We can also argue that three materials have different specific surfaces of aggregates related to the size of the aggregates: in mortar, specific surface is higher than in concretes due to presence of fine sand. Higher specific surface of aggregates implies longer paths for fluid passage (if we could refer to an example of water filter made of sand or gravel) hence lower permeability, which is confirmed for the case of mortar. In concrete 2, the largest aggregates having twice the size of aggregates in concrete 1 have shorter length for fluid path, which would enable this material to have twice as high permeability as concrete 1.

We plot in Figures 3.63b, 3.64b and 3.65b the evolution of a ratio of intrinsic permeability and intrinsic permeability measured at 80 °C as a function of temperature for mortar, concrete 1 and concrete 2. We can see that intrinsic permeability for reference cementitious mixes increases with temperature. A slight increase of the intrinsic permeability observed at 150 °C in comparison to values at 80 °C: 1.2 times for M-0, 1.3 times for C1-0 and 1.4 times for C2-0. This increase of intrinsic permeability is related to a creation of microcracks at the interface of the cement paste-aggregate due to their differential thermal expansion. At 200 °C, mixes without polypropylene fibers (M-0, C1-0 and C2-0) experience an increase of intrinsic permeability related to growth of existing cracks and initiation of new cracks due to thermal incompatibility of cement paste and aggregates (1.8, 15.2 and 6.2 times the reference state for M-0, C1-0 and C2-0 respectively) .

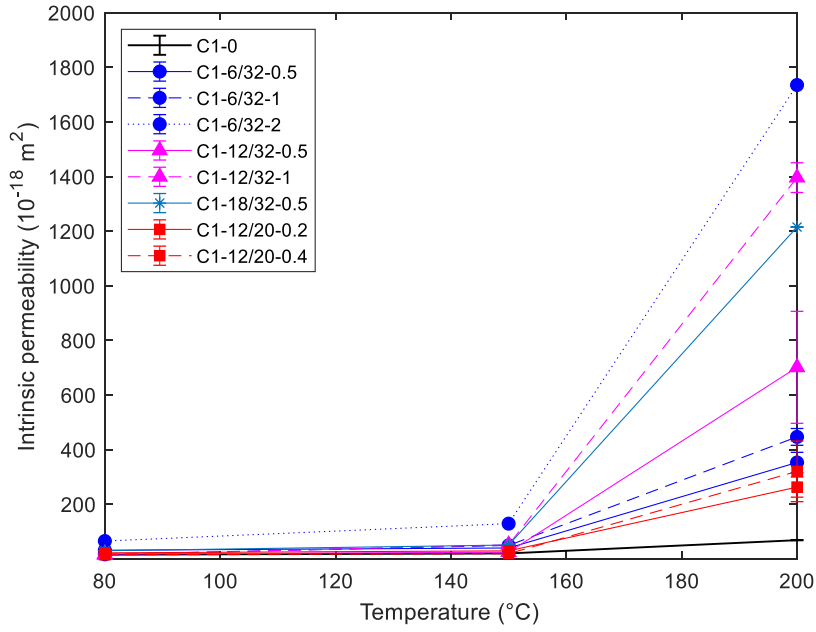


(a)

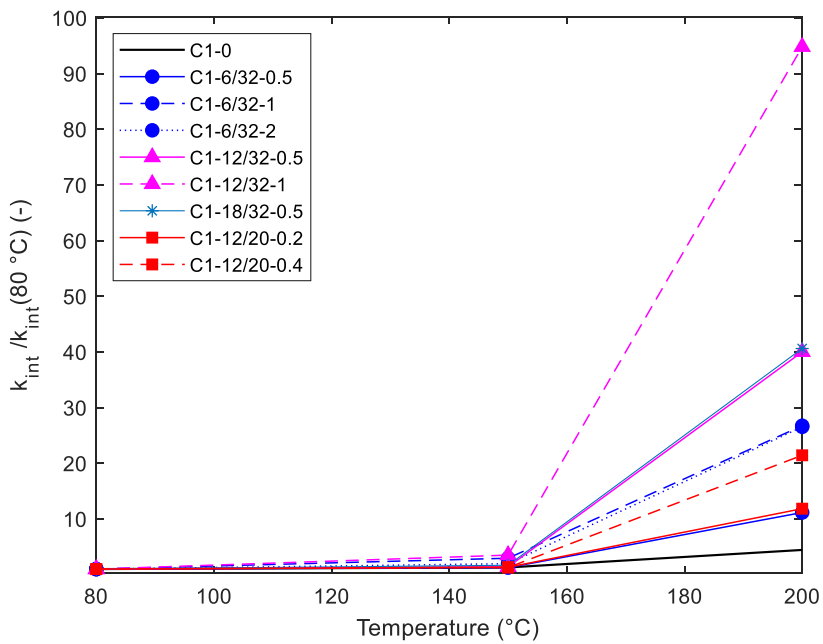


(b)

**Figure 3.63** Evolution of intrinsic permeability (a) and a ratio of intrinsic permeability and intrinsic permeability at 80  $^{\circ}\text{C}$  (b) as a function of temperature for mortar (M).

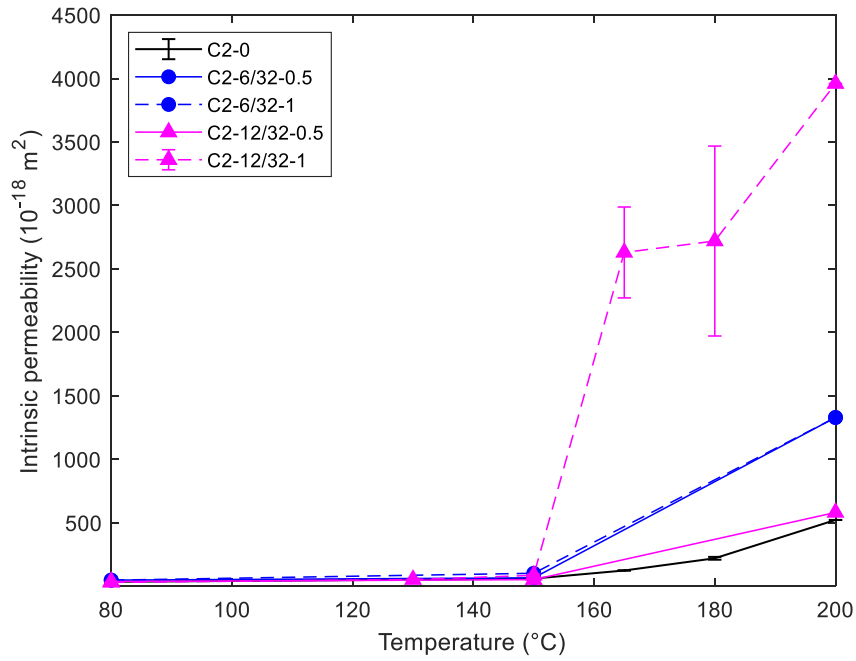


(a)

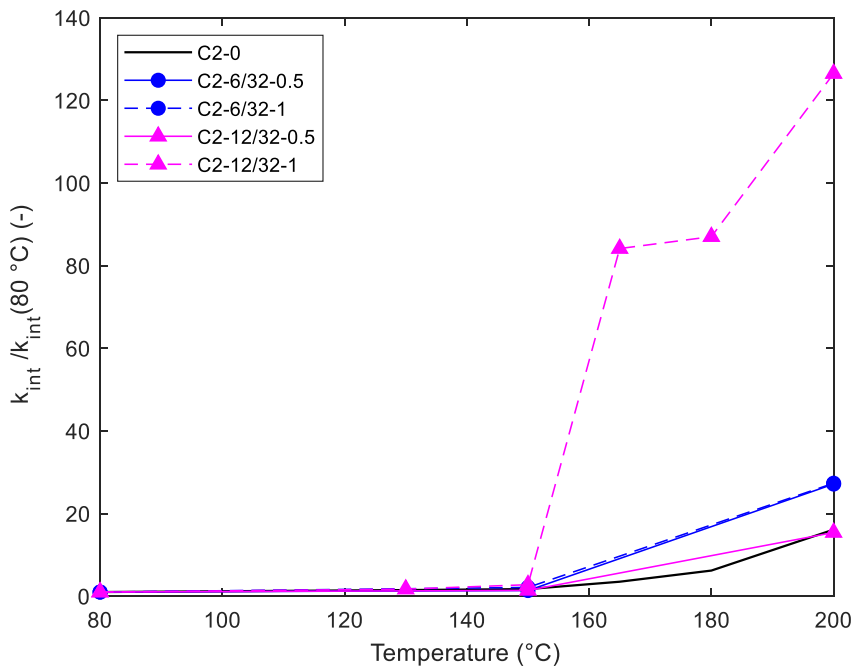


(b)

**Figure 3.64** Evolution of intrinsic permeability (a) and a ratio of intrinsic permeability and intrinsic permeability at 80  $^{\circ}\text{C}$  (b) as a function of temperature for concrete 1 (C1).



(a)



(b)

**Figure 3.65** Evolution of intrinsic permeability (a) and a ratio of intrinsic permeability and intrinsic permeability at 80 °C (b) as a function of temperature for concrete 2 (C2).

## Evolution of intrinsic permeability of fiber reinforced mixes with temperature

### *Influence of temperature*

As reference mixes, intrinsic permeability of fiber reinforced cementitious mixes increases with temperature as seen in Figures 3.63b, 3.64b and 3.65b. A slight increase at 150 °C is noted for all the mixes due to initiation of microcracking at paste-aggregate interface. At 150 °C, the range of permeability increase from 80 °C is 1.2- 2.3 times for mortar, 1.3- 3.5 times for concrete 1 and 1.4- 2.8 times for concrete 2.

A work from literature states a significant increase of permeability at 150 °C [95] attributed to a formation of microcracks and softening of fibers (see Figure 3.34). In [85], SEM images reveal microcracking around fibers starting from 105 °C and evolution of these cracks with temperature that authors explain by higher coefficient of thermal expansion of polypropylene in comparison to cement paste (see Figure 3.33). It is interesting to note that our results do not support these findings.

Significant increase of permeability is noted for all fiber-reinforced mixes at 200 °C. In addition to microcracking due to thermal incompatibility of paste and aggregates, major contribution to evolution of permeability is attributed to melting of polypropylene fibers at 165 °C. At 200 °C, the range of permeability increase from 80 °C is 4.6- 42.3 times for mortar, 11.2– 94.8 times for concrete 1 and 15.4– 126 times for concrete 2.

Results show that increase of permeability of cementitious material depends on fiber geometry and dosage as well on percolation of individual fibers and fiber-crack network. Each of these points is addressed below.

### *Percolation*

Fibers can percolate between themselves as well with pores and cracks. Percolation threshold of individual fibers is an important parameter in moisture transport. In the work of [110], percolation threshold is estimated via 3D simulation of randomly placed rectangular sections that represent fibers in a cube of 5 cm length. Results show that for 33 μm fibers of 6, 12 and 18 mm length, percolation threshold is reached for volume fractions of 0.39, 0.18 and 0.12 % respectively which translates into 3.55, 1.64 and 1.09 kg/m<sup>3</sup>. Presented values are lower than expected due to simulation of fibers without presence of stresses exerted on fibers by cementitious matrix and aggregates, which bend fibers and reduce percolation probability.

We calculate percolation volume fraction  $\phi_{cf}$  for flexible fibers, which converges to 80 % of dense packing fraction  $\phi_{mf}$ . Using Equation 2.24 from Chapter 2, we estimate percolation threshold for fibers subjected to the yield stress of 20 Pa and elastic modulus of 1 GPa for polypropylene as 4.6, 4 and 3.69 % vol. (or 42, 36 and 33 kg/m<sup>3</sup>) for 6, 12 and 18 mm long fibers with a diameter of 32  $\mu$ m respectively. Percolation threshold depends significantly on apparent length of fiber that results from stresses applied by overall suspension. When these stresses are high, fiber bends more, which reduces its apparent length and probability of percolation. Presented estimation shows that percolation of individual fibers is unattainable within conventional range of fiber dosages used to prevent spalling and that percolation of fibers and crack network and pores is a more reliable approach to achieve it.

#### *Influence of fiber dosage*

We plot the evolution of relative intrinsic permeability (a ratio of the intrinsic permeability of cementitious material with polypropylene fibers and intrinsic permeability of reference cementitious material) with temperature for mortar, concrete 1 and concrete 2 mixes in Figures 3.66, 3.67 and 3.68. No significant evolution of permeability related to presence of polypropylene fibers and increase of fiber dosage is observed before 150 °C for three materials. We note that increase of the polypropylene fiber dosage provokes an increase of intrinsic permeability at 200 °C. In Figure 3.66, this increase of permeability is observed for mortar with 12 mm fibers but not for 6 mm. This is explained by initial lower porosity of M-6/32-1 compared to M-6/32-0.5 (15.2 % and 13.6 % accordingly). The influence of fiber dosage is very explicit in terms of permeability increase for concrete 1 as presented in Figure 3.67. For concrete 2 (see Figure 3.68), strong increase is noted for 12 mm fibers and no evolution of permeability is observed for 6 mm fibers between 0.5 and 1 kg/m<sup>3</sup>. This is related to a difference in initial porosity as C2-6/32-1 has lower porosity than C2-6/32-0.5.

Despite some deviations from expected trend, it is possible to conclude that generally permeability appears to increase with increase of polypropylene fiber dosage. It is possible to attribute some scattering of results related to experimental error.

#### *Influence of fiber length*

We note that the relative intrinsic permeability of cementitious materials, in general, increases with the length of the polypropylene fibers for mortar, concrete 1 and concrete 2. In case of mortar, the highest increase is noted for fibers of 12 mm fibers, for concrete 1 for 18 mm fibers.

For C2, the highest increase is noted for C2-12/32-1 than for C2-6/32-1. However, C2-6/32-0.5 has a higher intrinsic permeability than C2-12/32-0.5, which could be considered as an exception from expected trend.

Our results show that longer fibers are more effective in terms of increase of intrinsic permeability than shorter ones. Longer fibers create longer empty channels when melted; this consequently increases percolation probability. We have assumed that percolation is mainly ensured by connection of cracks developed by paste-aggregate thermal mismatch using fibers, which would mean that longer fibers are more efficient in connecting these cracks than shorter ones.

#### *Influence of fiber diameter*

We have studied the influence of fiber diameter on intrinsic permeability for C1 mixes only (Figure 3.67). We shall recall that C1-12/20-0.2 (0.4) and C1-12/32-0.5 (1) have the same total fiber number 58 million /m<sup>3</sup> (116 million /m<sup>3</sup>) and total fiber length 696 km/m<sup>3</sup> (1392 km/m<sup>3</sup>) allowing a direct comparison of the influence of fiber diameter. Concrete with 20 μm diameter fibers has lower permeability compared to concrete with 32 μm diameter fibers at both dosages at 200 °C. Lower permeability with thinner fibers can be explained by lower chance of percolation for thinner fiber due to its higher flexure. Indeed, using Equation 2.4 from Chapter 2, fiber deflection for 20 μm fiber is 4 times higher than for 32 μm fiber. Since apparent length of fiber is reduced under bending, thinner fibers produce less increase of permeability than thicker ones. It is also arguable that thermal expansion of polypropylene induces strains thus microcracking in surrounding paste. In such case, larger diameter would imply more open and propagated microcracks due to thermal expansion of polypropylene, another phenomenon potentially contributing to efficiency of 32 μm fibers over 20 μm fibers.

#### *Influence of physical state of fibers*

We have studied the influence of physical state of polypropylene fiber for mix C2-12/32-1 (see Figure 3.68). In addition to 80, 150 and 200 °C, heating temperatures of 130 °C (a start of detachment prior to melting), 165 °C (pic of melting) and 180 °C (melting is complete) are considered. We observe that there is a low increase of the permeability between 80 and 150 °C due to thermal incompatibility of paste - aggregate. No evolution of permeability is noted for 150 °C, before melting of fibers, as reported in literature [95]. Intrinsic permeability measured

after heating to 165 °C shows an increase in relative intrinsic permeability related to a high expansion of polypropylene due to phase change. After melting is completed and fiber are absorbed by porosity, polypropylene fibers have no contribution to permeability in terms of creation of vacated channels, however, empty fiber channels serve as additional points for crack localization that could improve permeability.

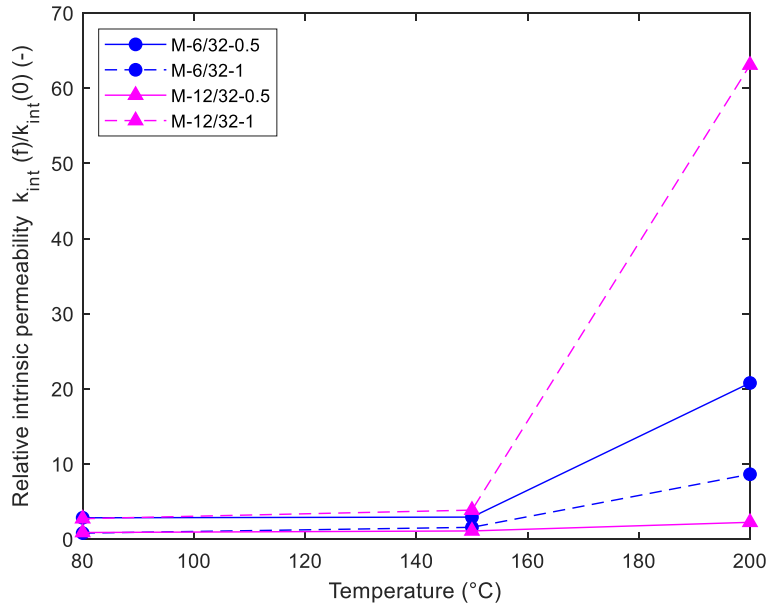


**Figure 3.66** Relative intrinsic permeability as a function of temperature for mortar (M) samples.

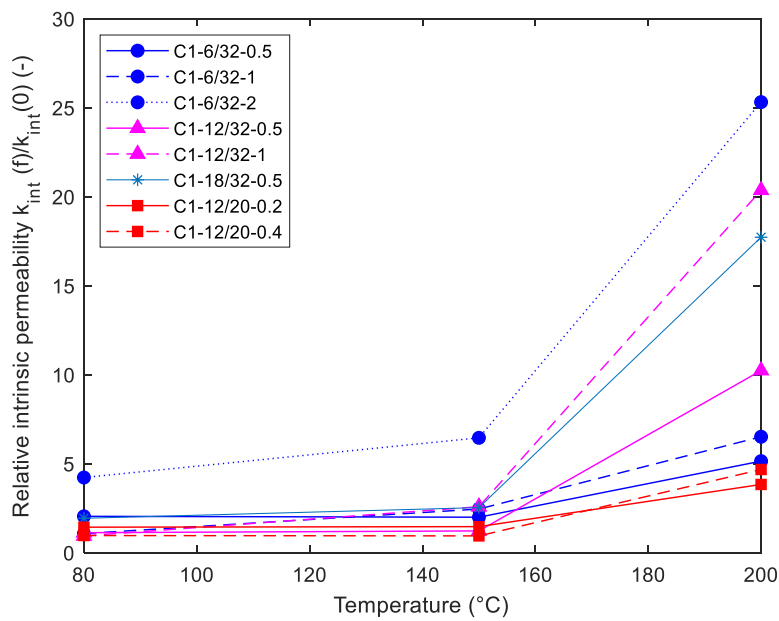


**Figure 3.67** Relative intrinsic permeability at 200 °C as a function of temperature for concrete 1 samples.

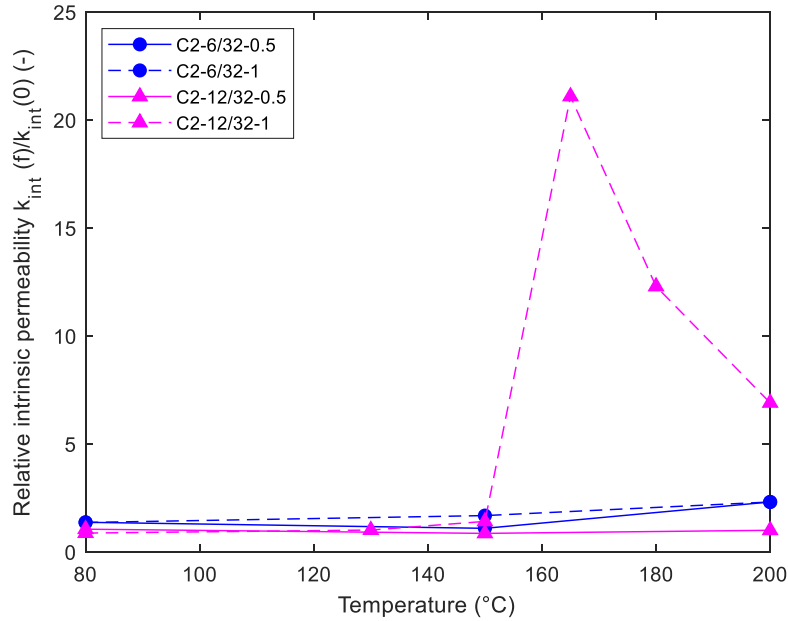


**Figure 3.68** Relative intrinsic permeability as a function of temperature for concrete 2 (C2) samples.

### 3.4.3 Fire test

In this part, we present and discuss the results of fire tests on uniaxially loaded prisms of three cementitious materials with different granular skeletons (mortar, concrete 1 and concrete 2) with a purpose of identifying optimal polypropylene fiber geometry and dosage.

#### Overview of results

We present in Figure 3.69 color maps of spalling depth of heated face of tested cementitious samples after fire obtained using photogrammetry. All images are aligned in the direction of the load application (see Figure 3.69). The images of heated faces are presented in Annex. We note dispersion between samples of the same mix in terms of spalling region and intensity. One of the reasons for dispersion is the small size of the sample, therefore, mostly 3 samples have been tested for one mix. We present results of fire tests in Table 3.12 in terms of spalling start and end, number of spalling events, mean and maximum spalling depth and spalled volume.

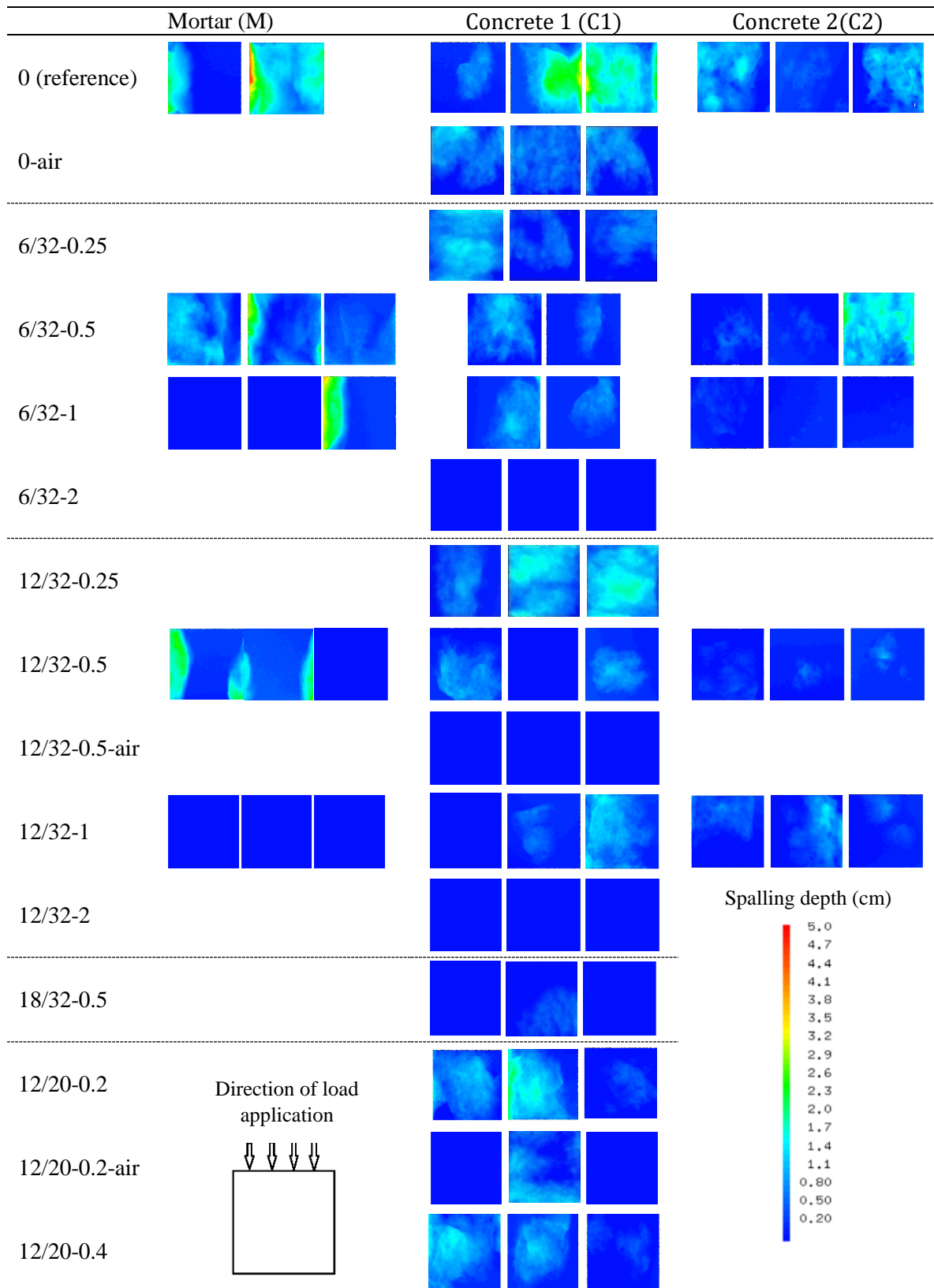


**Figure 3.69** Spalling maps of mortar (M), concrete 1 (C1) and concrete 2 (C2) samples tested.

**Table 3.12** Results of fire tests

Mix	N	tStart (min)	tEnd (min)	Nber of events	hmean (cm)	hmax (cm)	Vsp (cm3)
M-0	1	12	19	2	1.52	4.78	605.31
	2	18	18	1	0.38	2.73	150.33
M-6/32-0.5	1	16	16	1	0.77	2.04	307.59
	2	12	12	1	0.41	1.20	163.12
	3	8	13	3	0.68	3.29	271.09
M-6/32-1	1	-	-	0	0	0	0
	2	-	-	0	0	0	0
	3	15	15	1	0.82	3.91	327.83
M-12/32-0.5	1	15	15	1	0.70	3.08	282.42
	2	14	14	1	0.78	2.62	311.33
	3	-	-	0	0	0	0
M-12/32-1	1	-	-	0	0	0	0
	2	-	-	0	0	0	0
	3	-	-	0	0	0	0
C1-0	1	8	13	3	0.23	1.03	92.44
	2	12	22	3	1.29	3.66	517.71
	3	8	22	4	1.61	3.64	641.72
C1-0-A*	1	15	24	3	0.47	1.75	188.52
	2	15	15	1	0.48	1.11	192.35
	3	18	18	1	0.32	1.62	130.14
C1-6/32-0.25	1	16	27	7	0.81	1.89	325.34
	2	10	15	8	0.13	1.02	52.26
	3	10	16	6	0.24	0.24	97.78
C1-6/32-0.5	1	8	19	6	0.53	1.48	207.63
	2	8	8	1	0.17	0.86	68.05
C1-6/32-1	1	8	13	2	0.28	1.00	113.10
	2	10	13	3	0.50	2.37	201.73
C1-6/32-2	1	-	-	0	0	0	0
	2	-	-	0	0	0	0
	3	-	-	0	0	0	0
C1-12/32-0.25	1	9	13	4	0.29	1.14	117.69
	2	11	20	6	1.04	1.91	416.74
	3	11	19	6	1.17	1.95	468.53
C1-12/32-0.5	1	11	12	2	0.35	1.28	139.89
	2	-	-	0	0	0	0
	3	15	15	1	0.41	1.23	165.46
C1-12/32-0.5-A*	1	-	-	0	0	0	0
	2	-	-	0	0	0	0
	3	-	-	0	0	0	0
C1-12/32-1	1	-	-	0	0	0	0
	2	9	10	2	0.72	1.72	286.64
	3	9	18	3	0.17	0.79	67.58
C1-12/32-2	1	-	-	0	0	0	0
	2	-	-	0	0	0	0
	3	-	-	0	0	0	0
C1-18/32-0.5	1	-	-	0	0	0	0
	2	-	-	0	0	0	0
	3	12	12	1	0.04	0.88	17.18
C1-12/20-0.2	1	7	14	5	0.62	2.07	248.22
	2	7	18	3	1.10	2.56	378.11
	3	5	9	7	0.02	0.61	6.37
C1-12/20-0.2-A*	1	-	-	0	0	0	0
	2	20	20	1	0.51	1.46	205.12
	3	-	-	0	0	0	0
C1-12/20-0.4	1	7	16	5	0.33	1.33	130.48
	2	7	9	3	0.01	0.49	2/06
	3	11	13	2	0.64	1.54	192.74
C2-0	1	4	-	-	0.71	1.80	285.72
	2	7	12	6	0.23	0.63	92.98
	3	6	14	7	0.68	1.65	270.96
C2-6/32-0.5	1	8	9	2	0.02	0.68	6.17
	2	4	11	6	0.07	0.48	29.44
	3	5	15	-	1.35	2.68	544.43
C2-6/32-1	1	5	11	7	0.004	1.00	1.54
	2	7	7	1	0.08	0.29	30.59
	3	3	3	1	0.02	0.29	7.17
C2-12/32-0.5	1	4	7	8	0.02	0.48	7.04
	2	7	9	3	0.08	0.72	31.51
	3	7	11	3	0.21	1.18	82.89
C1-12/32-1	1	6	14	2	0.09	0.91	36.76
	2	7	8	2	0.12	1.17	48.08
	3	6	13	6	0.33	1.58	128.66

### Relationship between mean and maximum spalling depth and spalled volume

Mean spalling depth is calculated as a spalled volume over the exposed surface of the sample (reduced by taking into account of wall effect); thus, a linear relationship between these two variables is expected. We then plot an average value of maximum spalling depth as a function of an average value of mean spalling depth in Figure 3.70. It is observed that the relationship between these two quantities is almost linear. Therefore, we choose to presents results in terms of mean spalling depth.

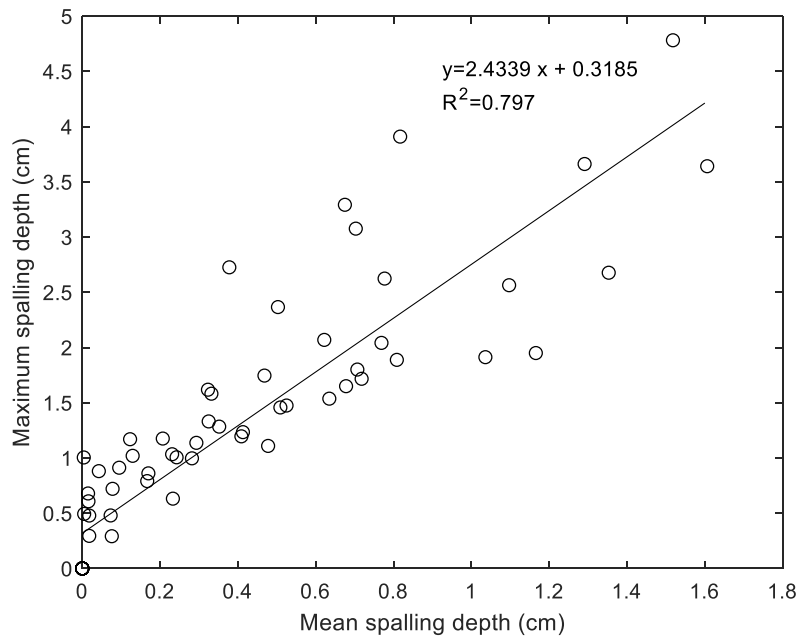


**Figure 3.70** Relationship between maximum spalling depth values and mean spalling depth for all mixes tested.

We plot the time of start of spalling depth and number of events as a function of fiber dosage for mortar, concrete 1 and concrete 2 in Figures 3.71 and 3.72 respectively. We plot in Figure 3.73, 3.74, 3.75 and 3.76 the evolution of mean spalling depth as function of: a) fiber dosage, b) total fiber number for mortar, concrete 1 and concrete 2.

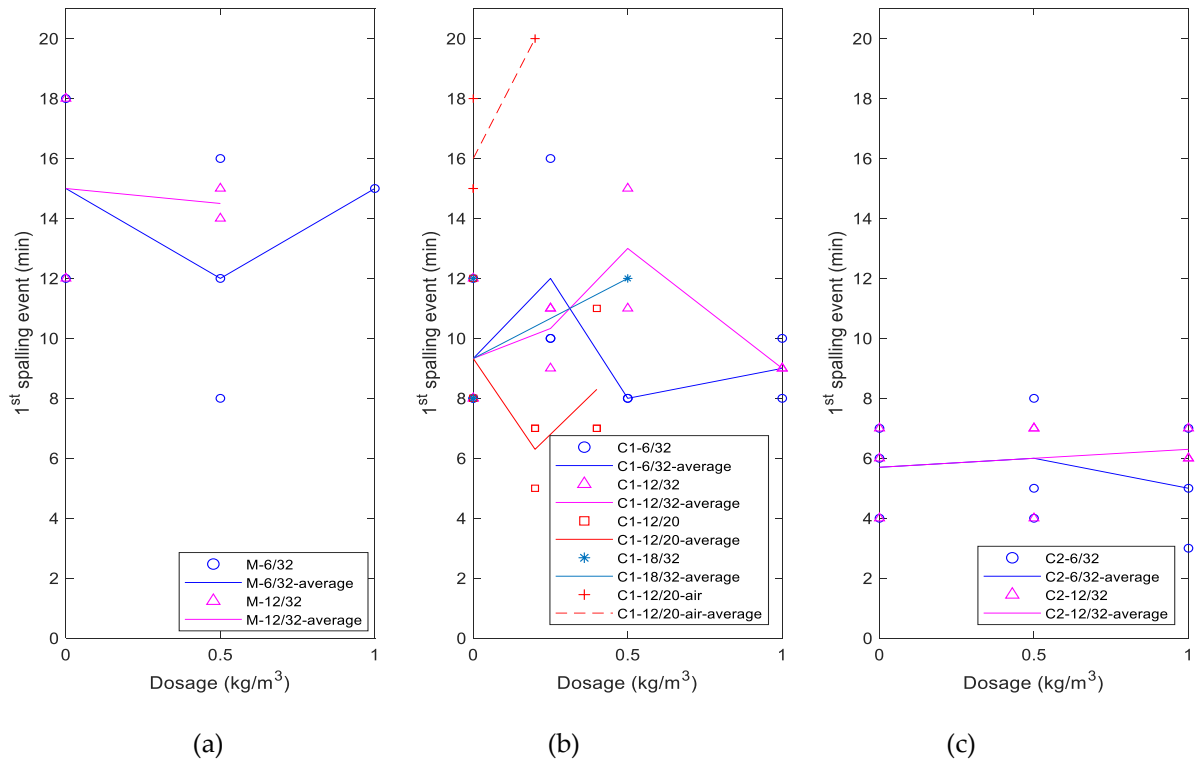


**Figure 3.71** Time of the first spalling event as fiber dosage for: a) mortar, b) concrete 1 and c) concrete 2.

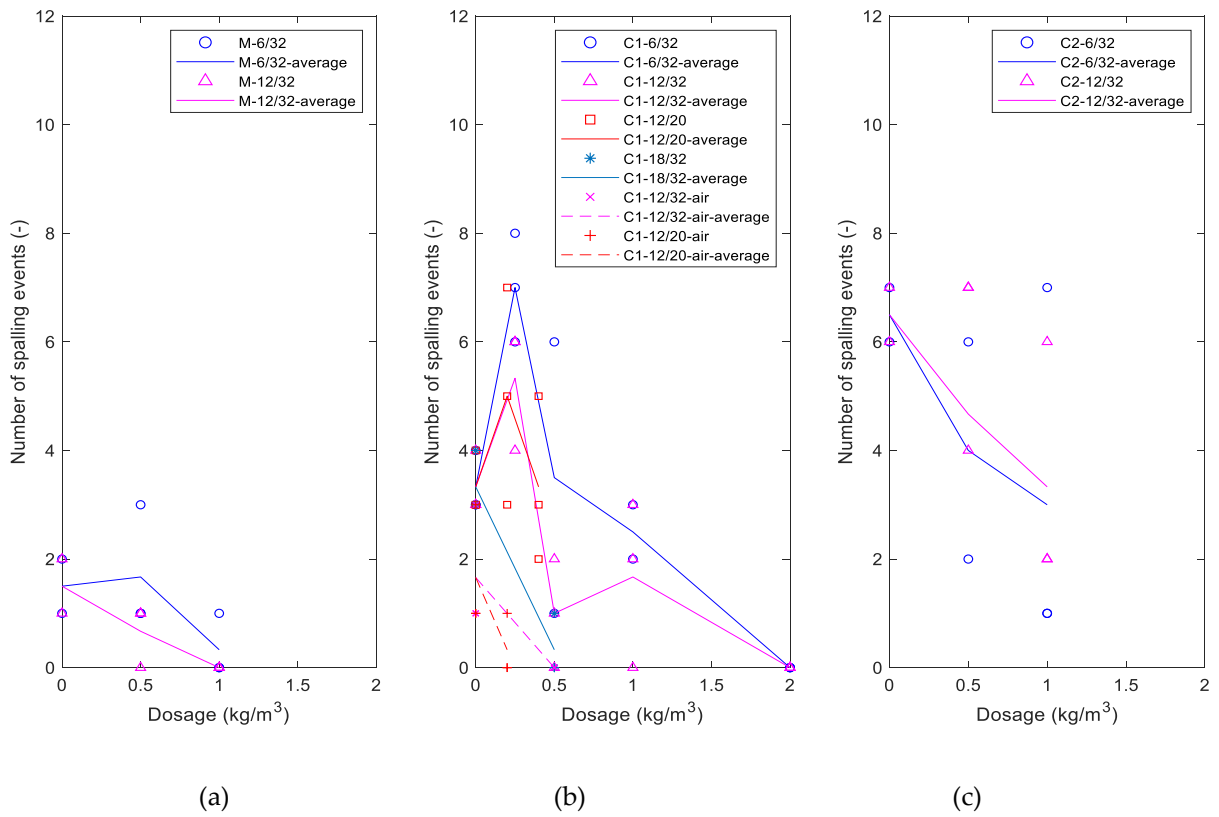


**Figure 3.72** Number of spalling events presented as a function of fiber dosage for : a) mortar, b) concrete 1 and c) concrete 2.

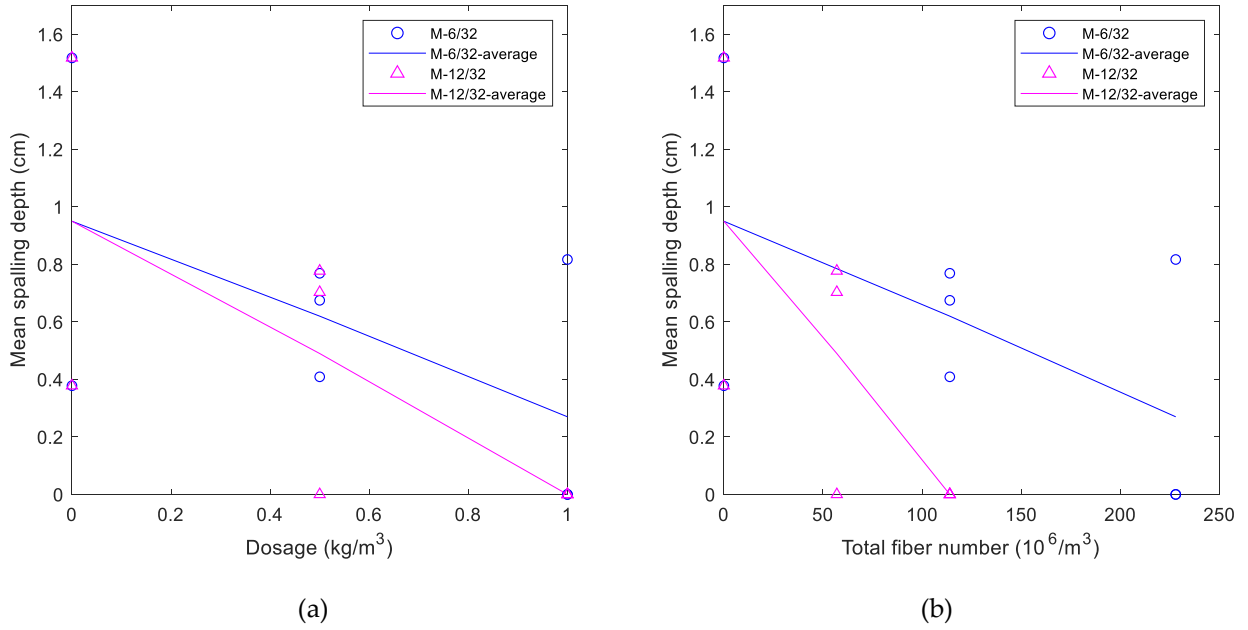


**Figure 3.73** Mean spalling depth presented as a function of: a) fiber dosages, b) total fiber number for mortar mixes.

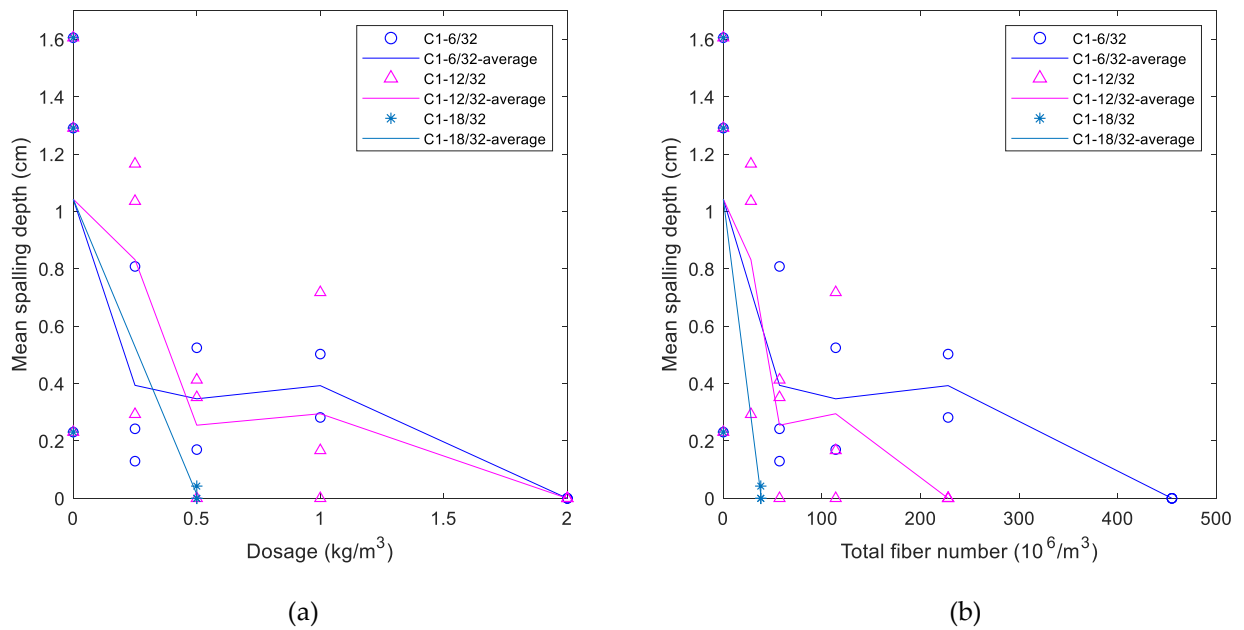


**Figure 3.74** Mean spalling depth presented as a function of: a) fiber dosages, b) total fiber number for concrete 1 mixes.

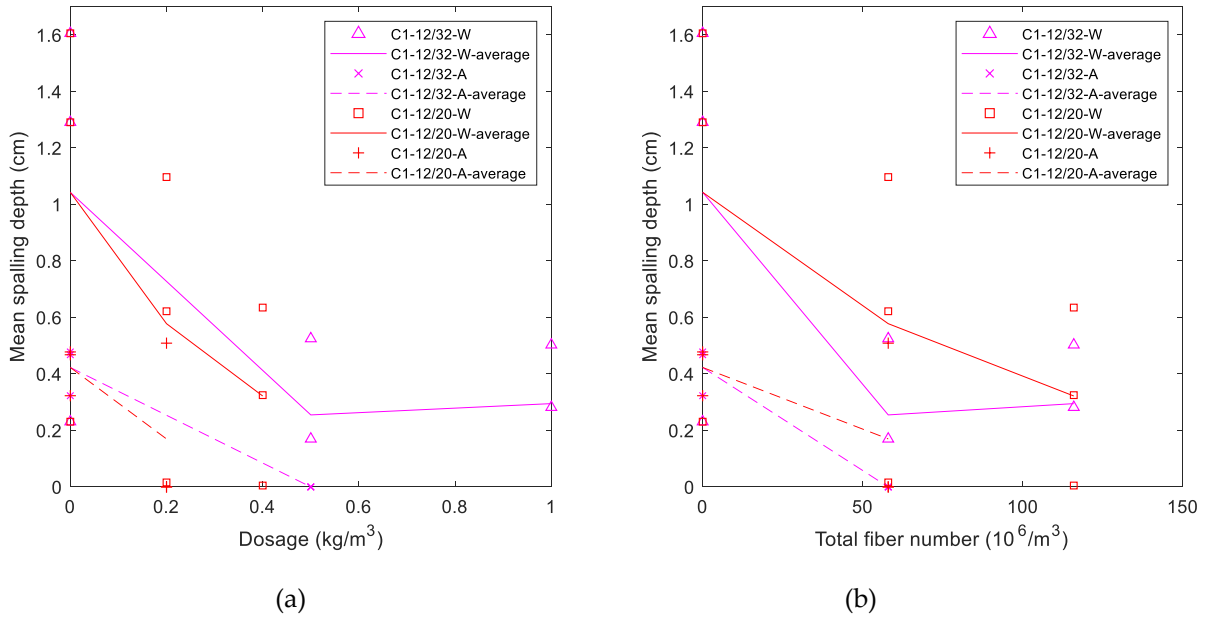


**Figure 3.75** Mean spalling depth for samples C1-12/32 and C1-12/20 cured in water (W) and air (A) as a function of : a) fiber dosage, b) total fiber number.

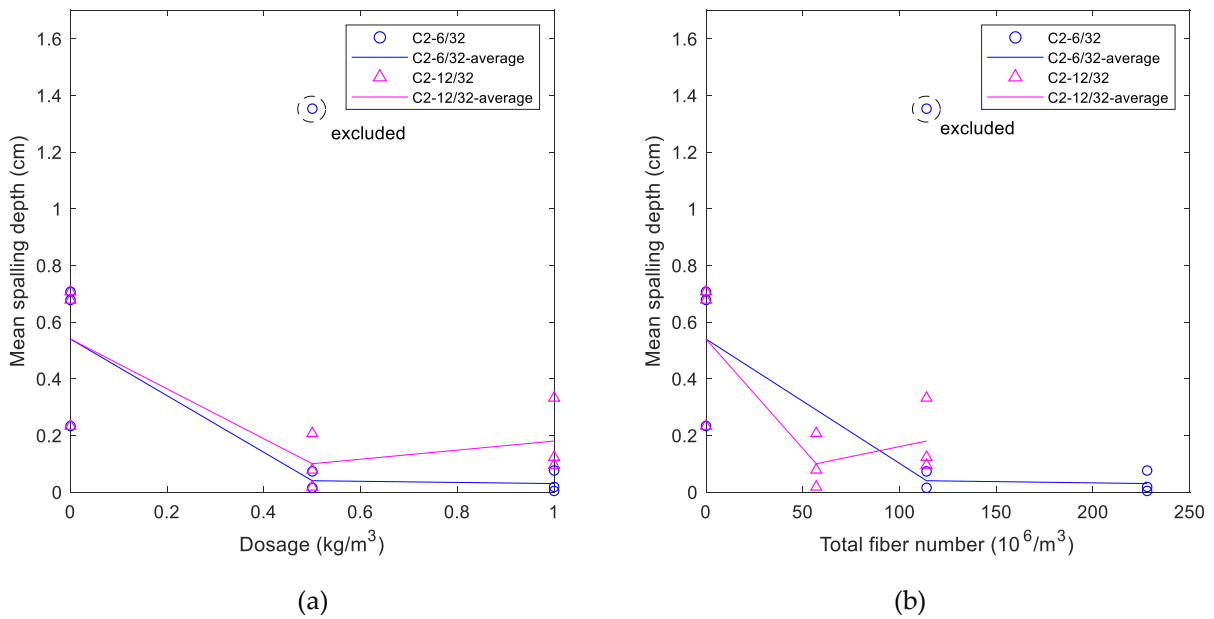


**Figure 3.76** Mean spalling depth presented as a function of: a) fiber dosages, b) total fiber number for concrete 2 mixes.

### **Influence of aggregate size and compressive strength on spalling**

We shall remind here that average compressive strength at 28 days measured on cylindrical samples of M-0, C1-0 and C2-0 is 41, 90 and 80 MPa respectively. As three cementitious mixes have different compressive strengths, a direct comparison of the results should be conducted with caution. Compressive strength at 28 days of mortar without fibers M-0, despite its lower strength compared to concretes C1-0 and C2-0 (2.5 and 2 times lower), is quite elevated and approaches a range of high strength mortars. Despite the differences in compressive strength, we note that size of aggregate has an impact on start of spalling, number of spalling events and intensity of spalling (mean, maximum depth and spalled volume). An average start of spalling for M-0, C1-0 and C2-0 is found to be 15, 9 and 6 min respectively. Number of spalling events for these mixes on average is 1.5, 3.3 and 6.5 times. It appears thus with increasing aggregate size, spalling occurs faster and more frequently.

We observe that, in general, increase of aggregate size leads to decrease of mean spalling depth. The decrease of spalling is observed for increased aggregate size in [111], [112]. Average values of mean spalling depth for references mixes M-0, C1-0 and C2-0 are 0.95, 1.04 and 0.54 cm accordingly. We note that spalling exhibited by mortar M-0 is as important as that of C1-0 and exceeds that of C2-0.

Some post fire images of cracks are presented in Figure 3.77 for mortar, concrete 1 and 2 samples. Most of mortar samples have one big vertical crack in the direction of mechanical loading with a possible orthogonal crack. Network of microcracks visible to eye is very limited with a distance between adjacent cracks of approximately 50 mm. For concrete 1 and concrete 2, cracks are more visible to eye, spaced by 8-10 mm and 10-15 mm respectively. It should be noted as well that crack opening for concrete 2 is wider than for concrete 1. The distance between cracks is evaluated using Fiji software. Cracks are represented by straight lines and shortest distance perpendicular to two adjacent lines that stand for cracks is considered.

It is possible to suggest that two phenomena occur at the same time. From perspective of thermo-hydral mechanism, lower permeability implies increased pore pressures and elevated risk of spalling. Initial permeability and intrinsic permeability at 200 °C for all mixes was comparably the lowest for mortar and the highest for concrete 2. Therefore, mortar, having the lowest permeability of all, spalls more than concrete 1 and 2. At the same time, heating of cementitious composites results in creation of cracks at the interface between cement paste and aggregate due to mismatch of their thermal expansion. Increase of aggregate size produces denser cracking network with wider crack opening that serves as transport channels allowing

faster evacuation of moisture and drying of layer susceptible to spalling, therefore, reducing spalling as seen on example of concrete 2.

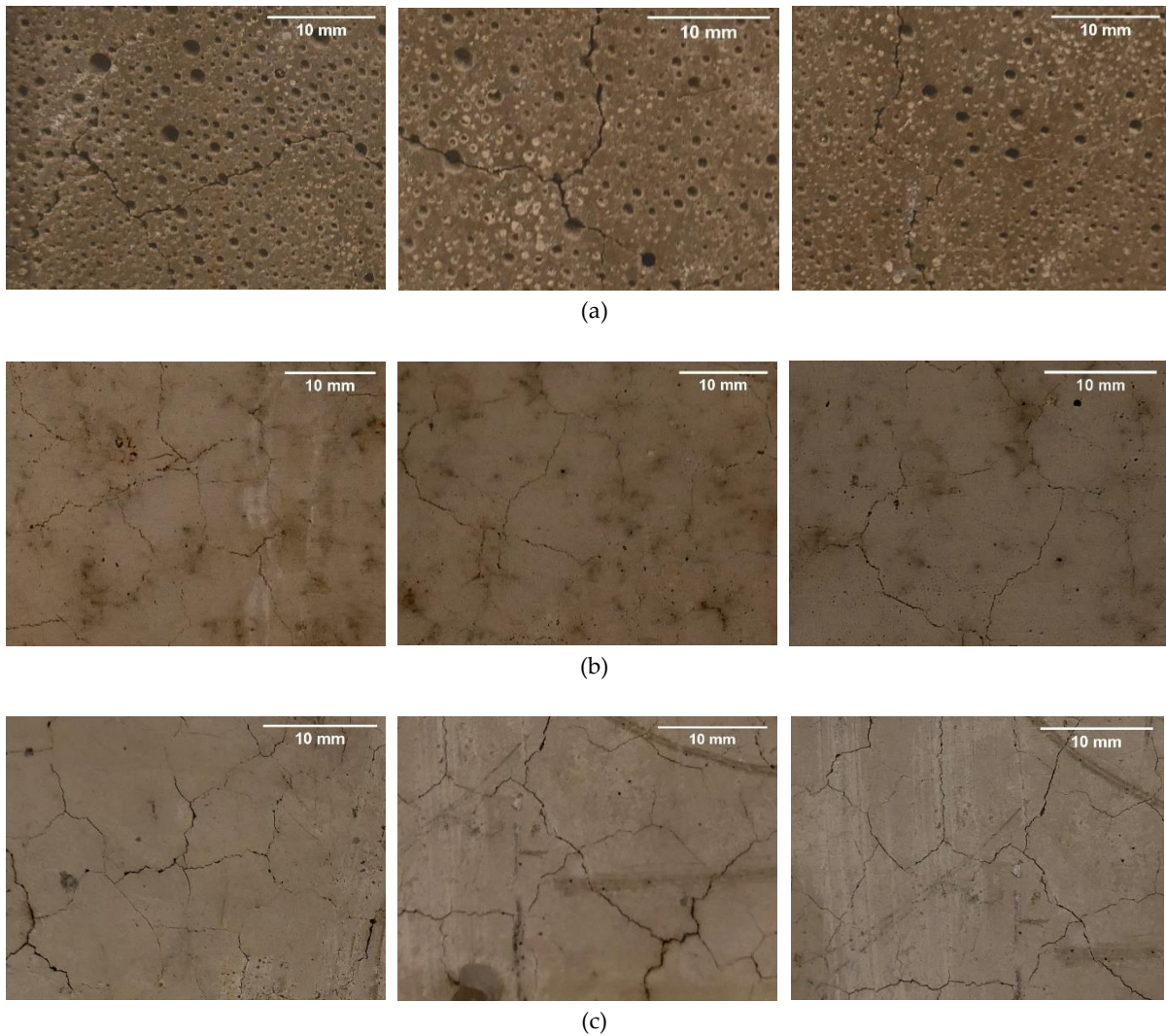


**Figure 3.77** Cracking patterns for: a) mortar, b) concrete 1 and c) concrete 2.

### **Influence of polypropylene fibers on spalling**

We note from Figures 3.71 and 3.72 that addition of polypropylene fibers has a slight influence on start of spalling and a great influence on number of spalling events. Number of spalling events is slightly higher at  $0.25 \text{ kg/m}^3$  compared to reference mixes (see Figure 3.72b) and is reduced significantly for fiber dosages higher than  $0.5 \text{ kg/m}^3$ .

### *Influence of fiber dosage*

From Figures 3.73, 3.74, 3.75 and 3.76, we observe that addition of polypropylene fibers reduces mean spalling depth for mortar, concrete 1 and concrete 2. Spalling appears to decrease with increase of polypropylene fiber dosage for majority of samples of mortar, concrete 1 and concrete 2. In case of mortar, we note a linear decrease of mean spalling depth with dosage of fibers. For concrete 1, spalling is decreased between 0 and 0.5 kg/m<sup>3</sup>; however, no evolution of spalling depth between 0.5 and 1 kg/m<sup>3</sup> is noted. Increase of dosage to 2 kg/m<sup>3</sup> has prevented spalling for concrete with 6 and 12 mm fibers. For concrete 2, with increase of fiber dosage mean spalling depth decreases slightly with 12 mm fibers and increases with 6 mm fibers for 0.5 and 1 kg/m<sup>3</sup>.

### *Influence of fiber length*

In terms of the influence of fiber length, 6 and 12 mm fibers are studied with additional 18 mm fibers for concrete 1 only. For mortar, use of 1 kg/m<sup>3</sup> of 12 mm fibers prevented samples from spalling. Despite the fact that M-6/32-1 contains twice as much fibers as M-12/32-1, a significant influence of fiber length is observed. Same conclusion on the importance of fiber length is found for concrete 1. Spalling of concrete is almost prevented with a use of 0.5 kg/m<sup>3</sup> 18 mm fibers while for 6 mm and 12 mm fibers no spalling was observed at 2 kg/m<sup>3</sup>. When comparing total fiber count, total fiber number is 39 million/m<sup>3</sup> for C1-18/32-0.5 opposed to 464 and 232 million/m<sup>3</sup> for C1-6/32-2 and C1-12/32-2 respectively, which shows the efficiency of lower dosage-longer fibers over higher dosage-shorter fibers. For concrete 2, 12 mm fibers appear to be slightly more efficient than 6 mm fibers. In terms of spalling prevention, we can note that choice of fiber length should be accomplished in accordance with the size of the biggest aggregate  $D_{max}$ . Considering the fact that distance between cracks (see Figure 3.77) varies with the size of aggregates and that fibers have a low probability of percolation among themselves, percolation is mainly achieved through connection of cracks and fibers. For mortar and concrete 1 with  $D_{max}$  of 1 and 10 mm accordingly, optimized fiber lengths are found to be 12 and 18 mm.

### *Influence of fiber diameter*

In terms of the influence of fiber diameter, we have studied mixes C1-12/32 and C1-12/20 (see Figure 3.75) stored in water and in air. We remind that total fiber number and total fiber length

for mixes C1-12/32 and C1-12/20 are fixed. For water-stored condition, mean spalling depth for reference mix without polypropylene fibers C1-0 varies between 0.23 and 1.61 cm with an average of 1.04 cm. For a total number of fibers of 57 million, average value of mean spalling depth has decreased to 0.26 and 0.58 cm for 32  $\mu\text{m}$  and 20  $\mu\text{m}$  fiber concrete respectively. Further increase of number of fibers to 114 million/ $\text{m}^3$  has no effect on mean spalling depth for concrete with 32  $\mu\text{m}$  fibers while for 20  $\mu\text{m}$  fibers spalling depth has decreased to 0.32 cm. We note that for a total fiber number of 114 million/ $\text{m}^3$ , mean spalling depth for both fibers almost coincides. Results show that at lower fiber number, 32  $\mu\text{m}$  fibers are slightly more effective in terms of spalling prevention than 20  $\mu\text{m}$  fibers. When the number of fibers is 114 million/ $\text{m}^3$ , no influence of fiber diameter on mean spalling depth is noted. Existence of slight influence of fiber diameter on spalling is confirmed on air-cured samples as well as for water-cured: with 32  $\mu\text{m}$  fibers, no spalling is observed while with 20  $\mu\text{m}$  fibers one sample out of three has spalled with mean spalling depth of 0.17 cm.

### **Influence of cure on spalling**

We have studied the influence of curing on mixes C1-0, C1-12/32-0.5 and C1-12/20-0.2 stored in two conditions: cure in water for 59 days (water) and cure for 7 days in tight bag then in 52 days in air (air). To remind, water content in the first centimeter from spalling surface is around 5.4 and 3.4 % for water and air curing conditions.

From Figure 3.71 and 3.72, start of spalling and number of spalling events for samples cured in air is 16 minutes and 1.66 events accordingly, whereas, for water-cured samples, these values are 9 minutes and 3.33 events. For air-cured mixes, spalling occurs later and is less frequent. The results of mean spalling depth demonstrated in Figure 3.75 show that for samples cured in air the mean spalling depth is 59 % less than for samples cured in water. In comparison to water cured samples, C1-12/32-0.5 cured in air have not spalled, while mean spalling depth for C1-12/20-0.2 has reduced by 47 %.

We conclude that curing conditions have an important influence on spalling. Dehydration front of samples through natural drying in air has decreased amount of moisture necessary to evacuate in the first centimeters of the heated face, which has consequently delayed moisture clog formation and reduced spalling depth.

### 3.4.4 Linking fire tests and permeability

We plot in Figure 3.78a and 3.78b average values of mean spalling depth as a function of average residual radial intrinsic permeability at 80 °C and after heating to 200 °C. A relation between spalling and initial permeability of materials (see Figure 3.78a) measured at 80 °C does not appear to be straightforward. Mortar samples having the lowest initial permeability at 80 °C have spalled more than concrete 1 and concrete 2 samples. Concrete 2 samples with the highest permeability have spalled the least of all. Cementitious materials with higher initial permeability develop lower gas pore pressures inside of materials, which makes them less sensitive to spalling.

It is necessary to add that from measurements of porosity accessible to water, mortar contains higher volume of pores than concrete 1 and concrete 2. Due to a higher porosity, in fully saturated samples, an average water content in mortar is higher than in concrete: 6.6 % for mortar, 5.5 % for concrete 1 and 5.6 % for concrete 2. Since increased water content elevates spalling risk due to higher amount of vapor and water required draining, this can participate in explaining why mortar samples spall more as well.

From Figure 3.78b we note that with increase of intrinsic permeability at 200 °C mean spalling depth decreases. This is true for all the data points except one, which represents an average for samples of C2-12/32-1 (marked with circle). Permeability at 200 °C for this mix is the highest; however, spalling of the samples has occurred.

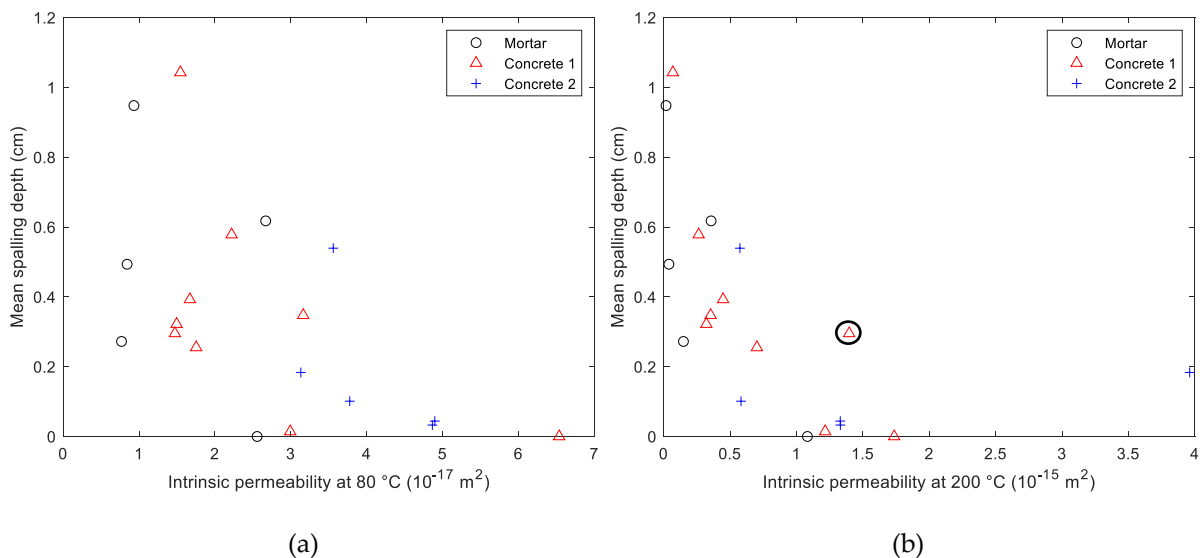


**Figure 3.78** Average value of mean spalling depth plotted against average value of intrinsic permeability a) at 80 °C, b) after heating to 200 °C.

We have observed an influence of fiber dosage and geometry on high temperature behavior of cementitious materials using fire tests and residual radial permeability tests. Increase of fiber length and dosage provokes an increase of intrinsic permeability at 200 °C and a decrease of mean spalling depth. Increasing fiber diameter (measured for C1 only) at constant number of fibers produces an increase of intrinsic permeability and slight decrease of mean spalling depth. We note that intrinsic permeability does not serve as a single indicator for spalling response due to its modification during fire tests. For example, intrinsic permeability at 200 °C of C1-12/32-1 is slightly higher than for C1-18/32-0.5 and during fire tests, C1-12/32-1 has spalled significantly while C1-18/32-0.5 has almost no spalling. Heating of samples for permeability tests allows for unrestricted expansion of sample and free longitudinal and radial strain development that leads to cracks parallel and perpendicular to loading direction. During permeability testing, applied compressive loading counteracts injected gas pressure without modification of cracks due to thermal loading. Fire tests are conducted with a uniaxial loading of 5 MPa. Polypropylene fibers increase permeability due to improvement of porous network by creation of empty channels through melting and connecting with thermally induced cracks from aggregate-paste interface. At the same moment, cracks perpendicular to loading direction are closed while parallel cracks are widened leading to modification of permeability.

There could exist as well an influence of time necessary to empty channel for fibers. During permeability test, temperature of 200 °C is maintained for 3 hours and taking into account a thickness of sample, a difference between outer and inner radius,  $\Delta R = 2.65$  cm, we could be certain that polypropylene fibers inside have melted and flown into cracks and surrounding cementitious matrix. During fire tests, these fibers located at heated face in the most sensitive to spalling centimeters, could require a time to empty channels as mentioned in [93]. Results of fire tests show that spalling occurs around minute 15 for mortar, minute 9 for concrete 1 and minute 6 for concrete 2. It is possible to suggest that at start of spalling polypropylene fibers have not melted yet and their positive influence is delayed due to a time necessary to empty a channel.

The start of the spalling and number of spalling events is different for three materials. Concrete 1 and concrete 2 are weakened more than mortar due to presence of larger aggregates that cause cracks due to higher thermal mismatch between paste and aggregates. With higher compressive strength, thermo-mechanical stresses are stronger for concrete 1 and concrete 2 than for mortar, and taking into account their weakened state it causes earlier start of spalling with higher number of spalling events.

### 3.5 Presentation of the numerical study

In this part of the chapter, we present the numerical investigation aimed at studying damage of cementitious materials at high temperature. It is composed of two separate studies: influence of fiber expansion on damage of mortar and 2D mesoscale high temperature modelling of cementitious materials presented in the experimental study.

#### 3.5.1 Numerical model

##### Mechanical model

Mechanical model used is isotropic damage model from Fichant - La Borderie [113], an extension of isotropic damage model of Mazars [114]. It allows for regularization of fracture energy  $G_f$  with a size of the mesh  $h$  as well as the coupling with plasticity and unilateral effects. The effective stress  $\bar{\sigma}$  is found from elastic strain  $\varepsilon_e$  and initial mechanical characteristic: elastic modulus  $E$  and Poisson's ratio  $\nu$ .

$$\bar{\sigma}_{ij} = \frac{E}{1+\nu} \varepsilon_{e\ ij} + \frac{E\nu}{(1+\nu)(1-2\nu)} \varepsilon_{e\ kk} \delta_{ij} \quad (3.20)$$

Total strain is found as:

$$\varepsilon_{e\ ij} = \varepsilon_e + \varepsilon_p \quad (3.21)$$

Total stress  $\sigma$  is then found using damage variable  $d$  as:

$$\sigma_{ij} = (1-d)\langle \bar{\sigma} \rangle_{ij}^+ + (1-d^\alpha)\langle \bar{\sigma} \rangle_{ij}^- \quad (3.22)$$

where  $\langle \bar{\sigma} \rangle_{ij}^+$  and  $\langle \bar{\sigma} \rangle_{ij}^-$  represent positive and negative parts of stress tensor. Damage  $d$  is calculated from equivalent deformation  $\tilde{\varepsilon}$  defined by Mazars [114] where  $f_t$  is tensile strength:

$$d = 1 - \frac{f_t}{E\tilde{\varepsilon}} \exp\left(\frac{hf_t}{G_f}\left(\frac{f_t}{E} - \tilde{\varepsilon}\right)\right) \quad (3.23)$$

where  $\tilde{\varepsilon} = \sqrt{\sum_{i=1}^3 \langle \varepsilon_i^e \rangle_+^2}$ .

##### Thermo-mechanical coupling

Thermo-mechanical calculations are accomplished in quasi-stationary condition. The imposed temperature is constant over surface of sample. We consider an evolution of mechanical

properties of mortar and polypropylene fiber with temperature. We calculate thermal deformations related to expansion of polypropylene and mortar as a function of coefficient of thermal expansion  $\alpha$  as:

$$\varepsilon_{th} = \alpha(T) * (T - T_{ref}) \quad (3.24)$$

where  $T$  is temperature and  $T_{ref}$  is reference temperature usually taken as 20 °C or 293.15 K.

### 3.5.2 Influence of fiber expansion on mortar damage at HT

This study is aimed at understanding the conditions of cracking at small scale around a polypropylene fiber due to the thermal expansion of polypropylene.

#### Material properties

##### *Mortar*

We present in Table 3.13 the evolution of mortar properties with temperature such as coefficient of thermal expansion  $\alpha$ , elastic modulus  $E$ , tensile strength  $f_t$  and fracture energy  $G_f$  determined experimentally in [115]. Several properties are considered constant with temperature: density  $\rho$ , Poisson's ratio  $\nu$ , thermal conductivity  $k$  and specific heat  $C_p$  (see Table 3.14).

**Table 3.13** Evolution of mortar properties with temperature [113].

T (°C)	$\alpha$ (x 10 <sup>-5</sup> /°C)	E (GPa)	$f_t$ (MPa)	$G_f$ (J/m <sup>2</sup> )
20	1	24.09	4	40
120	1.3	14.17	3.20	47
250	1.5	12.73	3.48	69
400	1.5	8.43	3.36	71
600	1.5	3.30	2.40	122

**Table 3.14** Mortar properties considered constant with temperature [115].

$\rho$ (kg/m <sup>3</sup> )	$\nu$ (-)	$k$ (W/m/K)	$C_p$ (J/K)
2300	0.2	1.69	993

We introduce the heterogeneity of the mortar in the form of the arbitrary distribution of elastic modulus as in [114] presented in Figure 3.79. A turning band method is used with an isotropic correlation length  $\lambda = 0.02$  mm and a standard deviation of 10 %.

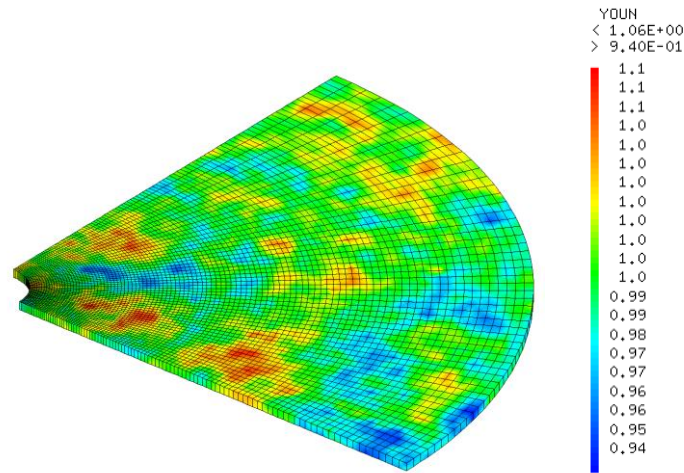


**Figure 3.79** Random distribution of Young's modulus.

### Polypropylene fiber

We present in Table 3.15 an evolution of density and Poisson's ratio of polypropylene with temperature. We consider an evolution of elastic modulus and coefficient of thermal expansion presented in Figures 3.26 and 3.27. Thermal conductivity and specific heat are 0.2 W/m/K and 1680 J/K [81], [83] respectively. While most of the data comes from literature, some of the hypothesis are considered in these simulations:

- Isotropic expansion of polypropylene fibers
- Phase change with temperature is not taken into account
- Density at 120 °C of 870 kg/m<sup>3</sup>
- Poisson's ratio is 0.45 and 0.49 (for an amorphous rubbery material) at 120 and 220 °C.

**Table 3.15** Evolution of density and Poisson's ratio of polypropylene with temperature [81].

T (°C)	$\rho$ (kg/m <sup>3</sup> )	$\nu$ (-)
20	910	0.42
120	870	0.45
250	850	0.49

### Modelled geometry

We present a mesh generated for calculations in Figure 3.80. A 3D mesh of the quarter of cylinder comprises a fiber in the center with a surrounding mortar of 1 mm radius. Height of the 3D mesh is 50  $\mu\text{m}$  and size of the mesh is a few  $\mu\text{m}$ .

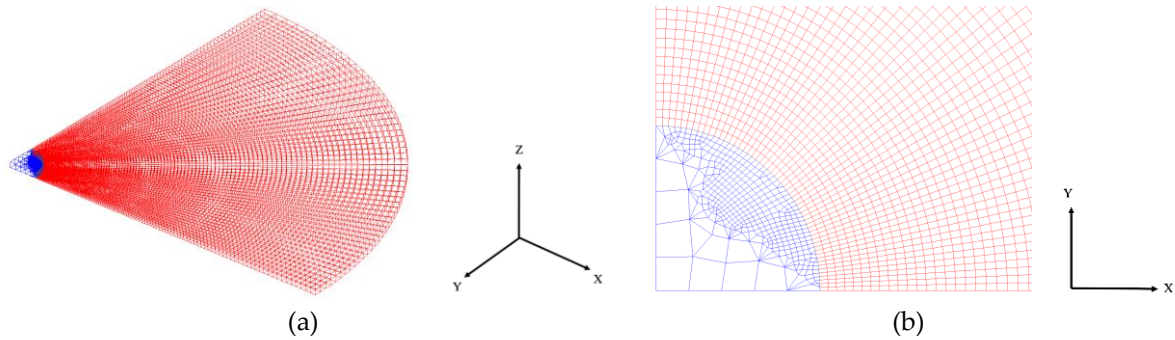


**Figure 3.80** View of the modelled mesh : a) 3D view- red is mortar, blue is polypropylene fiber, b) top view: mesh near polypropylene fiber-mortar interface is finer than the rest.

### Loading and boundary conditions

We apply self-weight of modelled geometry as a compressive load. In terms of mechanical boundary conditions, we impose symmetry in x- and y-axis and block the displacement in z-axis. These calculations do not correspond neither to plane stresses nor to plane strains. No transient thermal calculations are considered as temperature is imposed over the surface.

### Results

We present an evolution of damage of mortar around polypropylene fiber at different temperatures in Figure 3.81. The damage is 0 for an undamaged material (blue) and 1 for fully damaged (red). Images show that intensity and propagation of damage of mortar around polypropylene fiber increase with temperature. Evolution of the damage is controlled by incompatibility of coefficient of thermal expansion of polypropylene presented in Figure 3.27 and of mortar. First, no damage is observed at 20 °C. At 50 °C, a slight damage noted around polypropylene fiber is related to a mismatch of coefficient of thermal expansion of mortar and polypropylene. At this temperature, the values of  $\alpha$  are 15.3 and  $10.9 \times 10^{-6} / ^\circ\text{C}$  for polypropylene and mortar accordingly. The damage zone increases continuously for mortar until 115 °C and does not evolve until 155°C. At 155 °C, during start of phase transition, the values of coefficient of thermal expansion  $\alpha$  are 22.9 and  $13.8 \times 10^{-6} / ^\circ\text{C}$  for polypropylene and mortar respectively. During phase transition from semi crystalline to amorphous, material increases in its volume due to rearrangement of molecules. Once melted, polypropylene experiences shrinkage as can be seen in Figure 3.27. At 180 °C, the values of  $\alpha$  are 2.3 and  $15 \times 10^{-6} / ^\circ\text{C}$  for polypropylene and mortar accordingly. In our calculation, no evolution of damage zone occurs after the phase change of polypropylene despite this decrease.

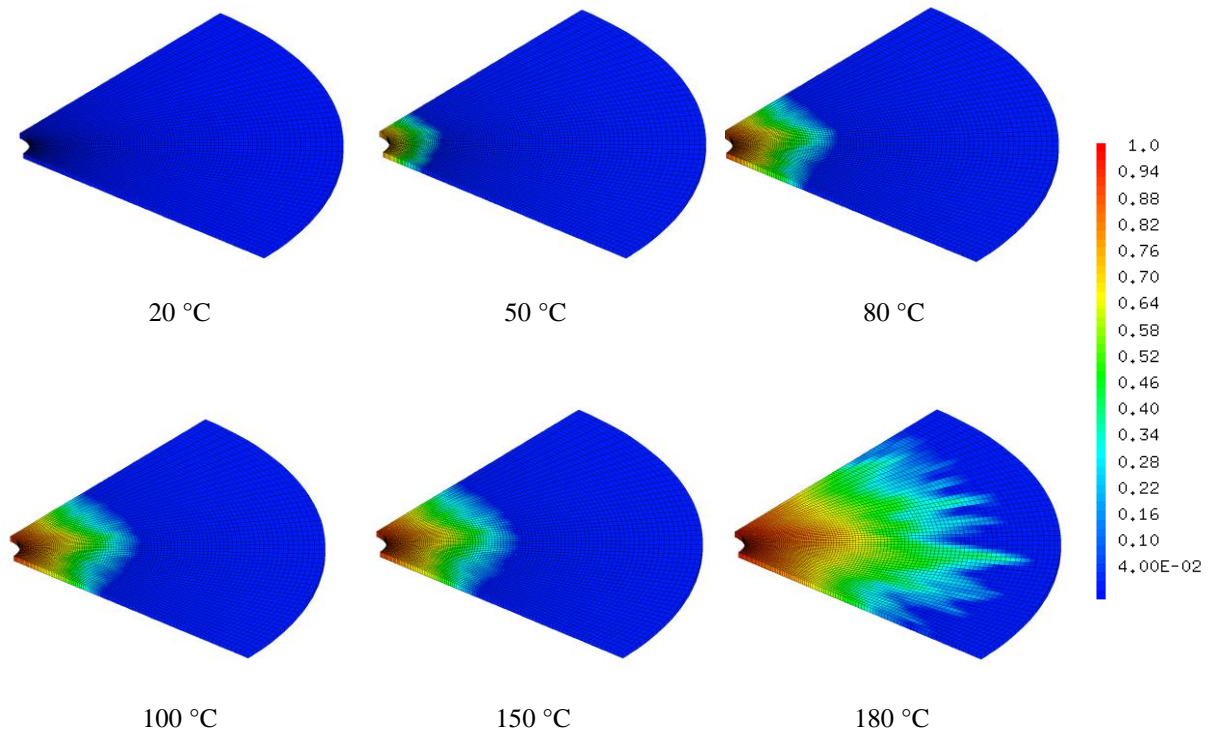


**Figure 3.81** Damage of mortar at different temperatures.

We plot in Figure 3.82 the evolution of the damage thickness (a measure of damage propagation) as a function of temperature for mortar containing 20 and 32  $\mu\text{m}$  diameter fiber. We note that increase of fiber diameter induces an increase of damage zone: thicker fibers tend to have larger damage zone than thinner ones. As damage localizes cracks, in this case, we would have some tangential cracks at fiber-matrix interface and some radial cracks around polypropylene fiber. As damage zone increases with size of fiber, so does the length of radial cracks. Some analogy of this result with another study on relationship between aggregate size and length of the cracks induced by shrinkage [119] can be drawn. In this study, increase of aggregate size has shown to increase the crack length. In both studies, our study and [119], a restraint of inclusion, either fiber or aggregate, by surrounding matrix causes cracks that increase with aggregate size despite differences in origin of these cracks (hydral or thermal).

It is interesting to note that damage zone propagates to several tens of  $\mu\text{m}$ , a result different from what has been reported in literature [85] (see Figure 3.33b). Our result shows a minor influence of radial cracks induced by thermal dilation of polypropylene fiber but images in Figure 3.33b seem to contradict this conclusion.

According to our simulations, these cracks develop before melting of polypropylene fibers; therefore, their influence should be observed on permeability. Our residual radial permeability

measurements of concrete at 150 °C agrees with findings in [65] and do not show a major increase of permeability as reported in [94], [95]. We can explain this by two possible reasons. First, these cracks are so small (order of few  $\mu\text{m}$ ) that during cooling phase of permeability test these cracks close. Since permeability test is residual and not performed at hot state, the influence of these cracks on intrinsic permeability at 150 °C cannot be observed. Second, we can expect at 150 °C for these cracks to be small and disconnected that they do modify local permeability but on global permeability, which results from combined action of empty fiber beds, thermally induced cracks around aggregates and cracks around fiber, is weak. At 200 °C, after melting of polypropylene, empty fiber beds along with cracks at the fiber-matrix interface serve to localize cracks due to thermal mismatch of aggregates and matrix, which contributes to increase of global permeability.

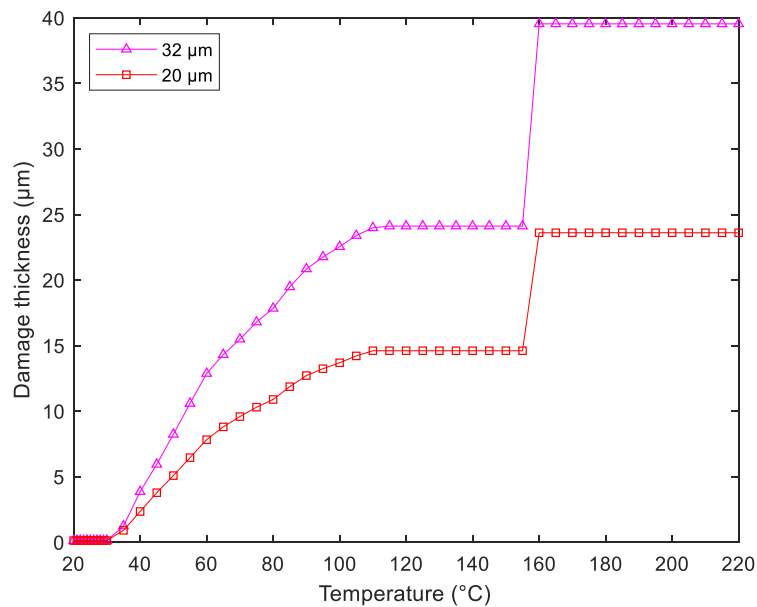


**Figure 3.82** Evolution of damage radius of mortar containing 32  $\mu\text{m}$  and 20  $\mu\text{m}$  fiber at different temperatures.

### 3.5.3 Mesoscale HT modelisation of cementitious materials

In this study, experimentally studied materials are simulated in 2D in order to investigate different cracking patterns under uniaxial loading of 5MPa.

## Material properties

We consider that cementitious composites are composed of cement paste and aggregates as opposed to mortar and aggregates. Considering mortar instead of cement paste would be wrong for a reason that it would suggest homogeneous material, which in fact is not true. We have therefore modelled the smallest size of 1 mm to represent these fine particles and to save computational time.

We present in Figure 3.83 an evolution of cement paste and aggregates properties with temperature such as elastic modulus, tensile strength, fracture energy and coefficient of thermal expansion. We consider tensile strength and fracture energy of aggregates to be constant and we fix the value of coefficient of Poisson for cement paste and aggregate to 0.2.

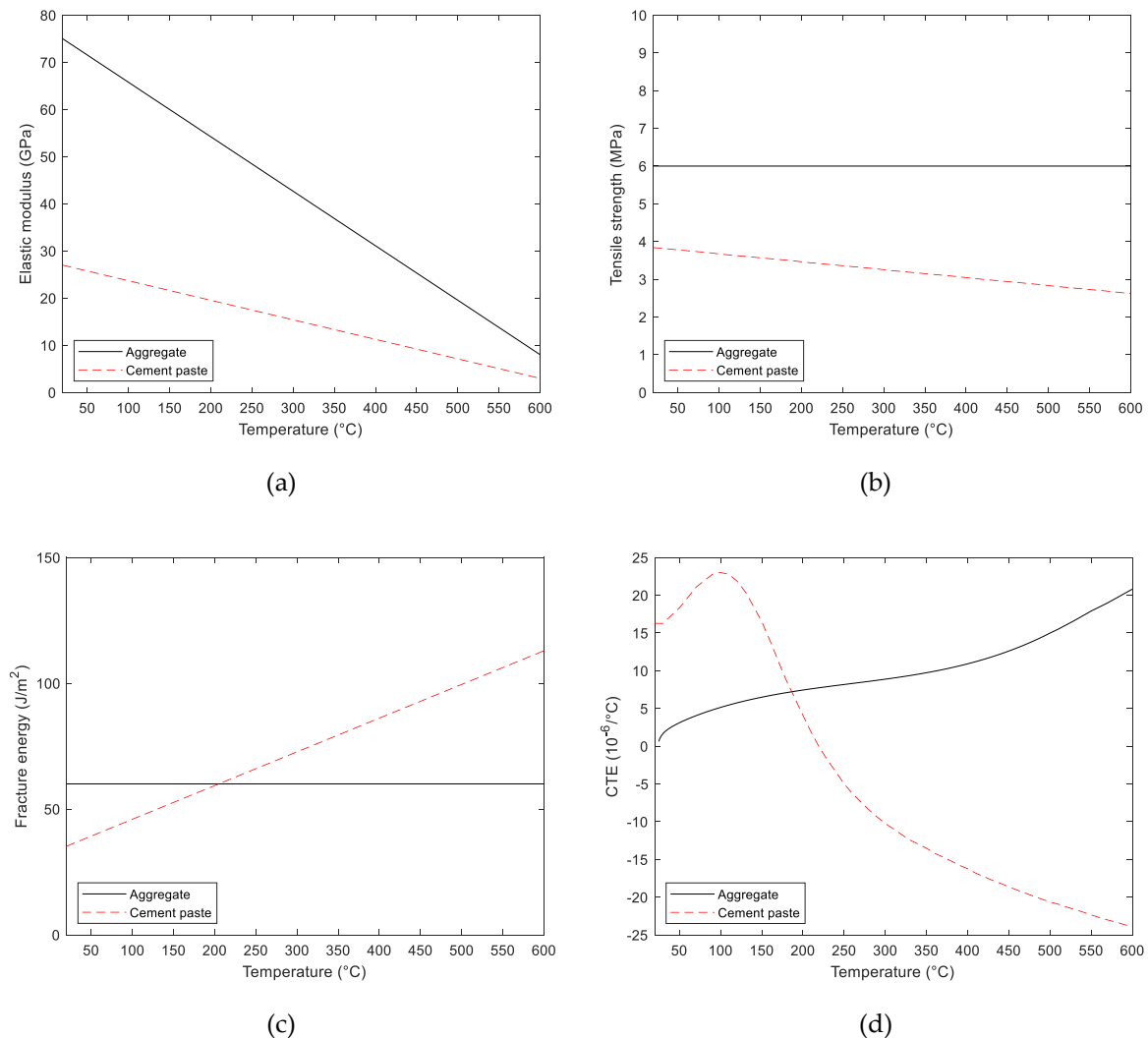


**Figure 3.83** Evolution of cement paste and aggregate properties with temperature: a) elastic modulus, b) tensile strength, c) fracture energy and d) coefficient of thermal expansion [11],[115],[116].

## Modelled materials

We model three cementitious materials presented in experimental study (mortar, concrete 1, concrete 2) and concrete with full granular skeleton for a sake of comparison of the influence of aggregate removal. Concrete with a full aggregate skeleton composed of 30 % sand 0/1 + 20 % gravel 4/10 + 50 % gravel 10/20 is obtained using Dreux- Gorisse method. In order to create a mesostructure, we use a draw of aggregates with an arbitrary placement described in details in [117], [118]. The draw consists of the following steps:

- Draw of X and Y coordinates of gravity centers of aggregates: from the largest to the smallest
- Each coordinate has an associated diameter, if crossing of an aggregate with existing ones occurs, a new draw for the aggregate is accomplished
- Selection between partial and full size of aggregates at the borders and corners for a realistic representation of mesostructure is possible.

In order to limit computational time while still having a representative granular skeleton for concrete, aggregates with a diameter smaller than 1 mm are not drawn. The validation of this approach is provided in [118]. We present in Table 3.16 and in Figure 3.84 a number of drawn aggregate classes with their mean diameter and volume fraction for mortar, concrete 1, concrete 2 and concrete with full skeleton.

**Table 3.16** Mean diameter  $D_{\text{mean}}$  and volume fraction  $\phi_{\text{gr}}$  of different aggregate classes for mortar, concrete 1, concrete 2 and concrete with full skeleton.

Class	Mortar		Concrete 1		Concrete 2		Concrete - full skeleton	
	$D_{\text{mean}}$ (mm)	$\phi_{\text{gr}}$ (%)	$D_{\text{mean}}$ (mm)	$\phi_{\text{gr}}$ (%)	$D_{\text{mean}}$ (mm)	$\phi_{\text{gr}}$ (%)	$D_{\text{mean}}$ (mm)	$\phi_{\text{gr}}$ (%)
1	0.25	19.20	1	39.36	1	39.36	1	29.50
2	0.5	73.60	1.4	0.64	1.4	0.64	1.4	0.48
3	1	5.60	6.3	21.05	14	24.68	2	0.52
4	1.4	1.60	7.1	4.68	20	35.32	4	1.56
5			10	34.27			5	3.53
6							6.3	4.14
7							7.1	2.21
8							10	7.64
9							14	20.45
10							20	26.55
11							22.4	2.85
12							28	0.55

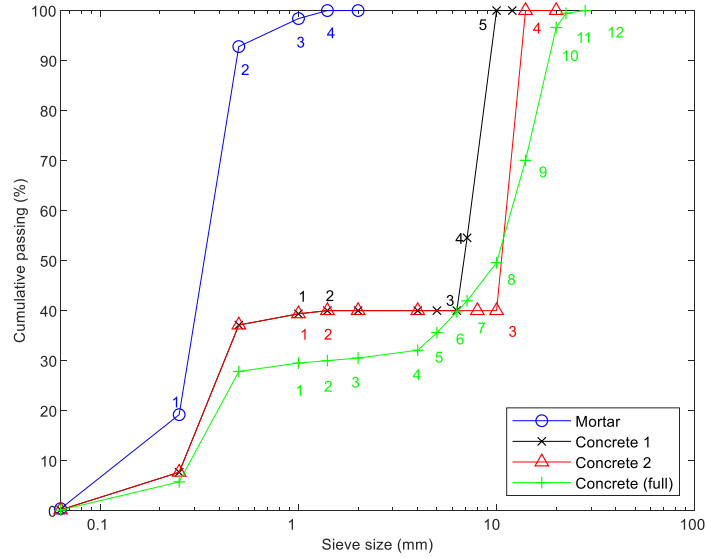


**Figure 3.84** Particle size distribution for materials modelled along with granular classes selected.

The size of the modelled structure is  $2 \times 2 \text{ cm}^2$  for mortar and  $10 \times 10 \text{ cm}^2$  for three concrete types. The size of the element is three times smaller the size of the smallest aggregate as advised by [117]. Then element size is 0.08 mm for cement paste (mortar) and 0.33 mm for concrete 1, concrete 2 and concrete with full skeleton.

We use a diffused method for mesh modelling described in [117], [118] for a simplified meshing. Parameter has value of 0 for cement paste (mortar) and 1 for aggregates. A visual representation of the application of this method is provided in Figure 3.85. Aggregates and cement paste share the same model, parameters are distributed across Gauss points of the mesh according to material.

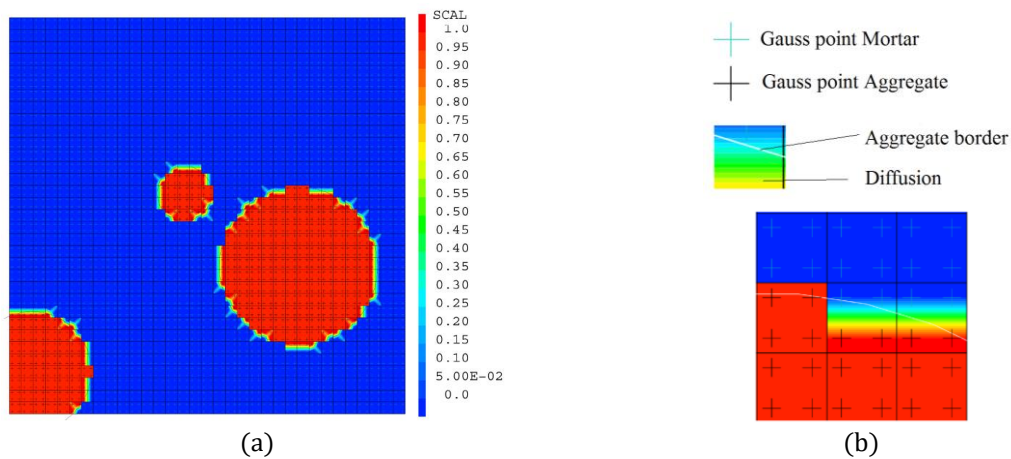


**Figure 3.85** Diffused mesh creation: a) Diffused mesh, b) Zoom on several elements [118].

We present in Figure 3.86 obtained geometries for mortar, concrete 1, concrete 2 and concrete with full skeleton using random draw of aggregates and diffused method.

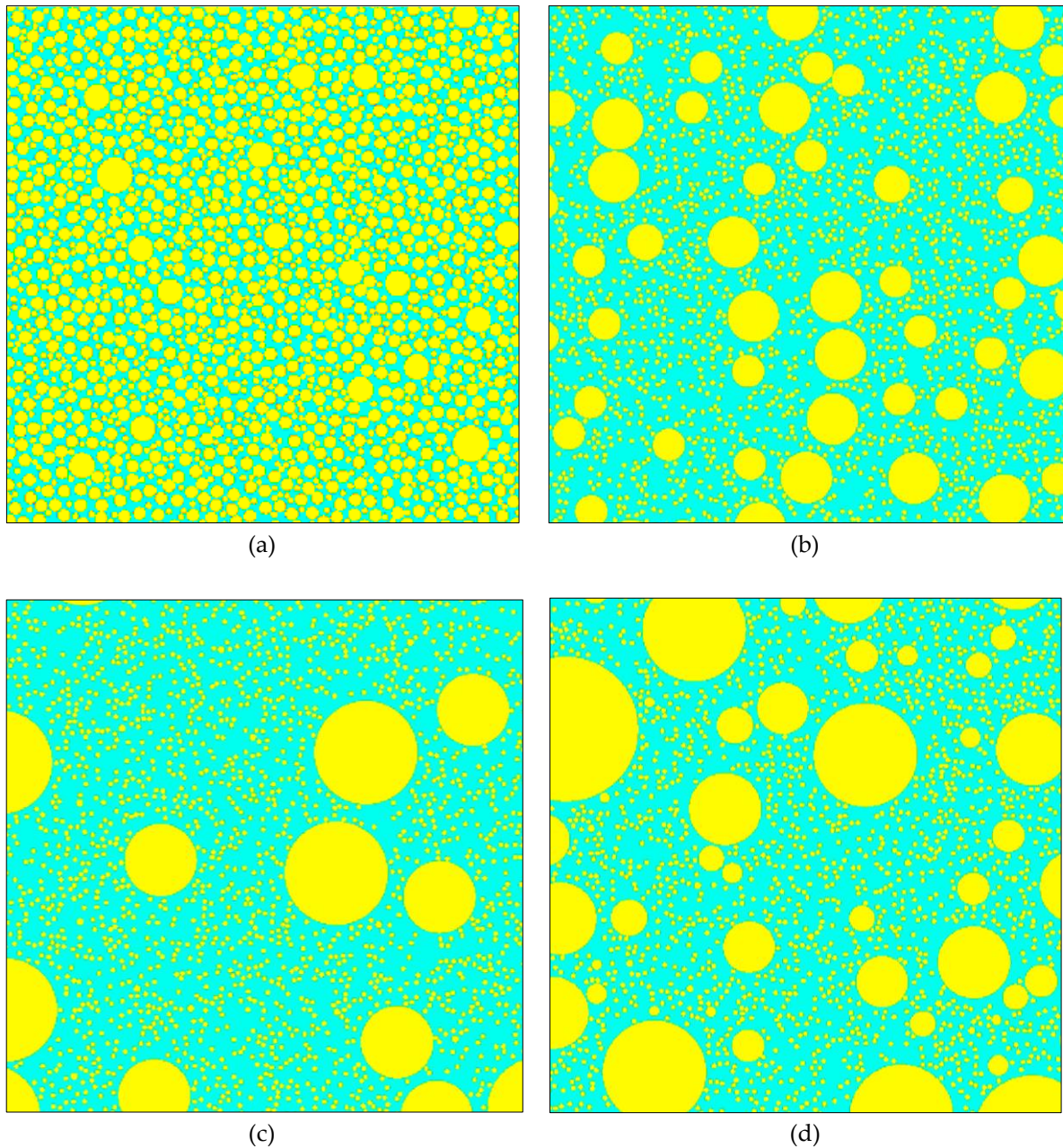


**Figure 3.86** Geometries modelled: a) mortar -  $2 \times 2 \text{ cm}^2$  (zoomed), b) concrete 1 -  $10 \times 10 \text{ cm}^2$ , c) concrete 2-  $10 \times 10 \text{ cm}^2$ , d) concrete with full granular skeleton -  $10 \times 10 \text{ cm}^2$ .

### Loading and boundary conditions

We present loading and boundary conditions used in our calculations in Figure 3.87. 2D plane stress computations are accomplished to limit the degrees of freedom. In terms of mechanical boundary conditions, symmetry in x- and y-axis is imposed. All the simulations are conducted

with a uniaxial compressive loading of 5 MPa in y-axis. Temperature is imposed over mesh, the effect of temperature gradient along the depth of the specimen is not taken into account.

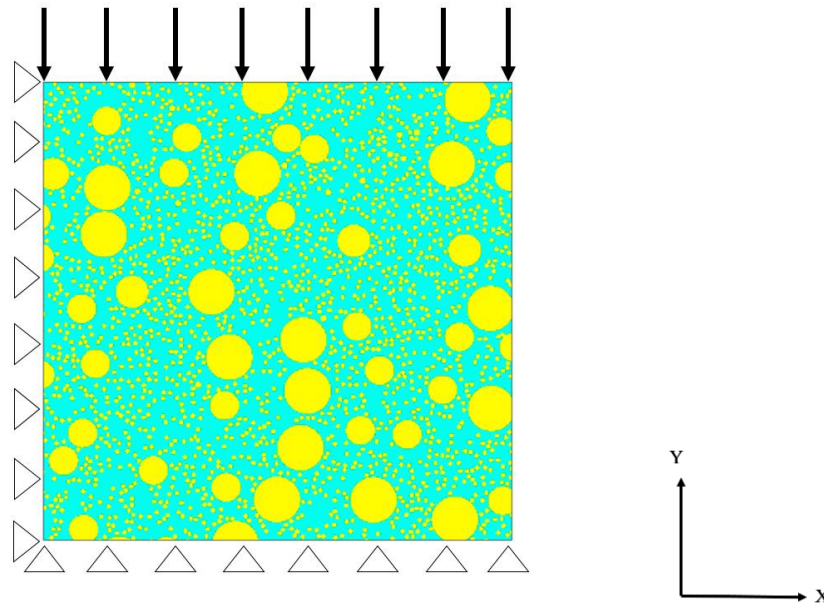


**Figure 3.87** Loading and boundary conditions.

## Results

We present images of damage at 150 and 350 °C for three materials studied experimentally (mortar, concrete 1 and concrete 2) and concrete with full granular skeleton in Figure 3.88. We shall remind in here that temperature is imposed over meshed surface. We have limited our simulation to 350 °C. It is important to remember that mortar has the largest aggregate size  $D_{\max}=1$  mm, while concrete 1, concrete 2 and concrete with full skeleton have  $D_{\max}$  of 10, 20 and 20 mm respectively. The images at 150 °C show that damage is localized around paste-aggregate interface (red color) due to their thermal mismatch for three concretes. It is however less evident in case of mortar since damage is diffused due to the absence of large aggregates. We note that 350 °C cement paste is completely damaged and aggregate damage appears in direction parallel to compressive loading.

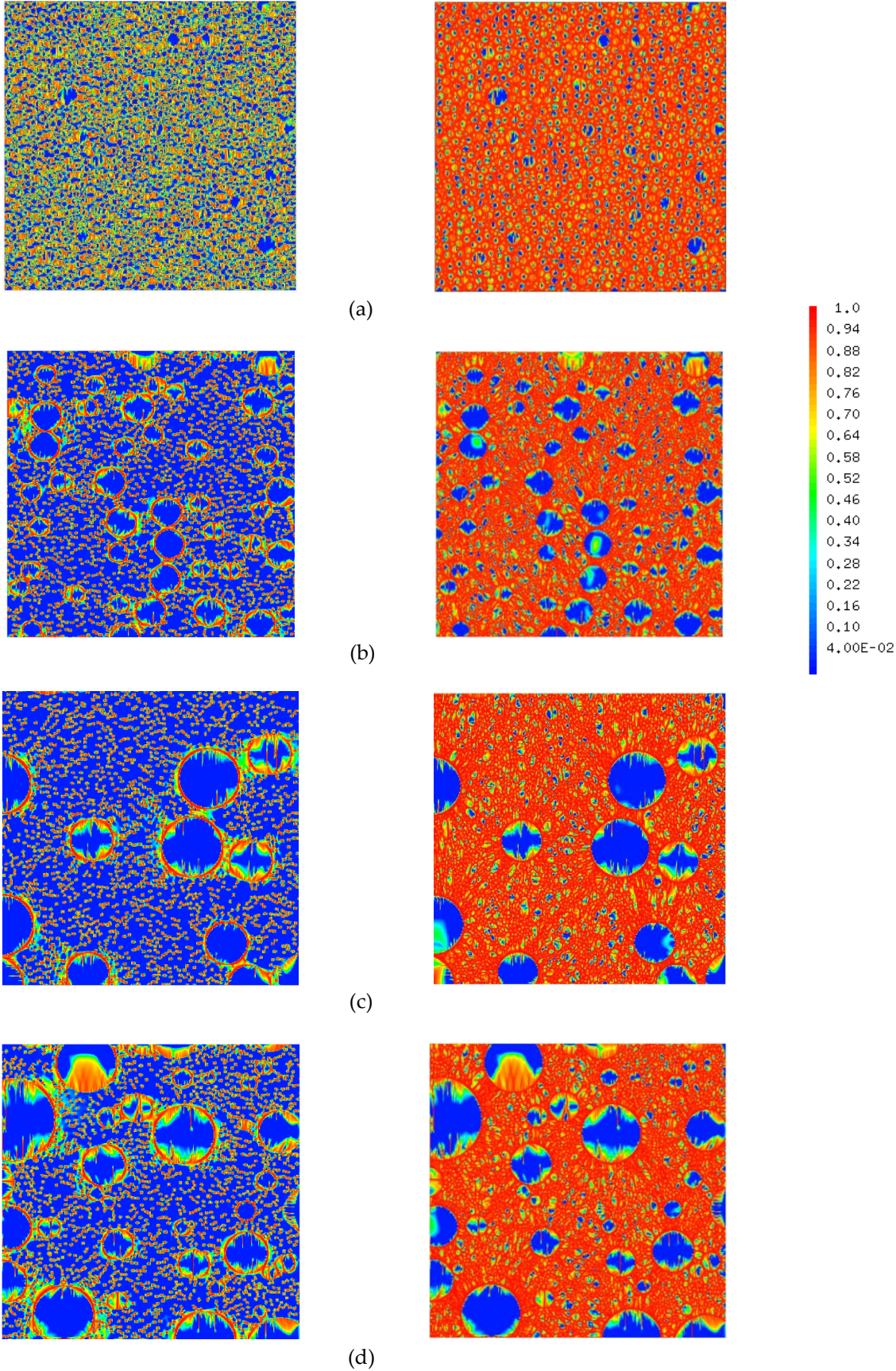
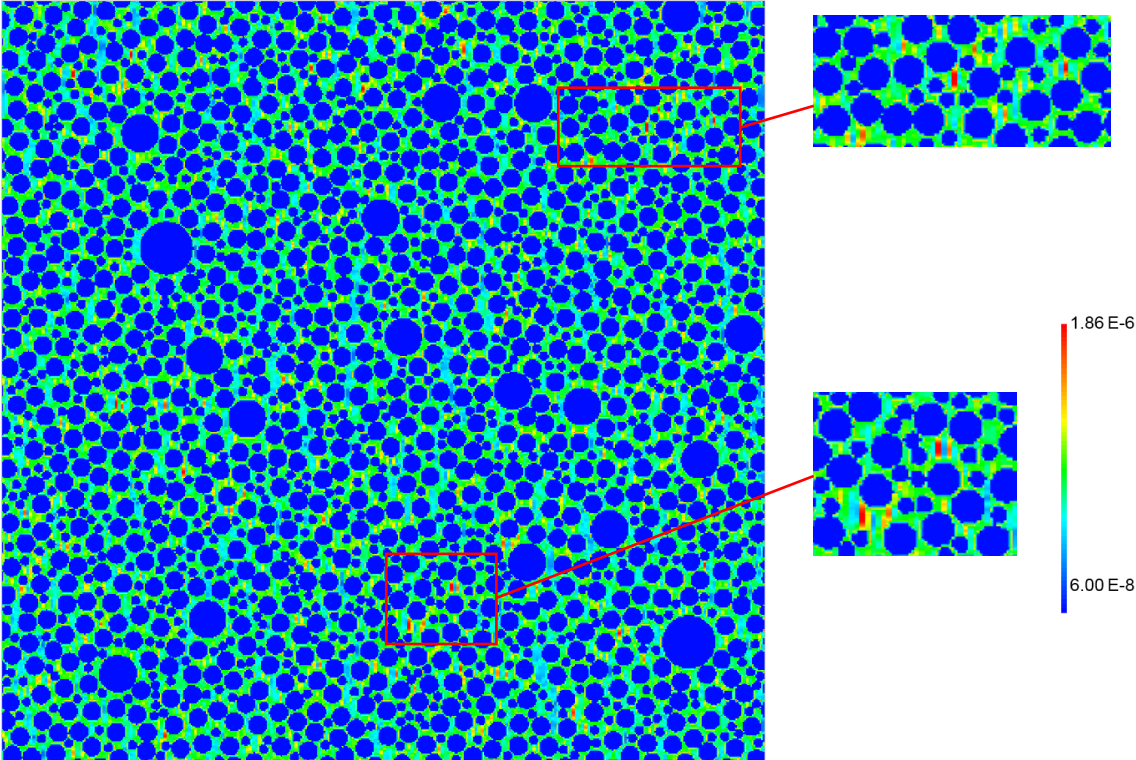
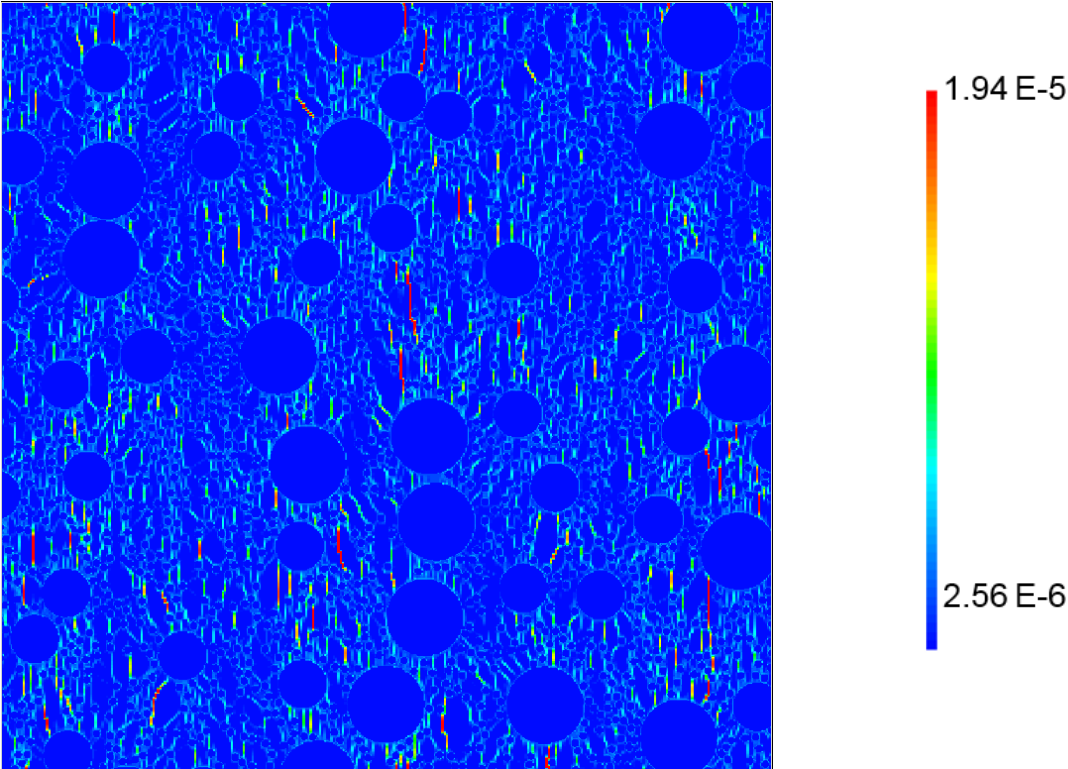


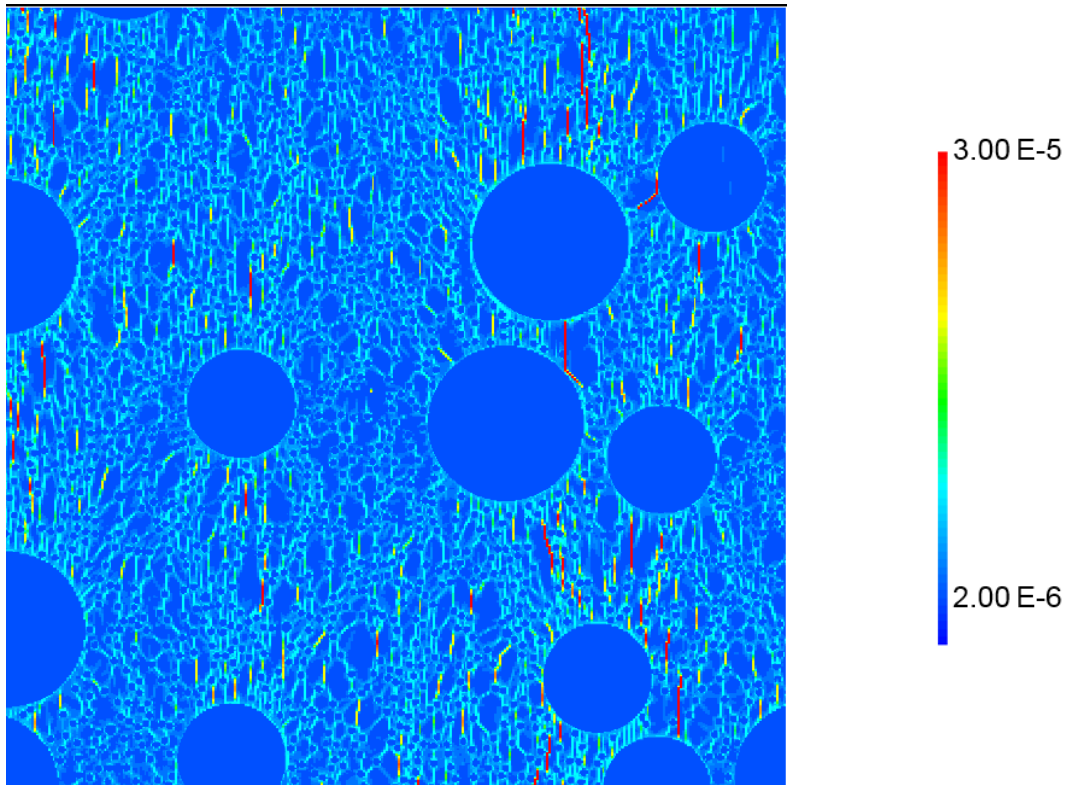
Figure 3.88 Damage field at 150 and 350 °C for: a) mortar (image zoomed), b) concrete 1, c) concrete 2 and d) concrete with full aggregate skeleton.



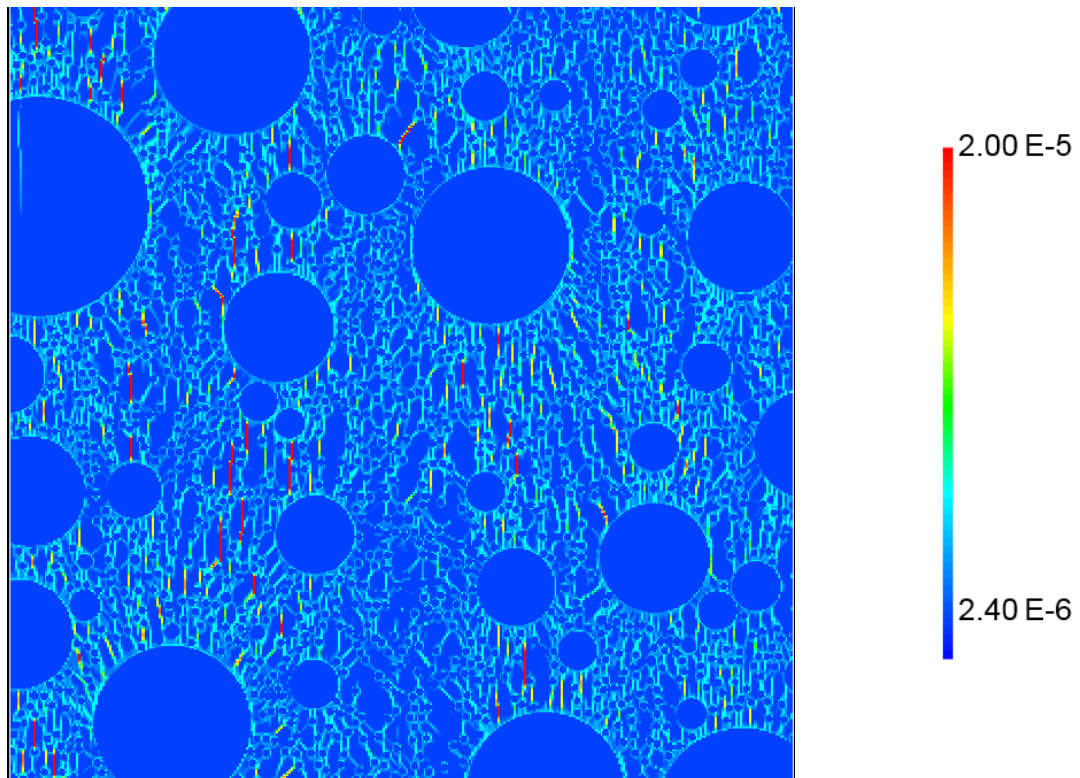
(a)



(b)



(c)



(d)

**Figure 3.89** Crack opening with values at 350 °C for: a) mortar (image zoomed), b) concrete 1, c) concrete 2 and d) concrete with full aggregate skeleton.

Crack opening is computed as described in [119] with a method, that takes into account the effects of non-linear thermal dilation. We present crack opening in x-direction obtained at 350 °C for materials modeled in Figure 3.89. As expected, cracks appear mostly in direction parallel to compressive loading. Overall, in terms of crack localization, cracks appear near the largest aggregates due to thermal mismatch of cement paste and aggregates. For mortar (Figure 3.89a), damage is diffused with a presence of network of very small microcracks.

We have used Fiji software in order to evaluate the distance between two adjacent cracks, which is taken as a minimum distance perpendicular to both cracks. The analysis of crack distance shows that for concrete 1 (Figure 3.89b) the average distance between cracks is  $1.3 \pm 0.5$  cm while for concrete 2 (Figure 3.89c) its value is  $1.9 \pm 1.3$  cm. In terms of crack opening, the results of simulations show that crack opening for concrete 2 is larger than for concrete 1.

We have studied the influence of continuity of granular curve on example of concrete 2 (40 % sand 0/1+ 60 % gravel 14/20) and concrete with full skeleton (30 % sand 0/1 + 20 % gravel 4/10 + 50 % gravel 10/20). We shall add here that for concrete 2, due to screening and sieving of aggregates the largest aggregates, present for concrete with full skeleton, do not appear. Results of this study presented in Figure 3.89c and Figure 3.89d show that concrete 2 with discontinuous granular curve has cracks with larger opening that more distanced from one another than in case of concrete with full skeleton. In fact, the distance between cracks has shown that for concrete with full skeleton its value is 1.5 cm (standard deviation 0.6 cm) which is lower than that for concrete 2. This can be explained by the difference in granulometric curve of two concretes. Concrete 2 has a different cracking compared to concrete with complete granular skeleton, which shows, that not only the largest size of aggregates but granular curve as well have the influence on crack localisation.

The results show that granular skeleton governs cracking patterns of cementitious materials. Since fibers are used to percolate these thermally induced cracks, the choice of fibers should be accomplished in accordance with granular skeleton. Therefore, optimal fiber length should increase with the largest aggregate size. The results also show that in real concrete optimal fiber length could be shorter than what is found in concrete with discontinuous curve.

We have considered some issues that could be addressed in order to improve the calculation:

- 3D simulations with thermal gradient are required. These thermal gradients are important in generating stresses that would allow a better localization of cracks;
- Ideally, 3D calculations with addition of polypropylene fibers to compute percolation of fibers and cracking is necessary, however, such computations require a high number of elements due to a small diameter of fibers. For example, for 32  $\mu\text{m}$  fibers it would

require to have an element size of 10  $\mu\text{m}$ , which would result in total of  $10^{10}$  elements for mesh of size 10 x 10  $\text{cm}^2$ ;

- In any numerical model, the issue of sensitivity to input parameters such as mechanical properties (e.g. fracture energy) is a crucial aspect. Assumptions on these parameters may have a significant impact on the quantification of effects at high temperature. Even though, quantification of the results was not an objective of these simulations, in ideal case, it is required to input parameters obtained experimentally and validate the numerical model on the macroscopic level.

Despite the fact that simulations are conducted in 2D and that further improvement are to be considered, evident differences between three materials could be observed and valuable conclusions on optimal fiber choice could be drawn.

### 3.5.4 Conclusions of the numerical study

In this part of the chapter, numerical simulations of two different fibers are accomplished. First, the influence of fiber expansion on damage of mortars at high temperature is investigated. It has been found that thermal strains produced by differential expansion of fiber and mortar can cause damage of mortar and that damage zone thickness increases with fiber diameter. However, the influence of this damage and its increase with fiber diameter can be considered negligible as these cracks being disconnected, slightly affecting local permeability and not increasing global permeability as observed from permeability test.

In the second part, 2D mesoscale thermo-mechanical simulations are accomplished on four different materials: mortar, concrete 1, concrete 2 and concrete with full granular skeleton in order to study the influence of aggregate size and granular curve on damage and cracks at high temperature. For mortar, we observe diffused damage, while for three concretes damage is localized at the interface of matrix-aggregate due to thermal mismatch. We see that cracks are more distant and more open for concrete 2 than for concrete 1. From comparison of the influence of distribution curve on example of concrete 2 and concrete with full skeleton, we see that for discontinuous granular curve with a higher volume of larger aggregates cracks are less distant and less open than for concrete with full aggregate curve and smaller volume of larger aggregates. Presented results show an importance of aggregate size and granular curve in terms of cracking of cementitious materials at high temperature and provide some basis for future development of this calculation in 3D (thermal gradients, percolation with polypropylene fibers, etc). The results outline the influence of granular skeleton on localization of cracks and suggest that optimal fiber length to connect these cracks should depend on granular skeleton.

### 3.6 Conclusions

This chapter is a contribution to optimization of choice of polypropylene fibers for reduction of spalling of cementitious materials. We have conducted fire tests and residual radial permeability tests for three different materials with different skeletons (mortar, concrete 1 and concrete 2) in order to optimize choice of fiber geometry and dosage. Alongside, we have completed thermo-mechanical simulations in Cast3m in order to study: a) damage due to expansion of fibers, b) cracking patterns of materials with different granular curves.

The results of both studies have allowed concluding on several important points:

- Addition of polypropylene fibers and increase of polypropylene fiber dosage leads to increase of intrinsic permeability and decrease of mean spalling depth.
- We have found that fiber length should be selected in accordance with aggregate size. As fibers are used to bridge thermally induced cracks, their length should increase with size of the largest aggregate. The distance between cracks observed from experiments and simulations are found to increase with aggregate size. For mortar ( $D_{\max}=1$  mm), the damage is diffused. Cracks are more open and spaced for concrete 2 ( $D_{\max}=20$  mm) than for concrete 1 ( $D_{\max}=10$  mm). For mortar and concrete 1, the optimized fiber lengths are 12 and 18 mm at dosages 1 and 0.5 kg/m<sup>3</sup> respectively. For concrete 2, despite spalling the least of all, an optimal fiber length is not identified and longer fiber lengths should be tested.
- At same number of fibers, 20  $\mu\text{m}$  fibers produce lower increase in permeability due to higher bending of fibers that reduces percolation probability. Diameter of fibers (comparison between 20 and 32  $\mu\text{m}$ ) has found to have no significant influence on spalling when compared at same number. However, at same dosage, 20  $\mu\text{m}$  fibers are advisable due to their higher count that results in higher increase of permeability and decrease of spalling.
- Mismatch of thermal expansion of polypropylene fibers and matrix can cause damage and crack development at the interface of fiber-matrix before melting of polypropylene. The damage zone thickness is found to evolve with diameter of fiber. However, cracks at the interface paste-fiber are so small and disconnected that their contribution to global permeability is negligible.
- Curing conditions have a significant influence on spalling. Mean spalling depth for samples cured in air-condition is lower than for samples cured in water due to formation of drying front and lower moisture content.

- Fire test results cannot be explained by permeability measurements only due to modification of permeability during fire test related to opening and growth of cracks parallel to direction of loading and closing of cracks perpendicular to loading direction.

It is important to remind that conclusions on choice of fibers from this chapter are relevant to materials with a certain composition (cement CEM III/A, calcareous aggregates, etc.), curing conditions (in water), mechanical strength (high strength) and tested under uniaxial compressive loading of 5 MPa.

### 3.7 Reference list

- [1] Moranville-Regourd M. (1990). Microstructure des bétons à hautes performances. Presse de l'Ecole Nationale des Ponts et Chaussées.
- [2] Feldman R.F. and Sereda P.J. (1968). The model for hydrated Portland cement as deduced from sorption-length change and mechanical properties. *Materials and Construction* 1 : 509-520.
- [3] Regourd M. (1982). L'eau, dans *Le béton hydraulique*. Presse de l'Ecole Nationales des Ponts et Chaussées : 59-68.
- [4] Bessaies-Bey H. (2015). Polymères et propriétés rhéologiques d'une pâte de ciment : une approche physique générique. PhD Thesis. Université Paris Est.
- [5] Baroghel-Bouny V. (1994). Caractérisation des pâtes de ciment et des bétons. Méthodes, analyse, interprétation. PhD Thesis. Ecole Nationale des Ponts et Chaussées.
- [6] Ecole Polytechnique Fédérale de Lausanne. (2010). Hydration of Cement. Lecture notes.
- [7] Khoury G.A. (1992). Compressive strength of concrete at high temperatures: a reassessment. *Magazine of Concrete Research* 44: 291-309.
- [8] Castellote M., Alonso C., Andrade C., Turillas X. and Campo J. (2004). Composition and microstructural changes of cement pastes upon heating, as studied by neutron diffraction. *Cement and Concrete Research* 34(9): 1633-1644.
- [9] Bažant Z.P. and Kaplan M.F. (1996). *Concrete at High Temperatures: Material Properties and Mathematical Models*. Pearson Education.
- [10] Khoury G.A., Sullivan P.J.E. and Grainger B.N. (1986). Strain of concrete during first cooling from 600 °C under load. *Magazine of Concrete Research* 38 : 195-215.
- [11] Hager G.I. (2004). Comportement à haute température des bétons à hautes performances -évolution des principales propriétés mécaniques. PhD Thesis. Ecole nationale des ponts et chaussées et l'école polytechnique de Cracovie.
- [12] Schneider U. (1982). *Verhalten von Beton bei hohen Temperaturen* Deutscher Ausschuss für Stahlbeton, ed., Ernst & Sohn.
- [13] Razafinjato R.N. (2015). Comportement des bétons à haute température : Influence de la nature du granulats. PhD Thesis. Université de Cergy Pontoise.
- [14] Mindeguia J.-C., Pimienta P., Carré H. and La Borderie C. (2013). Experimental analysis of concrete spalling due to fire exposure. *European Journal of Environmental and Civil Engineering* 17: 453-466.
- [15] Hattema M.H.H. (1996). The thermo-mechanical behaviour of sedimentary rock: an experimental study. PhD Thesis. TU Delft.

- [16] Mindeguia J.-C. (2009). Contribution expérimentale à la compréhension des risques d'instabilité thermique des bétons. Thèse de doctorat, Université de Pau et des Pays de l'Adour.
- [17] Xing Z., Beaucour A.-L., Hebert R., Noumowé A. and Ledesert B. (2011). Influence of the nature of aggregates on the behaviour of concrete subjected to elevated temperature. *Cement and Concrete Research* 41: 392-402.
- [18] Darcy H. (1856). *Les fontaines publiques de la ville de Dijon L. des C. imperiaux des ponts et chaussées et des mines Paris. (ed.) Dalmont.*
- [19] Lion M. (2004). Influence de la température sur le comportement poromécanique ou hydraulique d'une roche carbonatée et d'un mortier. Etudes expérimentales. PhD Thesis. Université des sciences et des technologies de Lille.
- [20] Choinska M. (2006). Effets de la température, du chargement mécanique et de leurs interactions sur la perméabilité du béton de structure. PhD Thesis. École Centrale de Nantes et l'Université de Nantes.
- [21] Sutherland W. (1893). LII. The viscosity of gases and molecular force. *Philosophical Magazine Series 5*: 507-531.
- [22] Klinkenberg L.J. (1941). The Permeability Of Porous Media To Liquids And Gases. *API-41-200.*
- [23] Picandet V. (2001). Influence d'un endommagement mécanique sur la perméabilité et sur la diffusivité hydrique des bétons. PhD Thesis. Ecole Centrale de Nantes.
- [24] Tsimbrovska M. (1998). Dégradation des bétons à hautes performances soumis à des températures élevées : Evolution de la perméabilité en liaison avec la microstructure. PhD Thesis. Université Joseph Fourier Grenoble 1.
- [25] Miah Md. J., Kallel H., Carré H., Pimienta P. and La Borderie Christian. (2019). The effect of compressive loading on the residual gas permeability of concrete. *Construction and Building Materials* 217 :12-19.
- [26] Irex. (2005). Synthèse des travaux du projet national BHP2000 sur les bétons à hautes performance. Presses de l'Ecole Nationale des Ponts et Chaussées.
- [27] Kanema M., de Morais M. V. G., Noumowé A., Gallias J.L. and Cabrillac R. (2007). Experimental and numerical studies of thermo-hydrous transfers in concrete exposed to high temperature. *Heat and Mass Transfer* 44(2): 149-164.
- [28] Lion M., Skoczylas F., Lafhaj Z. and Sersar M. (2005). Experimental study on a mortar. Temperature effects on porosity and permeability. Residual properties or measurements under temperature. *Cement and Concrete Research* (35): 1937– 1942.
- [29] Li Y., Tan K.H. and Yang E.-H. (2018). Influence of aggregate size and inclusion of polypropylene and steel fibers on the hot permeability of ultra-high performance concrete (UHPC) at elevated temperature. *Construction and Building Materials* 169:629-637.
- [30] Choinska M., Khelidj A., Chatzigeorgiou G. et Pijaudier-Cabot G. (2007). Effects and interactions of temperature and stress-level related damage on permeability of concrete. *Cement and Concrete Research* 37(1): 79-88.
- [31] Gary M. (1916). Fire tests on reinforced concrete buildings. Verlag WillielmEmst und Sohn. Heft 11. Germany.
- [32] Tunnel sous la Manche: 20 ans après, plus peurs que de mal. [https://www.rtf.be/info/monde/detail\\_tunnel-sous-la-manche-20-ans-apres-plus-de-peurs-que-de-mal?id=8260426](https://www.rtf.be/info/monde/detail_tunnel-sous-la-manche-20-ans-apres-plus-de-peurs-que-de-mal?id=8260426)
- [33] Devastating Distasters. <https://devastatingdisasters.com/the-mont-blanc-tunnel-fire-1954/>

- [34] McNamee R.(2019). Fire spalling theories-Realistic and more exotic ones. Proceedings of the 6th International Workshop on Concrete Spalling. Sheffield, UK.
- [35] Sjöström J., Lange D., Jansson McNamee R. and Boström L. (2017). Anisotropic Curvature and Damage of Unbonded Post-tensioned Concrete Slabs during Fire Testing. *Fire Technology* 53: 1333–1351.
- [36] Bažant Z.P. (1997). Analysis of pore pressure, thermal stresses and fracture in rapidly heated concrete. Proceedings of International Workshop on Fire Performance of High-Strength Concrete. Gaithersburg, USA.
- [37] Khoury G.A. (2008). Concrete spalling assessment methodologies and polypropylene fibre toxicity analysis in tunnel fires. *Structural Concrete* 9: 11-18.
- [38] Harmathy T. Z. (1964). Moisture in materials in relation to fire test. ASTM. Special Technical Publication 385: 74-95.
- [39] Anderberg Y. (1997). Spalling phenomena of HPC and OC, International Workshop on fire performance of high-strength concrete. NIST, Gaithersburg MD.
- [40] Kalifa P., Chéné G. et Gallé C. (2001). High-temperature behaviour of HPC with polypropylene fibres: From spalling to microstructure. *Cement and Concrete Research* 31(10): 1487-1499.
- [41] Kalifa P. et Menneteau F.-D. (1999). Mesures de pression, température et perte en masse dans les bétons à hautes températures. CSTB.
- [42] Lankard D. R., Birkimer D. L., Fondriest F.F. et Snyder M.J. (1971). Effects of moisture content on the structural properties of Portland cement concrete exposed to temperatures up to 500 F. 21st ACI Fall Meeting. Memphis, Tennessee.
- [43] Jansson R. and Boström L.(2009). The Influence of Pressure in the Pore System on Fire Spalling of Concrete. *Fire Technology* 46.
- [44] Felicetti R., Lo Monte F. and Pimienta P. (2017). A new test method to study the influence of pore pressure on fracture behaviour of concrete during heating. *Cement and Concrete Research* 94:13-23.
- [45] Miah M.J. (2017).The Effect of Compressive Loading and Cement Type on the Fire Spalling Behaviour of Concrete. PhD Thesis. Université de Pau et des Pays de l'Adour.
- [46] Boström L. and Jansson, R. (2008). Self-compacting concrete exposed to fire SP Report. SP, Borås, Sweden.
- [47] Phan L.T and Carino N.J. (2002). Effects of Test Conditions and Mixture Proportions on Behavior of High-Strength Concrete Exposed to High Temperatures. *ACI Materials Journal* 99: 54–66.
- [48] Rivaz B. (2006). Technical performance of reinforced concrete with steel fibers and polymers, *Tunnels et Ouvrages Souterrains* 198:367–371.
- [49] Chen B. and Liu J. (2004). Residual strength of hybrid-fiber-reinforced high-strength concrete after exposure to high temperatures. *Cement and Concrete Research* 34:1065–1069.
- [50] Bilodeau A., Kodur V.K.R and Hoff G.C. (2004). Optimization of the type and amount of polypropylene fibres for preventing the spalling of lightweight concrete subjected to hydrocarbon fire. *Cement and Concrete Composites* 26: 163- 174.
- [51] Han C.-C., Hwang Y.-S., Yang S.-H. and Gowripalan N. (2005). Performance of spalling resistance of high performance concrete with polypropylene fiber contents and lateral confinement. *Cement and Concrete Research* 35: 1747- 1753.
- [52] Shuttleworth P. (2001). Fire protection of precast concrete tunnel linings on the Channel Tunnel Rail Link. *Concrete* 35(4): 12-22.

- [53] Chan Y. N., Peng G. F. and Anson M. (1999). Fire Behavior of High-Performance Concrete Made with Silica Concrete Fume at Various Moisture Contents. *ACI Materials Journal* 96: 405–9.
- [54] Horvath J., Hertel C., Dehn F. et Schneider U. (2004). Einfluß der Vorlagerung auf das Temperaturverhalten von selbstverdichtendem Beton. *Beton-und Stahlbetonbau* 99(10): 813-815.
- [55] Taillefer N., Pimienta P. and Dhima D. (2013). Spalling of concrete: A synthesis of experimental tests on slabs. *Proceedings of the 3rd International Workshop on Concrete Spalling*. Paris, France.
- [56] Mindeguia J.-C., Pimienta P., Carré H. and La Borderie C. (2015). Experimental discussion on the mechanisms behind the fire spalling of concrete. *Fire and Materials* 39: 619-635.
- [57] Choe G., Kim G., Yoon M., Hwang E., Nam J., Guncunski N. (2019). Effect of moisture migration and water vapor pressure build-up with the heating rate on concrete spalling type. *Cement and Concrete Research* 116: 1-10.
- [58] Jansson, R. (2004). *Material Properties Related to Fire Spalling of Concrete*. PhD Thesis. Lund Institute of Technology.
- [59] Kanéma M. (2007). *Influence des paramètres de formulation sur le comportement à haute température des bétons*. PhD Thesis. Université de Cergy Pontoise.
- [60] Klimek A., Hothan S. and Rogge A. (2019). Investigation of size effects in concrete spalling. *Proceedings of the 6th International Workshop on Concrete Spalling*. Sheffield, UK.
- [61] Jansson R. and Boström L. (2013). Factors Influencing Fire Spalling of Self Compacting Concrete. *Materials and Structures* 46: 1683-1694.
- [62] Boström L., Wickström U. and Adl-Zarrabi B. (2007). Effect of Specimen Size and Loading Conditions on Spalling of Concrete. *Fire and Materials* 31: 173-186.
- [63] Kodur V. K. R. and Phan L. (2007). Critical Factors Governing the Fire Performance of High Strength Concrete Systems. *Fire Safety Journal* 42: 482-488.
- [64] Carré H., Pimienta P. La Borderie C., Pereira F. and Mindeguia J.-C. (2013). Effect of compressive loading on the risk of spalling. *Proceedings of the 3rd International Workshop on Concrete Spalling*. Paris, France.
- [65] Hager I. and Mroz K. (2019). Role of Polypropylene Fibres in Concrete Spalling Risk Mitigation in Fire and Test Methods of Fibres Effectiveness Evaluation. *Materials* 12: 1-20.
- [66] Hertz K.D. (1992). Danish investigations on silica fume concretes at elevated temperatures, *ACI Materials Journal* 89: 345–347.
- [67] Ali F. A., O'Connor D. and Abu-Tair A. (2001). Explosive spalling of high-strength concrete columns in fire. *Magazine of Concrete Research* 53: 197-204.
- [68] Noumowé A., Carré H., Daoud A. and Toutanji H. (2006). High-Strength Self-Compacting Concrete Exposed to Fire Test. *Journal of Materials in Civil Engineering* 18: 754-758.
- [69] Yan X., Li H. and Wong Y.L. (2007). Effect of aggregate on high-strength concrete in fire. *Magazine of Concrete Research* 59: 323–328.
- [70] Heo Y.-S., Sanjayan J.G., Han C-G. and Han M.-C. (2012). Limited effect of diameter of fibres on spalling protection of concrete in fire. *Materials and Structures* 45: 325- 335.
- [71] Heo Y.-S., Sanjayan J.G., Han C-G. and Han M.-C. (2012). Relationship between inter-aggregate spacing and the optimum fiber length for spalling protection of concrete in fire. *Cement and Concrete Research* 42: 549-557.
- [72] Knack I. (2011). The use of pp fibers in tunnel construction to avoid explosive concrete spalling in case of fire. New test results for the clarification of the mode of action. *Proceedings of the 2nd International Workshop on Concrete Spalling due to Fire Exposure*. Delft, the Netherlands.

- [73] Pliya B.A.P. (2010). Contribution des fibres de polypropylène et métalliques à l'amélioration du comportement du béton soumis à une température élevée. Thèse de doctorat, Université de Cergy-Pontoise.
- [74] Bangi M.R., Fukuda D. and Horiguchi T. (2009). Effect of heating rate on pore pressure spalling of fibre-reinforced high strength concrete subjected to high temperatures. Proceedings of 1<sup>st</sup> International Workshop on Concrete Spalling due to Fire Exposure. Leipzig, Germany.
- [75] Yermak N., Pliya P., Beaucour A.-L. and Noumowé A. (2017). Influence of steel and/or polypropylene fibres on the behaviour of concrete at high temperature: Spalling, transfer and mechanical properties. *Construction and Building Materials* 132: 240-250.
- [76] Bangi M.R. and Horiguchi T. (2012). Effect of fibre type and geometry on maximum pore pressures in fibre-reinforced high strength concrete at elevated temperatures. *Cement and Concrete Research* 42: 459-466.
- [77] Liu J.-C. and Tan K.H. (2018). Mechanism of PVA fibers in mitigating explosive spalling of engineered cementitious composite at elevated temperature. *Cement and Concrete Composites* 93:235-245.
- [78] Heo Y.-S., Sanjayan J.G., Han C.-G. and Han M.-C. (2011). Critical parameters of nylon and other fibres for spalling protection of high strength concrete in fire. *Materials and Structures* 44: 599-610.
- [79] Li Y. Tan K.H. and Yang E.-H. (2019). Synergistic effects of hybrid polypropylene and steel fibers on explosive spalling prevention of ultra-high performance concrete at elevated temperature. *Cement and Concrete Composites* 96: 174-181.
- [80] Malpass D.B. and Band E.I. (2012). Introduction to Industrial Polypropylene: Properties, Catalysts, Processes. Scrivener Publishing LLC.
- [81] Khoury G.A. and Willoughby B. (2008). Polypropylene fibres in heated concrete. Part I: Molecular structure and materials behaviour. *Magazine of Concrete Research* 60 (2): 125-136.
- [82] Maier C. and Calafut T. (1998). Polypropylene: The Definitive User's Guide and Databook. William Andrew.
- [83] Tripathi D. (2002). Practical Guide to Polypropylene. iSmithers Rapra Publishing.
- [84] Mears P. (1965). Polymers: Structure and Bulk Properties. Van Nostrand. London.
- [85] Zhang D., Dasari A., Tan K.H. (2018). On the mechanism of prevention of explosive spalling in ultra-high performance concrete with polymer fibers. *Cement and Concrete Research* 113:169-177.
- [86] Kanapitsas A., Tsonos C., Pandis C., Pissis P., Kontou E., Mamunya Y.P., Lebedev E.V. and Delides C.G. (2006). PTC Effect and Structure of Polymer Composites Based on Polypropylene/Co-Polyamide Blend Filled with Dispersed Iron. Proceedings of the 25th International Conference on microelectronics. Belgrade, Serbia and Montenegro.
- [87] Wang C., Guo Z. and Niu D. (2020). Influence of the fiber volume content on the durability-related properties of polypropylene-fiber-reinforced concrete. *Sustainability* 12: 549.
- [88] Khoury G.A. (2008). Polypropylene fibres in heated concrete. Part 2: Pressure relief mechanisms and modelling criteria. *Magazine of Concrete Research* 60(3):189-204.
- [89] Enfedaque A., Alberti M. G., Gálvez J. C. and Paredes J. (2020). Microstructural Study of the Interface of Polyolefin Fibers Embedded in Self-Compacting Concrete Matrices with Bond Improver Admixture. *Journal of Materials in Civil Engineering* 32: 1-11.
- [90] Askarinejad S. and Rahbar N. (2017). Effects of Cement-Polymer Interface Properties on Mechanical Response of Fiber-Reinforced Cement Composites. *Journal of Nanomechanics and Micromechanics* 7: 1-10.

- [91] Noumowé A. (2005). Mechanical properties and microstructure of high strength concrete containing polypropylene fibres exposed to temperatures up to 200 °C. *Cement and Concrete Research* 35: 2192-2198.
- [92] Pistol K., Weise F., Meng B. and Schneider U. (2011). The mode of action of polypropylene fibres in high performance concrete at high temperatures. *Proceedings of 2<sup>nd</sup> International Workshop on Concrete Spalling due to Fire Exposure*. Delft, the Netherlands.
- [93] Bentz D.P. (2000). Fibers, Percolation, and Spalling of High Performance Concrete. *ACI Materials Journal* 97: 351-359.
- [94] Bošnjak J., Ožbolt J. and Hahn R. (2013). Permeability measurement on high strength concrete without and with polypropylene fibers at elevated temperatures using a new test setup. *Cement and Concrete Research* 53: 104-111.
- [95] Li Y. and Tan K.H. (2016). Effects of polypropylene and steel fibers on permeability of ultra-high performance concrete at hot state. *Proceedings of the 9<sup>th</sup> International Conference on Structures in Fire*. Princeton, USA.
- [96] Garboczi E.J., Snyder K.A. and Douglas J.F.(1995). Geometrical percolation threshold of overlapping ellipsoids. *Physical review E* 52: 819-828.
- [97] Li Y., Zhang Y., Yang E.-H. and Tan K.H. (2019). Effects of geometry and fraction of polypropylene fibers on permeability of ultra-high performance concrete after heat exposure. *Cement and Concrete research* 116: 168-178.
- [98] Mazzucco G., Majorana C.E., Salomoni V.A. (2015). Numerical simulation of polypropylene fibres in concrete materials under fire conditions. *Computers and Structures* 154: 17–28.
- [99] Suhaendi S.L. and Horiguchi T. (2006). Effect of short fibers on residual permeability and mechanical properties of hybrid fibre reinforced high strength concrete after heat exposition. *Cement and Concrete Research* 36: 1672-1678.
- [100] Lu F. and Fontana M. (2016). Effects of Polypropylene Fibers on Preventing Concrete Spalling in Fire. *Proceedings of the 9th International Conference on Structure in Fire SiF'16*. Princeton, USA.
- [101] Haniche R., Debicki G., Bouamrane A. and Zeltz E. (2011). Gas transferts and flow process through concrete maintained in temperature. *Proceedings of 2<sup>nd</sup> International Workshop on Concrete Spalling due to Fire Exposure*. Delft, the Netherlands.
- [102] Jansson R. (2008). Material properties related to fire spalling of concrete Division of Building Materials. Lund University.
- [103] Bei S. and Zhixiang L. (2016). Investigation on spalling resistance of ultra-high-strength concrete under rapid heating and rapid cooling. *Case Studies in Construction Materials* 4:146- 153.
- [104] Knack I. (2009). New pp-fibre with exceptional melting characteristics for improved fire protection in concrete building. *Proceedings of 1<sup>st</sup> International Workshop on Concrete Spalling due to Fire Exposure*. Leipzig, Germany.
- [105] Mugume R. B. and Horiguchi T. (2012). Effect of fibre type and geometry on maximum pore pressures in fibre reinforced high strength concrete at elevated temperatures. *Cement and Concrete Research* 42: 459-466.
- [106] La Borderie C., Lawrence C. and Menou A. (2007). Approche mésoscopique du comportement du béton: Apport de la représentation géométrique. *Revue européenne de génie civil* 11:407–421.
- [107] Xotta G., Mazzucco G., Salomon V., Majorana C. and William K. (2015). Composite behavior of concrete materials under high temperatures. *International Journal of Solids and Structures* 64-65: 86-99.

- [108] Dauti D.(2016). A combined experimental and numerical approach to spalling of high-performance concrete due to fire. PhD Thesis. Université Grenoble Alpes.
- [109] Khaddour F. (2014). Amélioration de la production de gaz des « Tight Gas Reservoirs ». PhD Thesis. Université de Pau et des Pays de l'Adour.
- [110] Zhang D. (2020). Spalling resistance of fiber embedded ultra-high performance concrete. PhD Thesis. Nanyang Technological University.
- [111] Nince A. and Figueiredo A.D. (2005). The influence of aggregate size in the risk of spalling in normal and high-strength concrete subjected to hydrocarbon fire”, Proceedings of the 5<sup>th</sup> International Conference on Concrete for Structures. Coimbra, Portugal.
- [112] Pan Z., Sanjayan J.G. and Kong D.L.Y. (2012). Effect of aggregate size on spalling of geopolymer and Portland cement concretes subjected to elevated temperatures. *Construction and Building Materials* 36: 365-372.
- [113] Fichant S., La Borderie C. and Pijaudier-Cabot G. (1999). Isotropic and anisotropic descriptions of damage in concrete structures. *Mechanics of cohesive frictional materials* 4: 339–359.
- [114] Mazars J. (1984). Application de la mécanique de l'endommagement au comportement non linéaire et à la rupture du béton de structure. PhD Thesis. Paris 6.
- [115] Carré H. (2011). Mesure de caractéristiques mécaniques à haute température :  $\varepsilon$  transversales lors d'essais de compression, essais de flexion à haute température. Report CSTB.
- [116] Menou A., Mounajed G., Boussa H., Pineaud A. and Carré H. (2006). Residual fracture energy of cement paste, mortar and concrete subject to high temperature. *Theoretical and Applied Fracture Mechanics* 45: 64-71.
- [117] Nguyen T.D. (2010). Apport de la modélisation mésoscopique dans la prédiction des écoulements dans les ouvrages en béton fissuré en conditions d'accident grave. PhD Thesis. Université de Pau et des Pays de l'Adour.
- [118] Gagnant A. (2016). Etude de la rupture quasi-fragile d'un béton à l'échelle mésoscopique. Aspects expérimentaux et modélisation. PhD Thesis. Université de Bordeaux.
- [119] La Borderie C., Maurel O. and M. Matallah (2009). Couplage endommagement fissuration : application aux calculs de structures en béton armé. Proceedings of 19<sup>th</sup> Congrès Français de Mécanique. Marseille, France.

## **CHAPTER 4**

# **FORMULATION OF FIRE RESISTANT SELF-COMPACTING CONCRETE WITH POLYPROPYLENE FIBERS**

### **4.1 Introduction**

Self-compacting concrete (SCC), or self-consolidating concrete, is a special type of concrete that spreads under its own weight. It outperforms ordinary concrete due to a faster construction, thinner section of structural elements and easier placement, reduction in noise and labor and better surface finishing. Modern self-compacting concretes are usually high performance as well. Today SCC is widely used for various applications from small construction segments to massive structures. Increasing industrial demand, special requirements on concrete performance and addition of new elements into composition create a challenge for engineers and researchers working on formulation of SCC.

The aim of this chapter is to produce a mix design of fire resistant self-compacting concrete with polypropylene fibers. We first present a basis for this work that consists of requirements imposed by project, conclusions from rheology and fire tests, and mix design protocol. We then proceed with a mix design specifying all the steps required. Final mixes are completed and verified for fresh and hardened state concrete performance criteria. Alongside, some numerical simulations of drying of concrete are performed to determine water content distribution along the sample. Finally, these mixes are tested for resistance to thermal instability with fire tests conducted on uniaxially loaded samples. Based on results, we select mixes for tests in intermediate scale (slabs) and full scale (waste storage container), the next steps of the project. These tests lie outside the scope of this thesis and will not be presented in this thesis.

Our results prove a possibility of formulating concrete with polypropylene fibers, which is fluid and fire resistant at the same time.

## 4.2 Basis of mix design

### 4.2.1 Requirements on concrete

The requirements of ANDRA [1] on mix design of concrete for underground radioactive waste disposal consider a development of self-compacting fiber-reinforced fire resistant concrete. This constitutes a high performance concrete of durable nature. Reversibility of 100 years, i.e. a period during which waste container can be removed from underground disposal area and redirected to surface, should be taken into account. The main requirements on concrete formulation imposed by ANDRA are following:

- Use of cement, aggregates and fillers located close to Cigéo Project (see Section 1.1.2)
- Thermal stability withstanding standard ISO 834-1 fire curve
- Self-compacting nature of concrete
- Robustness of concrete with respect to temperature and dosage variations.

Choice of concrete components and their dosage is regulated as well in the project [1]:

- CEM I and CEM V is recommended as cement but CEM III could be considered
- Water to binder ratio is fixed to a maximum value of 0.4
- Cement dosage is equal or superior to 400 kg/m<sup>3</sup>
- Dry extract of organic admixture is limited to 1.5 % of total binder content.

ANDRA imposes criteria for fresh and hardened concrete presented in Tables 4.1 and 4.2.

**Table 4.1** Requirements on fresh concrete [1].

Performance criterion	Specified values or criteria
Spread flow via Abram's cone	70 ± 5 cm
Rheological maintain	> 1.5 hour
L-Box	80 %
Sieve stability	< 15 %
Bubbling	Minimum bubbling
Measurement of bleeding	≤ 1 mm
Entrapped air	≤ 3 %

**Table 4.2** Requirements on hardened concrete [1].

Type	Performance criterion	Specified values at 28 days
Mechanical	Compressive strength	60 – 80 MPa
	Tensile strength by splitting test for non-fibred concrete	≥ 5 MPa
	for fibered concrete	≥ 4.5 MPa
	Elastic modulus	< 50 GPa
Physical	Total shrinkage	< 400 μm/m
	Porosity accessible to water	< 14 %
Transfer	Permeability to gas	< 10 <sup>-17</sup> m <sup>2</sup>

### 4.2.2 Conclusions from rheology and fire tests

Conclusions from rheology and fire tests completed in Chapters 2 and 3 respectively serve as basis for this work. As addition of polypropylene fibers has a negative effect on rheology and positive effect on fire resistance, we have developed some guidelines in terms of selection of an optimized fiber geometry and dosage for formulation of fire resistant fluid concrete with polypropylene fibers.

In rheology, we have developed a physical model that allows for predicting the contribution of polypropylene fibers to evolution of the yield stress of cement pastes using such parameters as fiber volume fraction, diameter and length as well as elastic modulus of polypropylene and the yield stress of suspending fluid. A simplified scheme for suspensions containing fibers and sand allows for a summation of contributions of each inclusion to the yield stress. We can therefore counterbalance the influence of fibers on rheology by reducing aggregate volume (or increasing paste volume).

To choose the most efficient geometry and dosage of fibers in terms of thermal stability of concrete, we have studied three cementitious mixes with different granular skeletons. We have found that fiber length should be selected according to maximum size of aggregates. For mortar, with  $D_{\max} = 1$  mm, in tested configuration, an optimal fiber length and dosage are 12 mm and  $1 \text{ kg/m}^3$ . For concrete 1 with  $D_{\max} = 10$  mm, an optimal fiber choice is 18 mm long fibers at  $0.5 \text{ kg/m}^3$ . For concrete 2 with  $D_{\max} = 20$  mm, no significant difference between 6 and 12 mm long fibers is noted. No significant influence of fiber diameter is noted; however, at same fiber count thinner fibers are preferred to thicker ones for fluidity of concrete.

### 4.2.3 Mix design protocol

Having presented project requirements and conclusions from previous chapters, we proceed with our mix design protocol.

For self-compacting concrete design, we use packing based approach used in IFSTTAR [2]. This method is widely used in literature as well [3], [4], [5], [6], [7].

We reduce a number of varying parameters by establishing water to cement ratio (W/C) to be equal to 0.4 [2]. Choice of this W/C increases robustness of concrete at fresh state towards variation of water contained in aggregates. For lower W/C, slight variations of water content in aggregates has a significant influence on fresh state properties.

We present mix formulation protocol used in this study, which is composed of following stages:

### **Stage 1. Choice and characterization of materials**

We first select concrete components such as cement, filler, aggregates, polypropylene fibers, superplasticizer and viscosity agent. Characterization of these materials is presented as well.

### **Stage 2. Design of reference mix without fibers**

1. Optimization of granular skeleton. This step allows determining proportions between volumes of aggregates for an optimized granular mix.
2. Determination of paste and aggregate volume. This step determines the volume of aggregates and volume of paste.
3. Design of paste. In this step, we select a quantity of cement and filler.
4. Adjustment of admixture dosage.

### **Stage 3. Design of fiber-reinforced mix**

1. Steps 2- 4 described in Stage 2.
2. Computation of volume of additional paste (or extractable aggregate volume). This step is necessary to recover concrete fluidity lost with addition of polypropylene fibers.

### **Stage 4. Verification of properties at fresh and hardened state**

At this stage, the compliance of fresh state and hardened state concrete properties to imposed criteria is verified.

## **4.3 Formulation of self-compacting concrete**

### **4.3.1 Materials choice**

#### **Cement**

Requirements on cement state a preference for use of CEM I or CEM V with a possible use of CEM III. We choose to use CEM III/A 52.5 L CE PM-ES-CP1 NF from Eqiom, Heming.

We shall remember here that waste storage containers present massive structures. The size of structure requires use of cement with a low heat of hydration in order to prevent development of significant thermal gradients and early age cracking. Maximum temperature developed in the concrete should not exceed 65 °C and one way of achieving this target is accomplished

through limitation of content of C3A. Selected cement presents mineralogical composition that shows resistance to chemical attacks during setting time and at hardened state, which indeed satisfies requirement imposed by project. In addition, it has a low quantity of sulphates and sulfites in its composition. Concrete cast with CEM III/A would also present a finer microstructure that would result in a higher durability of concrete.

For reasons presented above, we thus choose this cement for our concrete design. The information on physical properties and composition of cement can be found in Section 3.3.1.

### **Filler**

We use filler for an optimization of granular packing in order to fill the voids between the smallest sand grains (around 100  $\mu\text{m}$ ) and cement particles (around 10  $\mu\text{m}$ ). Another reason for use of filler is maintaining paste volume despite limitation of cement content. Filler selected for concrete mixes is siliceous filler from Sibelco. A detailed information on filler is available in Section 3.3.1.

### **Aggregates**

Calcareous aggregates from crushed rock, commercially available from Calin and selected for concrete formulation, are sand 0/4, gravel 4/6 and gravel 6/10. The choice of these aggregates lies in the geographic proximity to construction area and thermal stability of calcareous rocks with respect to high temperature. The characteristics of aggregates such as size distribution, density, water absorption and water content are provided in Figure 4.1 and Table 4.3. Aggregates selected for the project have been previously studied in IFSTTAR [2]. The packing of aggregates is measured by vibro-compaction method presented in Section 2.3.2. Dense packing fraction is found to be equal to 56.8 % for sand 0/4, 52.4 % for gravel 4/6 and 52.6% for gravel 6/10.

For self-compacting concrete mix design, rolled aggregates are preferable to crushed ones for an optimized granular mix. However, due to geographic unavailability of these aggregates, this problem can be solved by designing concrete with a higher volume of paste.

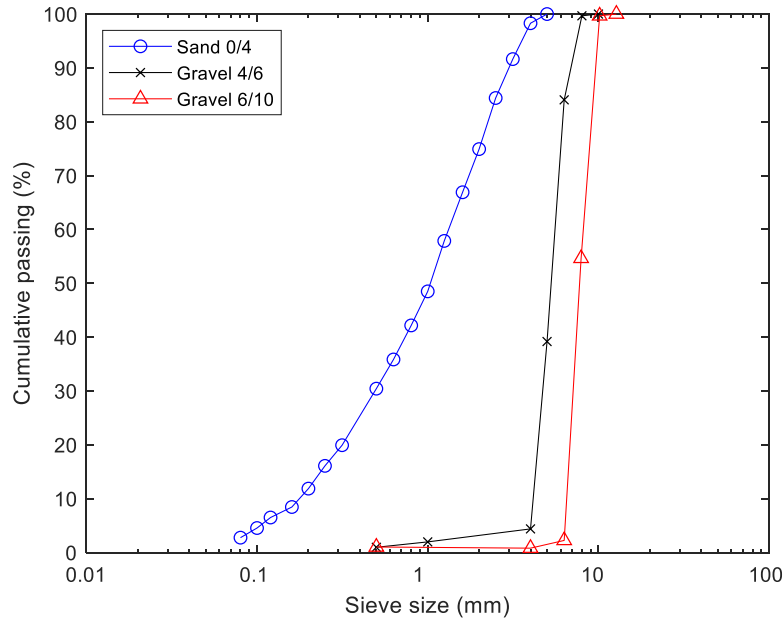


**Figure 4.1** Particle size distribution of aggregates studied.

**Table 4.3** Density ( $\rho$ ), water absorption ( $WA_{24}$ ) and water content ( $w$ ) of aggregates.

	$\rho$ ( $\text{kg/m}^3$ )	$WA_{24}$ (%)	$w$ (%)
Sand 0/4	2540	1.94	0.26
Gravel 4/6	2610	1.09	0.28
Gravel 6/10	2620	1.01	0.17

### Polypropylene fibers

Choice of polypropylene fiber geometry and dosage is mainly based on conclusions of rheology and fire tests, where an optimal performance for concrete 1, high strength self-compacting concrete of 90 MPa with  $D_{\max}=10$  mm, is found with  $0.5 \text{ kg/m}^3$  of 18 mm long  $32 \mu\text{m}$  diameter fibers.

We know that for prevention of spalling, an optimal fiber length for maximum size of aggregate  $D_{\max} = 10$  mm should be at least 18 mm, therefore, we select 18 and 24 mm long fibers, which would be as efficient at lower dosage as shorter fibers (6 and 12 mm long) at higher dosage. For fresh state concrete, adding of  $1 \text{ kg/m}^3$  of 24 mm long fibers or 18 mm long fibers is less impactful on rheology than adding  $2 \text{ kg/m}^3$  of 6 mm long fibers or 12 mm long fibers.

From the study on the influence of diameter at the same total fiber number during fire tests, we have found no major influence of fiber diameter. From rheological point of view, for same number of fibers, thinner fibers ( $20 \mu\text{m}$ ) are preferential to thicker ones ( $32 \mu\text{m}$ ). This would allow us reducing the dosage of fibers to produce less impact on fluidity of concrete due to

inclusion of fibers. Due to the absence of 24 mm long fibers with 20  $\mu\text{m}$  diameter, we choose fibers of 34  $\mu\text{m}$  for commercially available lengths of 18 and 24 mm.

We have found that spalling is almost prevented for concrete 1 under uniaxial compressive loading of 5 MPa (1 out of 3 samples has slightly spalled) using 0.5  $\text{kg}/\text{m}^3$  of 18 mm long fibers. Despite a good performance at 0.5  $\text{kg}/\text{m}^3$ , for security reasons we choose higher dosages of fibers of 1, 1.5 and 2  $\text{kg}/\text{m}^3$  in our mixes.

It is therefore established that we choose 18 and 24 mm long fibers with diameter of 34  $\mu\text{m}$  and dosages of 1, 1.5 and 2  $\text{kg}/\text{m}^3$  as an optimized fiber choice for our concrete. Table 4.4 presents an information on polypropylene fibers studied. Polypropylene fibers 18/34 are commercially available from BASF and fibers 24/34 are from Belgian Fibers.

**Table 4.4** Polypropylene fibers studied: Name, length (L), diameter (D), aspect ratio (R), and mass ( $\phi^{\text{mass}}$ ) and volumetric dosage ( $\phi^{\text{vol}}$ ), total number ( $N_{\text{tot}}$ ) and total length ( $L_{\text{tot}}$ ).

Name	L (mm)	D ( $\mu\text{m}$ )	R (-)	$\phi^{\text{mass}}$ ( $\text{kg}/\text{m}^3$ )	$\phi^{\text{vol}}$ (%)	$N_{\text{tot}}$ ( $\times 10^6/\text{m}^3$ )	$L_{\text{tot}}$ ( $\text{km}/\text{m}^3$ )
18/34	18	34	529	1.0	0.110	67	1210
				1.5	0.165	101	1816
				2.0	0.220	134	2421
24/34	24	34	706	1.0	0.110	50	1210
				1.5	0.165	76	1816
				2.0	0.220	101	2421

## Superplasticizer

Five different polymers are tested in this work. The information on the polymers is provided in Table 4.5. Superplasticizers are evaluated based on their compatibility with cement and ability to maintain concrete fluidity for at least 90 minutes.

**Table 4.5** Information on superplasticizers tested.

Brand	Name	Molecule type	Dry extract (%)	Dosage range (% cement mass)
SIKA	Krono 26	Acrylic	$40.5 \pm 2$	0.1 - 5
SIKA	Tempo 653	Polycarboxylate	$30 \pm 1.5$	0.1 - 5
SIKA	Tempo 12	Polycarboxylate	$29.5 \pm 1.4$	0.1 - 5
CHRYSO	Optima 175	Polycarboxylate and modified phosphonate	$30.5 \pm 1.5$	0.3 - 3
CHRYSO	Optima 145	Polycarboxylate and modified phosphonate	$31.5 \pm 1.5$	0.3 - 3

We evaluate polymer efficiency using Concrete Equivalent Mortar (CEM) method in which CEM has rheological characteristics well correlated with those of concrete [8]. In this method, slump or slump flow is measured using a mini-cone with following dimensions: upper and

lower diameters of 50 and 100 mm and 150 mm height. Experimental procedure for measurement of slump or slump flow is discussed in detail in Section 4.3.2.

CEM method consists of using mortar derived from concrete through replacement of larger aggregates by sand using the same specific surface contribution. We present mortar mix derived from an example concrete in Table 4.6.

**Table 4.6** Example concrete and concrete equivalent mortar derived from it.

	Concrete mix (kg/m <sup>3</sup> )	CEM mix (kg/m <sup>3</sup> )
Cement	496	609
Effective water	222	266
Filler	121	148
Sand 0/4	899	1204
Gravel 4/6	308	-
Gravel 6/10	309	-

Figures 4.2a and 4.2b show an evolution of spread flow and relative yield stress (a ratio of the yield stress with polymer and the yield stress without polymer) as a function of superplasticizer dosage (% mass of cement). We shall note that reference mix without superplasticizer has a slump of 2 mm or the yield stress of 1868 Pa. It is important to note that for most of the superplasticizers saturation has not been achieved due to a start of segregation at higher dosages. Out of five superplasticizers tested, SIKA Krono 26 appears to be the most effective in terms of fluidity increase. SIKA Tempo 653 is eliminated from consideration due to a low range of dosages that would produce a stable mix. Taking a criterion of a minimal 30 cm spread (equivalent of 50 cm for concrete [8]), four superplasticizers at selected dosages (% mass of cement) are left for further examination:

- SIKA Krono 26 at 0.75 %
- SIKA Tempo 12 at 3 %
- CHRYSO Optima 175 at 1.5 %
- CHRYSO Optima 145 at 2 %

We shall note that Figure 4.2 presents results of delayed addition of superplasticizer, i.e. 80 % of superplasticizer is added with water directly and 20 % is added 1 minute after start of mixing. In the direct addition of the superplasticizer, 100 % of superplasticizer is added with water. We have therefore compared direct and delayed methods of superplasticizer addition. The results are presented in Table 4.7. We have found that direct addition of superplasticizer is more efficient and more practical in industrial context.

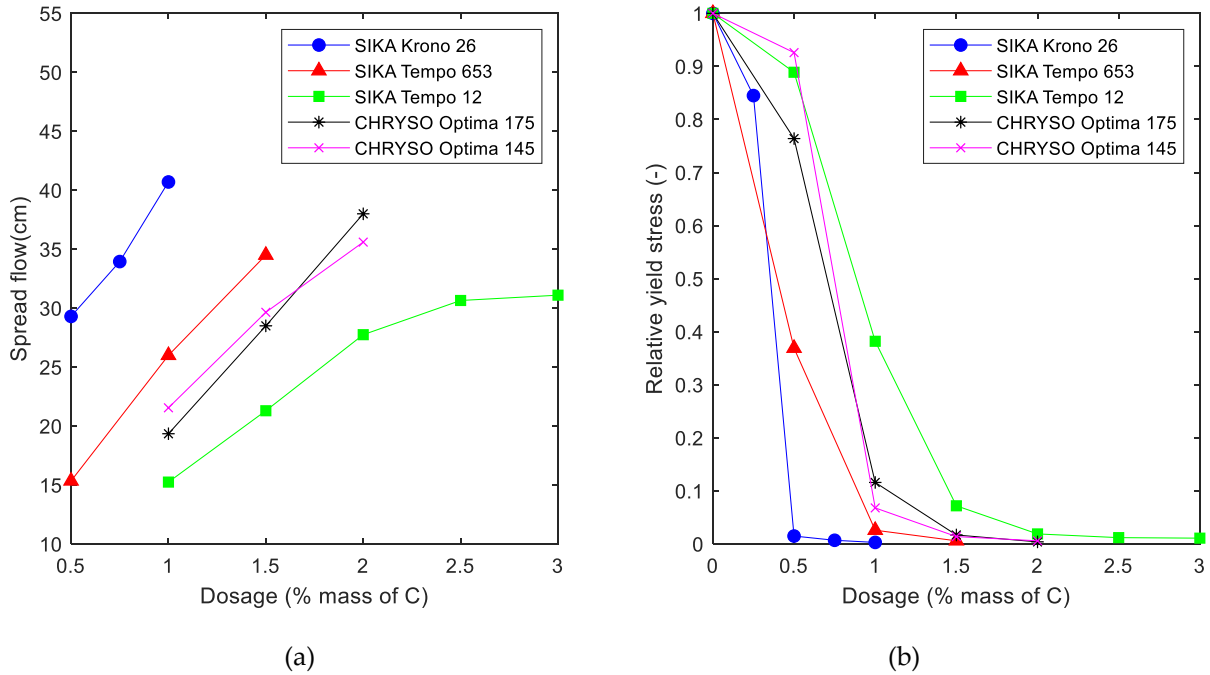


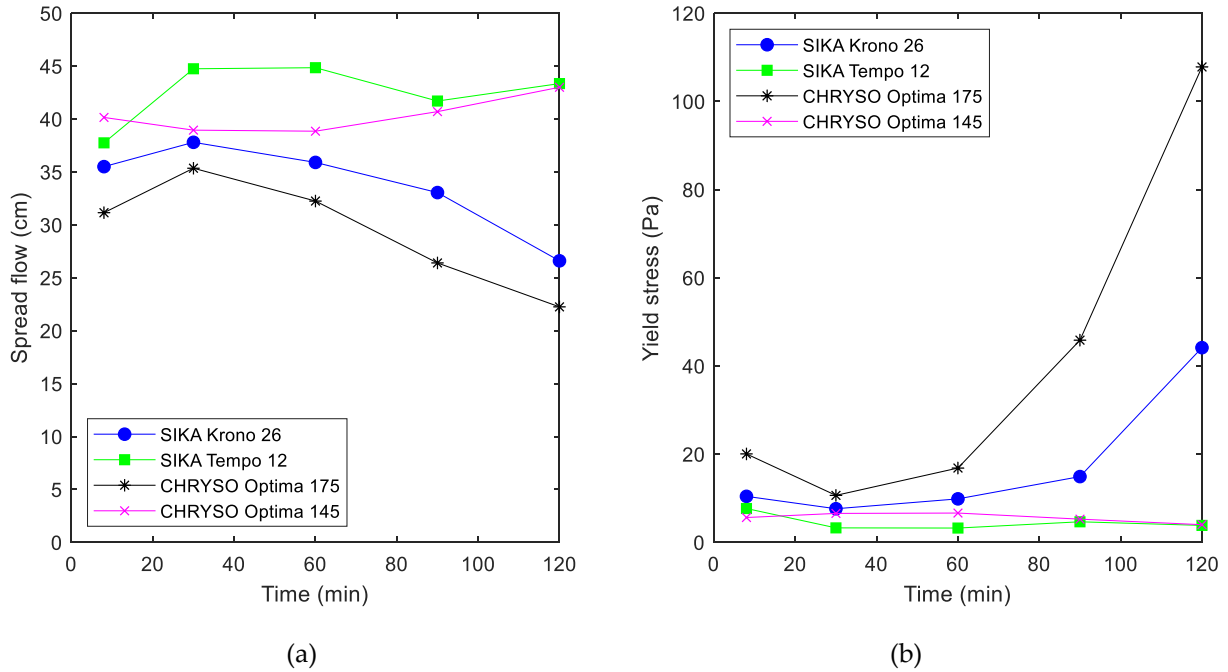
Figure 4.2 Spread flow (a) and relative yield stress (b) as a function of superplasticizer dosage.

Table 4.7 Yield stress measurements for delayed and direct addition of superplasticizers.

Type	SIKA Krono 26 (0.75 % m <sub>c</sub> )	SIKA Tempo 12 (3 % m <sub>c</sub> )	CHRYSO Optima 175 (1.5% m <sub>c</sub> )	CHRYSO Optima 145 (2% m <sub>c</sub> )
Delayed addition (80 % + 20%)	13.04	20.21	31.27	10.28
Direct addition (100 %)	10.43	7.67	20.05	5.63

Four selected superplasticizers at various dosages with direct addition of polymer are evaluated for rheological maintain for at least 90 minutes. The results of rheological maintain in terms of flow spread and the yield stress are presented in Figure 4.3a and 4.3b respectively. Mortars containing SIKA Krono 26 and CHRYSO Optima 175 has lost their fluidity or, in other words, experienced an increase in the yield stress over a time. Despite excellent rheological maintain, SIKA Tempo 12 requires an extremely high dosage that does not allow enough margin for fiber reinforced concrete design. We note as well a start of instability at this dosage for SIKA Tempo 12 marked with segregation and aureole of paste formed around (see Annex), which can be avoided with a lower dosage of superplasticizer.

We therefore select CHRYSO Optima 145 as our superplasticizer due to its compatibility with cement and excellent rheological maintain.



**Figure 4.3** Spread flow (a) and yield stress (b) as a function of time.

### Viscosity agent

Self-compacting concretes can present problems that include loss of mix stability such as bleeding and segregation. In order to increase viscosity of mixes without important perturbation of the yield stress (or spread), we have chosen a viscosity agent Plast 90 from CHRYSO. The dry extract of this polymer is  $5.3 \pm 0.5$  % with a recommended dosage range of 0.2 to 1 % of cement mass. It is important to note that this viscosity agent is compatible with selected superplasticizer and with no competition in adsorption of two polymers, superplasticizer and viscosity agent.

### 4.3.2 Experimental protocols

#### Mixing protocol

Dry components are placed into mixer in the following order: coarse aggregates, filler, cement and sand. Then, they are mixed for 1 minute and machine is stopped. Water containing superplasticizer and viscosity agent is added and mixing is done for 2 additional minutes. Mixer is stopped for addition of polypropylene fibers. Fibers are manually dispersed and mixing for 2 more minutes is done.

## Testing protocols

### *Slump flow test*

Slump flow test is a measure of concrete's fluidity at fresh state. The testing equipment consists of slump cone, or Abrams cone, and a flow table. The cone has following standard dimensions: top and bottom diameters are 100 and 200 mm respectively and height is 300 mm. During the test, flow table is placed on horizontal flat surface and is humidified as well as the inner surface of cone. Concrete is poured in the cone resting on the flow table and cone is lifted upwards allowing concrete to spread under gravity forces. Two orthogonal spread diameters are measured and an average of two is considered.

### *Rheological maintain*

Test for rheological maintain follows the same procedure as slump flow test. The time increments for this test are 8 (directly after mixing), 30, 60, 90 and 120 minutes. It is necessary to avoid drying of concrete in between the tests by covering the concrete mixer. Prior to testing, concrete is remixed for 30 seconds.

### *L-box*

L-box test measures a passing ability of concrete. The schematic representation of the test is provided in Figure 4.4. The L-box is placed on the flat surface and the walls are humidified before the test. The gate is closed as presented in Figure 4.4a and volume of concrete necessary to fill it out a vertical section is poured. One minute later, gate is fully opened allowing flow of concrete. When flow stops, concrete heights at the extremity of horizontal part ( $h_2$ ) and in the vertical part ( $h_1$ ) of L-box are measured. A ratio of  $h_2/h_1$  is then calculated. For self-compacting concrete, the lowest limit for this ratio is 0.8.

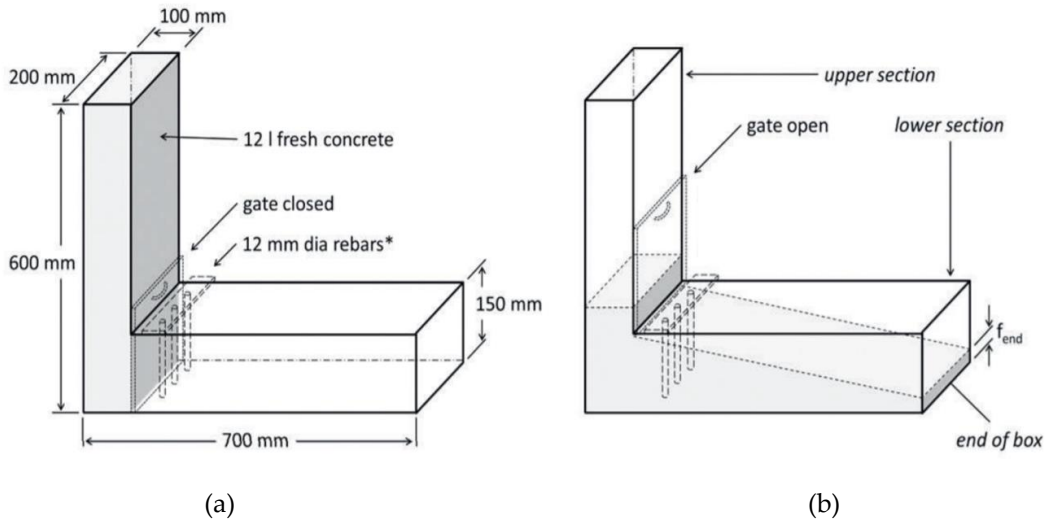


**Figure 4.4** L-box test: a) gate closed, b) gate opened [9].

*Sieve test*

Sieve test determines resistance of self-compacting concrete to segregation. The testing equipment is composed of a 10 l bucket with a lid and sieve with an opening of 5 mm. First, 10 l concrete sample is collected into a bucket, which is then covered with lid in order to avoid evaporation. It rests undisturbed for  $15 \pm 0.5$  minutes. Scales are placed on a flat horizontal surface and sieve with bottom of sieve are placed on them. Concrete sample of  $4.8 \pm 0.2$  kg is poured from bucket on the bottom of sieve from the vertical distance of  $500 \pm 50$  mm as presented in Figure 4.5. After two minutes, the sieve is taken away and the mass resting in the bottom of sieve is measured. Potential of segregation is computed as a ratio of mass accumulating in the bottom of sieve and mass poured through sieve. Higher value of this ratio indicates a greater liability to segregation.

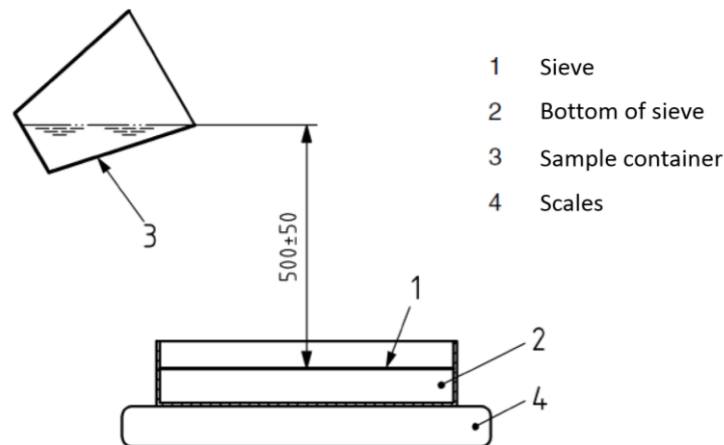


**Figure 4.5** Sieve test as adapted from [10].

### *Entrained air test*

The aim of entrained air test is to determine the percentage of entrapped air in fresh concrete. The image of aerometer with its components is presented in Figure 4.6. Testing procedure involves filling out concrete into specimen holder and removing the excess. The recipient is closed using closing valves (3) and two valves (5) and (7) remain open. The water is injected through a valve (7) until it flows out of valve (5). The air is pumped manually until reaching start position and, if wrong, can be corrected using correction valve (6). The two valves (5) and (7) are closed, test button (green) is pushed, and the reading shows the percentage of entrapped air. During this test, it is also possible to measure fresh concrete density from mass of concrete tested.

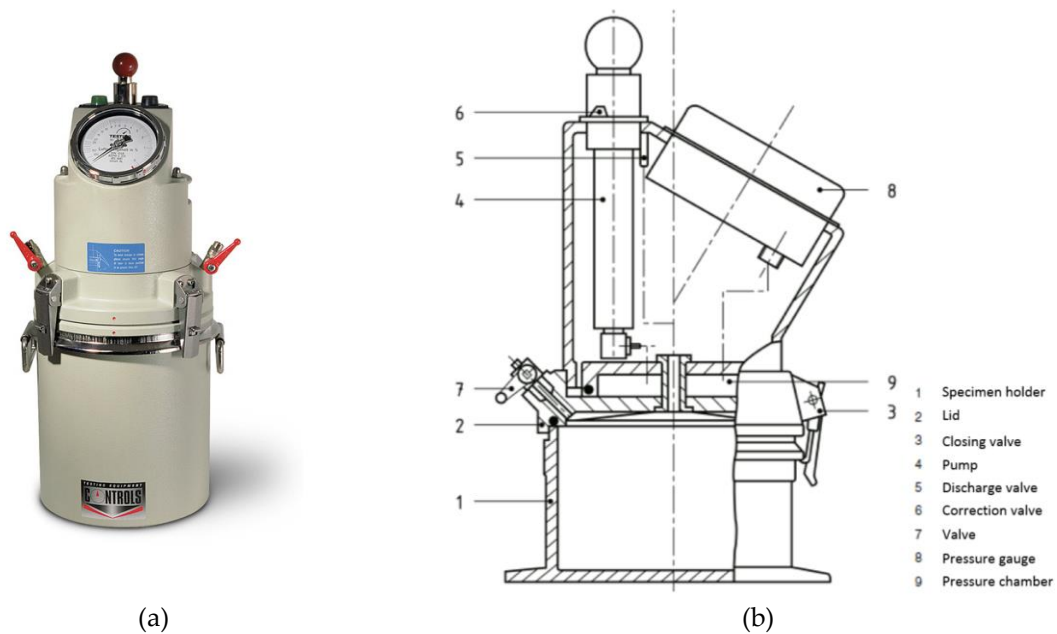


**Figure 4.6** Entrained air testing machine (a) [11] and its structure (b) adapted from [10].

### **Sample preparation protocol**

Samples are prepared for characterization of hardened state properties of concrete mixes. Samples are demolded 24 hours after casting and cured in water. We present a list of samples prepared for a verification of mechanical properties.

- Compressive strength: cylinders with diameter of 11 cm and 22 cm height. Average compressive strength is determined on basis of test on two samples at age of 28, 60 and 90 days.

- Tensile strength measured indirectly with Brazilian or split test at 28 days: cylinders with diameter of 16 cm and 32 cm height
- Elastic modulus at 28 days: cylinders with diameter of 16 cm and 32 cm height
- Porosity accessible to water at 90 days: cylinders of diameter 5 cm and 15 cm height
- Water content at 90 days: cylinders of diameter 11 cm and 10 cm height
- Intrinsic permeability at 80 °C: cylinders of inner and outer diameters of 55 and 110 cm, 14 cm height cored from 15 x 15 x 15 cm<sup>3</sup>
- Fire test at 90 days: prisms 20 x 20 x 10 cm<sup>3</sup>.

### 4.3.3 Design of reference mix

#### Optimization of granular skeleton

The work on optimization of granular mix, based on packing model of de Larrard [3], has been accomplished in IFSTTAR [2]. This model computes the maximum packing fraction possible for a mix of aggregates of different classes. As an entry information, the maximum packing fraction and particle size distribution of each aggregate is necessary.

The compacity determined for our aggregate mix (see the red circle at the bottom between isolines) is presented in Figure 4.7. It suggests a mix of 55% of sand 0/4 and 45 % of gravel 6/10 with a maximum packing between 73 and 74%. An absence of intermediate aggregate class of 4/6 is expected to weaken the stability of mix and cause segregation issues.

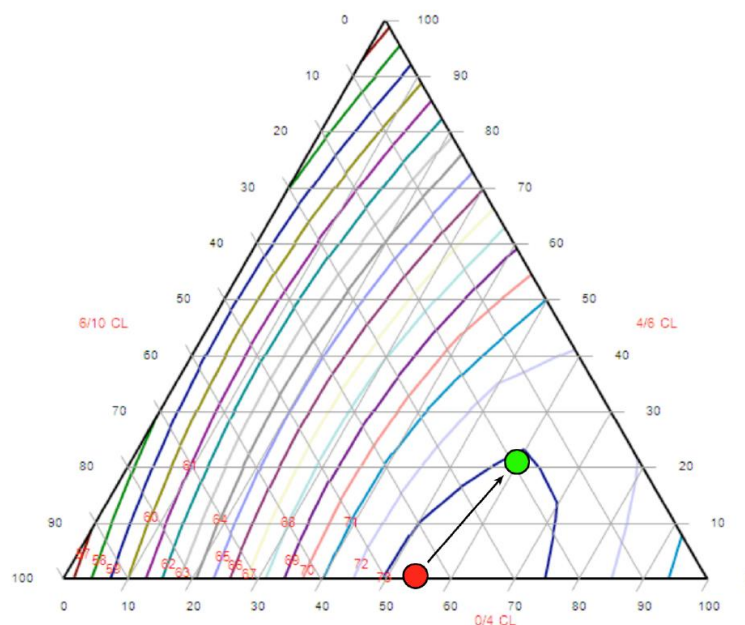
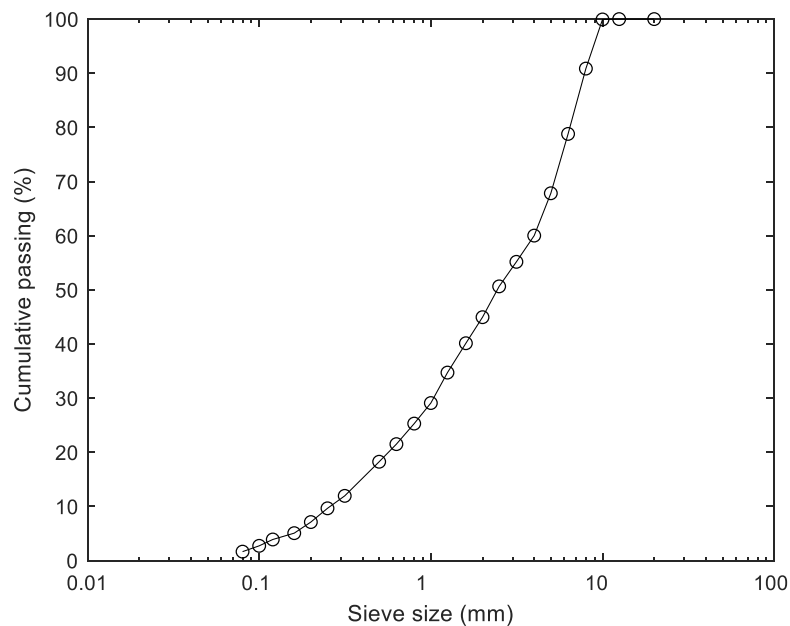


Figure 4.7 Compacity of aggregate mix [2].

A modification of aggregate mix is proposed in Figure 4.7 (see green circle) which allows for obtaining the packing fraction of the final mix of 73 %. Final aggregate skeleton is composed of 60 % sand 0/4, 20 % of gravel 4/6 and 20 % of gravel 6/10. This mix is better than previous one due to a presence of all aggregate sizes without change of maximum packing fraction. The particle size distribution of an optimized granular mix is presented in Figure 4.8.



**Figure 4.8** Particle size distribution of aggregate mix.

### Determination of paste and aggregate volume

We are now interested in evaluation of paste and aggregate volumes. Design of self-compacting concrete involves a minimization of direct frictional contacts between aggregates, which can be achieved with a sufficient volume of paste. Percolation of aggregates starts from 80 % of dense packing fraction. Below this value, contribution of aggregates to the yield stress and viscosity is low and material remains fluid. Above this value, flow of material is restricted or material does not flow.

Following this logic, we limit the aggregate volume to 80 % of dense packing of aggregates, which results in 580 L/m<sup>3</sup> of aggregate volume. This means that minimum paste volume is 420 L/m<sup>3</sup>. Knowing that an optimized granular mix is composed of 60 % sand 0/4, 20 % of gravel 4/6 and 20 % of gravel 6/10, we then compute the masses of aggregates such as 919, 315 and 315 kg/m<sup>3</sup> respectively for each aggregate class [2].

### Design of paste

We have decided to fix a cement dosage to 400 kg/m<sup>3</sup> in order to reduce the heat of hydration, which would be problematic in such massive structures. Knowing that paste volume is 420 l/m<sup>3</sup>, cement content is 400 kg/m<sup>3</sup>, we find that it is necessary to use 280 kg/m<sup>3</sup> of filler for a concrete with W/C= 0.4. This represents a rather significant filler content but is necessary for mix design of self-compacting concrete.

### Adjustment of polymer dosage

Once all the masses are determined, it is possible to adjust polymer dosage in order to obtain required fluidity of concrete. Series of tests for a various dosages of superplasticizers are accomplished until a desired performance at fresh state is achieved.

#### 4.3.4 Design of fiber-reinforced mix

Design of fiber reinforced self-compacting concrete follows the steps presented earlier but includes an additional step: determination of volume of supplementary paste.

#### Determination of additional paste volume

We compute a volume of additional paste (or volume of aggregates removed) that would allow compensating the negative influence of polypropylene fibers on fluidity of fresh concrete. A simplified estimation of total packing fraction of inclusions consisting of aggregates and fibers writes as:

$$\frac{\phi_f}{\phi_{mf}} + \frac{\phi_a}{\phi_{ma}} \quad (4.1)$$

where  $\phi_f$  and  $\phi_a$  are volume fractions of fibers and aggregates,  $\phi_{mf}$  and  $\phi_{ma}$  are dense packing fractions of fibers and aggregates. We can then consider canceling the contribution of polypropylene fibers at total packing fraction, which leads to removal of a certain volume of aggregates (or introduction of additional paste).

We know that relative packing fraction for synthetic fibers  $\frac{\phi_f}{\phi_{mf}}$  writes as  $\frac{\phi_f}{45 \left(\frac{E}{\tau_0}\right)^{-\frac{1}{5}} D^{\frac{2}{5}} L^{-\frac{1}{5}}}$  where

$E$  is elastic modulus,  $\tau_0$  is the yield stress of cementitious material,  $D$  and  $L$  are diameter and length of fiber. Taking into account that dense packing for aggregates is 73% x 80 % = 58 %, we can find values for additional paste required for selected polypropylene fibers.

Values of additional paste achieved with this calculation are rather low and in practice have not shown good fluidity. Final volumes of additional paste can be found in Table 4.8.

**Table 4.8** Volume of additional paste for 18 mm and 24 mm fibers at different dosages.

Dosage (kg/m <sup>3</sup> )	Additional paste volume (l/m <sup>3</sup> ) for PP fibers (D=34 μm)	
	L= 18 mm	L= 24 mm
1	22	23
1.5	33	35
2	44	47

## 4.4 Presentation of final mixes

### 4.4.1 Overview of mixes

We present an overview of composition of final mixes that include reference mix C-0 and fiber-reinforced mixes C-18/34 and C-24/34 at different fiber dosages in Table 4.9.

**Table 4.9** Mix proportions in kg/m<sup>3</sup>.

	C-0	C-18/34-1	C-18/34-1.5	C-18/34-2	C-24/34-1	C-24/34-1.5	C-24/34-2
Cement				400			
Filler	280	338	368	397	342	373	404
Effective water				160			
Sand 0/4	919	885	868	851	883	865	847
Gravel 4/6	315	303	297	292	302	296	290
Gravel 6/10	315	303	297	292	302	296	290
Superplasticizer	8.84	14.02	16.90	17.53	14.10	14.69	16.08
Viscosity agent	-	3.32	3.46	2.79	1.86	1.55	2.01
SP (% C+F)	1.30	1.90	2.20	2.20	1.90	1.90	2.00
VA (% C+F)	-	0.45	0.45	0.35	0.25	0.2	0.25

### 4.4.2 Validation of fresh and hardened state properties

We present in Table 4.10 fresh state concrete properties measured for mixes. The results satisfy most of the criteria imposed for concrete. We have observed that for mixes C-18/34-2 and C-24/34-2 with 2 kg/m<sup>3</sup> of polypropylene fibers is a little harder to achieve desired slump flow despite an additional paste to compensate influence of polypropylene fibers.

We note that high dosages of superplasticizers have affected negatively the stability and required a use of viscosity agent. Several mixes have shown a slight bleeding and signs of segregation while still meeting a requirement for sieve test (< 15 %). Visual inspection of spread for reference mix C-0 with C-24/34-2 presented in Figure 4.9 shows a slight instability of fiber reinforced mix. Reference mix is homogeneous and stable while C-24/34-2 has a small aureole

of paste around the spread and a little accumulation of aggregates in the center. Graphs of rheological maintain presented in terms of spread flow with a time is plotted in Figure 4.10. Reference mix C-0 experiences a slight loss of fluidity, however, still satisfies slump flow criteria (see Figure 4.11). Fiber reinforced mixes exposed better maintain due to high dosage of superplasticizer, which has a retardant effect.

**Table 4.10** Fresh state properties of concrete mixes.

	Criterion	C-0	C-18/34-1	C-18/34-1.5	C-18/34-2	C-24/34-1	C-24/34-1.5	C-24/34-2
Slump flow (cm)	$70 \pm 5$	75	72	68	63	70	65	63
Fresh density ( $\text{kg/m}^3$ )	NA	2392	2332	2364	2361	2354	2368	2359
Sieve test (%)	$< 15$	7	8.7	13.6	10.6	9.8	11.7	7.9
L-Box (%)	80	81	77	84	80	77	79	81
Entrained air (%)	$\leq 3$	0.70	0.55	0.70	0.50	0.45	0.60	0.70
Rheological maintain 1.5 h (cm/cm)	$D_{90\text{min}}/D_{8\text{min}}$	72/75	68/72	66/68	60/63	68/70	64/65	62/63



**Figure 4.9** Spread flow for a) C-0 and b) C-24/34-2.

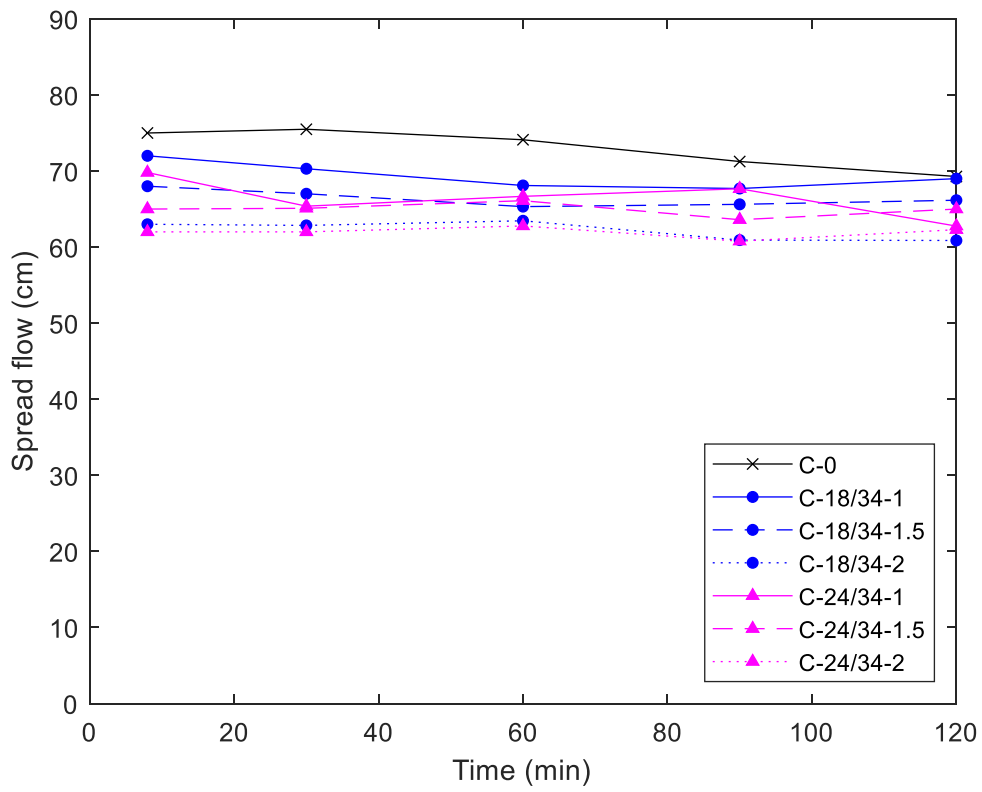


Figure 4.10 Spread flow as a function of time.



Figure 4.11 Spread flow C-0 at: a) 8 min, b) 90 min.

In terms of hardened state properties, we have selected to study only reference C-0 and C-24/34-2 mixes as two extreme boundaries. The results are demonstrated in Table 4.11. We note that compressive strength of concrete is higher than one required by ANDRA. Despite the lowest quantity of cement added ( $400 \text{ kg/m}^3$ ), at 28 days the obtained compressive strength surpasses the highest limit by 15 %. Such high value for the compressive strength is related to cement choice. No major evolution of compressive strength is found from 28 days to 90 days. In terms of tensile strength determined by Brazilian test, two mixes meet the criterion. Elastic modulus of concrete is imposed to be less than 50 GPa, however, measurements show a little abundance. The reason for this lies in the choice of cement and high volume of paste. Intrinsic permeability is found to be within required range. Porosity accessible to water is satisfactory for both C-0 and C-24/34-2.

**Table 4.11** Hardened state properties of concrete mixes.

Criterion	C-0				C-24/34-2				
	1	2	3	Average	1	2	3	Average	
$f_{c, 28 \text{ cyl}}$ (MPa)	60-80	90.13	90.49	-	90.31	91.71	93.10	-	92.41
$f_{c, 60 \text{ cyl}}$ (MPa)	-	90.60	85.82	-	88.21	89.31	95.40	-	92.36
$f_{c, 90 \text{ cyl}}$ (MPa)	-	93.60	93.68	-	93.69	96.09	100.40	-	98.25
$f_{t,28}$ (MPa)	$\geq 5$	6.4	5.52	6.71	6.21	5.94	4.77	5.67	5.46
E (GPa)	$< 50$	55.13			-	57.22			-
P (%)	$< 14$	14.46	14.31	-	14.38	13.48	13.88	-	13.68
k ( $10^{-17} \text{m}^2$ )	$< 10^{-17}$	0.61	1.35	-	0.98	1.42	1.01	-	1.22

## 4.5 Fire tests on final mixes

### 4.5.1 Samples and curing conditions

Fire test samples are casted and demolded 24 hours following the casting. They are then stored in three different curing conditions:

- Water: cure in water for 89 days
- Tight bag: cure in water for 7 days and in tight bag for 82 days
- RH 75 %: cure in water for 7 days and in containers with relative humidity of 75 % for 82 days. Relative humidity in containers is controlled by saturated solution of NaCl (360 g of salt crystals per 1 L of water) at the bottom of containers.

For each curing condition and mix, three fire test samples and one water content sample are prepared making a total of 63 fire test samples and 21 water content samples. Procedure for determination of water content can be found in Section 3.3.1. The values of water content for different conditions are presented in Table 4.12. In addition to this, in order to obtain distribution of water content across the sample for RH 75% curing condition, we have completed numerical simulations of drying of concrete.

Due to a high number of samples and time limitation, majority of samples are tested in one storage condition. The curing condition is selected based on fire tests on concrete without fibers C-0 stored in three conditions: water, tight bag and RH 75%. In addition, samples of C-24/34-1.5 are tested in three conditions. Then, one curing condition is chosen for the tests on other mixes.

**Table 4.12** Overall water content (%) for mix stored in differed conditions.

Curing condition	C-0	C-18/34-1	C-18/34-1.5	C-18/34-2	C-24/34-1	C-24/34-1.5	C-24/34-2
Water	5.89	-	-	-	-	4.60	-
Tight bag	4.86	-	-	-	-	4.24	-
RH 75%	4.76	4.37	4.26	4.17	4.52	4.58	4.55

## 4.5.2 Numerical simulations of moisture distribution

We have conducted numerical study of concrete drying in order to identify moisture distribution in case of curing condition RH 75%. We first present the phenomenon of drying. We provide conservation equations at macroscopic level. Then, constitutive equations of the model are provided with presentation of model parameters. Finally, implementation of the model followed by results and conclusions is presented.

### Drying of concrete

Drying of concrete is linked to hydal misbalance created by movement of water from interior of material to exterior environment at presence of gradient of relative humidity between environment and concrete sample. Drying is a complex phenomenon consisting of multiple mechanisms of water transport in concrete presented in Figure 4.12. These mechanisms are diffusion, movement of water and gas, evaporation/condensation and adsorption/desorption agreed to occur in a coupled way.

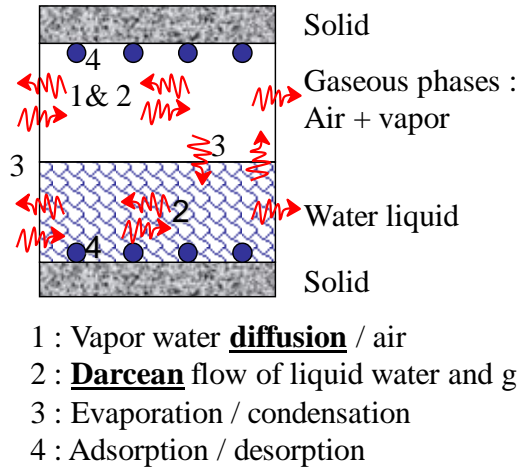


**Figure 4.12** Mechanisms that occur in drying as adapted from [12].

### Conservation equations

#### Mass balance

Mass balance equation for liquid water, water vapor and dry air writes as:

$$\dot{m}_l + \text{div}(m_l v_l) = -\dot{m}_{vap} - \dot{m}_{hyd} \quad (4.2)$$

$$\dot{m}_v + \text{div}(m_v v_v) = \dot{m}_{vap} \quad (4.3)$$

$$\dot{m}_a + \text{div}(m_a v_a) = 0 \quad (4.4)$$

where  $m_l$ ,  $m_v$  and  $m_a$  are masses of liquid water, water vapor and dry air per volume in concrete,  $m_{vap}$  is mass of vaporized water per unit volume and  $m_{hyd}$  is mass of water per volume due to hydration,  $v_l$ ,  $v_v$  and  $v_a$  are velocities of fluid water, vapor water and dry air. Mass per unit volume depends on porosity  $\phi$  and fluid masses depend on saturation degree  $S_l$ . Mass per unit volume can then be expressed as (where  $\rho_x$  is density,  $x$  is material) :

$$m_s = (1 - \phi)\rho_s \quad (4.5)$$

$$m_l = \rho_l S_l \phi \quad (4.6)$$

$$m_v = \rho_v (1 - S_l)\phi \quad (4.7)$$

$$m_a = \rho_a (1 - S_l)\phi \quad (4.8)$$

The flow of liquid water in the material is described using Darcy's law:

$$v_l = -\frac{Kk_{rl}}{\mu_l} \text{grad}(p_l) \quad (4.9)$$

where  $v_l$  is velocity of liquid water,  $K$  is coefficient of water permeability,  $k_{rl}$  is relative water permeability,  $\mu_l$  is viscosity of liquid water and  $p_l$  is pressure of liquid water.

Fick's law is used to describe diffusion of relative humidity in vapor and gas. Considering only liquid water permeation, we obtain the following forms for mass flux of liquid water, water vapor and dry air:

$$m_l v_l = -\rho_l \frac{Kk_{rl}}{\mu_l} \text{grad}(p_l) \quad (4.10)$$

$$m_v v_v = -\frac{M_v p_{atm}}{RT} D \text{grad}\left(\frac{p_v}{p_g}\right) \quad (4.11)$$

$$m_a v_a = -\frac{M_a p_{atm}}{RT} D \text{grad}\left(\frac{p_a}{p_g}\right) \quad (4.12)$$

where  $M_v$  and  $M_a$  are molar masses of vapor water and gas,  $p_{atm}$  is atmospheric pressure,  $R$  is gas constant,  $T$  is temperature,  $D$  is coefficient of diffusion,  $p_v$ ,  $p_a$  and  $p_g$  are vapor water, dry air and gas pressures.

#### *Simplified approach for drying*

For ambient temperature drying, following hypotheses are considered [12], [13]:

- Deformation of solid skeleton is negligible
- Temperature is constant
- Gas transfer is not considered
- Gas pressure is equal to atmospheric pressure and is negligible in comparison to liquid water pressure and capillary pressure, thus, liquid water pressure is equal to capillary pressure,  $p_l = p_c$ .

Taking into account these hypotheses, we can then obtain the following relationship:

$$S_l \phi v_l = -\frac{Kk_{rl}(S_l)}{\mu_l} \text{grad}(p_c) \quad (4.13)$$

Using Equation 4.6, we obtain the following form to describe drying of concrete due to liquid water migration:

$$\frac{\partial S_l}{\partial \rho_c} \frac{\partial \rho_c}{\partial t} = \text{div} \left( \frac{K k_{rl}}{\mu_l \phi} \text{grad} (p_c) \right) \quad (4.14)$$

### Constitutive equations

Degree of saturation is calculated such as :

$$S_l = \frac{w \rho_c}{\phi \rho_l} \quad (4.15)$$

where  $w$  is water content.

Capillary pressure is found as a function of external relative humidity  $h$ :

$$p_c = \frac{\rho_l R T \ln(h)}{M_w} \quad (4.16)$$

where  $M_w$  is molar mass of water.

We can then compute degree of saturation as a function of capillary pressure using model of van Genuchten [14]:

$$S_l(p_c) = \left[ \left( \left( \frac{p_c}{a} \right)^{\frac{b}{b-1}} + 1 \right)^{-\frac{1}{b}} \right] \quad (4.17)$$

where  $a$  and  $b$  are material parameters. Or, in other words:

$$p_c = a \left[ (S_l^{-b} - 1)^{1-\frac{1}{b}} \right] \quad (4.18)$$

Relationship for relative permeability as a function of degree of saturation is proposed in [14]:

$$k_{rl}(S_l) = S_l^{n_k} \left[ \left( 1 - (1 - S_l^{b_{mu}})^{\frac{1}{b_{mu}}} \right)^2 \right] \quad (4.19)$$

The model for concrete drying is presented in Equation 4.14. Model parameters required are:

- evolution of  $\frac{\partial S_l}{\partial \rho_c}$ ,  $S_l(p_c)$  determined from isotherm of desorption
- $K$  is determined from inverse analysis of mass loss
- $k_{rl}$  (see Equation 4.19)
- $\phi$  is measured experimentally using Equation 3.15.

## Implementation

We present implementation of this model developed in LMT Cachan for case of reference concrete drying at 75 % RH for 90 days. We have used Cast3M for thermal problem, which has a similar form as hydral problem.

### *Material properties*

First, we are interested in identification of parameters  $a$  and  $b$  presented in [14] which can be identified from desorption isotherm. We have selected an experimental study from literature [15] for a high strength concrete with a similar W/C. Results of desorption isotherm obtained using identified parameters are presented in Figure 4.13 and appear to fit experimental data.

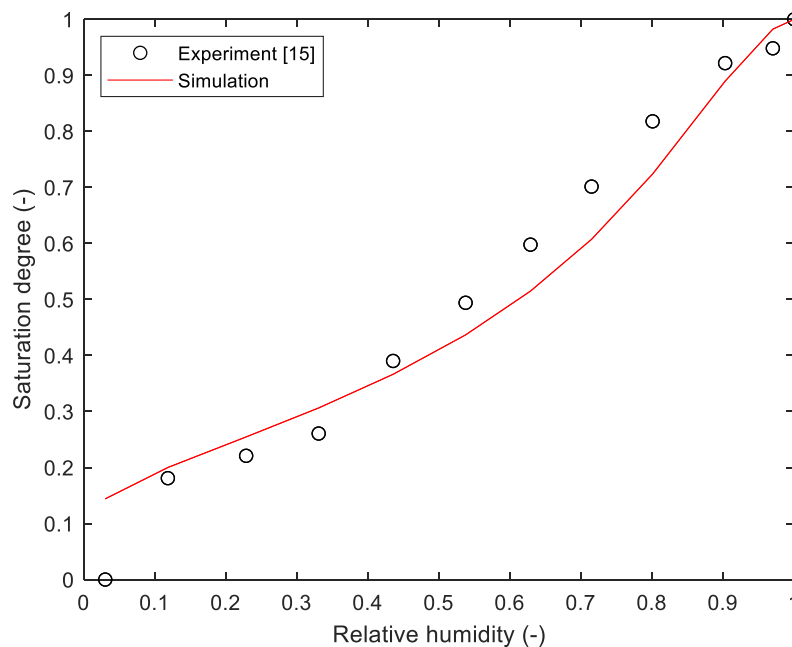


**Figure 4.13** Desorption isotherm: experiment [15] and our simulation.

We present in Table 4.13 material properties considered for simulations. Most of the data is well known, such as viscosity and molar mass of water, while some parameters such as water permeability are not known. Due to absence of mass loss measures during storage in RH 75%, inverse analysis to determine water permeability cannot be accomplished. We however consider a range of possible values for high strength concrete:  $10^{-21}$  -  $10^{-22}$   $m^2$ . The values of porosity and density are determined experimentally.

**Table 4.13** Properties of materials used.

Property	Value
a	-26.5 MPa
b	2.49 MPa
K	$10^{-21}$ - $10^{-22}$ m <sup>2</sup>
$\rho_c$	2400 kg/m <sup>3</sup>
$\phi$	14 %
$\rho_l$	1000 kg/m <sup>3</sup>
$\mu_l$	0.001 Pa.s
$M_w$	0.018 kg/mol

### *Geometry and boundary conditions*

Axisymmetric simulations have been conducted in 2D using a mesh size of  $5.5 \times 5$  cm<sup>2</sup> with 30 elements in  $e_z$  and  $e_r$  directions making it total of 900 elements. Modelled section is presented in Figure 4.14. In terms of boundary conditions, there is an exchange with environment with RH fixed to 75%.

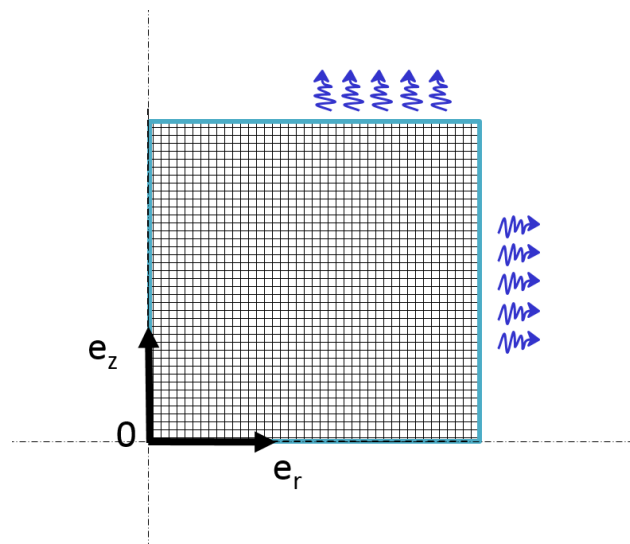


**Figure 4.14** Modelled mesh. Arrows represents exchange with environment.

### **Results of numerical simulations**

We present in Figure 4.15 water content distribution of concrete curing in RH 75 % for 90 days obtained via numerical simulations. The results show that during storage in RH 75%, drying of saturated samples occurs. With increase of water permeability by one order, drying is significantly accelerated. Water content at the surface is found to be 3.5 % in both cases and at depth of 1 cm is 3.8 and 4.7 % for water permeability of  $10^{-21}$  and  $10^{-22}$  m<sup>2</sup> respectively. Unfortunately, during storage condition at RH 75% mass of samples has not been measured to

avoid perturbation. Adjustment of water permeability through mass loss curves obtained experimentally and numerically could have been a solution to missing data. Nevertheless, the results show the importance of water permeability in drying calculations and show a significant drying front for RH 75%.

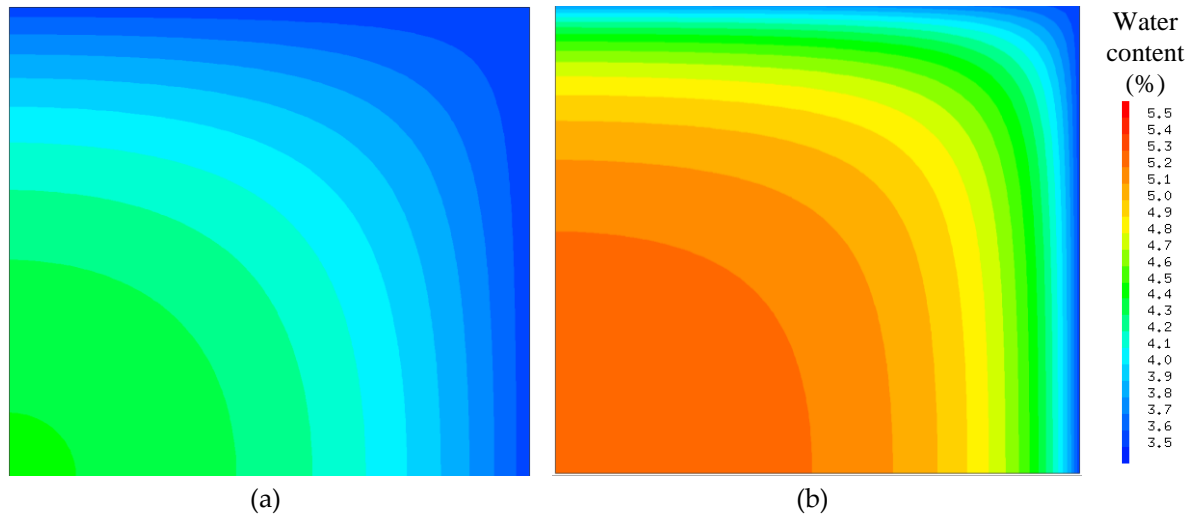


**Figure 4.15** Water content at 90 days obtained for water permeability: a)  $10^{-21} \text{ m}^2$ , b)  $10^{-22} \text{ m}^2$ .

### 4.5.3 Experimental apparatus and procedure

Fire tests are accomplished using experimental apparatus and procedure presented in Section 3.3.2. One exception is that instead of 5 MPa for uniaxial compressive loading, we apply 20 MPa. This value is obtained using a thermo-mechanical simulation for three containers piled on top of one another. The results of these simulations are not presented here. The loading for 20 MPa is found as a maximum mechanical stress that container located at the bottom experiences under ISO 834-1 fire curve. The 3D mesh for a single container is shown in Figure 4.16.

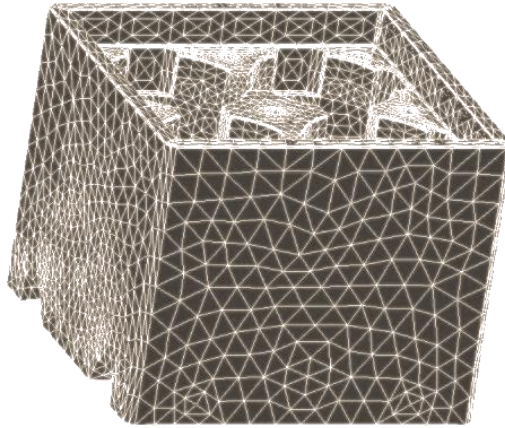


**Figure 4.16** 3D mesh of waste storage container.

#### **4.5.4 Fire test results**

##### **Overview of results**

During fire tests, occurrence of each spalling event is noted which provides an information on the start, end and number of spalling events. After fire tests, mean and maximum spalling depth as well as spalled volume are evaluated by means of photogrammetry. It is important to note that exposed surface is reduced to account for wall effects. We present in Table 4.14 results of fire tests containing an information on start and end of spalling and number of spalling events, mean and maximum spalling depth and spalled volume.

We plot in Figure 4.17 a relation between maximum and mean spalling depth (or spalled volume as calculated surface remains the same) for all concrete mixes. Due to a correlation between the two, we choose to present all the results in terms of mean spalling depth.

**Table 4.14** Results of fire tests.

Mix	Condition	N	t <sub>Start</sub> (min)	t <sub>End</sub> (min)	Nbr of events (-)	h <sub>mean</sub> (cm)	h <sub>max</sub> (cm)	V <sub>sp</sub> (cm <sup>3</sup> )
C-0	Water	1	11	27	10	1.82	2.97	472.87
		2	12	24	16	1.80	3.29	721.48
		3	11	24	9	1.15	2.31	458.95
		Average	11.3	25	11.7	1.59	2.86	551.10
	Tight bag	1	14	28	8	2.50	4.08	1001.40
		2	12	25	12	1.55	2.92	621.24
		3	13	28	13	0.86	1.99	343.15
		Average	13	27	11	1.64	3.00	655.26
	RH 75%	1	14	29	24	1.77	3.20	709.33
		2	12	28	16	1.94	3.17	783.06
		3	13	29	21	1.52	2.78	606.43
		Average	13	28.7	20.3	1.74	3.05	699.61
C-18/34-1	RH 75%	1	14	14	1	0.52	1.37	209.39
		2	-	-	0	0	0	0
		3	13	16	3	0.37	1.38	148.50
		Average	13.5	15	1.3	0.30	0.92	119.30
C-18/34-1.5	RH 75%	1	-	-	0	0	0	0
		2	-	-	0	0	0	0
		3	-	-	0	0	0	0
		Average	-	-	0	0	0	0
C-18/34-2	RH 75%	1	-	-	0	0	0	0
		2	-	-	0	0	0	0
		3	-	-	0	0	0	0
		Average	-	-	0	0	0	0
C-24/34-1	RH 75%	1	17	22	3	0.73	2.58	290.75
		2	15	15	1	0.22	0.94	87.82
		3	15	15	1	0.33	1.28	131.72
		Average	15.7	17.3	1.7	0.43	1.60	170.10
C-24/34-1.5	Water	1	-	-	0	0	0	0
		2	-	-	0	0	0	0
		3	-	-	0	0	0	0
		Average	-	-	0	0	0	0
C-24/34-1.5	Tight bag	1	-	-	0	0	0	0
		2	-	-	0	0	0	0
		3	-	-	0	0	0	0
		Average	-	-	0	0	0	0
C-24/34-1.5	RH 75%	1	-	-	0	0	0	0
		2	-	-	0	0	0	0
		3	-	-	0	0	0	0
		Average	-	-	0	0	0	0
C-24/34-2	RH 75%	1	-	-	0	0	0	0
		2	-	-	0	0	0	0
		3	-	-	0	0	0	0
		Average	-	-	0	0	0	0

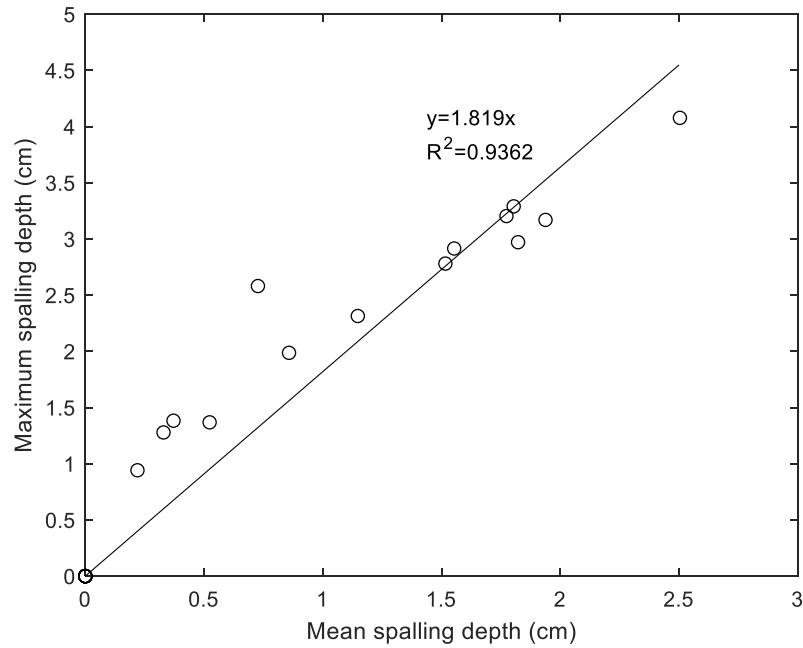


**Figure 4.17** Maximum spalling depth vs. mean spalling depth.

### **Selection of curing condition for fire test**

We shall remind that concrete prisms are stored in three different curing conditions:

- Water: 89 days in water
- Tight bag: 7 days in water and 82 days in tight bag
- RH 75%: 7 days in water and 82 days in RH 75%.

Since we are interested in selecting one storing condition based on average mean spalling depth, we conduct fire tests on C-0 and C-24/34-1.5 stored in three conditions. As a result, all reference samples have spalled while none of C-24/34-1.5 have spalled despite the difference in storing conditions.

We present in Figure 4.18a and 4.18b the images of surfaces exposed to fire and spalling depth maps for reference mix C-0. All of the samples after tests present at least one vertical crack in the direction of loading. We note a similarity in spalling patterns between curing conditions.

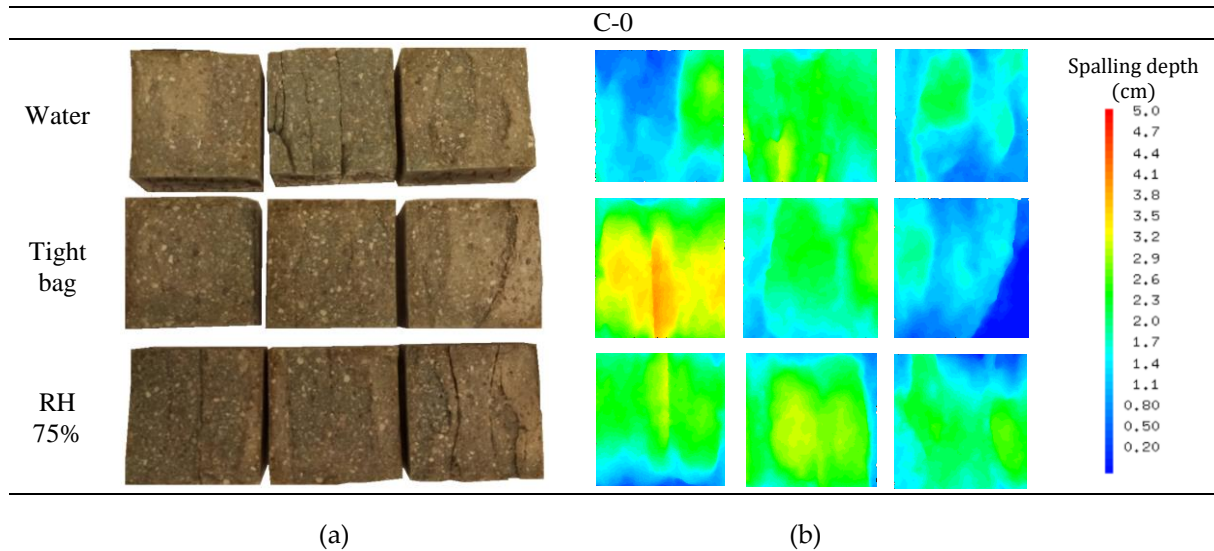


**Figure 4.18** Surfaces of C-0 cured at different conditions: a) after fire test, b) spalling depth maps.

After fire test, a visual inspection has revealed a variation of thickness of spalled pieces with curing conditions presented in Figure 4.19. We note that the thickness of the spalled parts varies with curing: it is the lowest for RH 75% and the highest for water-stored samples.

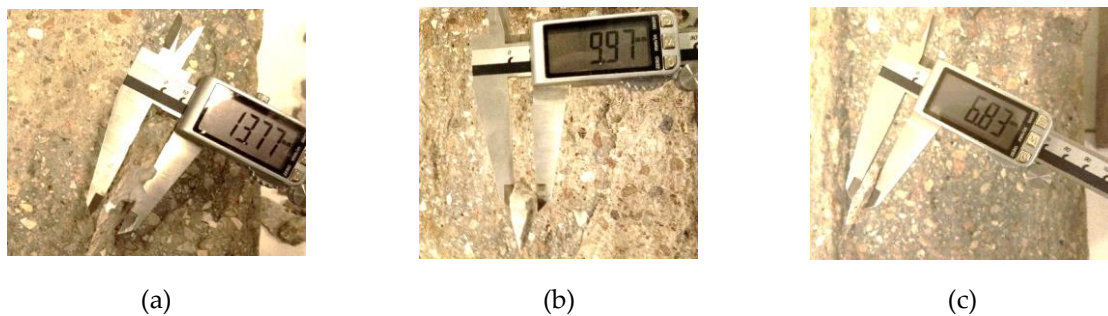


**Figure 4.19** Thickness measurements of spalled pieces for concrete stored under: a) water, b) tight bag, c) RH 75%.

We plot Figure 4.20a and 4.20b to present an evolution of the start of spalling events and number of spalling events for reference mix C-0 as a function of storage conditions. From Figure 4.20a we note that on average spalling starts earlier for water stored samples than for tight bag and RH 75%, both of which present same start of spalling events. In terms of number of spalling events presented in Figure 4.20b, we note that on average for samples stored in RH 75% number of spalling events is the highest: 20.3 events compared to 11.7 and 11 events for water and tight bag conservations respectively. It is interesting to note that compared to water cure, samples in RH 75% spall later, with a greater frequency and a thinner section of spalled pieces.

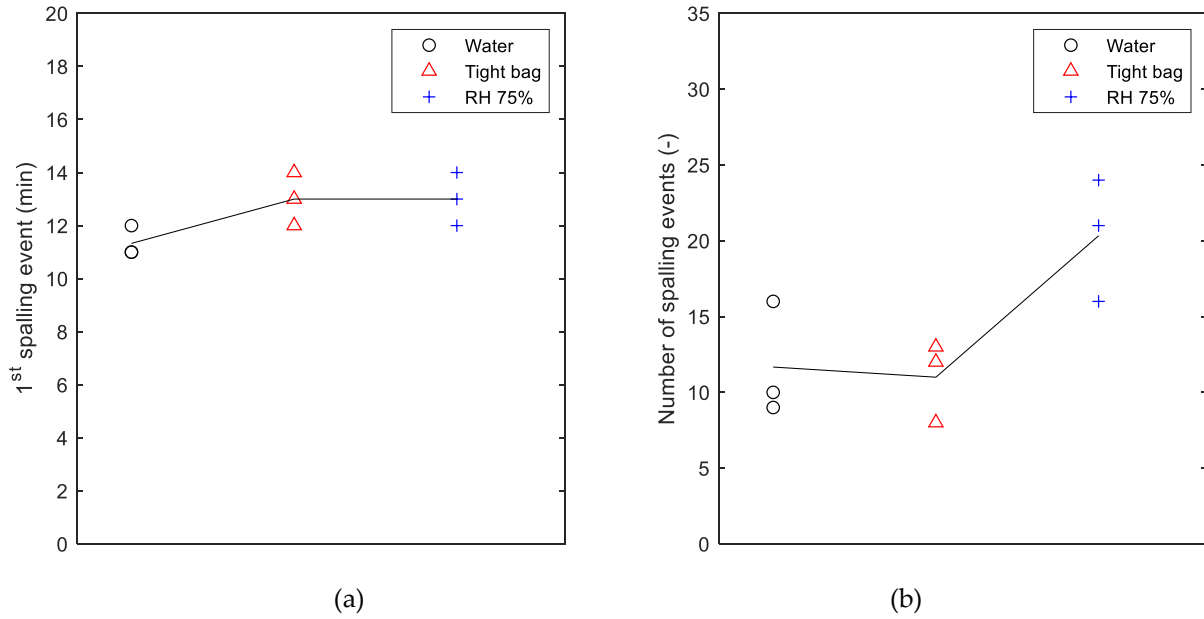


**Figure 4.20** Influence of curing conditions on a) start of spalling, b) number of spalling events of C-0 mix.

Results show that storing condition has a great influence on spalling start and number of spalling events. Saturation level in tight bag condition should be same as for water condition due to limitation of moisture transfer. However, it is possible to suppose that a little surface drying has occurred in tight bag due to a possible moisture transfer related to presence of small defects in sealing. This drying is enough to delay start of spalling for tight bag condition compared to water stored samples. In terms of number of spalling events, we see that despite delay in spalling start, number of spalling events for water and tight bag is same. For RH 75%, a significant drying process has occurred, creating important hydral gradients across the sample, i.e. low water content in first centimeters compared to high water content in the heart. Our numerical simulations of drying at 75 % RH confirm this statement. A network of microcracks has been developed due to restrained shrinkage of cement paste, decreasing mechanical performance of concrete after drying. These cracks, however, are found to be beneficial in terms of moisture redistribution during fire in terms of delay in formation of moisture clog and start of spalling. It is possible to suggest that existing shrinkage induced cracks would localize thermo-mechanical cracks and with reduced mechanical strength, concrete would spall more often with lower thickness of spalled pieces. In fact, for RH 75% thickness of spalled piece is the lowest with the highest number of spalling events.

This finding is however surprising from a point of view of moisture clog formation. Moisture clog occurs at a depth where moisture coming from the hot drying surface accumulates up to the point of the saturation. In case of samples cured in water, moisture clog should be present at smaller depth compared to material that underwent drying due to higher initial saturation and higher moisture flow from the heated surface. In addition, water-cured material is less prone to microcracking developed during curing stage as it is the case for dried samples, which would suggest high thermal stresses and pore saturation next to the surface driving process into earlier and thinner spalled pieces. It is however peculiar to note that the thickness of these spalled pieces is twice as thick as of that cured at 70 % RH, which is the opposite of the expected result according to moisture clog theory. It is possible to suggest a presence of competition between moisture clogging and drying front mechanism. Therefore, even though the clogging occurs earlier for water-cured samples, splinters are thinner in dried samples due to presence of drying induced microcracks.

We plot Figure 4.21 to present an evolution of mean spalling depth for three curing conditions. Dispersion among the samples noted in images of Figure 4.18b is clearly observed. Average mean spalling depth is slightly higher for samples stored in RH 75% than for tight bag and water storage. Despite the fact that spalled pieces were thinner for dried samples, higher occurrence of spalling events has led to higher spalling depth. Presented results show a significant influence of storing conditions on sensitivity of concrete to spalling. Based on slightly higher severity, we choose RH 75% as a storage condition to be tested for the rest of the mixes.

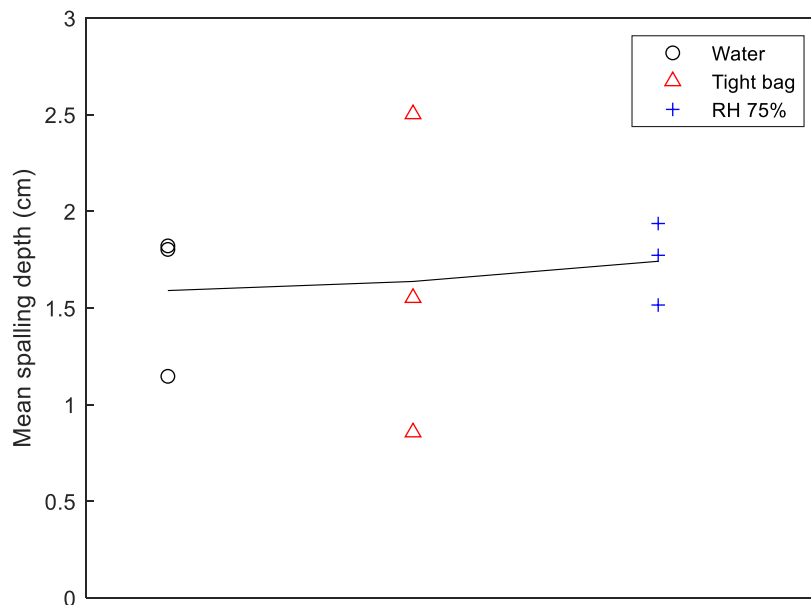


**Figure 4.21** Mean spalling depth for C-0 for three curing conditions.

### Fire tests on fiber reinforced mixes

In this part, we present results of fire tests on concretes containing 18 and 24 mm fibers at dosages of 1, 1.5 and 2 kg/m<sup>3</sup>. We shall remind as well that paste volume (or filler content) varies for each mix (see Table 4.9).

Spalling has occurred for two mixes C-18/34-1 (2 samples out of 3) and C-24/34-1 (3 samples out of 3). Post-fire and photogrammetry images presented in Figure 4.22 show a dispersion in spalling tendencies explained by the small size of the samples.

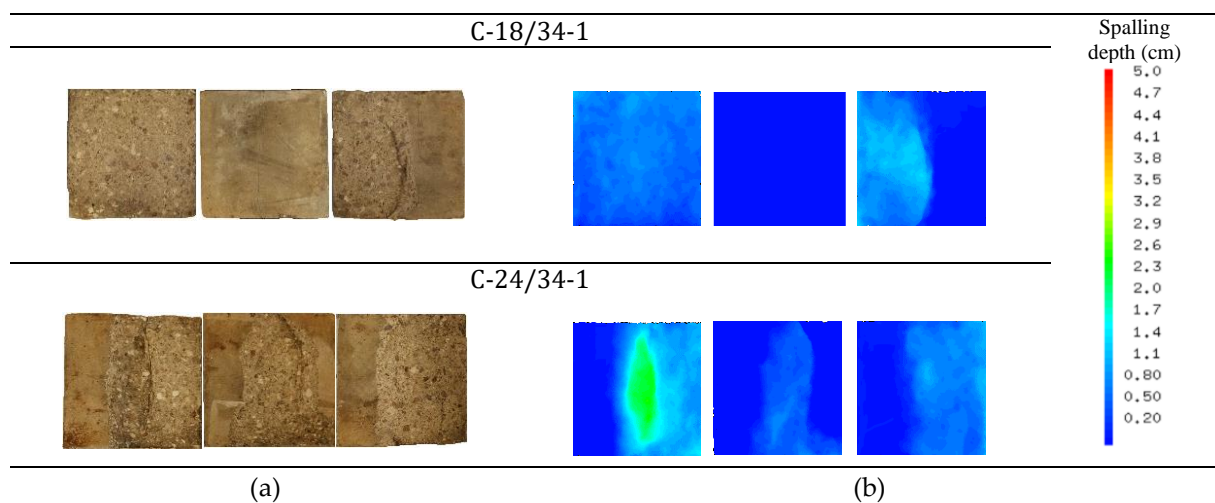


**Figure 4.22** Surfaces of C-18/34-1 and C-24/34-1 cured at RH 75% condition: a) after fire test, b) spalling depth maps.

We plot in Figure 4.23a and 4.23b the time of the first spalling event and number of spalling events for mixes C-18/34 and C-24/34 as a function of fiber dosage. We note in Figure 4.23a that increase of fiber dosage from to 1 kg/m<sup>3</sup> delays a start of spalling: on average, 30 seconds later for mixes C-18/34 and 2.6 minutes later for C-24/34. Due to absence of spalling for 1.5 and 2 kg/m<sup>3</sup> for concretes of both fiber length, no data for these dosages is available. In terms of number of spalling events for C-18/34 and C-24/34 (see Figure 4.23b), we note no difference between two fiber lengths.

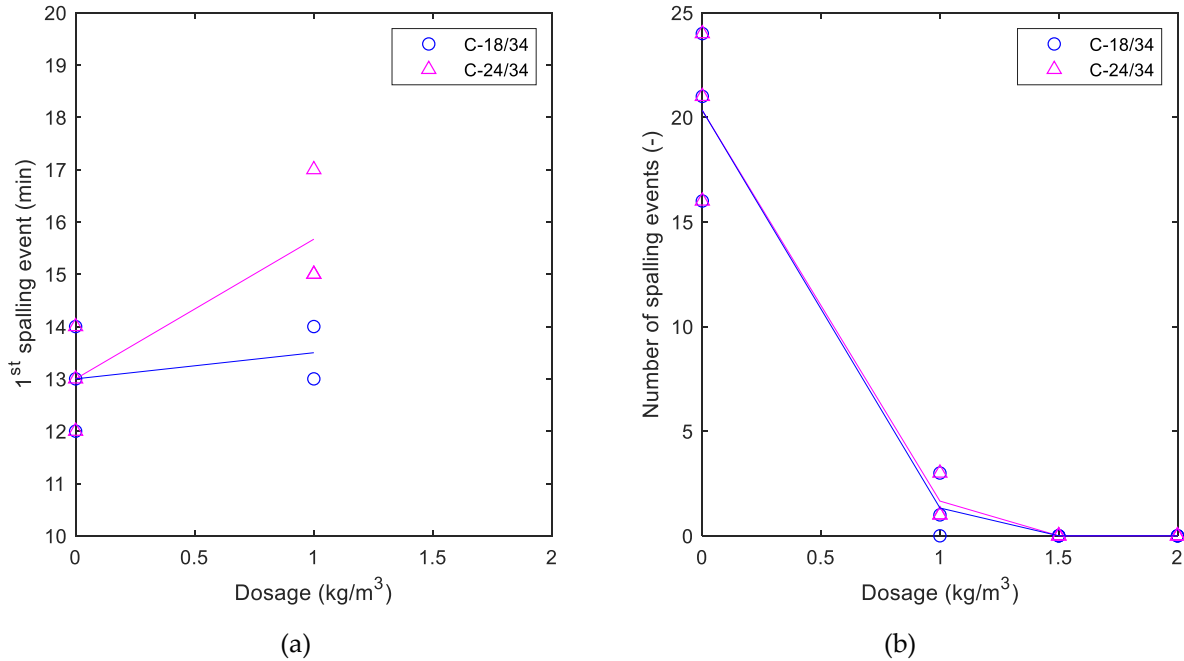


**Figure 4.23** Influence of fiber dosage on a) start of spalling, b) number of spalling events.

We plot in Figure 4.24a and Figure 4.24b an evolution of mean spalling depth as a function of dosage and total number of fibers for C-18/34 and C-24/34 respectively. We note that addition of polypropylene fibers has significantly reduced spalling extent: on average, mean spalling depth of concrete is reduced by 83 % and 76 % with a use of 1 kg/m<sup>3</sup> of 18 and 24 mm fibers respectively. With a further increase of fiber dosage to 1.5 and 2 kg/m<sup>3</sup>, no spalling is observed for concrete containing both fiber lengths. We notice that at dosage of 1 kg/m<sup>3</sup> 18 mm fibers are slightly more efficient than 24 mm fibers in mean spalling depth reduction. This result is mainly linked to a higher number of fibers for same dosage of fibers: 67 million/m<sup>3</sup> for 18 mm fibers compared to 50 million/m<sup>3</sup> for 24 mm fibers. We shall note as well that mix C-24/34-1 has 1.3 l/m<sup>3</sup> more paste volume or 3 kg/m<sup>3</sup> of filler than mix C-18/34-1. Increase of paste volume increases risk of spalling, however, such slight increase can be considered negligible. According to these results, we find that use of polypropylene fibers is effective for spalling reduction even at high level of load. Out of six mixes containing fibers, four mixes present no spalling. At lower dosage, 18 mm fibers are slightly more efficient than 24 mm fibers due to a higher number of fibers. Residual permeability tests performed in Chapter 3 has shown that 18 mm fibers were sufficient in increase of permeability due to improved percolation with thermally induced cracks.

We can now propose mixes for intermediate scale fire tests on small slabs. First, since we have observed spalling with mixes containing 1 kg/m<sup>3</sup> under loading of 20 MPa, it would be

interesting to investigate whether some spalling would be observed on slabs under lower levels of loading. Second, validation of mixes C-18/34-1.5 and C-24/34-1.5 on larger scale is important, as these mixes have shown to be optimized from rheological point of view and to present no spalling at laboratory scale small fire tests.

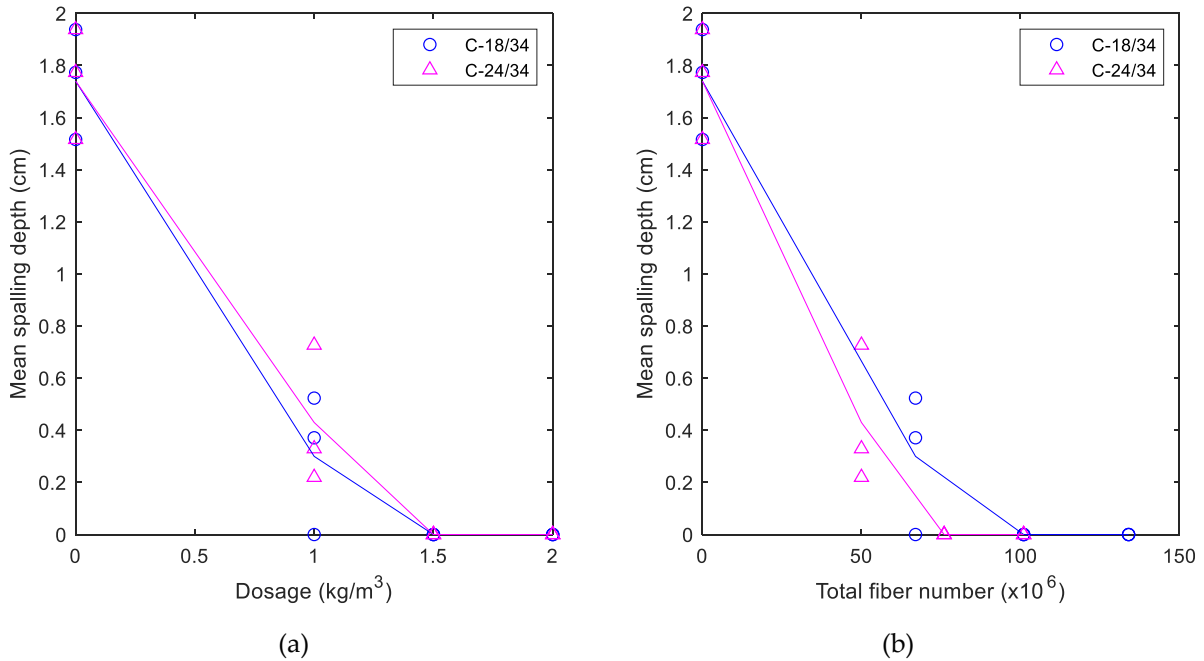


**Figure 4.24** Mean spalling depth as a function of : a) fiber dosage, b) total fiber number.

## 4.6 Conclusions

This chapter presents a method of formulation of concrete with polypropylene fibers optimized both from rheological and fire performance perspectives. Requirements on concrete composition and performance as well as main conclusions of previous chapters have served as guidelines for mix design. We have presented our formulation procedure that consists of four main stages: 1) choice of materials, 2) mix design of reference concrete and 3) of fiber-reinforced concrete and 4) verification of performance at fresh and hardened state. Using this design method, seven final mixes have been developed: a reference without polypropylene fibers and six mixes with 18 mm and 24 mm fibers at dosages of 1, 1.5 and 2 kg/m<sup>3</sup>. The fresh and hardened state properties of the mixes have shown to satisfy, in general, the imposed requirements. Finally, fire tests conducted on uniaxially loaded prisms showed no spalling for concretes with 18 and 24 mm fibers at dosages of 1.5 and 2 kg/m<sup>3</sup> stored in containers with a relative humidity of 75 %. All reference samples tested in three different curing conditions have

spalled as well as concrete with 18 mm and 24 mm fibers at dosage of  $1 \text{ kg/m}^3$  cured in a relative humidity of 75 %. Some simulations developed to study moisture distribution for RH 75% show a presence of strong drying front that has influenced spalling. At  $1 \text{ kg/m}^3$ , 18 mm fibers are found to be a little more efficient than 24 mm fibers due to a higher fiber count. No spalling is observed at 1.5 and  $2 \text{ kg/m}^3$  for both 18 and 24 mm long fibers. It could be concluded that 18 mm long fibers at  $1.5 \text{ kg/m}^3$  are sufficient to prevent spalling of high strength concrete under selected curing and testing conditions.

Presented work shows that it is possible to design concrete that can be both fluid and fire resistant. Further investigation at a higher scale fire testing will be produced using mixes selected from this study in order to assess size effect.

## 4.7 Reference list

- [1] ANDRA. (2016). Cahier des charges- Développement d'une formulation béton pour conteneur de stockage MAVL et réalisation de prototypes.
- [2] Roussel N. (2014). Rapport formulation béton. AREVA.
- [3] Sedran T. and Larrard F. (1999). Optimization of self-compacting concrete thanks to packing model. Proceedings of the 1<sup>st</sup> International RILEM Symposium on Self-Compacting Concrete. Stockholm, Sweden.
- [4] Su N., Hsu K.-C. and Chai H.-W. (2001). A simple mix design method for self-compacting concrete. *Cement and Concrete Research* 31: 1799–1807.
- [5] Su N. and Miao B. (2003). A new method for the mix design of medium strength flowing concrete with low cement content. *Cement and Concrete Composites* 25 : 215–222.
- [6] Sebaibi N., Benzerzour M., Sebaibi Y. and Abriak N.E. (2013). Composition of self-compacting concrete (SCC) using the compressible packing model, the Chinese method and the European standard. *Construction and Building Materials* 43: 382–388.
- [7] Brouwers H. J. H. and Radix H. J. (2005). Self-Compacting Concrete: Theoretical and experimental study. *Cement and Concrete Research* 35: 2116–2136.
- [8] Schwartzenruber A. and Catherine C. (2000). Method of the concrete equivalent mortar (CEM) - A new tool to design concrete containing admixture. *Materials and Structures* 33: 475-482.
- [9] Larisch M., Qin Z. and Alehossein H. (2013). Performance control tests and numerical simulations for concrete in deep foundations. *Concrete in Australia* 39 : 26-34.
- [10] TP Matériaux cimentaires. (2014). Travaux Pratiques. ISA BTP, Université de Pau et des Pays de l'Adour.
- [11] Air entrainment meters. Controls Group. <https://www.controls-group.com/eng/concrete-testing-equipment/air-entrainment-meters.php>
- [12] Mainguy M., Coussy O. and Baroghel-Bouny V. (2001). Role of air pressure in drying of weakly permeable materials. *Journal of Engineering Mechanics* 127: 582-592.
- [13] Thiery M., Baroghel-Bouny V., Bourneton N, Villain G. and Stéfani C. (2007). Modélisation du séchage des bétons. *Revue Européenne de Génie Civil* 11: 541-577.

- [14] van Genuchten M. (1980). A closed-form equation for predicting the hydraulic conductivity of unsaturated soils. *Soil Science Society of America* 44: 892-898.
- [15] Baroghel-Bouny V.(2007). Water vapour sorption experiments on hardened cementitious materials Part I: Essential tool for analysis of hygral behaviour and its relation to pore structure. *Cement and Concrete Research* 37: 414-437.

## CHAPTER 5

### CONCLUSIONS AND PERSPECTIVES

#### 5.1 Overview of the thesis

In this thesis, we have worked on developing formulation of self-compacting fire resistant concrete with polypropylene fibers for storage of radioactive waste of long live and medium activity. The challenge of this work is presented by polypropylene fibers in concrete that have contradictory effects on rheology and fire resistance: adding polypropylene fibers improves resistance to fire while reducing fluidity of concrete at fresh state. We have therefore worked on two different research axes, such as rheology and fire resistance, in order to understand the influence of fiber geometry and dosage on both properties and to be able to optimize these parameters to achieve desired concrete performance. The conclusions on choice of polypropylene fibers have been used as guidelines for formulation of fire resistant fluid concrete containing polypropylene fibers.

To quantify the influence of polypropylene fibers on the yield stress of fresh cementitious composites, we have completed spread tests and slump tests on fresh cement paste and mortars using polypropylene fibers of different geometry and dosage. We have shown bending of polypropylene fibers by means of microtomography on cement paste samples containing 6 and 24 mm long fibers. We have conducted total organic carbon measurements that have shown a presence of organic compound that could have a slight deflocculant effect on cement paste. The main part of the work is development of a physical model that can predict the yield stress of cement paste using a set of parameters such as fiber geometry, volume fraction, elastic modulus of polypropylene and the yield stress of cement paste without fibers. Using this predictive scheme, we have obtained a master curve for our experimental results on cement paste containing a large range of polypropylene fiber geometries of aspect ratio 176 to 706. On mortar scale, we have presented a simple model that can predict the evolution of the yield stress of

mortars containing polypropylene fibers with a simple addition of contributions of sand and fibers to the total packing fraction. We have found that bending of fibers occurs due stresses exerted by entire suspension. These results have allowed us to quantify the amount of additional paste or extractable aggregate volume necessary to retrieve the fluidity of fresh concrete lost due to influence of polypropylene fibers. This part of the work is found to be particularly interesting in design of self-compacting concrete with polypropylene fibers.

For experimental investigation of fire resistance of concrete, we have aimed at optimizing the choice of polypropylene fiber dosage and geometry for different cementitious materials with various granular skeletons and maximum size of aggregates. These materials are mortar ( $D_{\max}=1$  mm), concrete 1 ( $D_{\max}= 10$  mm) and concrete 2 ( $D_{\max}= 20$  mm). First, we have completed a thermal analysis of two types of polypropylene fibers (normal and low melt viscosity) in order to retrieve the exact information on melting and degradation temperature, as well as viscosity of polypropylene at 180 °C. Our experimental plan for high temperature investigation has included residual radial permeability test and fire test under uniaxial compressive loading of 5 MPa on prisms. The results of this work have allowed us to understand better the influence of fiber dosage and geometry on intrinsic permeability and response to spalling. With these results, we have selected an optimized fiber geometry and dosage for cementitious material of particular granular skeleton. The conclusions of this work has served as a basis for choice of fibers with respect to cementitious material to enhance its performance in fire.

For numerical investigation of this chapter, we have completed finite element simulations of damage of cementitious materials at high temperature using thermo-mechanical models in Cast3M studying two different questions. First, we have investigated whether expansion of polypropylene fibers could induce damage of mortar at high temperature and evolution of this damage with increase of fiber diameter. Second, we have completed 2D mesoscale simulations of three cementitious materials studied in experimental part as well as of concrete containing a full granular skeleton in order to investigate cracking patterns of each material.

In final part of this thesis, we proceed with formulation of self-compacting fire resistant concrete with polypropylene fibers. The choice of polypropylene fibers is based on conclusions of rheology and high temperature tests. We have presented a procedure for mix design based on packing model for aggregates and its application in our case. We have developed one reference concrete mix and six concrete mixes with polypropylene fibers verified for fresh state and hardened state performance. In addition to this, some numerical simulations of drying of concrete have been completed in order to analyze moisture distribution across the sample. In

the final part, fire tests under uniaxial compressive loading have been conducted in order to verify resistance of mixes to spalling at small scale. The results of this chapter show that it is possible to design concrete, which can be both fluid and fire resistant.

The challenge of this thesis lies in tackling two different research topics such as rheology and fire resistance. It is worth noting that conclusions of this work are not limited to radioactive waste storage and transferrable to other applications of concrete.

## 5.2 Main conclusions

Main findings of the thesis from both experimental and numerical studies are presented and summarized below.

From study on rheological behavior of fiber reinforced cementitious composites we have made following conclusions:

- The yield stress of fresh cement pastes and mortars increases with addition of polypropylene fibers. We have noted that increase of fiber dosage provokes an increase in the yield stress or decrease in slump flow of cement pastes and mortars. In terms of the influence of fiber geometry, we note that increase fiber length and decrease of fiber diameter provokes an increase of the yield stress.
- Polypropylene fibers are flexible synthetic fibers whose conformation depends on the yield stress of suspending fluid. In cement paste with  $W/C=0.35$ , we have observed a simple curvature for 6 mm long fibers and multiple curvatures for 24 mm long fibers both with diameter of  $34\ \mu\text{m}$  via microtomography scans. We have noted that for  $34\ \mu\text{m}$  diameter, 12 mm long fibers tested in two different cement pastes ( $W/C = 0.5$  and  $0.45$ ), fibers bend more in rigid paste.
- Surface coating of polypropylene fibers presents an organic compound that can lightly reduce the yield stress of cement paste. This organic molecule found present using TOC analyzer has shown to decrease slightly the yield stress of cement paste at low fiber dosage. However, it has been suggested that this influence is negligible at higher dosages and should not be taken into account in industrial applications.
- The yield stress of cementitious materials containing polypropylene fibers can be described using a physical model that takes into account fiber geometry, elastic modulus of polypropylene, volume fraction of fibers and the yield stress of suspending medium. Using a large set of experimental data on polypropylene fibers with a wide range of aspect ratios

from 176 to 706, we have been able to obtain a master curve for evolution of the relative yield stress of cement paste with polypropylene fibers.

- As a first approach, it is possible to sum linearly contributions of fibers and aggregates to the evolution of the relative yield stress of mortars. It is important to note that this simplified approach does not take into account interactions between fibers and aggregates and in order to establish real model non-linear calculations should be developed.
- We have found that in fresh suspensions comprising of several inclusions types such as fibers and aggregates, conformation of fibers depends on stresses exerted by overall resulting suspension.
- It is possible to calculate the amount of additional volume of paste (or volume of aggregates to be removed) necessary to cancel the influence of polypropylene fibers on fluidity of fresh concrete. This conclusion is especially useful for design of self-compacting concrete with polypropylene fibers.

From study on high temperature behavior of fiber reinforced cementitious composites we have concluded that:

- Intrinsic permeability increases with temperature for all mixes of mortar, concrete 1 and concrete 2. For reference materials without polypropylene fibers this increase starting from 150 °C is related to presence of microcracks caused by thermal mismatch of paste and aggregates. This increase of intrinsic permeability is much lower compared to mixes with polypropylene fibers.
- Presence of polypropylene fibers provokes a significant increase of intrinsic permeability of cementitious materials at 200 °C due to melting of polypropylene fibers and this increase depends on fiber geometry and dosage. The increase of fiber dosage is shown to produce an increase of intrinsic permeability. The influence of fiber length is clear: longer fibers have shown to be more efficient than shorter ones. The results have shown a clear influence of increase of fiber diameter on increase of permeability. An influence of fiber diameter has been observed when comparing two diameter fibers at same fiber number showing that thicker fibers increase permeability more than thinner ones. A possible reason for this lies in reduced apparent length thinner fibers due to its higher curvature.
- No increase of intrinsic permeability has been noted at 150 °C due to possible microcracks induced by differences in thermal expansion of matrix and fibers. Thermo-mechanical simulations have presented radial damage of surrounding matrix before melting of polypropylene fibers that suggest presence of microcracks at matrix-fiber interface. We

suggest that these cracks are disconnected one from another, affecting local permeability without much perturbation of global permeability.

- We have seen that spalling depends on maximum size of aggregates, compressive strength and initial intrinsic permeability of cementitious materials. Despite the difference in compressive strength, between mortar, concrete 1 and concrete 2, we have noted that with increase of aggregate size, spalling has occurred faster with a higher number of spalling events. Direct relation between initial permeability and spalling is found: concrete 2 having the highest initial permeability has spalled the least of all and mortar with lowest permeability has spalled the most.
- From images of cracks, we have seen that for concrete 2 cracks are located further from each other with higher crack opening than in mortar and concrete 1. 2D thermo-mechanical simulations of damage of three cementitious materials have shown localization of cracks at paste-aggregate interface due to their thermal mismatch. The distance between cracks has been found to be higher for concrete 2 than for concrete 1 which agrees with our findings. For mortar, diffused damage is noted. In addition to this, it has been found that tested materials present further located cracks due to discontinuous granular skeleton than concrete with full skeleton.
- Addition of polypropylene fibers is found to be beneficial in terms of reduction of spalling. Compared to reference samples without polypropylene fibers, spalling is reduced even at low fiber dosages for all mixes.
- Fiber length is found to be as a key parameter that play a major role in efficiency of fibers. Longer fibers are more efficient in terms of spalling prevention compared to shorter fibers. We explain this by the fact that fibers are used to bridge thermally induced cracks and longer fibers are better for ensuring percolation between fibers and thermo-mechanical cracks. For mortar, 12 mm fibers are found to be more efficient than 6 mm fibers. For concrete 1, 18 mm fibers are the most efficient compared to 6 and 12 mm long fibers. For concrete 2, 6 and 12 mm fibers have not shown complete efficiency at dosages studied. Longer fibers could be investigated for concrete 2.
- It has been found that fiber length should be selected in accordance with maximum aggregate size. For our experimental campaign, for mortar with  $D_{\max}$  of 1 mm the optimal length is 12 mm and for concrete 1 with  $D_{\max}$  of 10 mm the optimal fiber length is 18 mm.
- An influence of fiber diameter studied at same number of fibers is noted only at low dosage of fibers. With increase of fiber dosage, no influence of diameter is observed. This result

is confirmed for both water-cure and air-cure samples. At the same dosage of fibers, thinner fibers would be more effective due to higher number of fibers.

- Major influence of curing conditions has been shown. For air-cured samples, spalling has occurred later with less number of spalling events and significantly smaller spalling depth than for water-cured samples. It is explained by redistribution of water across sample thickness and presence microcracks related to drying in air, which retards formation of moisture clog and reduces spalling extent.
- During fire tests, uniaxial compressive loading provokes a modification of intrinsic permeability due to closing of cracks perpendicular to loading and initiates growth and development of cracks parallel to loading. It is therefore hard to explain results of fire tests solemnly by residual radial permeability measured at 200 °C. This shows that spalling is a coupled phenomenon originating from thermo-hydro-mechanical mechanism.

From formulation of fire resistant self-compacting concrete with polypropylene fibers, we have concluded that:

- It is possible to design concrete optimized both from rheological and fire resistant perspectives. We have developed seven mixes (one without polypropylene fibers and six with polypropylene fibers) using this approach. These mixes are found to satisfy project requirements of fresh and hardened state behavior of concrete.
- Curing conditions are confirmed to a significant factor in concrete spalling. Reference samples stored in RH 75% have spalled slightly more compared to water and tight bag cures under compressive loading of 20 MPa. Spalling for these samples has occurred later with a higher number of spalling events. We explain these results by significant drying of concrete that has created drying front of concrete delaying creation of moisture clog.
- From fire tests under loading of 20 MPa, 18 mm fibers at 1 kg/m<sup>3</sup> are found to be slightly more efficient than 24 mm fibers due to higher fiber count and lower paste volume. At higher dosages of 1.5 and 2 kg/m<sup>3</sup>, no spalling is observed with both fibers. The study identifies efficiency of long fibers at dosages lower than conventional ones (< 2 kg/m<sup>3</sup>) for high performance concrete with high water content.

### 5.3 Perspectives

Several perspectives in terms of experimental and numerical work rising from this work are presented below.

#### Experimental study

##### *Rheological behavior*

- A physical model that predicts an evolution of the yield stress of cement paste with polypropylene fibers has been developed. A further step forward would be to develop a packing model for a mix of inclusions of different size and geometry such as flexible fibers and aggregates.
- Numerical simulations of fiber reinforced composites that study conformation and orientation of fibers are necessary.

##### *High temperature behavior*

- One of the mechanisms of polypropylene fibers in heated concrete lies in their ability to flow and empty channels, i.e. melt viscosity. In this study, concrete with regular polypropylene fibers (melt viscosity of 800 Pa.s at low shear rate) have been tested. In future, it could be interesting to perform several fire tests on concrete with controlled rheology fibers (fibers HPR commercially available from Baumhüter with melt viscosity of 20 Pa.s at low shear rate) in order to comprehend better the influence of viscosity of polypropylene on mechanism of polypropylene fibers against spalling.
- Additional proposals for fire tests could include:
  - a) testing under biaxial loading
  - b) use of thermocouples and pressure sensors
  - c) testing under different compressive loads
  - d) testing under other fire curves and fire duration
  - e) testing of concrete at different age (different moisture condition)
  - f) use of steel fibers or fiber cocktail
- Increase of sample size is known to increase concrete spalling due to fire exposure. For small scale, fire tests on samples with dimensions  $0.2 \times 0.2 \times 0.1 \text{ m}^3$  have been accomplished. Next step should involve an evaluation of spalling on intermediate scale (small slabs with dimensions of  $1.7 \times 1 \times 0.3 \text{ m}^2$ ) and full scale (container with dimensions  $2.02 \times 2.02 \times 1.65 \text{ m}^2$ ) for study of size effect.

- Future work should involve measurements of mechanical properties of concrete at high temperature including: elastic modulus, compressive strength and indirect measurement of tensile strength (disk-shaped compact test or DCT), and Poisson's ratio for complete characterization of material and obtaining experimental data for numerical simulations.
- Intrinsic permeability plays a great role in development of pore pressure in heated concrete. Numerical simulations of pore pressure cannot obtain correct results when using initial intrinsic permeability measured experimentally; therefore, the values are reduced by 2-4 orders of magnitude. During heating of concrete under compressive loading, a significant modification of permeability due to opening and closing of cracks occurs. Unfortunately, a few studies present measurements of intrinsic permeability during high temperature under loading conditions. In future work, these measurements of permeability should be accomplished.
- Several first approaches in coupled X-ray and neutron imaging of concrete at high temperature are shown in literature. This impressive technique could be utilized on concrete samples with and without polypropylene fibers to have a better understanding of a) moisture clog development and b) mechanism of polypropylene fibers in moisture transport.

### **Numerical study**

- It could be interesting to compute time necessary for a polypropylene fiber to empty channel with a consideration of thermo-mechanical cracks.
- In this work, 2D mesoscopic thermo-mechanical computations of cementitious materials to have been accomplished to study different cracking patterns. 3D simulations with consideration of thermal gradients across the thickness are necessary. A further step in this direction could include a calculation of probability of fiber-crack network percolation.

# Annex

	Mortar (M)	Concrete 1 (C1)	Concrete 2 (C2)
0 (reference)			
0-air			
6/32-0.25			
6/32-0.5			
6/32-1			
6/32-2			
12/32-0.25			
12/32-0.5			
12/32-0.5-air			
12/32-1			
12/32-2			
18/32-0.5			
12/20-0.2			
12/20-0.2-air			
12/20-0.4			

**Figure A.1** Images of spalled surfaces for mortar, concrete 1 and concrete 2.

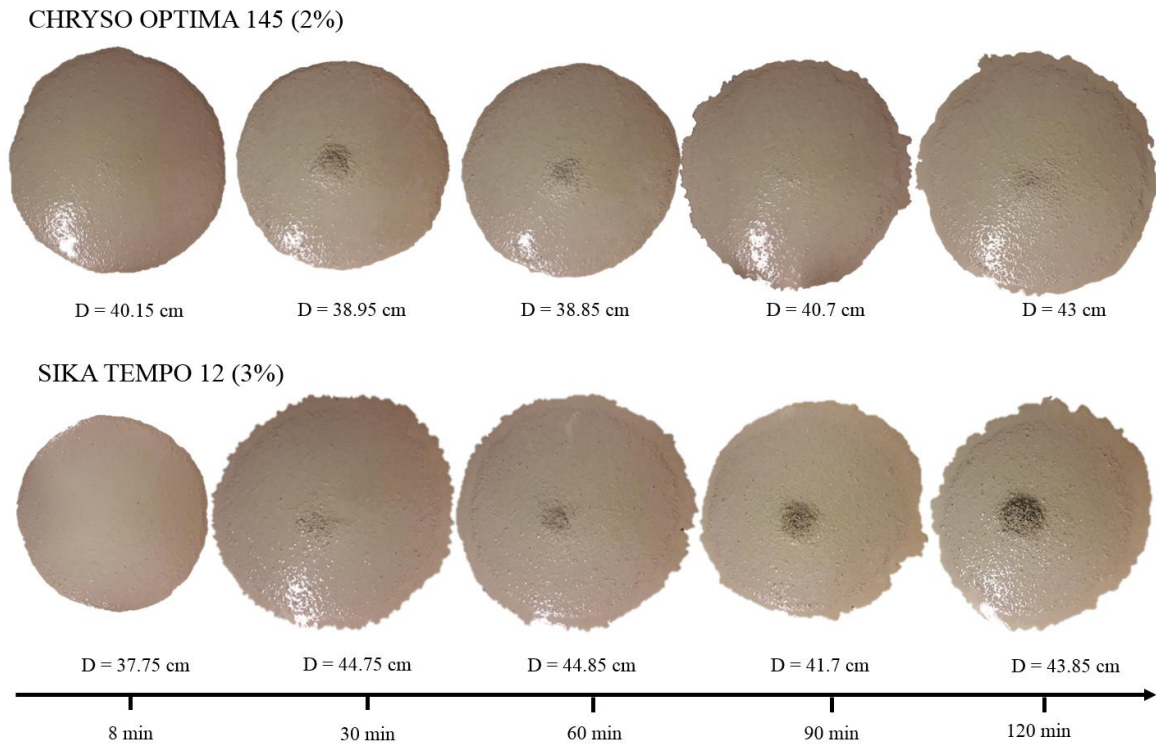


**Figure A.2.** Temporal evolution of slump flow for CEM (concrete equivalent mortar) containing Chryso Optima 145 at 2 % and Sika Tempo 12 % at 3% mass of cement.

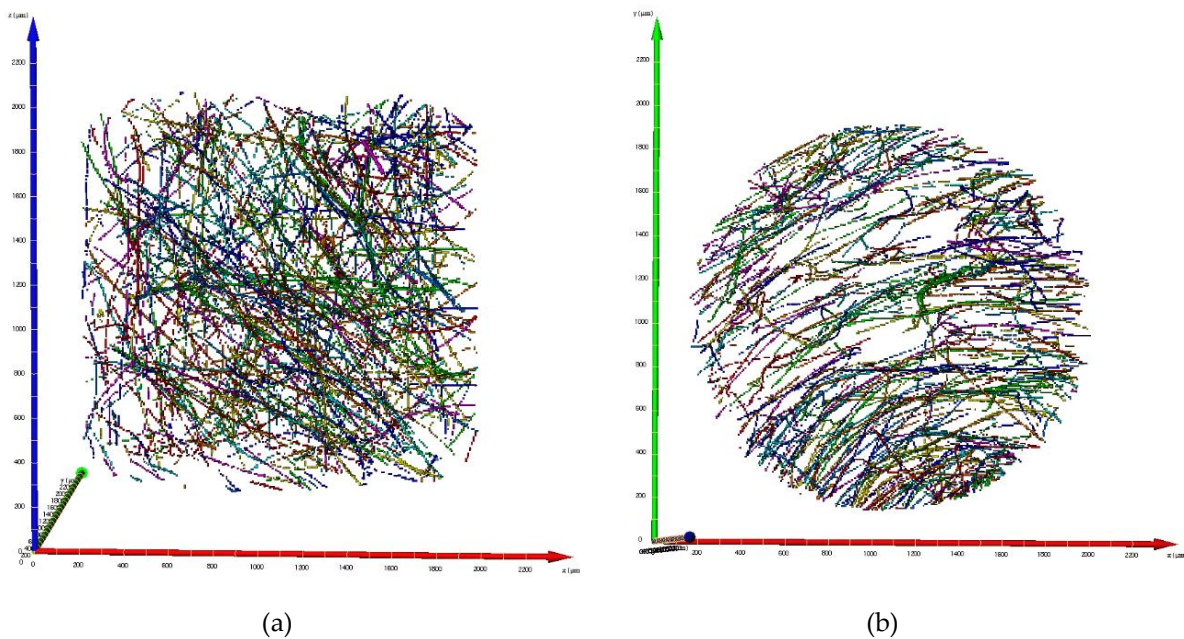


**Figure A.3.** Microtomography scanning of cement paste  $W/C = 0.5$  with polypropylene fibers  $L = 6$  mm,  $D = 34$   $\mu\text{m}$  (aspect ratio = 176) at dosage of  $2$   $\text{kg}/\text{m}^3$ . Scanned sample size is  $7.95$  mm in diameter and  $7.02$  mm in height with voxel size of  $4.5$   $\mu\text{m}$ . Images represent 3D reconstructed model (a) and 2D top view of reconstructed image (b).

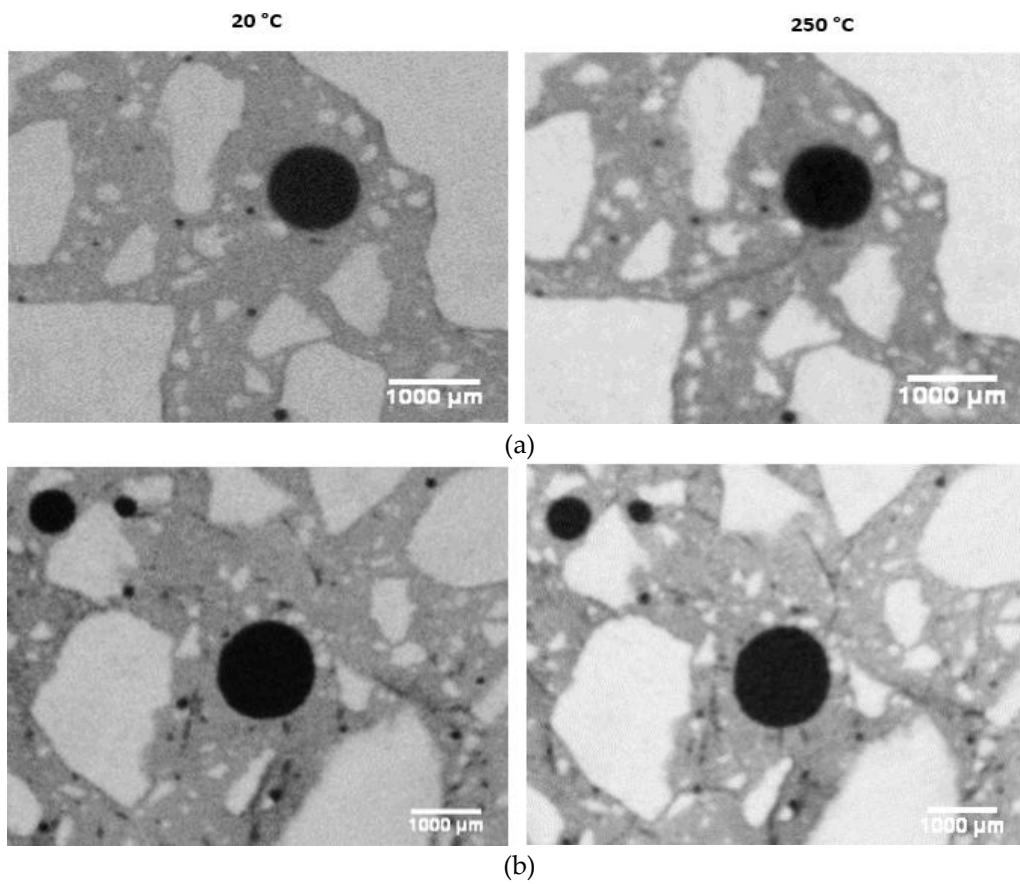


**Figure A.4.** Images of concrete at 20 and 250 °C obtained via microtomography for: concrete without fibers (voxel size 19  $\mu\text{m}$ ) (a), concrete with fibers (voxel size 21.67  $\mu\text{m}$ ) (b). Cracking is more pronounced for concrete with PP fibers at 250 °C.

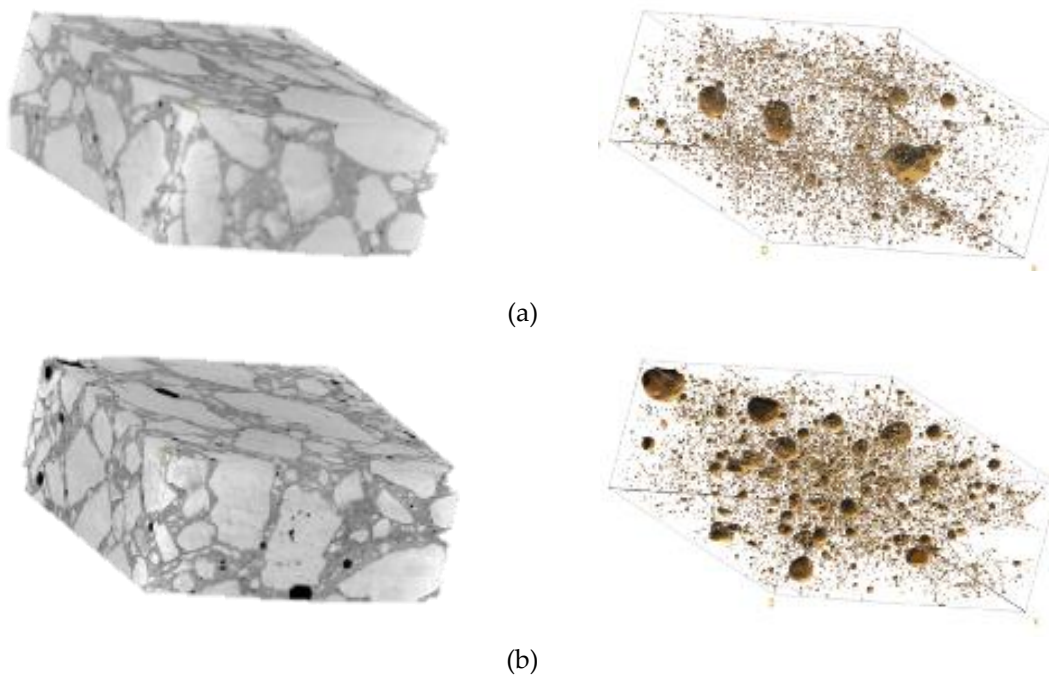


**Figure A.5.** 3D reconstruction of analyzed sample (left) and pores/air bubbles (right) in plain concrete (a), concrete with polypropylene fibers (b).